

On Modelling of Compact Tube Bundle Heat Exchangers as Porous Media for Recuperated Gas Turbine Engine Applications

Von der Fakultät für Maschinenbau, Elektrotechnik und
Wirtschaftsingenieurwesen der Brandenburgischen Technischen Universität
Cottbus zur Erlangung des akademischen Grades eines Doktor-Ingenieurs

vorgelegt von

M. Sc. Mech. Eng.

Stefan Ahlinder

geboren am 19.04.1967 in Uppsala

Vorsitzender: Prof. Dr.-Ing. C. Egbers
Gutachter: Prof. Dr.-Ing. H. P. Berg
Gutachter: Prof. Dr.-Ing. K. Vogeler
Tag der mündlichen Prüfung: 28.04.2006

Summary

A computational tool and a methodology for steady state heat exchanger simulations of recuperated gas turbines and aero-engines have been developed. As an example a compact tube bundle heat exchanger with oval shaped tubes was chosen. The simulation tool proved to work for different layouts of the heat exchanger and for different geometrical configurations of the gas turbine engine exhaust ducts. The resistance tensors were tuned against both CFD-data and experimental data and the computational model was to some extent validated against experimental results. For the validation isothermal experimental data from the Laboratory of Fluid Mechanics and Turbomachinery at the Technical University of Thessaloniki was used together with hot gas channel data from MTU. The calculated and measured velocity profiles showed an acceptable agreement that in some of the cases was even very good. The calculated pressure drop deviated less than 10% for the compared cases, which must be considered to be acceptable. The calculated results for the hot gas cases showed an exaggerated heat transfer rate, most likely due to the use of a cold side heat transfer correlation for fully turbulent flow, although the Reynolds numbers indicated transitional flow.

Zusammenfassung

Kernpunkt der vorliegenden Dissertation ist die Entwicklung eines Computerprogramms und einer Methodologie zur Simulation stationärer Wärmetauschertriebwerke. Als Beispiel wurde ein kompakter Röhrenbündel-Wärmetauscher mit ovalem Röhrenquerschnitt gewählt. Das Simulationsprogramm ist für unterschiedliche Konfigurationen von Wärmetauschern und verschiedene Abgasschachtgeometrien der Gasturbine anwendbar. Die Widerstandstensenoren wurden sowohl gegen CFD-Daten als auch gegen experimentelle Daten abgeglichen und das Simulationsprogramm wurde zu einem gewissen Grad anhand experimenteller Ergebnisse validiert. Für die Validierung wurden –neben Daten eines Heißgaskanals der MTU– isothermale experimentelle Daten des Strömungsmechanik- und Turbomaschinen-Labors der Technischen Universität Thessaloniki benutzt. Die berechneten und gemessenen Geschwindigkeitsprofile stimmen gut und in einigen Fällen auch sehr gut überein. Der berechnete Druckverlust hatte eine Abweichung von weniger als 10% für die gemessenen Fälle, was als hinreichend genau angesehen werden kann. Die berechneten Ergebnisse für die Heißgasströme zeigten eine erhöhte Wärmeübertragungsrate, die sehr wahrscheinlich durch die Anwendung einer Korrelation der kalten Seite für vollturbulente Strömung verursacht wird, obwohl die Reynoldszahlen transitionale Strömung nahelegen.

For

David

Contents

1 Introduction.....	1
1.1 Recuperated gas turbine engines.....	1
1.2 Gas turbine recuperators.....	4
1.3 Objectives.....	7
2 Tube bundle flow.....	7
3 CFD analyses of a staggered elliptic tube bundle.....	10
3.1 CFX-TASCflow.....	11
3.2 Computational grid.....	12
3.3 Computational procedure.....	13
3.3.1 Boundary conditions.....	13
3.3.2 Computational attributes.....	15
3.4 Results.....	16
4 Porous media.....	26
5 Porous media momentum sink terms.....	29
5.1 Source term expressions.....	32
5.2 Derivation of resistance tensors.....	33
5.3 Pressure gradient across the tube bundle.....	35
5.4 Pressure gradient along the tube bundle.....	38
5.5 Porous media results.....	40
6 Porous media energy sink term.....	45
6.1 Cold side energy equation.....	47
6.2 Hot side energy equation.....	50
6.3 Energy equation source term.....	51
6.4 Cold side heat transfer correlation.....	52
6.5 Hot side heat transfer correlation.....	55
7 Heat exchanger code.....	66
7.1 Temperature calculation procedure.....	69
7.2 Cold gas flow distribution.....	72
7.3 Structure of the heat exchanger simulation code.....	73
8 Validation.....	75

8.1 Hot gas experiments.....	76
8.2 Experiments on a 1:1 half heat exchanger matrix.....	86
8.2.1 Zero degree inclination angle.....	88
8.2.2 Inclination angle of 15 degrees.....	109
8.2.3 Inclination angle of 45 degrees.....	112
8.3 Conclusions.....	121
9 Applications.....	122
9.1 Exhaust gas casing of the CLEAN engine.....	122
9.1.1 Experimental Model.....	123
9.1.2 Operating Conditions.....	124
9.1.3 The CFD-model.....	124
9.1.4 Numerical settings.....	126
9.1.5 Results.....	127
9.1.6 Conclusions.....	137
9.2 Exhaust gas casing of an compact industrial gas turbine.....	137
9.2.1 The CFD model.....	138
9.2.2 Operating Conditions.....	139
9.2.3 Numerical Settings.....	140
9.2.4 Results.....	141
9.2.5 Conclusions.....	147
10 Suggestions for future work.....	148
11 Summary.....	149
Acknowledgements.....	151
References.....	152
Appendix A, Water channel tests.....	159
Appendix B, Angles used in the transformation matrices.....	164
Appendix C, Momentum sources and active coefficients.....	166
C1. Source Terms and Active Coefficients for the Straight Parts.....	166
C2. Source Terms and Active Coefficients for the Bends.....	169

List of figures

Figure 1.1 Simple gas turbine cycle with heat exchange.	2
Figure 1.2 Thermal efficiency of different engine concepts.	3
Figure 1.3 Advanced cycle concept for Intercooled Recuperative Aero engine (IRA)	4
Figure 1.4 Heat exchanger design used in the AEROHEX-project and the current study.	6
Figure 1.5 Oval shaped tube with two inner ducts.	6
Figure 1.6 Bundle of oval shaped tubes.	7
Figure 2.1 Hydraulic drag coefficient per tube row for three different staggered tube bundles	8
Figure 3.1 Mesh at the inlet part of the heat exchanger matrix.	12
Figure 3.2 Two dimensional projection of the tube. Angle of attack.	14
Figure 3.3 Three dimensional representation of the tube. Inclination angle.	14
Figure 3.4 Stream lines for zero degrees attack angle, turbulent case.	18
Figure 3.5 Stream lines for 20 degrees attack angle, turbulent case.	18
Figure 3.6 Stream lines for 40 degrees attack angle, turbulent case.	18
Figure 3.7 Stream lines for 60 degrees attack angle, turbulent case.	18
Figure 3.8 Stream lines for 80 degrees attack angle, turbulent case.	19
Figure 3.9 Pressure loss coefficient per tube row.	20
Figure 3.10 Turbulence intensity, zero degrees inflow angle.	21
Figure 3.11 Dimensionless dissipation, zero degrees inflow angle.	22
Figure 3.12 Ratio of turbulent to molecular viscosity, zero degrees inflow angles.	23
Figure 3.13 Decrease of crosswise velocity component, turbulent cases.	24
Figure 3.14 Decrease of crosswise velocity component, turbulent cases.	26

Figure 5.1 Heat exchanger lancet matrix with local Cartesian coordinate system.	33
Figure 5.2 Decrease of crosswise velocity component, attack angle 80 degrees, turbulent case.	37
Figure 5.3 Dimensionless pressure loss along the tubes.	39
Figure 5.4 Decay of the cross-wise velocity component for different number of nodes across the matrix for the attack angle 80 degrees, turbulent cases.	43
Figure 5.5 Ratio of turbulent and molecular viscosity, turbulence length scale 35 transversal pitches.	44
Figure 5.6 Turbulence intensity, $l=35$ transversal pitches.	45
Figure 6.1 Cold side indexing and sweep direction.	50
Figure 6.2 Heat exchanger lancets.	52
Figure 6.3 Heat transfer characteristics for fully developed pipe flow.	53
Figure 6.4 Measured local Nusselt number in the entry region of a circular tube for various entry configurations with constant wall temperature.	54
Figure 6.5 Tube bundle arrangement and definition of characteristic quantities.	59
Figure 6.6 Nusselt number for Ovalrohr 2, $t_1=1,01$ and $t_q=1,36$.	62
Figure 6.7 Nusselt number for Ovalrohr 2, $t_1=0,92$ and $t_q=1,73$.	63
Figure 6.8 Nusselt number for Ovalrohr 2, $t_1=0,665$ and $t_q=2,21$.	64
Figure 6.9 Ovalrohr 2, Correlated Nusselt number vs experimental Nusselt number.	65
Figure 7.1 Regions and naming conventions for the heat exchanger porosity model.	67
Figure 7.2 Cold side temperature convergence behaviour.	71
Figure 7.3 Hot gas energy equation convergence behaviour.	72

Figure 8.1 Sketch of the MTU heat exchanger showing the cold side inlet and outlet on the front.	77
Figure 8.2 Temperature measurement positions on the heat exchanger. Top view above and side view below.	77
Figure 8.3 Grid for the CFD-model of the hot gas experimental set-up.	78
Figure 8.4 Outlet temperature distribution, case 1.	84
Figure 8.5 Outlet temperature distribution, case 2.	85
Figure 8.6 Outlet temperature distribution, case 3.	86
Figure 8.7 Experimental set-up for the zero inlet angle cases.	88
Figure 8.8 Part of the grid with a leakage between bend and side wall.	88
Figure 8.9 Part of the grid with a blockage between bend and side wall.	89
Figure 8.10 $Re = 1077$, U-component at the outlet plane.	91
Figure 8.11 $Re = 1077$, W-component at the outlet plane.	92
Figure 8.12 $Re = 1077$, U-component at the 25 mm plane.	93
Figure 8.13 $Re = 1077$, W-component at the 25 mm plane.	94
Figure 8.14 $Re = 1077$, U-component at the 8 mm plane.	95
Figure 8.15 $Re = 1077$, W-component at the 8 mm plane.	96
Figure 8.16 Front and back covers on the heat exchanger.	97
Figure 8.17 $Re = 3320$, covered back, U-component at the outlet plane.	98
Figure 8.18 $Re = 3320$, covered back, W-component at the outlet plane.	99
Figure 8.19 $Re = 3320$, covered back, U-component at the 25 mm gap plane.	100
Figure 8.20 $Re = 3320$, covered back, W-component at the 25 mm gap plane.	101
Figure 8.21 $Re = 3320$, covered back, U-component at the 8 mm gap plane.	102
Figure 8.22 $Re = 3320$, covered back, W-component at the 8 mm gap plane.	103

Figure 8.23 Re = 3365, covered front, U-component at the outlet plane.	104
Figure 8.24 Re = 3365, covered front, W-component at the outlet plane.	105
Figure 8.25 Re = 3365, covered front, U-component at the gap 25 mm plane.	106
Figure 8.26 Re = 3365, covered front, W-component at the gap 25 mm plane.	107
Figure 8.27 Re = 3365, covered front, U-component at the gap 8 mm plane.	108
Figure 8.28 Re = 3365, covered front, W-component at the gap 8 mm plane.	109
Figure 8.29 Measurement planes for 15 degrees inclination angle, top view.	110
Figure 8.30 Grid for the 15 degrees inclination case.	110
Figure 8.31 Inclination 15 degrees, U velocity component at the outlet plane.	111
Figure 8.32 Inclination 15 degrees, W velocity component at the outlet plane.	112
Figure 8.33 Measurement planes for 45 degrees inclination angle, top view.	113
Figure 8.34 Part of the grid for the 45 degrees inclination case.	113
Figure 8.35 Inclination 45 degrees, U-component at the outlet plane.	114
Figure 8.36 Inclination 45 degrees, W-component at the outlet plane.	115
Figure 8.37 Inclination 45 degrees, U-component at the gap 25 mm plane.	116
Figure 8.38 Inclination 45 degrees, W-component at the gap 25 mm plane.	117
Figure 8.39 Inclination 45 degrees, covered back, U-component at the outlet plane.	118
Figure 8.40 Inclination 45 degrees, covered back, W-component at the outlet plane.	119

Figure 8.41 Inclination 45 degrees, covered back, U-component at the gap 25 mm plane.	120
Figure 8.42 Inclination 45 degrees, covered back, W-component at the gap 25 mm plane.	121
Figure 9.1 Heat exchanger shown in the 2 possible positions within the casing.	123
Figure 9.2 CFD model of configuration 1.	124
Figure 9.3 CFD model of configuration 2.	124
Figure 9.4 Grid for configuration 1.	125
Figure 9.5 Grid for half of the heat exchanger	125
Figure 9.6 Vector plot with velocity distribution on the symmetry plane for both configurations.	128
Figure 9.7 Hot gas temperature distributions in the symmetry plane for both configurations.	129
Figure 9.8 Velocity, in the normal direction, through the heat exchanger, symmetry plane.	130
Figure 9.9 Configuration 1, hot gas temperature distribution in three different planes in the heat exchanger.	131
Figure 9.10 Configuration 2, hot gas temperature distribution in three different planes in the heat exchanger.	132
Figure 9.11 Configuration 1, cold gas temperature distribution in three different planes in the heat exchanger.	133
Figure 9.12 Configuration 2, cold gas temperature distribution in three different planes in the heat exchanger.	134
Figure 9.13 Configuration 1, distribution of the temperature difference between the hot and the cold gas in three different planes in the heat exchanger.	135
Figure 9.14 Configuration 2, distribution of the temperature difference between the hot and the cold gas in three different planes in the heat exchanger.	136

Figure 9.15 Side view of the compact industrial gas turbine.	137
Figure 9.16 Front view of the compact industrial gas turbine.	137
Figure 9.17 Industrial gas turbine grid.	138
Figure 9.18 Heat exchanger grid, side view.	139
Figure 9.19 Grid in the heat exchanger bend, view parallel to the collector and distributor tubes.	139
Figure 9.20 Hot gas temperature distribution 5 cm above the heat exchanger.	142
Figure 9.21 Hot gas temperature distribution in the heat exchanger.	143
Figure 9.22 Cold gas temperature distribution in the heat exchanger.	144
Figure 9.23 Distribution of the temperature difference between the hot and the cold gases in the heat exchanger.	145
Figure 9.24 Velocity profiles for the heat exchanger outer parts.	146
Figure 9.25 Velocity profiles for the heat exchanger inner parts.	147
Figure A.1 Flow characteristics in the exhaust gas casing.	160
Figure A.2 Vortices at the HEX inlet, position 6.	160
Figure A.3 Flow field below the HEX, position 4.	161
Figure A.4 Calculated flow field just below the HEX, positions 4 and 6	161
Figure A.5 Flow field at the side below the HEX, position 5.	162
Figure A.6 Calculated flow field at the side below the HEX, position 5.	162
Figure A.7 HEX outlet flow field.	163
Figure A.8 Calculated HEX outlet flow field.	163

List of tables

Table 3.1 Investigated inflow angles.	14
Table 3.2 Numerical boundary conditions.	15

Table 3.3 Computational attributes.	16
Table 3.4 Pressure loss coefficients per tube row, normalized with the pressure loss coefficient for tube row 6 of the zero angle case, for different attack angles for the turbulent flow cases.	17
Table 3.5 Pressure loss coefficients per tube row, normalized with the pressure loss coefficient for tube row 6 of the zero angle case, for different attack angles for the laminar flow cases.	18
Table 3.6 Pressure loss coefficients per tube row, normalized with the pressure loss coefficient for tube row 6 of the zero angle case, for different inclination angles for the turbulent flow cases.	24
Table 3.7 Pressure loss coefficients per tube row, normalized with the pressure loss coefficient for tube row 6 of the zero angle case, for different inclination angles for the laminar flow cases.	24
Table 5.1 Summary of porous media results.	40
Table 5.2 Influence of number of nodes across the heat exchanger matrix on the pressure drop, turbulent cases.	40
Table 8.1 Numerical settings for the hot gas cases.	74
Table 8.2 Approximate Reynolds numbers.	74
Table 8.3 First numerical pressure drop results.	75
Table 8.4 Global results for hot gas case 1.	77
Table 8.5 Global results for hot gas case 2.	77
Table 8.6 Global results for hot gas case 3.	77
Table 8.7 Numerical settings for the half heat exchanger cases.	80
Table 8.8 Total pressure drop results for the cases without cover.	82
Table 8.9 Total pressure drop results for the cases with covered back of the bend.	87
Table 8.10 Total pressure drop results for the cases with covered front of the bend.	91

Table 8.11 Total pressure drop results for the 15 degrees inclination case.	95
Table 8.12 Total pressure drop results for the 45 degrees inclination case without cover.	98
Table 8.13 Total pressure drop results for the 45 degrees inclination case with covered back part of the bend.	101
Table 9.1 CLEAN application, numerical settings.	108
Table 9.2 CLEAN pressure drop and temperature results.	109
Table 9.3 Industrial gas turbine, summary of the results.	120

Nomenclature

Latin letters

A	Area
A_G	Tube cross section area
A_i	Active coefficients in the source term linearisation
c_F	Forchheimer drag constant
c_p	Specific heat at constant pressure
c_μ	k - ϵ turbulence model constant
d	Particle dimension, fluid volume per heat transfer area
D	Diameter
D_h	Hydraulic diameter
D_{ij}	Darcy second order flow resistance tensor equal to the inverse of the permeability tensor
Eu	Euler number
F_{ij}	Forchheimer second order flow resistance tensor
g	Gravitational acceleration
h	Specific enthalpy
i	index
I, J, K	Coordinate directions
k	Kinetic energy of turbulent fluctuations per unit mass, proportional constant
K	Permeability
K_{ij}	Second order flow resistance tensor
l	Dimension of the Representative Elementary Volume (REV)
L	Length scale, system dimension
N_R	Number of tube rows
Nu	Nusselt number
p	Pressure
Pe	Peclet number
Pr	Prandtl number
Pr_t	Turbulent Prandtl number
q'	Heat flux
Re	Reynolds number
S_{cold}	Cold side energy source term
S_{hot}	Hot side energy source term

S_i	Momentum source
S_l	Longitudinal pitch
S_q	Transversal pitch
St	Stanton number
t	Time
T_{cold}	Cold side temperature
T_{hot}	Hot side temperature
u, v, w	Mean velocity components in x, y, z directions
U	Velocity, Wetted perimeter
V	Volume
\mathbf{v}	Darcy velocity
V	Intrinsic velocity
x, y, z	Rectangular Cartesian coordinates

Greek letters

α	Heat transfer coefficient
α, β, γ	Angles of the transformation matrices
δ	Thickness
δ_{ij}	Kronecker delta
Δx	Incremental change in x
ε	Dissipation per unit mass
ϵ_H	Thermal eddy diffusivity
ϵ_M	Momentum eddy diffusivity
ζ	Pressure loss coefficient
η	Efficiency
θ	Angle in the heat exchanger bend cylindrical coordinate system
λ	Flow resistance factor, thermal conductivity
μ	Molecular viscosity
μ_t	Eddy viscosity
ρ	Mass density
τ	Shear stress
τ_{ij}	Viscous stress tensor
ϕ	Porosity

Subscripts

<i>f</i>	Fluid
<i>ref</i>	Reference
<i>th</i>	Thermal
<i>w</i>	Wall
<i>x</i>	Local
<i>x,y,z</i>	Rectangular Cartesian coordinate directions
∞	Final condition

Superscripts

mod	Modified quantity
+	Sublayer-scaled value

1 Introduction

Heat exchangers are found in various industrial applications and everyday life where there is a need for transportation of heat between different media. Examples of such applications are e.g. electronic devices, radiators, air-conditioning systems, etc. In this work the focus is put on the application of heat exchangers as recuperators in aero engines and gas turbines.

1.1 Recuperated gas turbine engines

Gas turbine engine development has so far mainly focused on the increase in pressure ratio and turbine inlet temperatures in addition to increased by-pass ratio. This has had a positive effect on noise, fuel consumption and thus also CO₂ emissions. A drawback of this strategy, however, has been an undesired increase in NO_x emissions. With growing awareness of the environmental impact of commercial aviation together with an annual growth of this industry of 5% (Scheugenpflug et al) the demand for more efficient and environmentally friendlier gas turbine engines has increased. Since the potential for raising the overall pressure ratio and turbine inlet temperature further is limited by the available turbine materials and the NO_x formation at high temperatures the only known ways to reduce fuel consumption and NO_x are to improve the efficiency of the gas turbine engine components or to use a more efficient cycle. The latter can be done by making use of heat exchangers. A recuperator placed in the exhaust gas stream and used to warm up the combustor inlet air can significantly improve the efficiency of the engine for low overall pressure ratios. This can easily be shown for a simple gas turbine cycle by using figure 1.1 below.

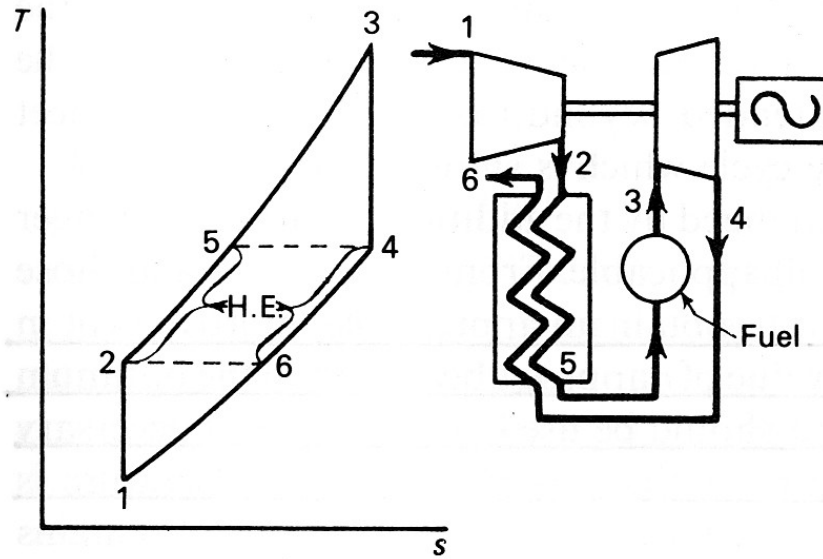


Figure 1.1 Simple gas turbine cycle with heat exchange.
(Cohen et al)

The thermal efficiency for the recuperated gas turbine cycle in figure 1.1 can be expressed as

$$\eta_{th} = \frac{c_p(T_3 - T_4) - c_p(T_2 - T_1)}{c_p(T_3 - T_5)} \quad (1.1)$$

If the cycle is studied without recuperator the efficiency looks like

$$\eta_{th} = \frac{c_p(T_3 - T_4) - c_p(T_2 - T_1)}{c_p(T_3 - T_2)} \quad (1.2)$$

and since $T_3 - T_5 < T_3 - T_2$ it is obvious that the thermal efficiency is higher for the recuperated engine. However, if the pressure ratio is too high the compressor outlet temperature will be higher than the turbine outlet temperature and the compressor air will get cooled in the recuperator and as a result lead to a reduced efficiency. This fact makes the recuperator only interesting for gas turbines with low pressure ratios. Such gas turbines could be attractive for different industrial applications such as reserve power generation or for applications where high compactness is of importance, e.g. in sea vessels or armed vehicles. Due to the additional pressure losses,

associated with the heat exchangers, the specific work output will be slightly lower for a recuperated gas turbine compared to a conventional one. Should, in some applications, from time to time maximum power output be of priority then the recuperators, on such occasions, could be by-passed. Since recuperated gas turbines have to be designed with lower overall pressure ratios, the demands on the gas turbine components are lower and the core engine can be manufactured cheaper than a conventional engine. If a highly efficient recuperator can be produced at low cost this concept would be very competitive compared to conventional gas turbines.

In order to achieve an increased efficiency for higher pressure ratios the compressor outlet temperature has to be reduced. This can be achieved by means of an intercooler. The intercooler will in addition to a lower compressor outlet temperature also lead to a reduction of the compression work. By using heat exchangers as intercooler and recuperators the efficiency can be increased for a large range of pressure ratios, as demonstrated in figure 1.2 below. If, in an intercooled and recuperated gas turbine engine, overall pressure ratio and combustion temperature are kept within acceptable limits a significant reduction of the NO_x emissions can be achieved.

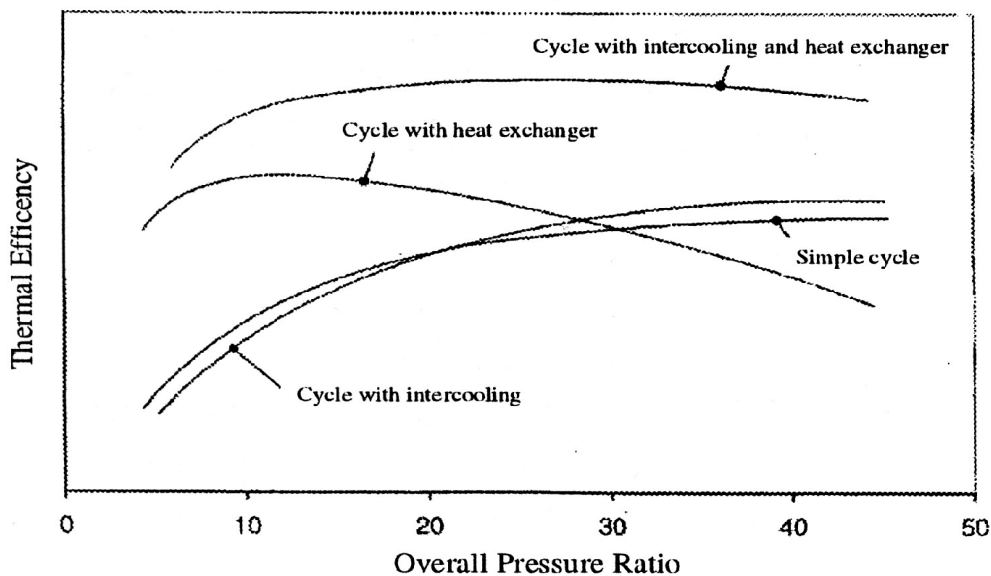


Figure 1.2 Thermal efficiency of different engine concepts.
(Scheugenpflug et al)

An example of an advanced cycle is the so called IRA-engine (Intercooled Recuperated Aero-engine) that is being investigated in the industry, see figure

1.3. This engine has in addition to the intercooler and the recuperator a geared fan that allows the by-pass ratio to be increased to around 15 in order to achieve lower noise levels. The IRA concept has the potential for a CO₂ reduction of 20% and a reduction of NO_x by 80% (Scheugenpflug et al). The intercooler and the recuperator reduce the fuel consumption and allow for less fuel to be carried. On the other hand heat exchangers increase engine weight and therefore it is of outermost importance that the thermal and aerodynamical efficiencies of the heat exchangers are high. Provided the heat exchangers are efficient enough the weight increase of the engine could be more than compensated for by the reduction in fuel load and thereby an increased pay load could be carried. It is therefore of great importance to have simulation tools for analysing different design alternatives in order to find optimum positions of the heat exchangers in new concepts for advanced intercooled and recuperated aero engines.

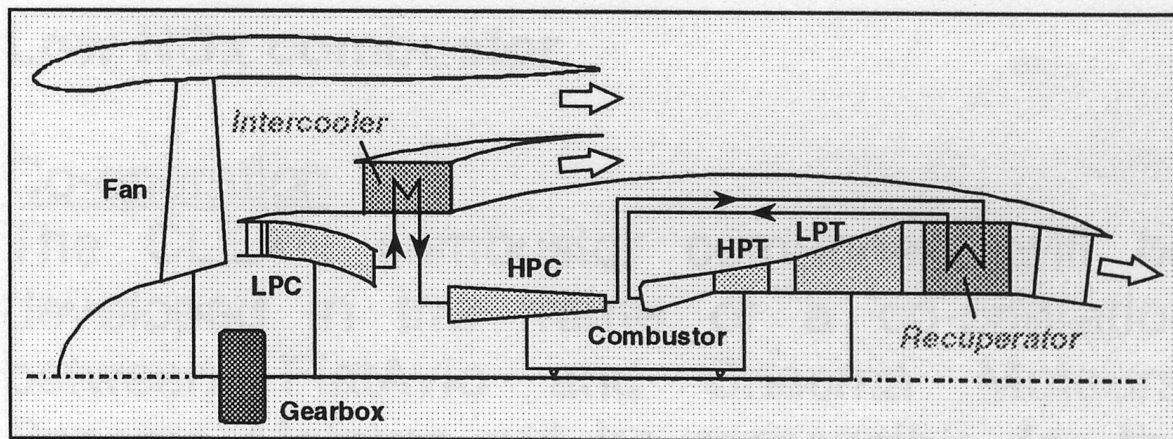


Figure 1.3 Advanced cycle concept for Intercooled Recuperative Aero engine (IRA) (Scheugenpflug et al).

1.2 Gas turbine recuperators

The design of heat exchangers involves consideration of both the heat transfer rates and mechanical pumping power expended to overcome fluid friction and move the fluids through the heat exchanger. For a heat exchanger operating

with high density fluids, the friction power expenditure is generally small relative to the heat transfer rate. This means that the friction power is seldom a controlling influence. However, for low density fluids, such as gases, it is very easy to expend as much mechanical energy in overcoming friction as the amount of transferred heat (Kays and London). Thus, it is of great importance that the gas turbine recuperators have a high thermal and aerodynamic efficiency. In addition to high thermal and aerodynamic efficiencies the following requirements apply for a gas turbine recuperator (Pellischek and Reile)

- Compactness
- Resistance to high temperatures
- Insensitivity to mechanical shock loads
- Good thermal shock behaviour
- Ability to withstand high differential pressures
- Low weight

These requirements render most heat exchangers unsuitable such as e.g. the plate fin type and the only known type of heat exchanger that can withstand the thermal and mechanical loads that will occur in a gas turbine application is the tube bundle heat exchanger. In order to improve thermal and aerodynamic efficiencies of tube bundle heat exchangers as well as the compactness different tube shapes have been investigated and the oval shape has been found to be superior to the circular one (Bähr, Hanke, Pellischek and Reile).

In this study a tube bundle heat exchanger with oval shaped tubes has been chosen as an example, see figures 1.4-1.6. This heat exchanger concept was originally developed by MTU and has been thoroughly described in a number of publications (e.g. Pellischek and Kumpf, Pellischek and Reile, Eggebrecht and Schlosser). It was also chosen for the AEROHEX-project (GRD1-1999-10602), the 5th EU frame work programme, and has been shown to perform very well (Eggebrecht and Schlosser). The heat exchanger consists of a distributor, from where the compressor air enters the tubes, and a collector, from where the air is delivered to the combustor, as can be seen in figure 1.4 below. The hot gas flows through the bundles which are mounted between the distributor and the collector. These bundles are bent making the heat exchanger a mixture of a cross flow and a counter flow heat exchanger. Furthermore, the bends have the advantage of making the heat exchanger

insensitive to thermal expansion, since the bundles have the possibility to expand freely.

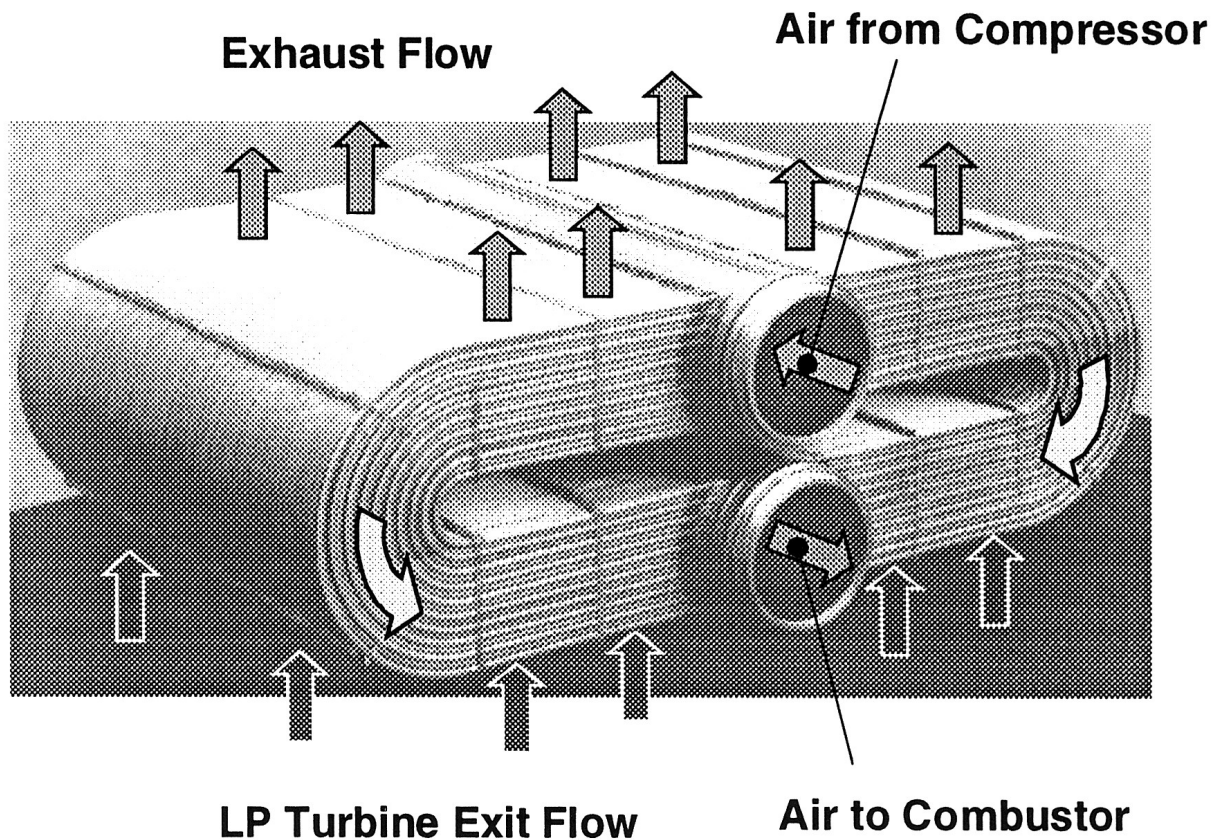


Figure 1.4 Heat exchanger design used in the AEROHEX-project and the current study. (Scheugenpflug et al).

The compressor air flows on the inside of the tubes. The inner part of the tubes is, of structural reasons, divided in two ducts, as shown in figure 1.5 below.

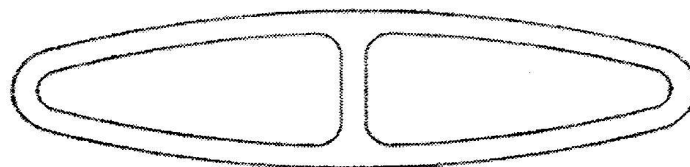


Figure 1.5 Oval shaped tube with two inner ducts.

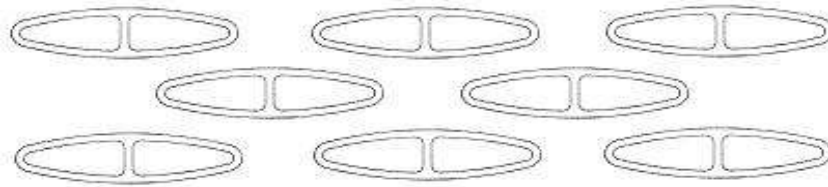


Figure 1.6 Bundle of oval shaped tubes.

1.3 Objectives

The objective of this thesis is to develop a computational software/tool and a methodology for steady state heat exchanger simulations of recuperated gas turbines and aero-engines. The simulation tool shall work for different layouts of the heat exchanger described in section 1.2 and for arbitrary geometrical configurations of the gas turbine engine exhaust ducts. The focus in this study has been put on the development of the computational software and the computational methodology and not on the optimisation of the heat transfer and/or pressure drop correlations of staggered elliptic tube bundle heat exchangers.

2 Tube bundle flow

Pressure drop and heat transfer rates are important parameters in the design of heat exchangers and a lot of the research work done on tube bundles has been focused on the study of these quantities. The drag of tube bundles is determined by the flow pattern in the space between the tubes. Significant accelerations and decelerations of the flow, characteristic to the tube bundles, form zones of vortices, which induce losses of the flow's kinetic energy. Consequently the arrangement of the tubes and the tube geometry affect the drag of the tube bundle. At low Reynolds numbers the drag is represented by viscous friction and is directly proportional to the velocity. When the Reynolds number is increased eddies are generated and cause loss of kinetic energy in addition to the viscous friction making the relation between the velocity and the drag, for very high Reynolds numbers, quadratic. This principal behaviour

is the same for different bundle configurations and tube geometries. An example of the variation of the drag coefficient with Reynolds number is shown in figure 2.1 below.

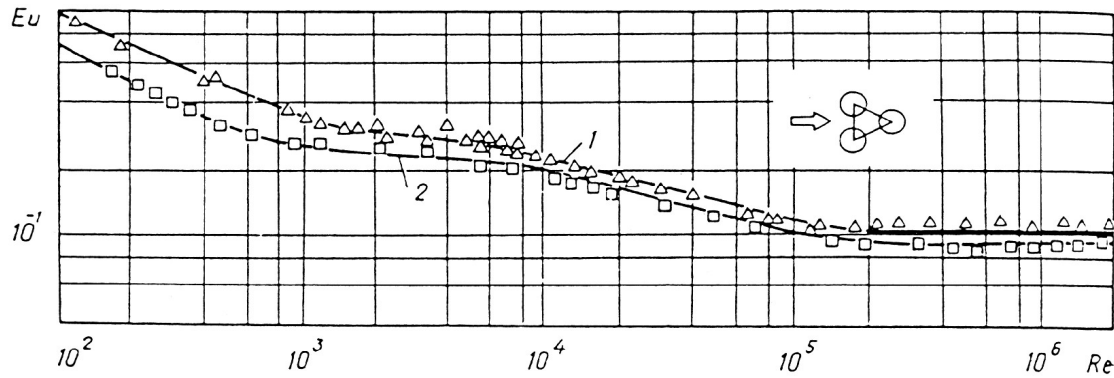


Figure 2.1 Hydraulic drag coefficient per tube row for three different staggered tube bundles with the following pitch/diameter ratios: 1) 1,30 x 1,30; 2) 1,50 x 1,50. (Zukauskas et al, 1988).

For low Reynolds number flows ($Re < 1000$), with no turbulence effects, the Nusselt number for the first row is close to the Nusselt number for the inner rows (Zukauskas, Hanke, Bähr). When the Reynolds number is increased turbulence first starts near the bundle exit and then works its way upstream (Bergelin). For flows at higher Reynolds numbers ($Re > 1000$), when turbulence is generated in the first tube rows, the heat transfer for the inner rows down stream of the 3rd row is almost constant with position and higher than for the first tube rows (Zukauskas, Stephan and Traub, Hanke, Bähr). In staggered banks the turbulence generating role of the first and second rows is more pronounced than in in-line banks. According to Zukauskas et al (1988) the free stream turbulence only affects tubes in the first and second rows and the turbulence further within a bundle is a function of the bundle configuration and the Reynolds number. Stephan and Traub investigated the influence of turbulence on pressure drop and heat transfer for staggered bundles of four and five tube rows for Reynolds numbers between 12000 and 70000. They varied the turbulence intensity between 0,8% and 25 % and noticed that the drag coefficient for staggered bundles was not affected at all by the turbulence intensity, but discovered that increased turbulence intensity leads to improved heat transfer rates for the first two rows in the entire investigated Reynolds number range.

Due to the more stream line shaped form of an elliptic tube with the major axis aligned with the flow direction the point of separation moves downstream at the same flow conditions compared to a cylindrical tube. The vortex area behind the tube is significantly smaller than behind a cylindrical tube and so is also the flow resistance. The pressure loss in an elliptic tube bundle is therefore smaller than in a bundle of cylindrical tubes. However, the difference is not as large as between the single tubes (VDI-Wärmeatlas). The drag on a tube bundle is proportional to the number of tube rows. When the bundle only contains a small number of tube rows the discharge loss from the bundle might contribute to a major part of the total bundle drag and has to be considered when estimating the tube bundle pressure drop. It was noticed by Scholz that, in the turbulent regime, the pressure loss coefficient for each tube row from the fifth row onwards is constant. The same is indicated by the experiments of Hanke where the number of rows is varied and no difference in pressure loss coefficient is seen after four to five rows.

A variation in properties of viscous fluids might have a significant effect on the drag of tube bundles at low Reynolds numbers (Zukauskas, 1989). At higher Reynolds numbers the effect of thermally induced physical properties in the boundary layer on the drag is insignificant, since surface friction is a small fraction of the total drag. Under non-isothermal conditions Zukauskas proposes the following compensation for Reynolds numbers below 1000

$$Eu_f = Eu \left(\mu_w / \mu_f \right)^p \quad (2.1)$$

where

Eu_f is the Euler number during heating or cooling.

Eu is the Euler number under isothermal conditions.

μ_w is the dynamic viscosity at the wall temperature.

μ_f is the dynamic viscosity at the flow temperature.

p varies between 0,5 at a Reynolds number of unity and 0 at a Reynolds number of 1000.

From equation (2.1) it is clear that for a gas flow with moderate temperature differences between the wall and the fluid the effect on the drag coefficient will be negligible. If, on the other hand, a fluid with significant variation of its physical properties with temperature is used then a compensation of the drag coefficient might be necessary.

Goulas et al (Goulas et al, 2003) performed wind tunnel tests on two identical staggered elliptic tube bundles one located a distance downstream of the other. Pressure drop measurements were made and it was observed that the second bundle had significantly lower, approximately 30%, drag than the first bundle although the bundles were geometrically identical. Responsible for this is the quality of the turbulence and the size of the dominating vortices entering the second matrix. The flow keeps its coherent nature while entering the second matrix and the existence of vortices helps the flow to roll on with small resistance while passing through the second matrix and yields as a result less drag. Goulas et al had their hypothesis verified by introducing a very fine grid between the matrices and thereby destroying large vortices and producing smaller when at the same time keeping the turbulence level constant. This led to a drag of the second matrix close to the drag of the first matrix. The effect mentioned was also, as could be expected, stronger for high Reynolds number flows.

3 CFD analyses of a staggered elliptic tube bundle

Since no detailed experimental data is available for the heat exchanger matrix in question CFD analyses are performed. These CFD analyses are made in order to investigate the flow field inside the matrix for a variation of inlet flow conditions. The flow through the heat exchanger matrix is highly complicated and time dependent with Karman vortices created at the bundle outlet. In order to simulate the flow correctly the boundary layers must be resolved and the flow field calculated unsteady. For turbulent flows the boundary layers undergo transition from laminar to turbulent and in order to capture this phenomena correctly a Reynolds stress model would have to be applied. However, with limited computer power the list of desiderata somehow has to be reduced. A reasonable compromise between accuracy and computer power would be steady calculations with a Low-Re eddy-viscosity turbulence model. This will predict a boundary layer transition too early and thereby *over predict* the viscous friction losses for the turbulent cases. However, compared to the overall matrix losses the effect of the boundary layer transition error should be minor. The flow field is mainly unsteady at the bundle outlet, where Karman vortices are formed. Thus, the pressure gradient inside the bundle

should be possible to estimate by steady calculations and the overall pressure drop should not be strongly affected by the unsteadiness at the bundle outlet. The operating Reynolds number range for the investigated heat exchanger varies from Reynolds number indicating that the flow might be laminar to Reynolds numbers that are in the turbulent region. This means that the flow in part of the operating range is in transition, which can not be simulated correctly by a Low-Re two-equation model (Wilcox). Therefore two operating conditions are chosen, for the investigations, that clearly lie within the laminar and turbulent regions.

3.1 CFX-TASCflow

CFX-TASCflow is a commercial fluid flow prediction software package that includes the flow solver and tools for pre- and post-processing of the flow simulation (AEA Technology). The code is able of handling subsonic, transonic and supersonic flows and has a number of different two-equation turbulence models implemented as well as second-moment closure models and sub-grid, models for LES.

The solver works on block structured hexahedral grids and make use of a finite element based finite volume method. The unsteady mass and momentum equations are solved in a coupled manner and the steady solution is approached by time integration.

In order to accelerate the convergence CFX-TASCflow applies a variable multigrid method. The multigrid method coarsens the grid in each direction in order to reduce high frequency errors and reduces the computing effort. The method has proven to be very efficient (see e.g. Ferziger and Peric).

CFX-TASCflow offers various advection differencing schemes of different accuracy and robustness. The simplest, and most robust, is the first order up-wind scheme. The most accurate and less robust is the second order Linear Profile Scheme (LPS) with Physical Advection Correction (PAC) (AEA Technology), which has been used for all calculations in this study, except for the examples of application.

CFX-TASCflow version 2.12.0-521 has been used for all CFD calculations presented in this work.

3.2 Computational grid

A computational model of a 4/3/4 heat exchanger matrix configuration is built assuming infinite long tubes. The inlet boundary is located one matrix length upstream of the tube bundle and the outlet boundary is positioned one matrix length down stream of the tube bundle. The domain borders are placed at symmetry planes in the crosswise directions in order to enable periodic conditions.

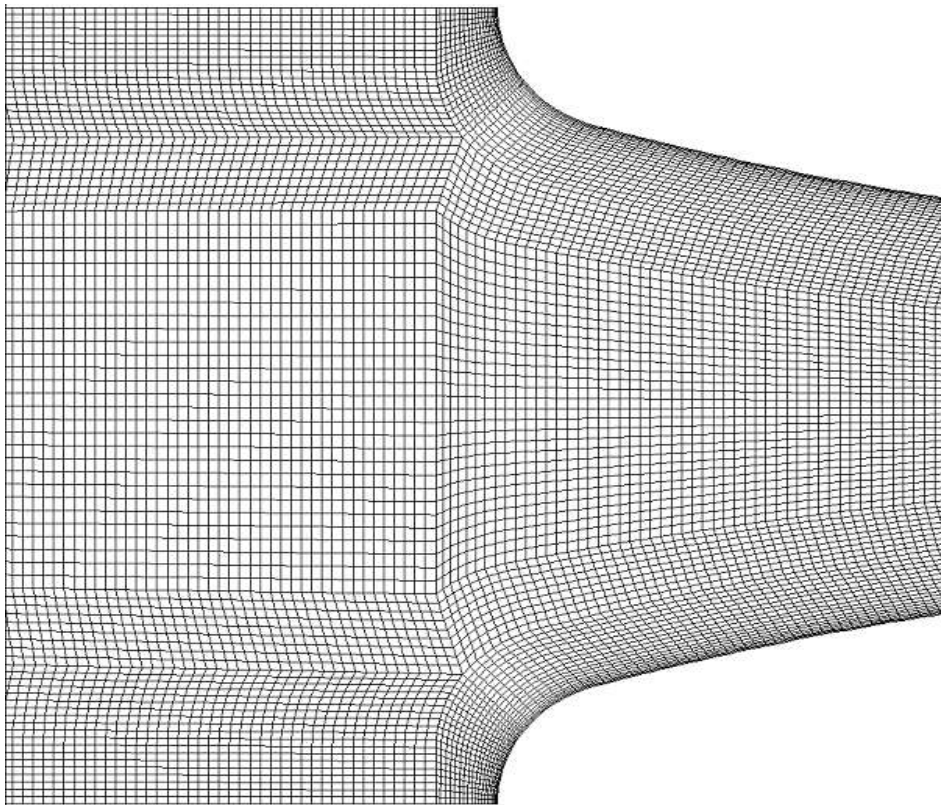


Figure 3.1 Mesh at the inlet part of the heat exchanger matrix.

The first computational node from the wall is located at a distance giving a y^+ value of around 1 for those nodes for all investigated turbulent cases. The number of nodes within the boundary layer is around 20 with some variation

between the calculated cases. The same computational grid, with a total number of nodes of 1,55 million, is used for all cases. The heat exchanger matrix inlet part of the computational grid is shown in figure 3.3.

3.3 Computational procedure

The 4/3/4 heat exchanger matrix configuration is calculated for two different Reynolds numbers. One corresponding to viscous flow ($Re = 3,36$) and the other to fully turbulent flow ($Re = 10066$). The flow is considered incompressible since the Mach number in all calculated cases is well below 0,3. The Reynolds number used is defined as

$$Re = \frac{U \cdot D_h \cdot \rho}{\mu} \quad (3.1)$$

where the hydraulic diameter of the heat exchanger matrix is defined as

$$D_h = \frac{4 \cdot A_{flow}}{U} \quad (3.2)$$

and U in equation (3.2) is the wetted perimeter of the heat exchanger matrix.

3.3.1 Boundary conditions

The inflow angles were varied one at a time, according to table 3.1, and the mass flow through the matrix held constant.

Angle	Laminar cases	Turbulent cases
Inclination	0, 40	0, 20, 40
Attack	0, 40, 80	0, 20, 40, 60, 80

Table 3.1 Investigated inflow angles.

The angle of attack is defined by the chord of the tube and the hot gas velocity direction as can be seen in figure 3.2.

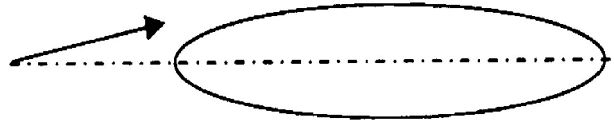


Figure 3.2 Two dimensional projection of the tube. Angle of attack.

The inclination angle is defined in the spanwise direction of the tube and is formed by the line of the leading edge extended in the spanwise direction and the vector of the hot gas velocity, see figure 3.3 below.

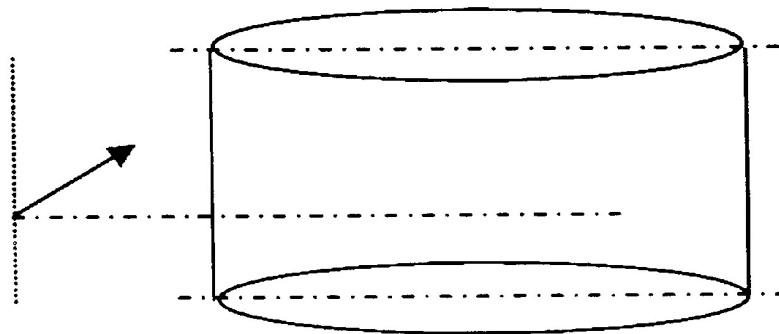


Figure 3.3 Three dimensional representation of the tube. Inclination angle.

The average static outlet pressure was held constant and the velocity components were varied, according to the attack and inclination angles, at the inlet. For the turbulent cases the turbulence intensity and length scale were given for the inlet boundary. A no-slip condition was applied for the walls and the remaining boundaries were supposed to be periodic. Periodic conditions were applied in order to avoid the flow to be forced to follow the boundaries, but allow for unsteady movements across them. The boundary conditions applied are summarized in table 3.2 below.

Boundary	Laminar cases	Turbulent cases
Inlet	u, v, w	u, v, w Tu = 2,5% and 20% L = 0,35 and 35 transversal pitches
Outlet	$p_{\text{average}} = 0 \text{ Pa}$	$p_{\text{average}} = 0 \text{ Pa}$
Walls	No slip	No slip
Other	Periodic	Periodic

Table 3.2 Numerical boundary conditions.

3.3.2 Computational attributes

The Low-Reynolds version of the SST turbulence model (AEA Technology) is applied for the turbulent cases and a 2nd order scheme is used for the advection terms. The flow is considered isothermal and thus the fluid properties held constant. The computational attributes are summarized below in table 3.3.

Attribute	Laminar cases	Turbulent cases
Reynolds number	3,36	10066
Advection scheme	2 nd order LPS	2 nd order LPS
Turbulence model	-	SST
Density [kg/m ³]	997	997
Dynamic viscosity [Ns/m ²]	$8,57 \cdot 10^{-4}$	$8,57 \cdot 10^{-4}$
Convergence criterion	10^{-4}	10^{-4}

Table 3.3 Computational attributes.

3.4 Results

High attack angles only have a very moderate effect on pressure drop, in the main flow direction, for laminar cases, as can be seen in tables 3.4 and 3.5. This is what could be expected since no boundary layer separation occurs. For the turbulent cases the effect of the attack angle is similar to the laminar cases as long as the flow does not separate. As can be seen in figures 3.4-3.8 the calculations predict separation at an attack angle between 40 and 60 degrees. The separation at 60 degrees attack angle is rather small and the effect on the pressure drop is moderate. For turbulent flow and attack angles up to 60 degrees a minor effect on the pressure drop is seen in the first tube rows (table 3.4) and from the 5th row the pressure drop behaviour is the same as for the zero angle case. When the attack angle is increased further the separation grows and for 80 degrees attack angle the separation causes a large blockage to the flow in the first row (figure 3.8). This leads to a significant pressure drop increase, at the inlet, but, as can be noticed in table 3.4, the effect is seen through the whole bundle, although weakening with the distance from the inlet. Unfortunately, no experimental data is available about separation size or at what attack angle separation occurs.

Apart from the pressure drop increase with increasing attack angle the pressure drop results also show the expansion loss at the outlet, included in the loss coefficients for row 7. This effect is seen in the results for the turbulent cases, but can not be seen in the laminar cases where the flow does not separate from the last tube row trailing edges.

The pressure loss coefficient in the tables below is normalized with the pressure loss coefficient for tube row 6 of the zero inflow angle case for which the pressure loss coefficient is defined as

$$\zeta = \Delta p_{row} / \left(\frac{1}{2} \rho u^2 \right) \quad (3.3)$$

where u is the velocity component corresponding to zero attack and inclination angle.

Attack angles for turbulent flow

Tube row	0	20	40	60	80
1	0,55	0,55	0,58	0,92	11,21
2	0,90	0,90	0,91	1,02	4,03
3	0,95	0,95	0,96	1,02	2,52
4	0,98	0,98	0,98	1,00	1,33
5	1,00	1,00	1,00	1,00	1,12
6	1,00	1,00	1,00	1,00	1,06
7	1,20	1,20	1,20	1,22	1,24

Table 3.4 Pressure loss coefficients per tube row, normalized with the pressure loss coefficient for tube row 6 of the zero angle case, for different attack angles for the turbulent flow cases.

Attack angles for laminar flow

Tube row	0	40	80
1	0,84	0,83	0,88
2	1,00	1,00	1,00
3	1,00	1,00	1,00
4	1,00	1,00	1,00
5	1,00	1,00	1,00
6	1,00	1,00	1,00
7	0,83	0,83	0,83

Table 3.5 Pressure loss coefficients per tube row, normalized with the pressure loss coefficient for tube row 6 of the zero angle case, for different attack angles for the laminar flow cases.

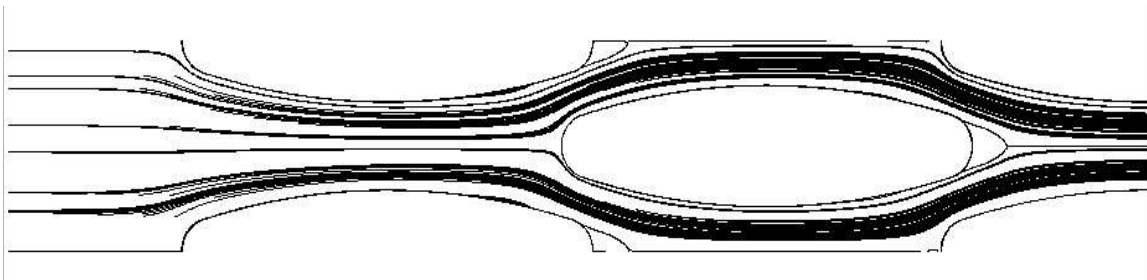


Figure 3.4 Stream lines for zero degrees attack angle, turbulent case.

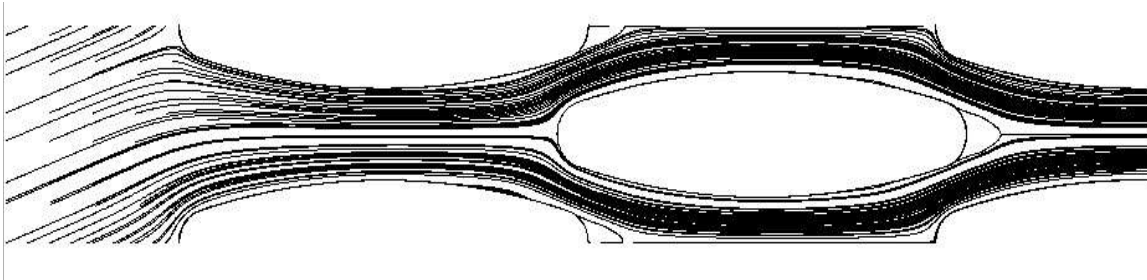


Figure 3.5 Stream lines for 20 degrees attack angle, turbulent case.

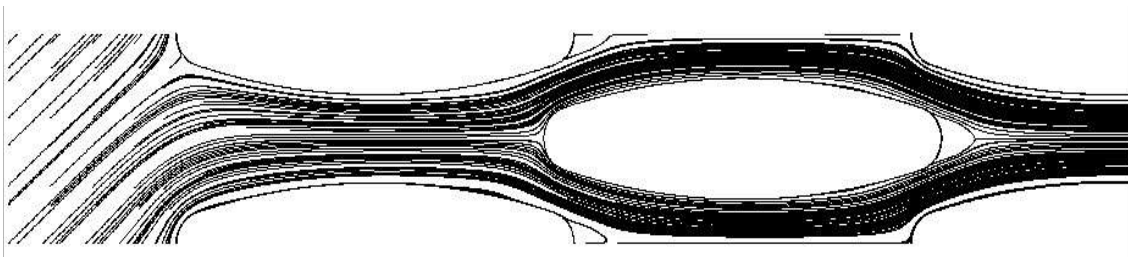


Figure 3.6 Stream lines for 40 degrees attack angle, turbulent case.

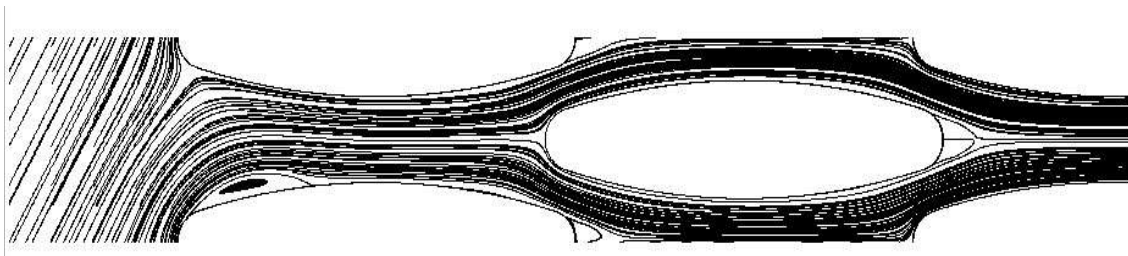


Figure 3.7 Stream lines for 60 degrees attack angle, turbulent case.

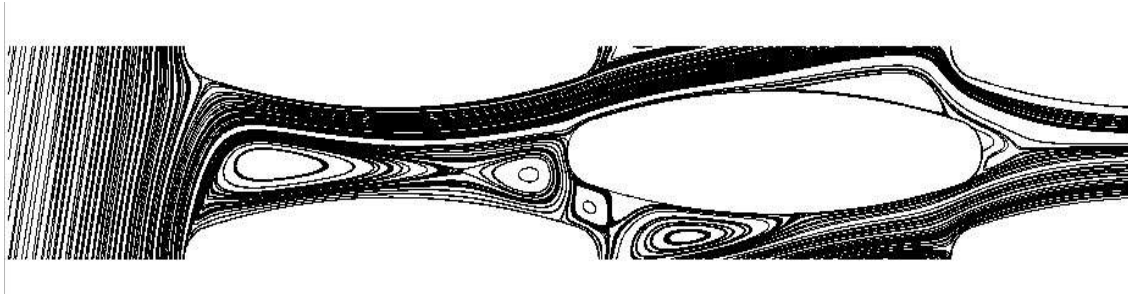


Figure 3.8 Stream lines for 80 degrees attack angle, turbulent case.

The turbulent zero degrees case qualitatively shows the same behaviour as has been reported by different researchers (e.g. Hanke) with an increase in the pressure drop coefficient with the row until row 4 or 5 from where it stabilizes. In figure 3.9 the calculated pressure loss coefficient per tube row is plotted together with the measured pressure loss coefficient per tube row for the bundles of oval shaped tubes investigated by Bähr. As can be seen the calculated pressure loss coefficient is somewhat lower than the measured ones.

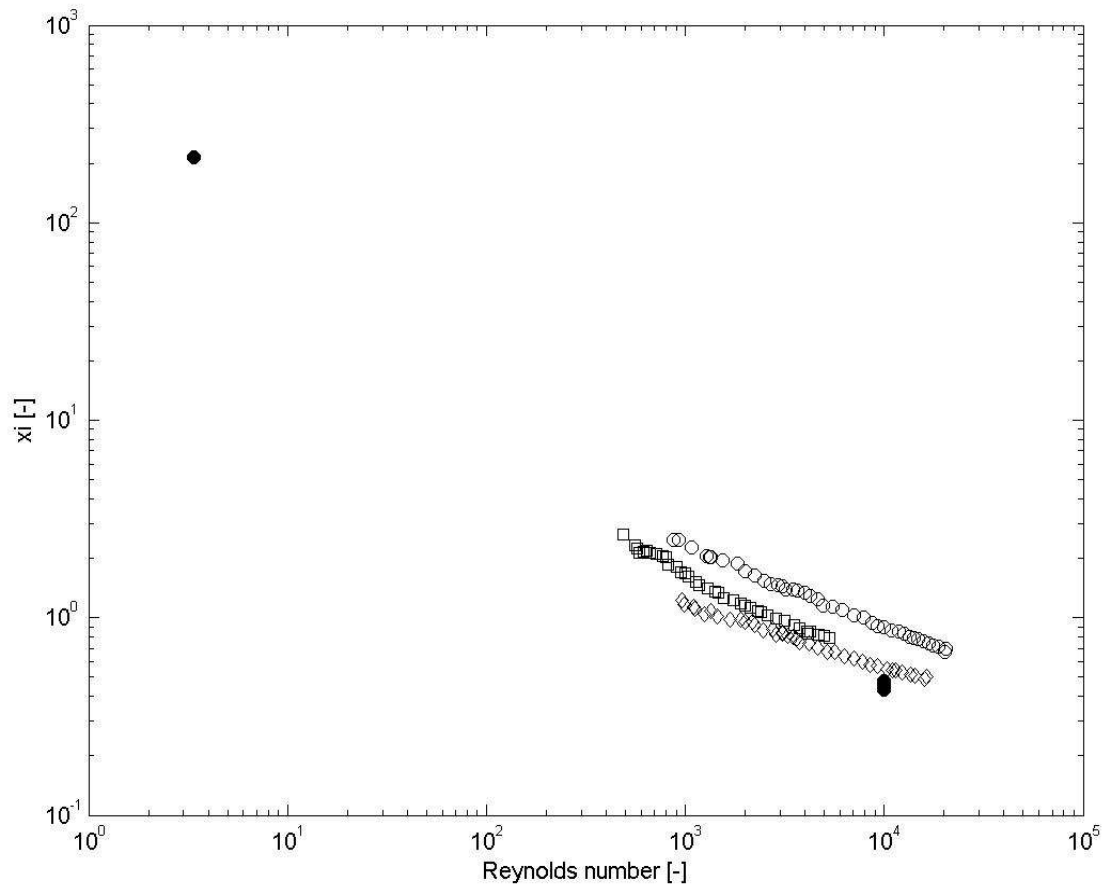


Figure 3.9 Pressure loss coefficient per tube row.

The Reynolds numbers upstream of the tube bundle is approximately two orders of magnitude higher than inside the tube bundle. This obviously leads to a significant increase in dissipation that in turn cause a reduction of the turbulent viscosity although the turbulence production is increased due to the strong mean velocity shear. In figures 3.10 – 3.12 the turbulence intensity, the normalized dissipation, and the ratio of turbulent to molecular viscosity are shown for different turbulent inlet boundary conditions. As can be seen the tube bundle has strong influence on all quantities and although the inlet conditions differ significantly the turbulence intensity and the turbulent viscosity are at the outlet the same. This is qualitatively in good agreement with experimental observations made by different researchers (e.g. Zukauskas) who noticed that the free stream turbulence only affected the first rows.

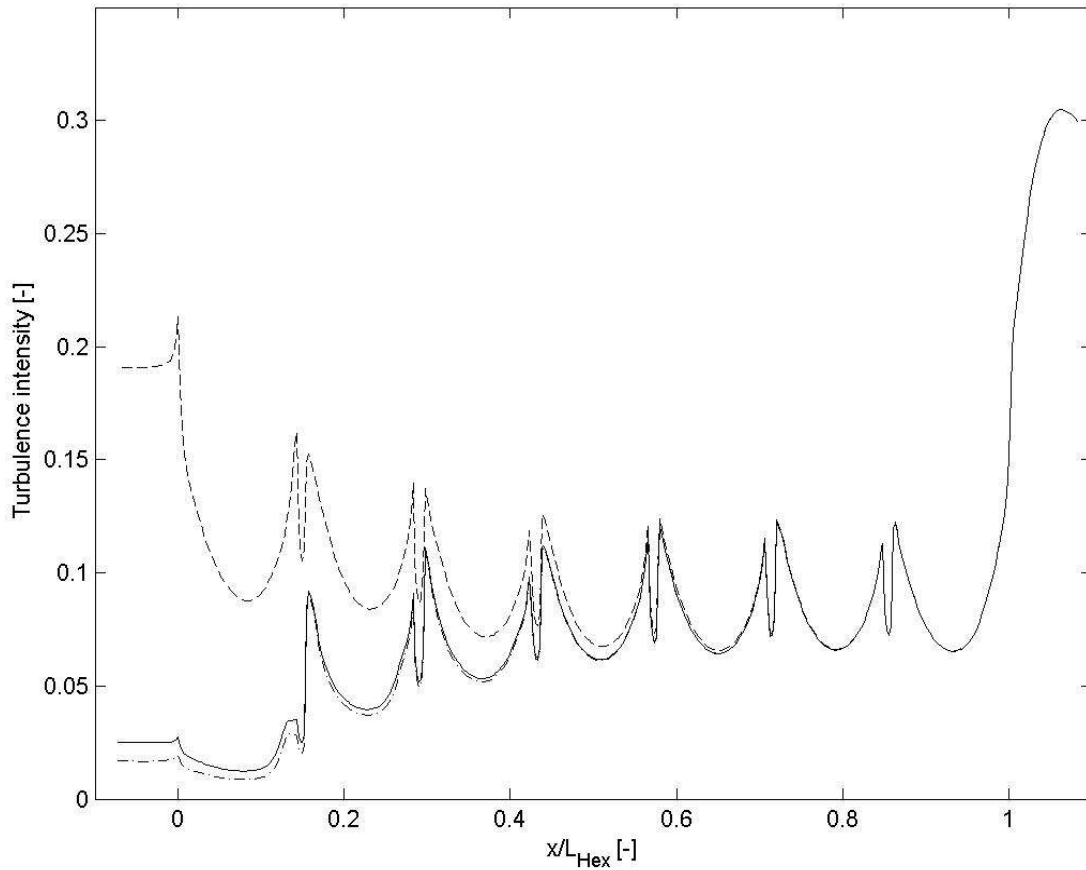


Figure 3.10 Turbulence intensity, zero degrees inflow angle.

Solid: $Tu_{inlet} = 2,5\%$, $L_{inlet} = 35$ transversal pitches. Dashed: $Tu_{inlet} = 20\%$, $L_{inlet} = 35$ transversal pitches. Dash-dotted: $Tu_{inlet} = 2,5\%$, $L_{inlet} = 0,35$ transversal pitches.

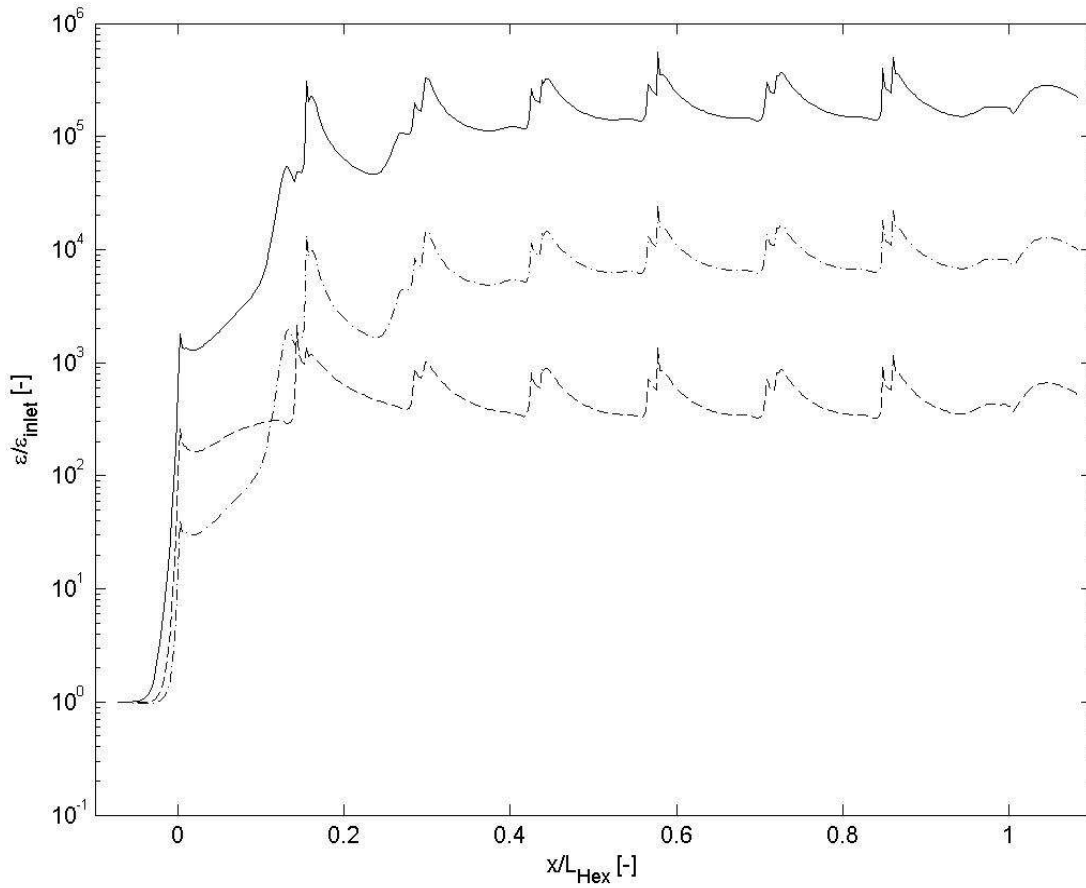


Figure 3.11 Dimensionless dissipation, zero degrees inflow angle.

Solid: $Tu_{\text{inlet}} = 2,5\%$, $L_{\text{inlet}} = 35$ transversal pitches. Dashed: $Tu_{\text{inlet}} = 20\%$, $L_{\text{inlet}} = 35$ transversal pitches. Dash-dotted: $Tu_{\text{inlet}} = 2,5\%$, $L_{\text{inlet}} = 0,35$ transversal pitches.

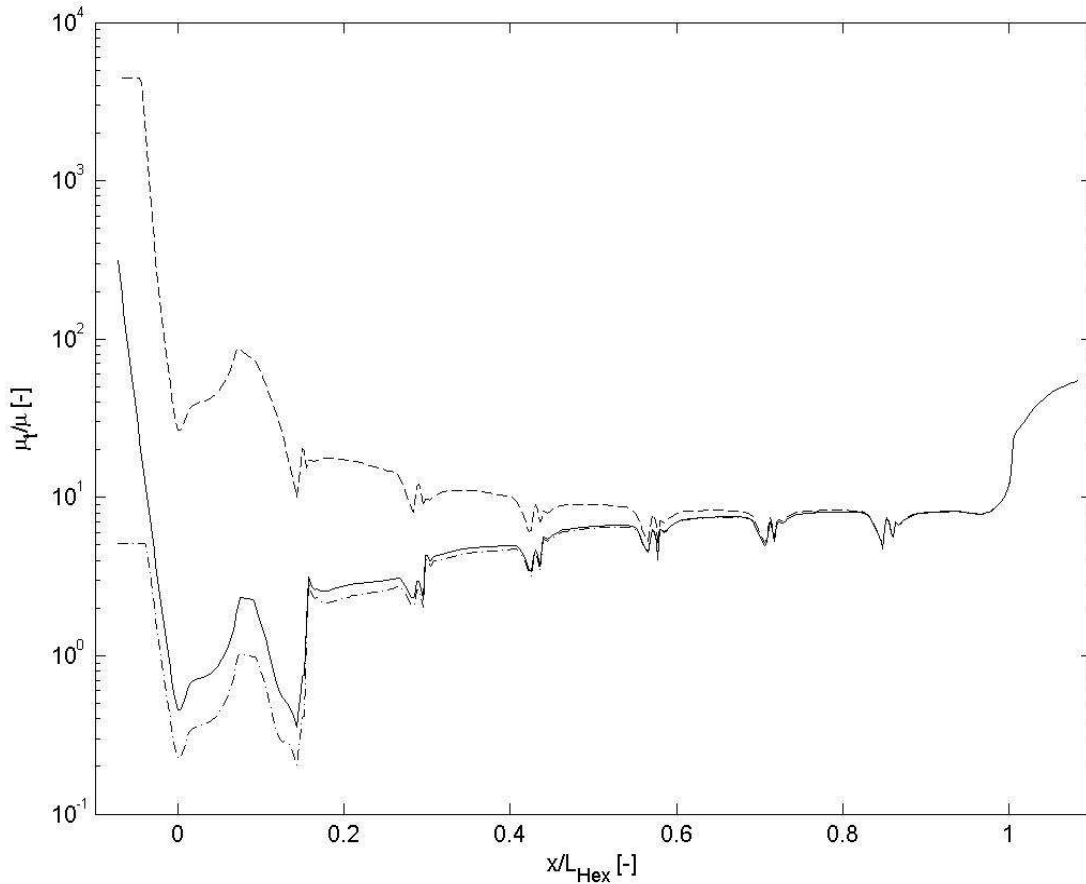


Figure 3.12 Ratio of turbulent to molecular viscosity, zero degrees inflow angles.
 Solid: $Tu_{inlet} = 2,5\%$, $L_{inlet} = 35$ transversal pitches. Dashed: $Tu_{inlet} = 20\%$, $L_{inlet} = 35$ transversal pitches. Dash-dotted: $Tu_{inlet} = 2,5\%$, $L_{inlet} = 0,35$ transversal pitches.

Due to the oval shape of the tubes and the relative compactness of the tube bundle the crosswise velocity component, caused by the attack angle, decreases very fast in the tube bundle inlet. This is true for all attack angles and in figure 3.13 shown for the 40 and 80 degrees attack angle cases, where the crosswise velocity components have more or less vanished after a couple of percent of the bundle length, i.e. within the first tube row. The wiggles in the results for the 80 degrees case are due to the separation zone.

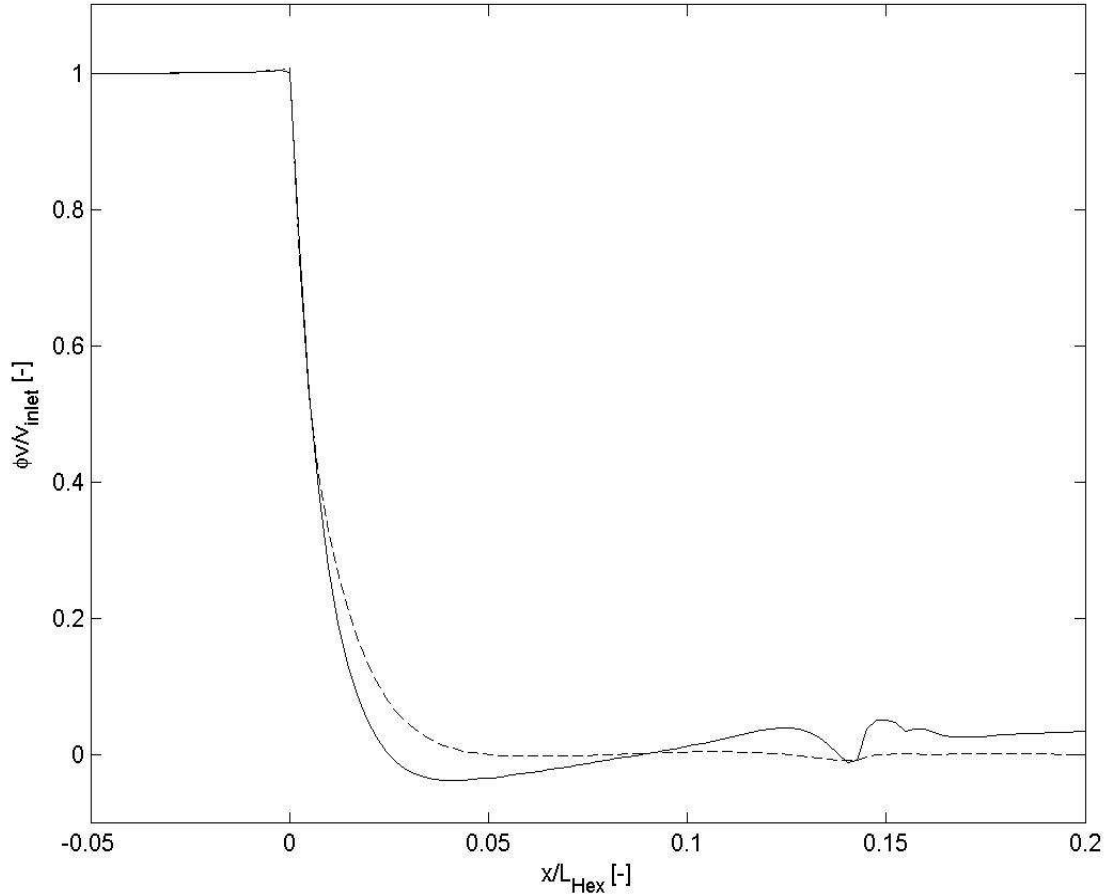


Figure 3.13 Decrease of crosswise velocity component, turbulent cases.
 Solid: 80 degrees attack angle, dashed: 40 degrees attack angle.

Since the flow resistance along the tubes is significantly lower than across the tubes the crosswise velocity component is not reduced as fast for the inclination angle cases as for the attack angle cases. This is the reason for the higher pressure loss coefficients, of the turbulent cases, for the inclination cases compared to the attack angle cases, as can be seen in table 3.6. Interesting to note is that the loss coefficients for rows 5 and 6 are slightly lower for the 20 degrees case than for the zero degree case. It is unclear if this has a physical explanation or if it is purely due to numerical errors.

Inclination angles for turbulent flow

Tube row	0	20	40
1	0,55	1,13	1,12
2	0,90	1,31	1,52
3	0,95	1,08	1,23
4	0,98	1,00	1,12
5	1,00	0,97	1,06
6	1,00	0,96	1,05
7	1,20	1,08	1,13

Table 3.6 Pressure loss coefficients per tube row, normalized with the pressure loss coefficient for tube row 6 of the zero angle case, for different inclination angles for the turbulent flow cases.

Inclination angles for laminar flow

Tube row	0	40
1	0,84	0,63
2	1,00	1,02
3	1,00	1,00
4	1,00	1,00
5	1,00	1,00
6	1,00	1,00
7	0,83	0,64

Table 3.7 Pressure loss coefficients per tube row, normalized with the pressure loss coefficient for tube row 6 of the zero angle case, for different inclination angles for the laminar flow cases.

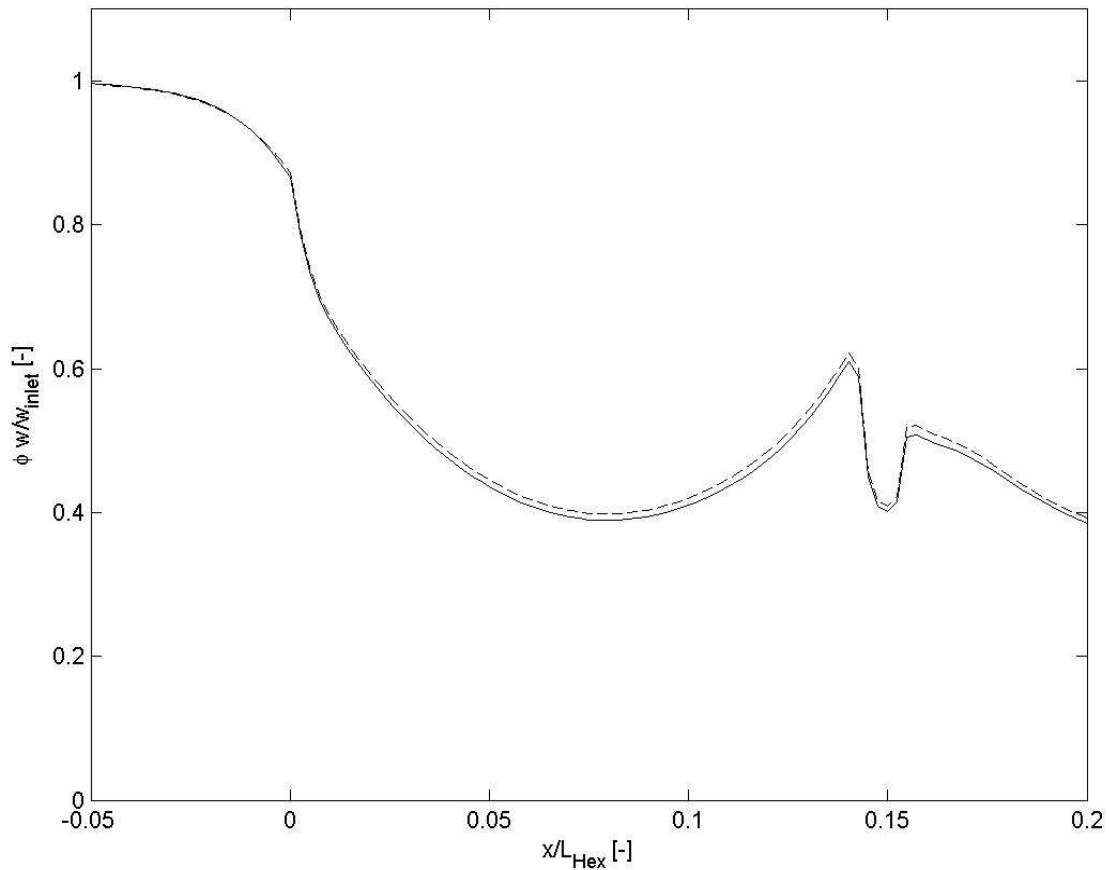


Figure 3.14 Decrease of crosswise velocity component, turbulent cases.
 Solid: 40 degrees inclination angle, dashed: 20 degrees inclination angle.

4 Porous media

A porous medium is a material consisting of a solid matrix with an interconnected void. The matrix can be either rigid or undergo deformation, and the void allows the flow of one or more fluids through the medium. Porous media can be naturally formed (e.g. rocks, sand beds, woods, the human lung etc) or fabricated (e.g. catalytic pellets, insulations, tube bundles etc). Calculation of fluid and heat flow variables in a porous medium is a demanding task. Although direct numerical simulations of transport phenomena is theoretically possible, it demands enormous computational resources even for simple geometries. Even the use of RANS-equations lead to extreme computational times. Thus, direct approaches are rarely seen in

engineering applications. In order to resolve most of the flow features and at the same time keep the model simple enough to serve as an engineering tool, an averaging of heat and fluid flow variables has to be performed. Due to such averaging procedures the resulting transport equations are not closed. In order to close them porous media flow models need to be applied. The first porous media flow model was introduced by Darcy in 1856 after having studied the fountains on Dijon, France. Darcy related the pressure drop linearly with flow velocity, using dynamic viscosity and specific permeability as additional constants and his model looks like

$$\mathbf{v} = -\frac{K}{\mu} \frac{dp}{dx} \quad (4.1)$$

where \mathbf{v} is the Darcy velocity and related to the volume average velocity by the Dupuit-Forchheimer relationship

$$\mathbf{v} = \phi \mathbf{V} \quad (4.2)$$

where

ϕ is the porosity, which is defined as the fluid volume fraction of the total volume. For a tube bundle heat exchanger it corresponds to the fluid volume that resides between the tubes over the total volume of the tube bundle. It is necessary that the porosity is correct in order to achieve energy continuity between the fluids of the porous medium, and the correct average velocity in the tube bundle.

Darcy's law has been verified by a number of experiments and is very well known. The deficit of the model is that it only holds for very low velocities. The Reynolds number must be of the order of unity or smaller, which works fine for e.g. geological applications but disqualifies it for high Reynolds number applications. When the velocity is increased, from where the Darcy equation is valid, there is a relatively smooth transition to non-linear drag. This was noticed by Forchheimer who added a quadratic term, often called the Forchheimer term, to the Darcy equation and thereby introduced the Forchheimer equation

$$\frac{dp}{dx} = -\frac{\mu}{K} \mathbf{v} - c_F K^{1/2} \rho |\mathbf{v}| \mathbf{v} \quad (4.3)$$

where c_F is a dimensionless form-drag constant.

If the source term in a porous medium is modelled according to equation 4.3 and added to the momentum equations then the resulting equations are the so called Brinkmann-Forchheimer equations that for an incompressible medium look like (Nield and Bejan)

$$\rho \left[\frac{1}{\phi} \frac{\partial \mathbf{v}}{\partial t} + \frac{1}{\phi} \nabla \left(\frac{\mathbf{v} \mathbf{v}}{\phi} \right) \right] = -\frac{1}{\phi} \nabla (\phi p) + \frac{\mu}{\phi \rho} \nabla^2 \mathbf{v} - \frac{\mu}{K} \mathbf{v} - \frac{c_F \rho}{K^{1/2}} |\mathbf{v}| \mathbf{v} \quad (4.4)$$

In the present work only single-phase flow is considered and the source terms are modelled using the Forchheimer equation assuming the solid matrix to be rigid. The resulting momentum equations used are analogue to the Brinkmann-Forchheimer equation above.

For porous media four different length scales can be defined (Kaviany). The smallest length scale is the so called *Brinkman screening distance* $K^{1/2}$ which is the square root of the permeability constant. The second length scale is the *particle dimension* d which normally is about two orders of magnitude larger than $K^{1/2}$. A third length scale is the *system dimension* L , which usually is significantly larger than d . The fourth length scale, l , is the dimension of the *representative elementary volume (REV)* which is the smallest differential volume that results in statistically meaningful local average properties. The four length scales can be written as

$$K^{1/2} \ll d \leq l \ll L \quad (4.5)$$

Applied to a tube bundle heat exchanger d would correspond to the tube thickness, l to the pitch and L to the outer dimension of the tube bundle.

Porous media has been investigated by numerous researchers over the last century. Most of the work has been undertaken on flow in the Darcy regime, often applied to geological problems. This kind of porous media flow can be studied in e.g. the works of Bear, Bachmat or Sahimi. High Reynolds flow in porous media, on the other hand, has been investigated by e.g. Skjetne, Nield and Bejan. More general information on porous media can be found in e.g.

the scientific journals *Transport in Porous Media* and *Journal of Porous Media* or in the works of e.g. Boer, Dullien, Kaviany, Vafai, Nield and Bejan. Different averaging techniques have been studied by Whittaker and Catton who also studied dispersion in porous media, a subject that also Bader-Shabeeb, Nield and Bejan, and Hsu and Cheng have investigated.

5 Porous media momentum sink terms

There are different ways to simulate turbulent flow associated with different computational efforts. The different approaches make use of different levels of simplification of the momentum equations. The reason for using a porous medium to simulate a heat exchanger is to save computational time and money. This means that when a porous medium is used a reasonable level of simplification, that to some extent match the porous media simplification, should be used for the momentum equations. There is e.g. no idea to simulate the flow in the computational domain outside the porous medium in extreme detail by e.g. using direct numerical simulation (DNS) or large eddy simulation (LES) when the flow in the porous medium itself is modelled rather roughly. The gain in computational time, by using a porosity model for the heat exchanger, in such a case would be rather small. A second problem that would occur regards the treatment of the boundaries between the porous medium and the rest of the domain. Since the geometry is left out and the grid is coarse in a porous medium fine scaled motions cannot be resolved adequately and the transfer of information on the fine scaled motions across the boundaries is questionable. On the other hand, it is often desired to calculate the flow field in the rest of the computational domain well enough to catch its main features. This is then in some way in contradiction to the difficulties to resolve flow features in the porous part of the domain. A reasonable compromise between good predictions in the non-porous part of the domain and the simplifications needed in the porous part is the use of the averaged momentum and transport equations in combination with a two-equation turbulence model. By using this alternative the mean velocities can be calculated throughout the whole computational domain. The drawback is that the turbulent quantities can not be calculated properly in the porous region without modification to those equations. This is a field that has not been investigated thoroughly. In the literature only very few examples can be found on this topic. The most interesting is the work of Antohe and Lage who

derived k - and ε -equations from the averaged momentum equations containing source terms of the Darcy-Forchheimer type (Antohe and Lage). Another interesting work is the paper of Pedras and de Lemos who averaged the transport equations for the turbulent kinetic energy, k , and its dissipation rate, ε for an infinite array of elliptic rods and proposed a macroscopic model for flow in porous media (Pedras and de Lemos). Modifying the equations for the turbulent quantities in these ways might introduce additional stiffness to the equation system due to the rapid increase of dissipation when the flow enters the porous media. This could in turn, depending on the momentum sink term tensors, lead to severe numerical difficulties.

The scales of the problem are inside the porous medium the scales of the heat exchanger matrix, i.e. the scales over which the averages have been made, which is of the same order as the longitudinal and transversal pitch of the matrix. If a no-slip condition is desired for the heat exchanger walls, knowing the scales of the problem, one realizes that it is not possible to calculate the velocity profile at the wall correctly, and it is also not necessary. Assuming the first node outside the wall to have a wall distance of around one transversal pitch, one can expect the y^+ value of that position to be relatively high, i.e. $\gg 10$, which in turn disqualifies any attempt to try to resolve the boundary layer and leaves the opportunity open only for the use of wall functions. The wall function used in this work is the one developed by Grotjans and Menter (Grotjans, Grotjans and Menter, and AEA Technology) where the viscous sublayer is neglected and y^+ is put equal to 11,062 on the wall. This leads to an error that is Reynolds number dependent and not, as for the standard wall function, grid dependent. The error that is introduced by the wall function is, however, negligible since the main momentum losses are caused by the momentum sink terms and not by the wall friction. As a matter of fact the increase in pressure drop when a no-slip condition is applied for the walls in the porous medium comes mainly from the increase of the momentum sinks due to the higher velocity of the bulk flow. This means that caution has to be used when deriving the sink terms and also when the grid is built in order to get a correct estimation of the momentum losses in the porous medium.

By definition, a compressible flow is one in which significant density changes occur, even if pressure changes are small (Wilcox). This means that the compressible formulation of the conservation equations has to be used when

heat transfer is simulated. The conservation of mass and linear momentum for a compressible fluid looks like

$$\frac{\partial \bar{\rho}}{\partial t} + \frac{\partial}{\partial x_i} (\bar{\rho} \tilde{u}_i) = 0 \quad (5.1)$$

$$\frac{\partial}{\partial t} (\bar{\rho} \tilde{u}_i) + \frac{\partial}{\partial x_j} (\bar{\rho} \tilde{u}_i \tilde{u}_j) = -\frac{\partial \bar{p}}{\partial x_i} - \frac{\partial}{\partial x_j} (\bar{\tau}_{ij} + \overline{\rho u_i' u_j'}) + \bar{\rho} g_i + S_i \quad (5.2)$$

where the Reynolds-averaged viscous stress, for low-speed compressible flows, is approximated as

$$\bar{\tau}_{ij} \approx -\bar{\mu} \left(\frac{\partial \tilde{u}_i}{\partial x_j} + \frac{\partial \tilde{u}_j}{\partial x_i} \right) \quad (5.3)$$

and

g_i is the acceleration due to gravity

S_i is the momentum source term

For the Reynolds stress term the Boussinesq approximation is applied yielding the following expression when two-equation or simpler turbulence models are used

$$\overline{\rho u_i' u_j'} = -\mu_t \left(\frac{\partial \tilde{u}_i}{\partial x_j} + \frac{\partial \tilde{u}_j}{\partial x_i} - \frac{2}{3} \frac{\partial \tilde{u}_k}{\partial x_k} \delta_{ij} \right) + \frac{2}{3} \bar{\rho} k \delta_{ij} \quad (5.4)$$

where the turbulent viscosity for the $k-\varepsilon$ model is defined as

$$\mu_t = \rho c_\mu \frac{k^2}{\varepsilon} \quad (5.5)$$

For isothermal calculations, which in most heat exchanger applications have low Mach numbers, the incompressible form of the momentum equations can be chosen.

For a more in depth description of the derivation of the Reynolds and Favre averaged equations, please refer to text books on the subject such as for the incompressible formulation e.g. the works by Pope or Tannehill and for the compressible formulation e.g. Wilcox.

The heat exchanger is subjected to thermal gradients leading to different thermal expansions in different parts of the heat exchanger. The investigated heat exchanger is manufactured of an Inconel alloy which typically has a thermal expansion coefficient between 7,6 and 15,5 $\mu\text{m/mK}$ (ASME). A typical maximum temperature difference, in the operating range, between inlet and outlet in the heat exchanger tubes is around 350 K (see chapter 9). This leads to, with the above coefficients, a difference in thermal expansion between the tube inlets and outlets of about 0,5%. The effect of thermal expansion on the porosity and flow resistance has thus been neglected. If, on the other hand, the material used has a large thermal expansion coefficient this has to be considered when deriving the pressure drop correlations.

5.1 Source term expressions

One of the problems in deriving a porosity model for a heat exchanger is to find suitable expressions for the momentum source terms. As discussed in chapter 4, when the operating conditions vary over a large range of Reynolds numbers, from laminar to in some cases fully turbulent, the preferable source term description is the Forchheimer equation. The standard form of the Forchheimer equation looks like (compare equation 4.3)

$$S = -\frac{\mu}{K} \mathbf{v} - c_F K^{1/2} \rho |\mathbf{v}| \mathbf{v} \quad (5.6)$$

If equation (5.6) is generalized to 3 dimensions it can be written as

$$S_i = -\mu \cdot D_{ij} \cdot u_j - F_{ij} \cdot \frac{\rho}{2} \cdot (u_k \cdot u_k)^{1/2} \cdot u_j \quad (5.7)$$

with the D_{ij} and F_{ij} , Darcy and Forchheimer, 2nd order resistance tensors instead of the permeability tensor and the form drag.

In addition to the sources the active coefficients are needed for the solution of the equation system. The active coefficients are defined as:

$$A_i = \frac{\partial S_i}{\partial u_i} \quad (5.8)$$

A first estimation of the resistance tensors will be made on the basis of the CFD-results in chapter 3. However, since the CFD calculations in chapter 3 are performed for laminar and fully turbulent flow, and the heat exchanger operating conditions lie in a Reynolds number range in between, where eddy-viscosity models perform badly, the derived D_{ij} and F_{ij} tensors will be impaired by uncertainties. Therefore an adjustment of the resistance tensors against experimental data might be necessary. A comparison between results from calculations for the heat exchanger matrix modelled as porous medium, with the derived resistance tensors, and the CFD-results in chapter 3 are presented at the end of this chapter.

The complete set of equations for the momentum source terms and active coefficients is presented in appendix B.

5.2 Derivation of resistance tensors

A coordinate system defined as in figure 5.1, makes the heat exchanger matrix symmetric in the x-, y- and z-directions, except for at the inlet and the outlet.

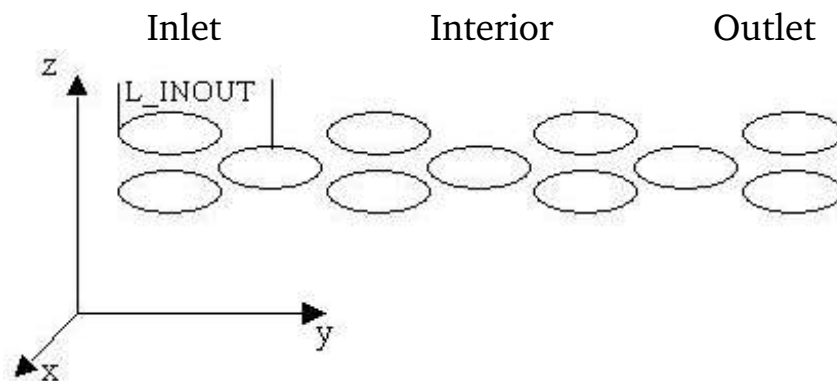


Figure 5.1 Heat exchanger lance matrix with local Cartesian coordinate system.

This means that the matrix can be treated in three different parts, namely the inlet, the interior and the outlet, see figure 5.1. The inlet is the domain going from the leading edge of the tube in the first row till the middle of the tube in the second row. The outlet domain is analogue to the inlet domain. The interior domain is the region between the inlet and the outlet. In the interior part the heat exchanger is symmetric in the directions of the axes, i.e. along the tubes and in the two directions across the tubes. This means that the tensors for this part will consist only of the diagonal elements. The inlet and the outlet, on the other hand, are symmetric only in the x- and z-directions, but not in the y-direction. Thus, their tensors will contain not only the diagonal elements, but also components giving a contribution from the velocity components in the x- and z-directions to the y-component of the pressure gradient. From the geometrical motivation above the following tensors for the different parts of the heat exchanger can be derived:

$$\text{Inlet: } D_{ij} = \begin{bmatrix} D_{xx} & 0 & 0 \\ D_{yx} & D_{yy} & D_{yz} \\ 0 & 0 & D_{zz} \end{bmatrix} \quad F_{ij} = \begin{bmatrix} F_{xx} & 0 & 0 \\ F_{yx} & F_{yy} & F_{yz} \\ 0 & 0 & F_{zz} \end{bmatrix} \quad (5.9 \text{ a-b})$$

$$\text{Outlet: } D_{ij} = \begin{bmatrix} D_{xx} & 0 & 0 \\ -D_{yx} & D_{yy} & -D_{yz} \\ 0 & 0 & D_{zz} \end{bmatrix} \quad F_{ij} = \begin{bmatrix} F_{xx} & 0 & 0 \\ -F_{yx} & F_{yy} & -F_{yz} \\ 0 & 0 & F_{zz} \end{bmatrix} \quad (5.10 \text{ a-b})$$

$$\text{Interior: } D_{ij} = \begin{bmatrix} D_{xx} & 0 & 0 \\ 0 & D_{yy} & 0 \\ 0 & 0 & D_{zz} \end{bmatrix} \quad F_{ij} = \begin{bmatrix} F_{xx} & 0 & 0 \\ 0 & F_{yy} & 0 \\ 0 & 0 & F_{zz} \end{bmatrix} \quad (5.11 \text{ a-b})$$

This is an assumption based purely on the geometry of the heat exchanger. As was noticed in chapter 3 and in tube bundle experimental data in the literature (see chapter 2) the pressure loss coefficient is increasing with tube row for the first rows and then stabilizing. This effect could be caught if the

tensors were made continuous functions of the position within the heat exchanger matrix. By treating the flow resistance as independent on tube row this effect will not be caught, however, the advantage of the above approach is that it is robust and easy to programme and does not lead to any difficulties handling flows recirculating back into the heat exchanger. As can be seen in table 3.6 the effect of this simplification on the over all tube bundle pressure drop will be reasonable and decrease with increasing number of tube rows. The average normalized pressure loss coefficient for tube rows 3 to 6 for the zero degrees case is 0,9825 (table 3.6), i.e., according to the CFD results in chapter 3, the pressure drop would be under estimated by 1.75%, for the 4/3/4-configuration, when treating the flow resistance as independent on tube row. For strong viscous flows the effect of treating the flow resistance tube row independent is negligible, as can be seen in table 3.7.

5.3 Pressure gradient across the tube bundle

The flow through and pressure drop over bundles, of mainly circular tubes, have been investigated by many researchers over the years (chapter 2). The characteristics of staggered bundles are qualitatively the same for different tube shapes and geometrical configurations. However, the exact pressure loss coefficients or flow resistance tensors need to be derived from experimental or numerical results for the shape and configuration in question. If, as in the bundle in this study, the tubes are oval shaped the flow characteristics of the bundle will be direction dependent, i.e. non-isotropic. This means that the bundle has different flow resistances across the tubes in the two main directions (y and z in figure 5.1). The diagonal tensor elements contributing to the source in the y-direction can be derived from the CFD-results for the cases with incoming flow normal to the tube bundle. If the tensor elements for the interior part are used as reference the diagonal tensor elements for the y-direction look like

$$\text{Inlet:} \quad D_{yy} = 0,84 D_{ref} \quad F_{yy} = 0,74 F_{ref}$$

$$\text{Outlet:} \quad D_{yy} = 0,84 D_{ref} \quad F_{yy} = 0,74 F_{ref}$$

$$\text{Interior:} \quad D_{yy} = D_{ref} \quad F_{yy} = F_{ref}$$

The expansion loss is implicitly included in the calculation when the momentum and mass conservation equations are solved and thus not included in the above elements.

Due to the configuration of the bundle, that nearly does not allow for any movement in the z-direction, the tensor elements acting in this direction have no other practical meaning than determining the rate at which the cross-wise velocity component will decrease when the flow is entering the bundle with a non-zero attack angle. In order to study this effect the heat exchanger matrix in chapter 3 was modelled as a porous medium, with 80 nodes across the matrix, and the tensor elements for the z-direction were varied. As can be seen in figure 5.2, the elements acting in the z-direction need to be about two orders of magnitude (100 times) larger than the elements in the y-direction in order to achieve the same decrease of the cross-wise velocity component as in the detailed CFD-results. However, tensor elements this large lead to a very stiff equation system that will require a dense grid for the calculations to converge. A way to overcome this problem is to reduce the tensor elements for the z-direction. If the tensor elements for the z-direction are chosen to be one order of magnitude larger than the elements for the y-direction the crosswise velocity component will still be reduced relatively fast and the equation system gets easier to solve. The gradients at the inlet also become less steep and can thus be resolved on a coarser grid. The drawback of this approach is that the crosswise velocity component and the source term will be over estimated. The over estimation of the pressure drop can be avoided by adjusting the tensor elements for the cross-wise velocity components in the inlet and outlet regions, acting in the y-direction, accordingly.

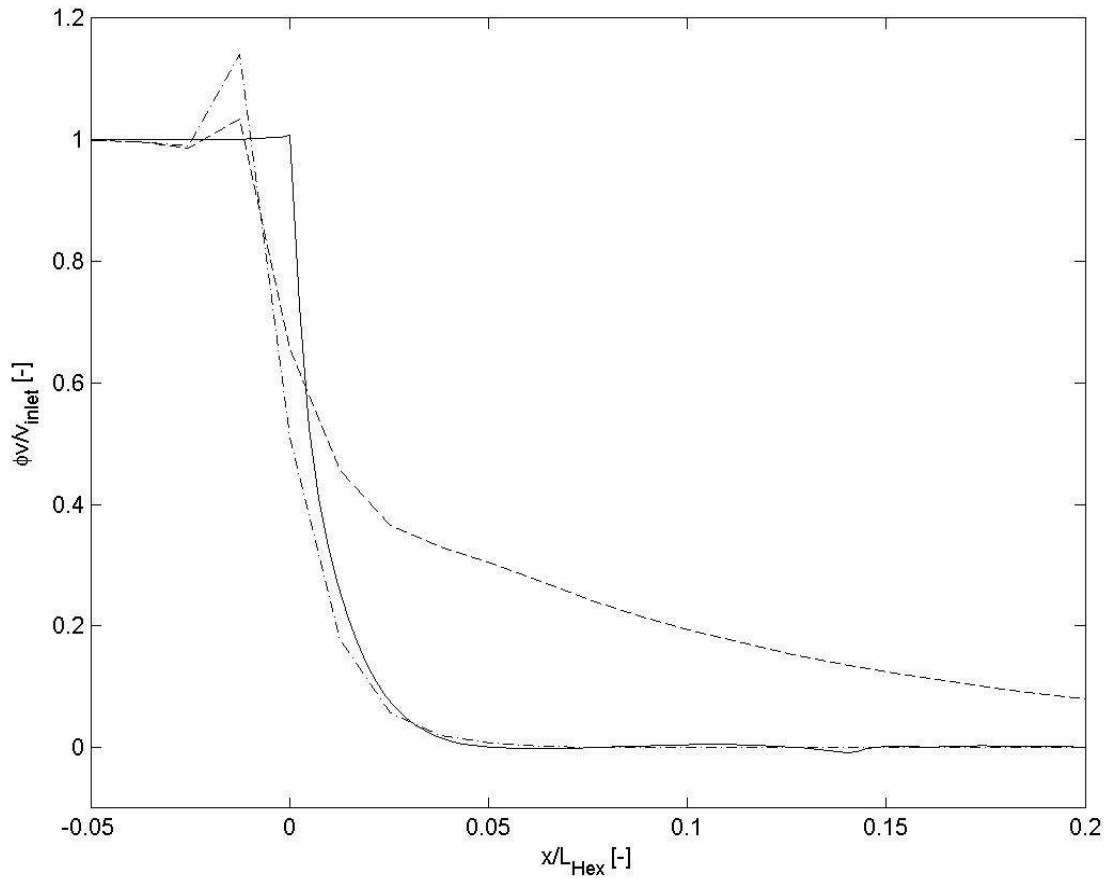


Figure 5.2 Decrease of crosswise velocity component, attack angle 80 degrees, turbulent case. Solid: detailed CFD-results, dashed: crosswise flow resistance/normal flow resistance = 10, dash-dotted: crosswise flow resistance/normal flow resistance = 100.

With the CFD-results in chapter 3 as a basis an estimation of tensor elements acting in the y-direction can be made by e.g. the least square or some other method. The components derived in this way, normalized with the D_{yy} and F_{yy} components for the interior part, then become

$$\begin{aligned} \text{Inlet:} \quad D_{yy} &= 0,84 D_{ref} & D_{yz} &= -1,85 D_{ref} \\ F_{yy} &= 0,74 F_{ref} & F_{yz} &= -1,63 F_{ref} \end{aligned}$$

$$\begin{aligned} \text{Outlet:} \quad D_{yy} &= 0,84 D_{ref} & D_{yz} &= 1,85 D_{ref} \\ F_{yy} &= 0,74 F_{ref} & F_{yz} &= 1,63 F_{ref} \end{aligned}$$

$$\text{Interior:} \quad D_{yy} = D_{ref} \quad F_{yy} = F_{ref}$$

5.4 Pressure gradient along the tube bundle

The flow along the tubes is approximated as pipe flow. It has been shown experimentally for smooth pipes (Swanson et al) that the following equations for the friction factor in pipe flow are valid for an enormous range of Reynolds numbers

$$\lambda = 64/Re \text{ laminar flow} \quad (5.12)$$

$$\lambda = 0,3164 Re^{-0,25} \text{ Blasius' equation for turbulent flow} \quad (5.13)$$

where the friction factor is defined as

$$\lambda = \frac{2 \cdot \Delta p \cdot D_h}{L_{tube} \cdot \rho \cdot U^2} \quad (5.14)$$

With the above expressions the tensor elements acting in the direction along the tubes (x-direction in figure 5.1), D_{xx} and F_{xx} , can be derived by using the least squares method. The Reynolds number and the hydraulic diameter used are defined in the same way as for cross flow (equation 3.1 and 3.2). Omitting the transition range and applying equation (5.12) for Reynolds number between 10 and 800, and equation (5.13) for Reynolds numbers between 2700 and 5000 yields the following tensor elements, normalized with D_{yy} and F_{yy} for the interior part

$$\text{Inlet and outlet: } D_{xx} = 0,29 D_{ref} \quad F_{xx} = 0,29 F_{ref}$$

$$\text{Interior: } D_{xx} = 0,30 D_{ref} \quad F_{xx} = 0,31 F_{ref}$$

The elements for the inlet and outlet regions are slightly different due to the somewhat different hydraulic diameter and porosity of those regions.

Figure 5.3 below demonstrates a comparison of the dimensionless pressure gradient calculated using equations (5.12) and (5.13) and by the use of the

tensor elements above for Reynolds numbers up to 5000. The dimensionless pressure gradient used on the ordinate is defined as

$$\hat{p} = \left| \left(\frac{dp}{dx} D_h / \left(\frac{1}{2} \rho U^2 \right) \right) \right| \quad (5.15)$$

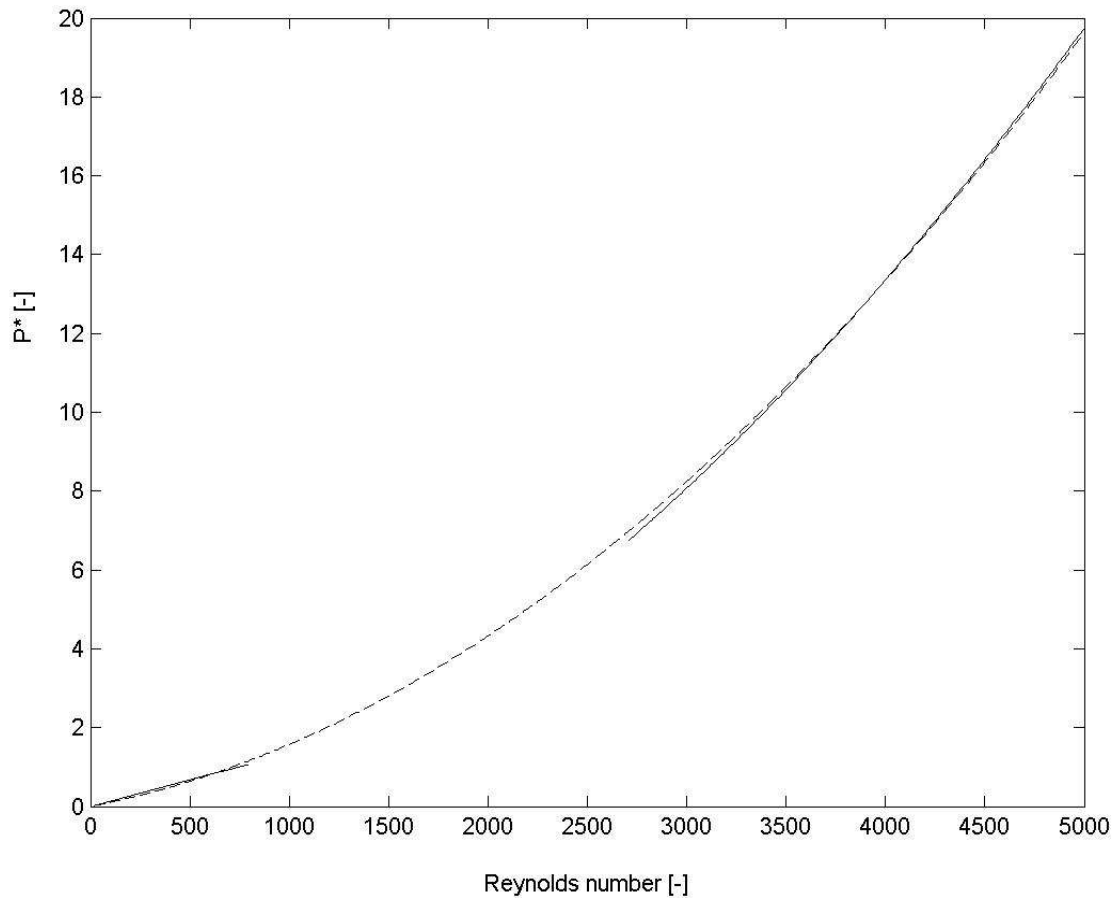


Figure 5.3 Dimensionless pressure loss along the tubes.

Solid line: Results by the use of eq. (5.12) and eq.(5.13).

Dashed line: Results with D_{xx} and F_{xx} (Darcy-Forchheimer equation).

Due to the asymmetry at the inlet and outlet, described earlier, the tensors for these regions include elements giving contribution from the velocity component along the tubes to the source acting in the y-direction. The corresponding elements are determined in the same way as the non-diagonal elements in chapter 5.3 using the CFD-results in chapter 3. The components

derived in this way, normalized with the D_{yy} and F_{yy} components for the interior part, then become

Inlet: $D_{yx} = 0,42 D_{ref} \quad F_{yx} = 0,37 F_{ref}$

Outlet: $D_{yx} = -0,42 D_{ref} \quad F_{yx} = -0,37 F_{ref}$

5.5 Porous media results

With the normalized tensor elements derived in chapter 5.3 and 5.4 put together the complete tensors look like

Inlet:
$$D_{ij} = \begin{bmatrix} 0,29 \cdot D_{ref} & 0 & 0 \\ 0,42 \cdot D_{ref} & 0,84 \cdot D_{ref} & -1,85 \cdot D_{ref} \\ 0 & 0 & 8,4 \cdot D_{ref} \end{bmatrix} \quad (5.16)$$

$$F_{ij} = \begin{bmatrix} 0,29 \cdot F_{ref} & 0 & 0 \\ 0,37 \cdot F_{ref} & 0,74 \cdot F_{ref} & -1,63 \cdot F_{ref} \\ 0 & 0 & 7,4 \cdot F_{ref} \end{bmatrix} \quad (5.17)$$

Outlet:
$$D_{ij} = \begin{bmatrix} 0,29 \cdot D_{ref} & 0 & 0 \\ -0,42 \cdot D_{ref} & 0,84 \cdot D_{ref} & 1,85 \cdot D_{ref} \\ 0 & 0 & 8,4 \cdot D_{ref} \end{bmatrix} \quad (5.18)$$

$$F_{ij} = \begin{bmatrix} 0,29 \cdot F_{ref} & 0 & 0 \\ -0,37 \cdot F_{ref} & 0,74 \cdot F_{ref} & 1,63 \cdot F_{ref} \\ 0 & 0 & 7,4 \cdot F_{ref} \end{bmatrix} \quad (5.19)$$

$$\text{Interior: } D_{ij} = \begin{bmatrix} 0,30 \cdot D_{ref} & 0 & 0 \\ 0 & D_{ref} & 0 \\ 0 & 0 & 10 \cdot D_{ref} \end{bmatrix} \quad (5.20)$$

$$F_{ij} = \begin{bmatrix} 0,31 \cdot F_{ref} & 0 & 0 \\ 0 & F_{ref} & 0 \\ 0 & 0 & 10 \cdot F_{ref} \end{bmatrix} \quad (5.21)$$

In order to verify the derived tensors the heat exchanger matrix in chapter 3 was modelled as a porous region and the above resistance tensors were applied. For this purpose four different grids were built with 5, 10, 40, and 80 nodes across the matrix. The pressure drop results are summarized below in tables 5.1 and 5.2, where the porosity model is shown to perform very well with the above tensors applied.

Attack angle	Inclination angle	$\frac{\Delta p_{porous}}{\Delta p_{CFD}} \Big _{Re=10066}$	$\frac{\Delta p_{porous}}{\Delta p_{CFD}} \Big _{Re=3,36}$
0	0	1,025	0,998
20	0	1,026	Not calculated
40	0	0,996	0,998
60	0	1,020	Not calculated
80	0	1,066	0,989
0	20	0,981	Not calculated
0	40	1,009	1,002

Table 5.1 Summary of porous media results, 40 grid nodes across the matrix.

When only few nodes are used to represent the matrix thickness the steep gradients at the inlet (see e.g. figure 5.4) can not be resolved very well. This could have a negative effect on the accuracy of the over all bundle pressure drop calculation, especially for non-zero inflow angles. By increasing the number of grid nodes, the gradients can be resolved better, and the negative

effect on the pressure drop is reduced. If the number of nodes is chosen in such a way that each tube row is represented by at least one cell row and the whole matrix by at least 10 nodes then the cross-wise velocity component is reduced in an almost grid independent way, as can be seen below in figure 5.4, and the pressure drop can be well predicted, as shown in table 5.2.

Number of nodes	$\frac{\Delta p}{\Delta p_{80nodes}} \Big _{\text{zero inflow angle}}$	$\frac{\Delta p}{\Delta p_{80nodes}} \Big _{\text{attack angle 80 degrees}}$
5	1,00	1,12
10	0,99	1,05
40	1,01	1,01
80	1,00	1,00

Table 5.2 Influence of number of nodes across the heat exchanger matrix on the pressure drop, turbulent cases.

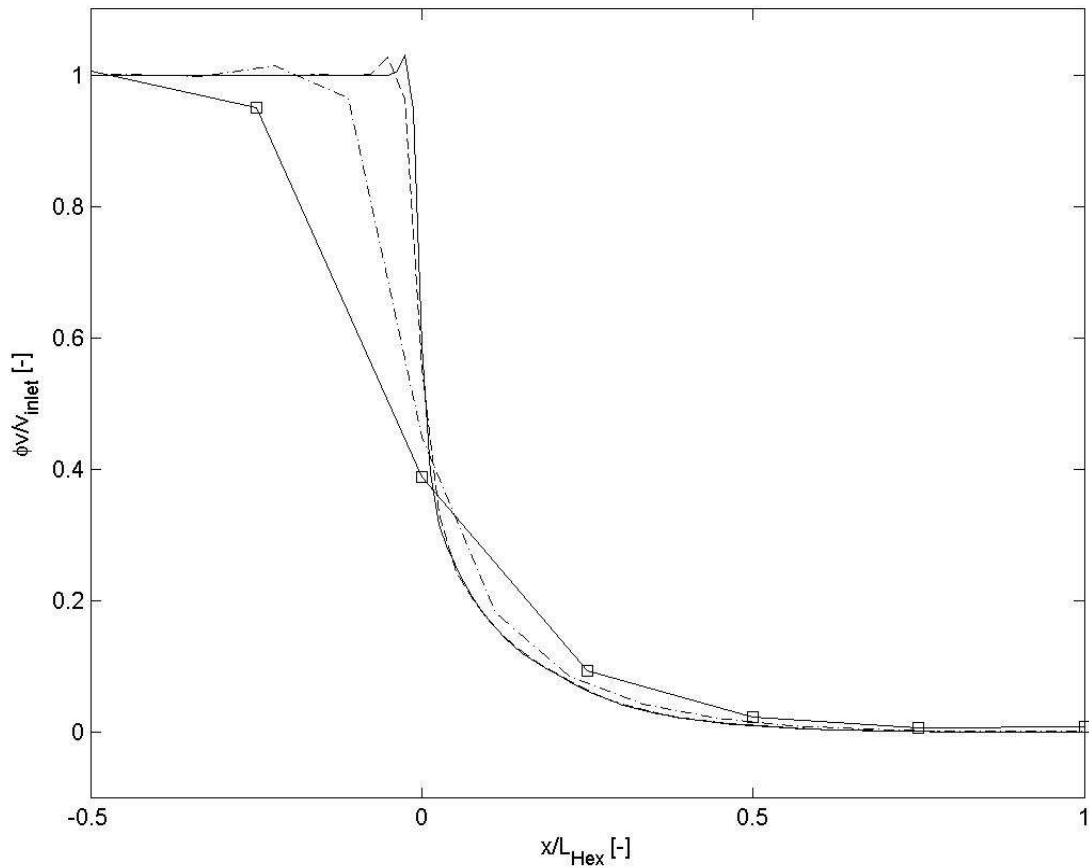


Figure 5.4 Decay of the cross-wise velocity component for different number of nodes across the matrix for the attack angle 80 degrees, turbulent cases.
 Solid with squares: 5 nodes, dash-dotted: 10 nodes, dashed: 40 nodes, and solid: 80 nodes.

In a tube bundle the turbulence is likely to be affected by small scale motions which can not be resolved adequately by a two-equation turbulence model on the relatively coarse porous media grid associated with the representation of the tube bundle. This problem is illustrated in figure 5.5 and 5.6 where the turbulence intensity and ratio of turbulent and molecular viscosity have been averaged over the REV's for the zero degree inflow case of chapter 3, and compared to the corresponding results for the porosity model. The turbulence intensity and length scale of the incoming flow is 2,5% and 35 transversal pitches, which is a realistic length scale of a typical heat exchanger application. A smaller length scale would lead to a less pronounced reduction of the turbulent viscosity. From the figures it is clear that the effect of the heat exchanger matrix on the turbulent quantities can not be modelled correctly in a porous medium without modifications to their transport equations.

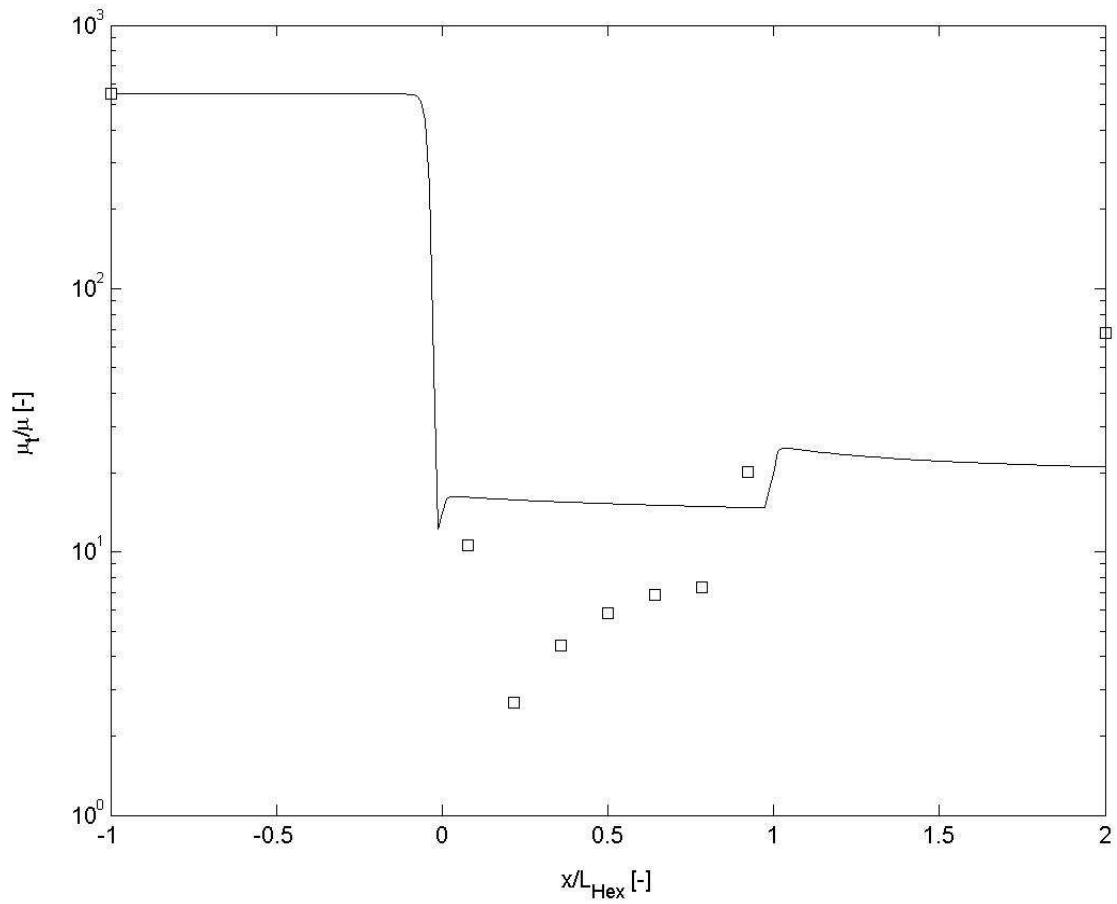


Figure 5.5 Ratio of turbulent and molecular viscosity, turbulence length scale 35 transversal pitches.

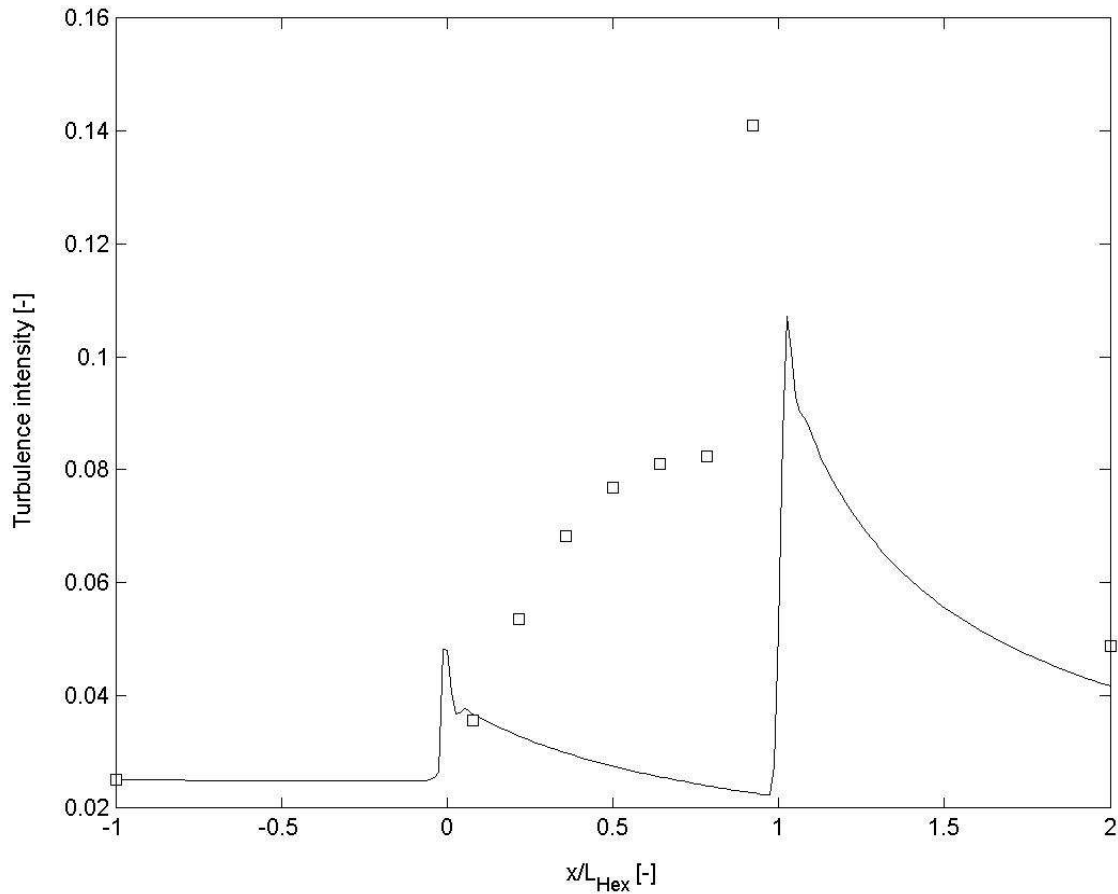


Figure 5.6 Turbulence intensity, $l=35$ transversal pitches.

6 Porous media energy sink term

The heat transfer is modelled by adding a source term to the energy equation for each of the fluids. The hot side temperature field is then calculated by the fluid solver. The temperature field on the cold side of the heat exchanger can not be calculated in a coupled manner together with the hot side temperature field at every iteration step, but has to be solved in an iterative manner. That is, the calculated cold side temperature field correspond to the hot side temperature field of the proceeding iteration. However, since the problems to be solved are of stationary art this is of no importance.

As noticed in previous chapters the turbulent viscosity is over predicted in the porous region. This leads to a too significant turbulent heat transport on the

hot gas side. If the level of the over estimation is known this can be compensated for in several ways. The easiest way would be to adjust the turbulent Prandtl number for the porous region accordingly. Another way would be to modify the energy sink term so that a fraction of the turbulent transport is subtracted. However, this is not recommended since it requires that the different derivatives are calculated in exactly the same manner as in the solver, which is difficult to obtain. A more complicated way would involve the addition of source terms to the transport equations of the turbulent quantities. Since the exact level of over estimation is unknown no compensation of the energy source terms will be made in this work.

Due to the geometry of the medium modelled as porous the effect of thermal dispersion might be significant. Two fluid elements entering a staggered heat exchanger matrix with a certain distance between them can not keep the same distance between each other on their way through the matrix. This effect is mostly handled by replacing the thermal diffusivity by a dispersion tensor that in turn is a function of the velocity and the geometry and the Peclet and Reynolds numbers (Nield and Bejan). In practice thermal dispersion has a smoothing effect on the temperature field and thereby leads to less steep temperature gradients than if thermal dispersion is neglected. For calculations of the heat exchanger temperature field it would be conservative from a thermal load point of view to neglect the effect of thermal dispersion. In this work the effect of thermal dispersion has not been estimated nor accounted for in the analyses.

When heat transfer takes place at high temperatures the effect of radiation might have to be considered for. In the chosen bundle the tubes are very tight packed and are shadowed by the neighbouring tubes and can thus be assumed to be exposed only to their neighbours. The radiation is most dominant where the temperatures are the highest, i.e. on the lower side of the heat exchanger close to the collector tube. In this region the surface temperatures of two neighbouring tubes differs at the maximum 10K. The emissivity of Inconel is approximately 0,4 (Perry and Green) and with a surface temperature of around 1000K the radiative heat flux is about 600W/m^2 , which shall be compared to the convective heat flux that in this region is around 12500W/m^2 , i.e. the radiative heat flux is at its maximum of the order of a few percent of the convective heat flux. The radiation will have a smearing effect on the temperature field and considering radiation will give non

conservative thermal loads. Thus radiation has not been accounted for in the energy source terms.

6.1 Cold side energy equation

If no compressibility effects are considered, and the fluid conductivity is considered constant, and the effects of viscous dissipation and pressure work are negligible the temperature of the gas on the cold side of the heat exchanger can be expressed by the following partial differential equation (Tannehill et al)

$$\frac{\partial}{\partial t}(\rho \bar{h}) - \frac{\partial \bar{p}}{\partial t} + \frac{\partial}{\partial x_j}(\rho \bar{U}_j \bar{h}) = \frac{\partial}{\partial x_j} \left(\lambda \frac{\partial \bar{T}}{\partial x_j} + \frac{\mu_t}{Pr_t} \frac{\partial \bar{h}}{\partial x_j} \right) \quad (6.1)$$

with the fluid assumed to be an ideal gas with constant c_p the equation above reduces to:

$$c_p \frac{\partial}{\partial t}(\rho \bar{T}) - \frac{\partial \bar{p}}{\partial t} + c_p \frac{\partial}{\partial x_j}(\rho \bar{U}_j \bar{T}) = \frac{\partial}{\partial x_j} \left(\lambda \frac{\partial \bar{T}}{\partial x_j} + \frac{\mu_t c_p}{Pr_t} \frac{\partial \bar{T}}{\partial x_j} \right) \quad (6.2)$$

if the problem is considered to be steady the equation is simplified to:

$$c_p \frac{\partial}{\partial x_j}(\rho \bar{U}_j \bar{T}) = \frac{\partial}{\partial x_j} \left(\lambda \frac{\partial \bar{T}}{\partial x_j} + \frac{\mu_t c_p}{Pr_t} \frac{\partial \bar{T}}{\partial x_j} \right) \quad (6.3)$$

if the transverse velocity components are assumed to be negligible, the mass flux to be constant and the contributions from transverse diffusion are lumped into a source term and the averaged temperature and velocity are called T_{hot} and U the following ordinary differential equation is obtained:

$$\rho c_p U \frac{dT_{cold}}{dx} = \left(\lambda + \frac{\mu_t c_p}{Pr_t} \right) \frac{d^2 T_{cold}}{dx^2} + S_{cold} \quad (6.4)$$

Where S_{cold} is the internal heat generation, or source term, per unit volume and can be expressed as proportional to the temperature difference between

the hot gas side and the cold gas side according to Newton's law (Isachenko et al) as below

$$S_{cold} = a \cdot (T_{hot} - T_{cold}) \quad (6.5)$$

Where a is defined as:

$$a = \frac{k \cdot A}{V} = \frac{k}{d} \quad (6.6)$$

where A is the heat transfer area, and V is the fluid volume and d is fluid volume per heat transfer area.

In order to judge the influence of diffusivity on the heat transport the Pe number is investigated. The Pe number is a measure of the ratio between convective and diffusive heat transport and is defined as follows:

$$Pe = \frac{\rho \cdot u \cdot c_p \cdot L}{\lambda_{eff}} \quad (6.7)$$

Typical values for the heat exchanger in operation are the following:

$$\begin{aligned} \rho &\approx 5 \text{ [kg/m}^3\text{]} \\ u &\approx 12 \text{ [m/s]} \\ c_p &\approx 1000 \text{ [kJ/kg]} \\ L &\approx 1 \text{ [m]} \end{aligned}$$

This gives the following value of Pe:

$$Pe = \frac{60000}{\lambda_{eff}} \quad (6.8)$$

which for all reasonable values of the diffusivity constant is $\gg 1$, which means that diffusion can be neglected (Patankar).

Knowing this, combined with equations (6.5) and (6.6), equation (6.4) can be further simplified to:

$$\frac{dT_{cold}}{dx} = \frac{k}{d \cdot \rho \cdot c_p \cdot U} \cdot (T_{hot} - T_{cold}) \quad (6.9)$$

Equation (6.9) can be solved analytically if information about T_{hot} is available. Unfortunately T_{hot} is a consequence of the result of equation (6.9) which means that, for an analytical solution, equation (6.9) needs to be solved together with an equation for T_{hot} . Another possibility to calculate the cold side gas temperature would be to solve equation (6.9) numerically. For numerical solutions of first order differential equations there are a number of different methods available of which the fourth order Runge-Kutta method has been implemented in the heat exchanger simulation software. The fourth order Runge-Kutta method has a truncation error of order $(\Delta x)^5$ (Kreyszig, Råde and Westergren) and applied to equation 6.9 it looks like

$$k_1 = \Delta x \cdot \frac{dT_{cold}}{dx}(x_i, T_{cold,i}, T_{hot,i}) \quad (6.10a)$$

$$k_2 = \Delta x \cdot \frac{dT_{cold}}{dx}\left(x_i + \frac{1}{2} \Delta x, T_{cold,i} + \frac{1}{2} k_1, T_{hot,i}\right) \quad (6.10b)$$

$$k_3 = \Delta x \cdot \frac{dT_{cold}}{dx}\left(x_i + \frac{1}{2} \Delta x, T_{cold,i} + \frac{1}{2} k_2, T_{hot,i}\right) \quad (6.10c)$$

$$k_4 = \Delta x \cdot \frac{dT_{cold}}{dx}(x_i + \Delta x, T_{cold,i} + k_3, T_{hot,i}) \quad (6.10d)$$

$$T_{cold,i+1} = T_{cold,i} + \frac{1}{6} \cdot (k_1 + 2k_2 + 2k_3 + k_4) \quad (6.10e)$$

The above equations are applied on the cold side as described in figure 6.1 with index i going in the flow direction and following the same grid line from the distributor to the collector.

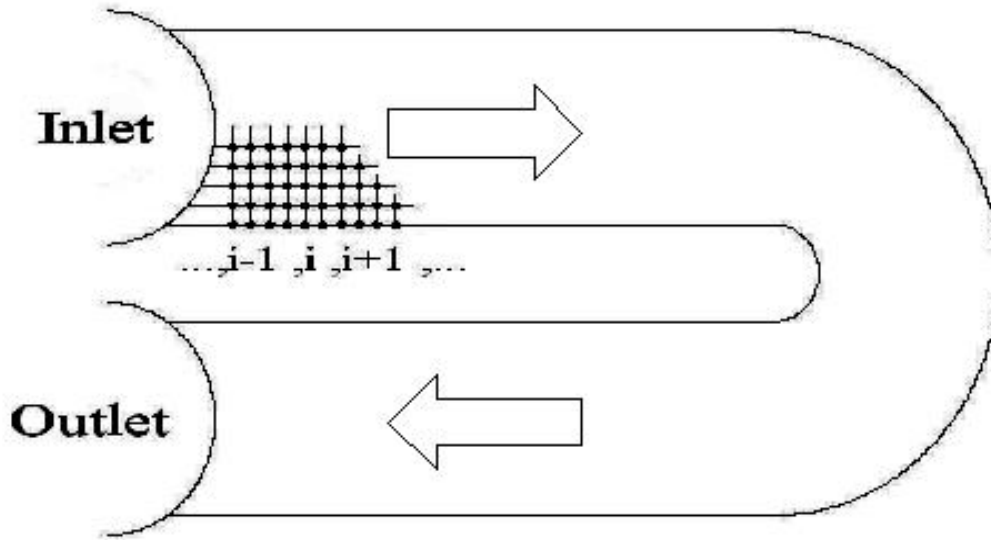


Figure 6.1 Cold side indexing and sweep direction.

6.2 Hot side energy equation

The form of the energy equation used for the hot side is the low speed form where viscous terms, modeled Reynolds stress terms and dynamic effects have been neglected (AEA Technology). The equation written in terms of static temperature looks like

$$\frac{\partial}{\partial t}(\rho c_p \bar{T}) - \frac{\partial \bar{P}}{\partial t} + \frac{\partial}{\partial x_j}(\rho c_p \bar{U}_j \bar{T}) = \frac{\partial}{\partial x_j} \left(\lambda \frac{\partial \bar{T}}{\partial x_j} + \frac{\mu_t}{Pr_t} \frac{\partial}{\partial x_j} (c_p \bar{T}) \right) + S_{hot} \quad (6.11)$$

where the source term looks like

$$S_{hot} = \frac{k \cdot A}{V} \cdot (T_{cold} - T_{hot}) \quad (6.12)$$

The source term to the energy equation is of the form “heat transfer rate per unit volume”, i.e. of the dimension [W/m³], which is the same for both the cold and the hot sides. However, the flow area and the fluid volume are different for the hot and the cold sides.

6.3 Energy equation source term

The energy equation source term looks like

$$S_E = \frac{k \cdot A}{V} \cdot (T_{hot} - T_{cold}) = \frac{k \cdot U \cdot L}{A_{flow} \cdot L} \cdot (T_{hot} - T_{cold}) = \frac{k \cdot U}{A_{flow}} \cdot (T_{hot} - T_{cold}) \quad (6.13)$$

where :
k is the heat transfer coefficient
V is the fluid volume
A is the heat transfer area
U is the perimeter
A_{flow} is the flow area

The factor $k \cdot U$ can be calculated by using the following expression:

$$\frac{1}{k \cdot U} = \frac{1}{\alpha_{hot} \cdot U_{hot}} + \frac{\delta_{wall}}{\lambda_{wall} \cdot U_{wall}} + \frac{1}{\alpha_{cold} \cdot U_{cold}} \quad (6.14)$$

where: α_{hot} heat transfer coefficient on the hot gas side
 U_{hot} wetted perimeter of one tube on the hot gas side
 δ_{wall} tube wall thickness
 U_{wall} perimeter of the tube
 λ_{wall} heat conductivity of the tube wall
 α_{cold} heat transfer coefficient on the cold gas side
 U_{cold} wetted perimeter of one tube on the cold gas side

In transient heat exchanger calculations, where the thermal resistance of the heat exchanger material plays an important role for the response of the heat exchanger to changing flow conditions, the heat conduction of the tube walls has to be taken into account. However, for the computational model for steady calculations described here the influence of the wall on the heat transfer coefficient can be neglected. This simplification reduces equation (6.14) to:

$$\frac{1}{k \cdot U} = \frac{1}{\alpha_{hot} \cdot U_{hot}} + \frac{1}{\alpha_{cold} \cdot U_{cold}} \quad (6.15)$$

The flow area, A_{flow} , is for the cold side equal to the flow area of one lancet. For the hot gas side the flow area, A_{flow} , is the product of the porosity and the area containing one lancet with the normal in the direction of the lancets as shown in figure 6.2 below.

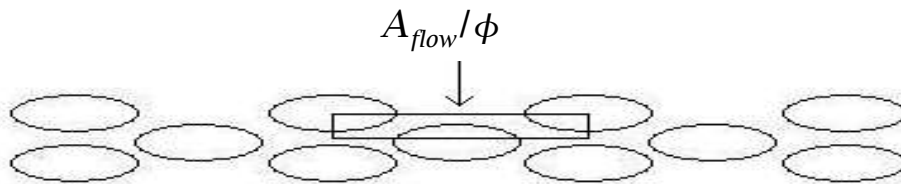


Figure 6.2 Heat exchanger lancets.

6.4 Cold side heat transfer correlation

The cold side of the heat exchanger consists in this case of the inner side of the tubes. The fluid enters the tubes from a distributor. In this distributor the Reynolds number is significantly higher, about two orders of magnitude, than in the tubes themselves indicating that the turbulence, to some extent, gets damped inside the tubes. Furthermore, inside the tubes the fluid is heated and with air as working medium the Reynolds number is reduced on the way through the tubes. If, on the other hand, the working fluid would be water the Reynolds number would instead increase when the fluid is heated. This is due to the different behaviours of the viscosity of the fluids with temperature. In this work, air is the only fluid considered as working medium of the heat exchanger and therefore the tube outlet Reynolds number will always be lower than the tube inlet Reynolds number. If the Reynolds number at the tube outlets is larger than what is considered to be the lower limit for turbulent flow then the flow inside the tubes, of course, is to be considered to be fully turbulent, when using air. On the other hand if the outlet Reynolds number is lower than the lower limit for turbulent flow then the flow is most likely in transition or maybe even laminar at the tube outlets, and possibly also in parts of the tubes. If the heat transfer characteristic for flow in a tube is studied, see figure 8.? below, one can notice that for fully developed pipe flow the transition region lies approximately in the Reynolds number range

2000-6000. The Reynolds number for the operating conditions of the investigated heat exchanger varies approximately between 1000 and 4000, which means that the flow might undergo transition for some of the operating conditions. Another feature of many tube bundle heat exchangers, such as the one in this study, is that the tubes have bends. The bends give rise to secondary flow that causes an additional pressure drop and increase the heat transfer (Schlichting and Hausen). This effect is stronger for laminar flow than for turbulent flow. Another effect that has been noticed in bends is that the critical Reynolds number where transition from laminar to turbulent flow takes place is higher than for straight tubes (Hausen). This effect is dependent on the D/d ratio, and it has been shown (Hausen) that the critical Reynolds number is 6000 with $D/d=50$ and about 9000 when $D/d=15$.

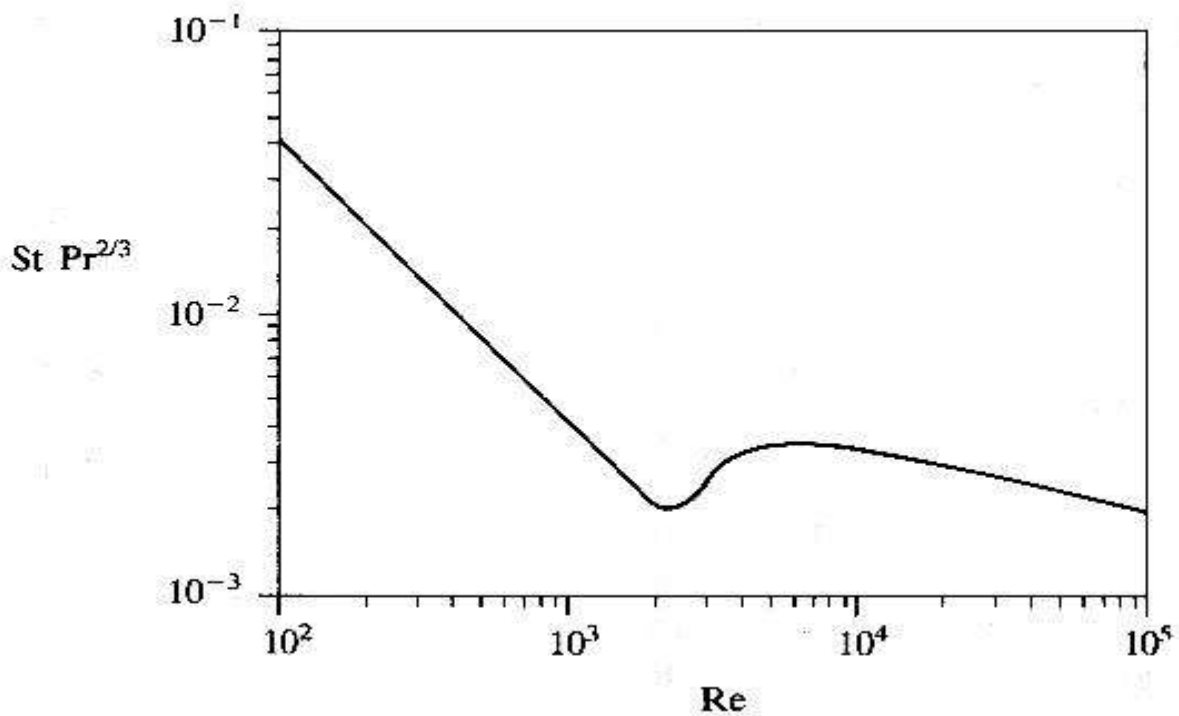


Figure 6.3 Heat transfer characteristics for fully developed pipe flow.
(Kays and Crawford)

To incorporate all the flow phenomena mentioned into a heat transfer correlation would raise the need for experiments or highly detailed numerical simulations for a variety of flow conditions, which is beyond the scope of this

work. Therefore the Nusselt number will be calculated under the assumption that the flow is turbulent and without the beneficial effect of the bends.

In typical tube bundle heat exchangers the tube inlet is sharp edged causing the flow to separate at the entrance and shedding vorticity into the main stream and thereby enhancing the heat transfer rate. Experiments on the turbulent flow entry region was performed for different configurations of circular tubes with constant wall temperature by Boelter, Young and Iversen presented in Kays and Crawford. Their results for the local Nusselt number, for turbulent flow, are shown below in figure 6.4.

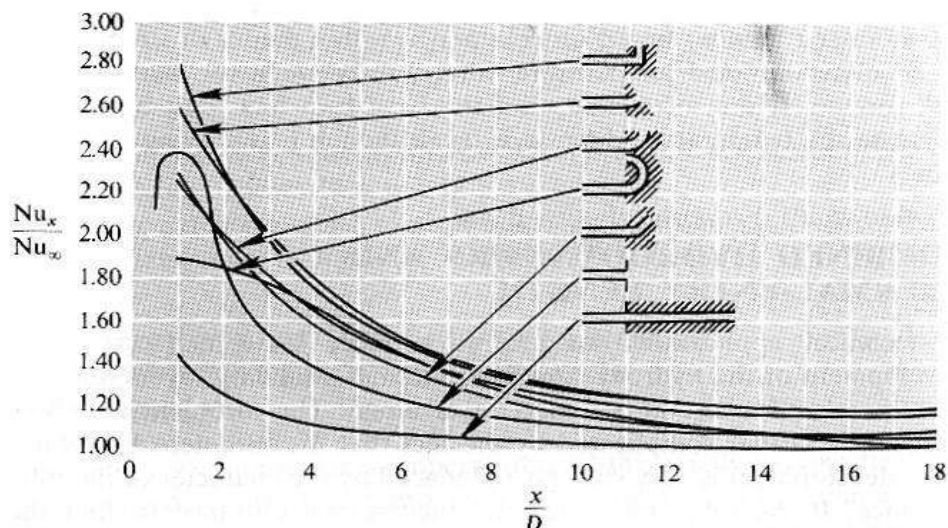


Figure 6.4 Measured local Nusselt number in the entry region of a circular tube for various entry configurations with constant wall temperature.
(Boelter, Young and Iversen in Kays and Crawford, 1993)

The lowest curve corresponds to the case with hydro dynamically fully developed flow and the second lowest to the case with an abrupt contraction, which corresponds to the flow conditions for most tube bundle heat exchangers.

A fairly good approximation of the improved heat transfer rate at the entry region is achieved by using the following expression for the ratio of the local Nusselt number to the Nusselt number for fully developed flow.

$$\frac{Nu_x}{Nu_\infty} = 1 + \frac{C}{x/D} \quad x > 0 \quad (6.16)$$

One of the most popular Nusselt number formulas for turbulent flow is the correlation by Dittus and Boelter (Dittus and Boelter in Bejan, 1991). They developed their formula for $0,7 \leq Pr \leq 120$ and $2500 \leq Re \leq 1,24 \cdot 10^5$ and the exponent of the Prandtl number is 0,3 when the fluid is cooled and 0,4 when the fluid is heated, as below.

$$Nu_\infty = 0,023 Re^{0,8} Pr^{0,4} \quad (6.17)$$

where all physical properties are to be taken at the bulk temperature.

If eq. (6.17) is combined with the equation above for enhanced heat transfer in the entry part of the tubes the following equation is obtained for the local Nusselt number inside the tubes.

$$Nu_x = \left(1 + \frac{C}{x/D}\right) \cdot 0,023 Re^{0,8} Pr^{0,4} \quad (6.18)$$

6.5 Hot side heat transfer correlation

Numerous studies of tube bundles have been performed by different researchers of which the works of Zukauskas are the most extensive. Zukauskas has made thorough investigations of the flow and heat transfer mainly in banks of circular tubes. However, in this study a heat exchanger with oval shaped tubes has been chosen and therefore the results of Zukauskas regarding heat transfer do not entirely apply. Oval shaped tube bundles have, on the other hand, been investigated by some other researchers e.g. by Bähr, Brauer, Hanke, Joyner and Palmer, Ruth, and Schad. Of which Hanke and Bähr performed measurements on tube bundles that are geometrically closest to the bundle chosen for this study. The other researchers have used geometries or configurations that differ too much to be used here. Brauer's tubes are e.g. significantly thicker, Joyner and Palmer only investigated the pressure drop, and Ruth used tubes with sharp front and back edges. Bähr and Hanke measured pressure drop over the tube bundle and the

mass transfer, by using naphthalene, for different positions on the tubes and for different locations in the tube bundle. The heat transfer coefficients were then deduced by using the analogy between heat and mass transfer. Merker et al (Merker, Hanke and Bähr) also studied the analogy between momentum and heat transport in cross flow tube banks with oval shaped tubes and came up with a method to calculate the mass transfer rate just from the overall pressure drop and the pressure distribution around a single tube inside the bank. They also showed that the pressure drop could be approximated by the pressure drop over a plane plate with a diffuser pressure drop added. Their results are however only valid for longitudinal pitches equal to the tube cord. For more compact configurations, such as the one in this work, other methods have to be used. Unfortunately no experimental data are available for exactly the configuration chosen for this study. Therefore the Reynold's analogy will be applied to the experimental data of Bähr and Hanke and the reference velocity will be approximated. Bähr and Hanke, like most of the others looking at tube bundles, have chosen to investigate the cross flow over the tube bundles where the fluid is passing the tubes from the sharp side. However, in many applications the flow conditions are a lot more complicated with significant velocity components in the other main directions (along the tubes and across the tubes from the blunt side). This means that a correlation that takes all velocity components into account has to be used to model the heat transfer phenomenon of the heat exchanger in this study.

If the flow through the tube bundle is looked upon as channel flow the transport of heat and momentum normal to the wall can be expressed as (Bejan, Merker)

$$-q_0'' = (k + \rho c_p \epsilon_H) \frac{d\bar{T}}{dy} \quad (6.19)$$

$$\tau_0 = (\mu + \rho \epsilon_M) \frac{d\bar{u}}{dy} \quad (6.20)$$

putting $Pr = Pr_t = 1$ and dividing the equations yields

$$\frac{\tau_0}{-q_0''} = \frac{1}{c_p} \frac{d\bar{u}}{d\bar{T}} \quad (6.21)$$

if this equation is integrated from the wall ($\bar{u}=0, \bar{T}=T_0$) to the free stream ($\bar{u}=U_\infty, \bar{T}=T_\infty$) the following equation is obtained

$$\frac{\tau_0}{-q_0''} = \frac{U_\infty}{c_p(T_\infty - T_0)} \quad (6.22)$$

The force caused by the shear stress can, for channel flow be written as

$$\tau_0 \cdot A_{wall} = \Delta p \cdot A_{flow} \quad (6.23)$$

and the heat flux can be expressed as

$$-q_0'' = \alpha \cdot (T_\infty - T_0) \quad (6.24)$$

Combining the equations above yields

$$\alpha = \frac{\Delta p \cdot c_p \cdot D_h}{U_\infty \cdot L \cdot 4} \quad (6.25)$$

or more general

$$\alpha = \frac{|\nabla p| \cdot c_p \cdot D_h}{4 \cdot |U|} \quad (6.26)$$

which leads to the following expression for the local Nusselt number

$$Nu_x = \frac{|\nabla p| \cdot c_p \cdot D_h^2}{4 \cdot \lambda \cdot |U|} \quad (6.27)$$

If we only consider the pressure losses caused by the momentum sink terms, and not the wall friction on e.g. the collector and distributor tubes, to have an influence on the heat transfer then the equation above can be written as

$$Nu_x = \frac{|\sqrt{S_x^2 + S_y^2 + S_z^2}| \cdot c_p \cdot D_h^2}{4 \cdot \lambda \cdot |\sqrt{u^2 + v^2 + w^2}|} \quad (6.28)$$

which gives information about the heat transfer for all possible directions of the flow.

One drawback of the Reynold's analogy is that Pr is assumed to be 1. However, in gas flow the variation of Pr with temperature, is for most applications, very moderate, and the Pr dependence could be put in a proportional constant. If this is not sufficient one way of improving the heat transfer calculation could be to make use of the Prandtl analogy (Merker). However, for tube bundle flow the estimation of the Nusselt number is rather rough, and without proper experimental data there is no need to try to improve the Reynold's analogy. For flow along the tubes there is no uncertainty about what velocity to use, but for cross flow this it is not obvious if e.g. the maximum velocity should be used or perhaps the area averaged velocity. If the experimental data is available for the tube bundle in question there is no problem in adjusting the Reynold's analogy above to the data, but when no experimental data is available for the bundle in question an assumption on the reference velocity has to be made. As already mentioned Hanke and Bähr have performed experiments on bundles of oval shaped tubes. The bundle arrangement and definition of the characteristic quantities in the experiments by Hanke and Bähr is shown in figure 6.5 below.

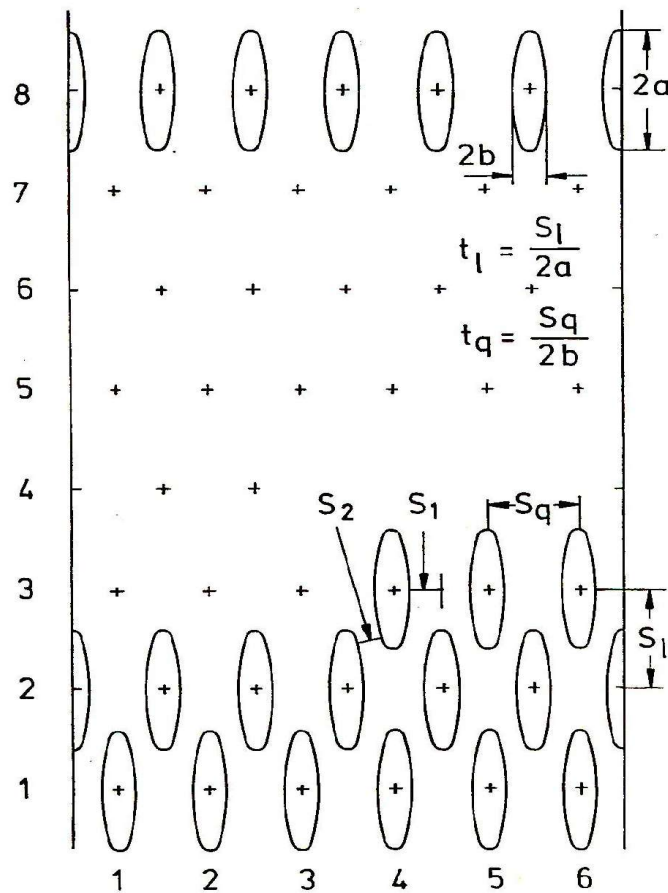


Figure 6.5 Tube bundle arrangement and definition of characteristic quantities. (Hanke).

The tube geometry closest to the one in this study is the one investigated by Bähr (Ovalrohr 2) for which he performed measurements on three different configurations. Bähr ran his experiments for a large variation of Reynold's numbers on a bundle consisting of ten rows. Three bundle configurations with staggered oval shaped tubes were tested. The characteristic quantities of the bundle were varied according to:

$$0,665 \leq t_l \leq 1,01 \text{ and } 1,36 \leq t_q \leq 2,21$$

that covers the configuration in this work.

A reference velocity for the Reynold's analogy must be dependent on the characteristic geometric quantities of the bundle as well as on the tube

geometry itself. An estimation of the reference velocity based purely on the geometric characteristics of the bundle can only lead to a relatively rough estimate of the velocity valid for a narrow range of geometric variations, but it is not the ambition of this work to come up with a general heat transfer correlation for staggered bundles of oval shaped tubes, but to estimate the Nusselt number for the bundle chosen and possibly to give some practical ideas on how to do such estimations. Bähr, to some extent, took the bundle characteristics into account when he defined his reference velocity

$$u_c = u_{in} \cdot \frac{L}{\frac{2a}{N_R} + S_l \cdot \left(1 - \frac{1}{N_R}\right) - \frac{A_G}{S_q}} \quad t_l \leq 1,0 \quad (6.29)$$

$$u_c = u_{in} \cdot \frac{L}{2a - \frac{A_G}{S_q}} \quad t_l > 1,0 \quad (6.30)$$

Unfortunately, Bähr's velocity is too high for the Reynold's analogy. Therefore, another reference velocity will be used here, defined as

$$\frac{1}{u_{ref}} = \frac{1}{u_c} + \frac{1}{u_{in}} \quad (6.31)$$

From this reference velocity the reference porosity can be defined as

$$\phi_{ref} = \frac{u_{in}}{u_{ref}} \quad (6.32)$$

If assuming the x-direction to be the direction across the tubes from the sharp side and using the expressions above the local Nusselt number can be written as

$$Nu_x = \frac{|\sqrt{S_x^2 + S_y^2 + S_z^2}| \cdot c_p \cdot D_h^2}{4 \cdot \lambda \cdot |\sqrt{u_{ref}^2 + v^2 + w^2}|} \quad (6.33)$$

This equation seems to be singular for stagnation points. To overcome this the limit of the equation above has to be found when the velocity components approach zero. If this is done the following equation for the local Nusselt number for stagnation points is obtained

$$Nu_x = \frac{\mu \cdot c_p \cdot D_h^2}{4 \cdot \lambda \cdot \phi / \phi_{ref}} \sqrt{D_{xx}^2 + D_{yx}^2 + D_{zx}^2} \quad (6.34)$$

Bähr and Hanke made measurements of the overall pressure drop of the tube bundle and mass transfer measurements for separate tubes and also locally on the tubes. This means that there is not really enough pressure drop data to calculate the Nusselt number for a certain position in the bundle by using the Reynold's analogy above. What Hanke and Bähr noticed, as did also other authors (e.g. Zukauskas) was that the heat transfer improves with the position inwards till about row 4 or 5 where it stabilizes.

If the above Nusselt number expressions are used in conjunction with the experimental data from Bähr, for the rows 4-9, correlated Nusselt numbers can be calculated that in average differ -3% from the experimental with a standard deviation of 10,2%. In the figures below the correlated Nusselt numbers are plotted against the experimental ones for Bähr's three measured configurations. In the fourth figure the correlated Nusselt numbers are plotted against the experimental.

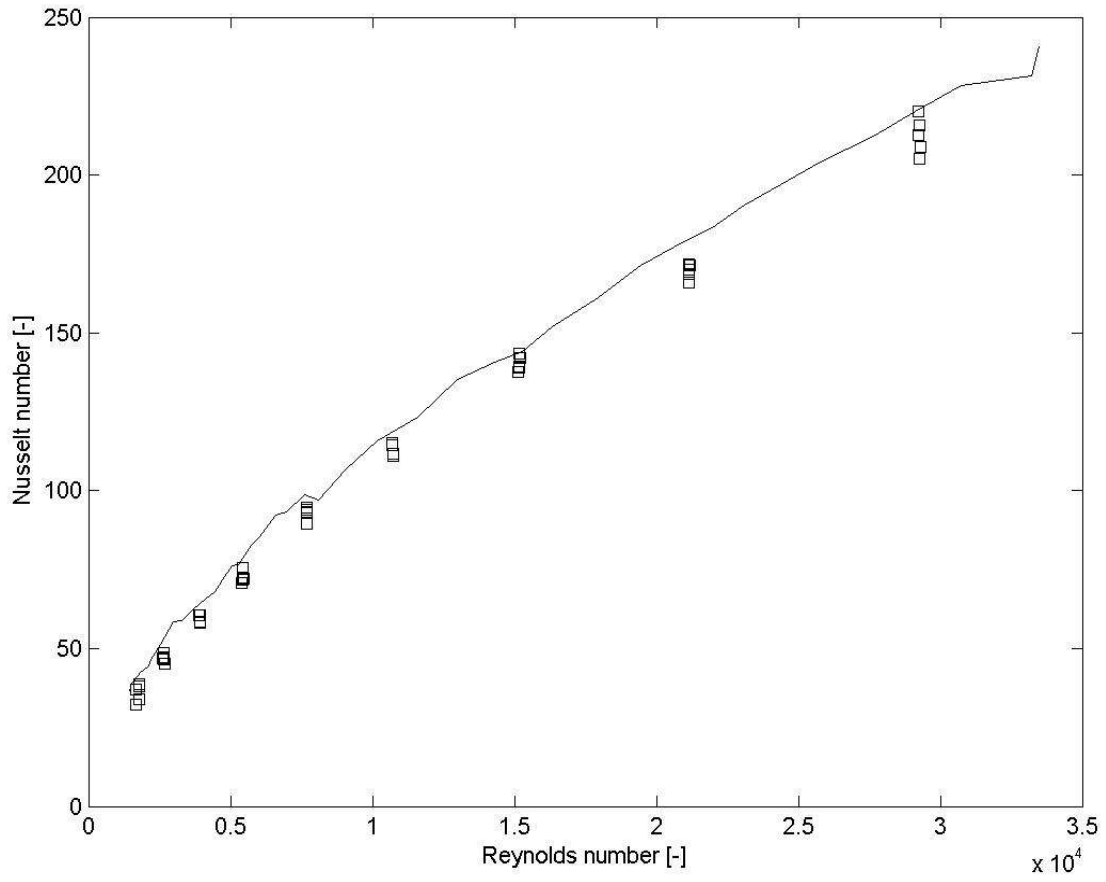


Figure 6.6 Nusselt number for Ovalrohr 2, $t_1=1,01$ and $t_q=1,36$.

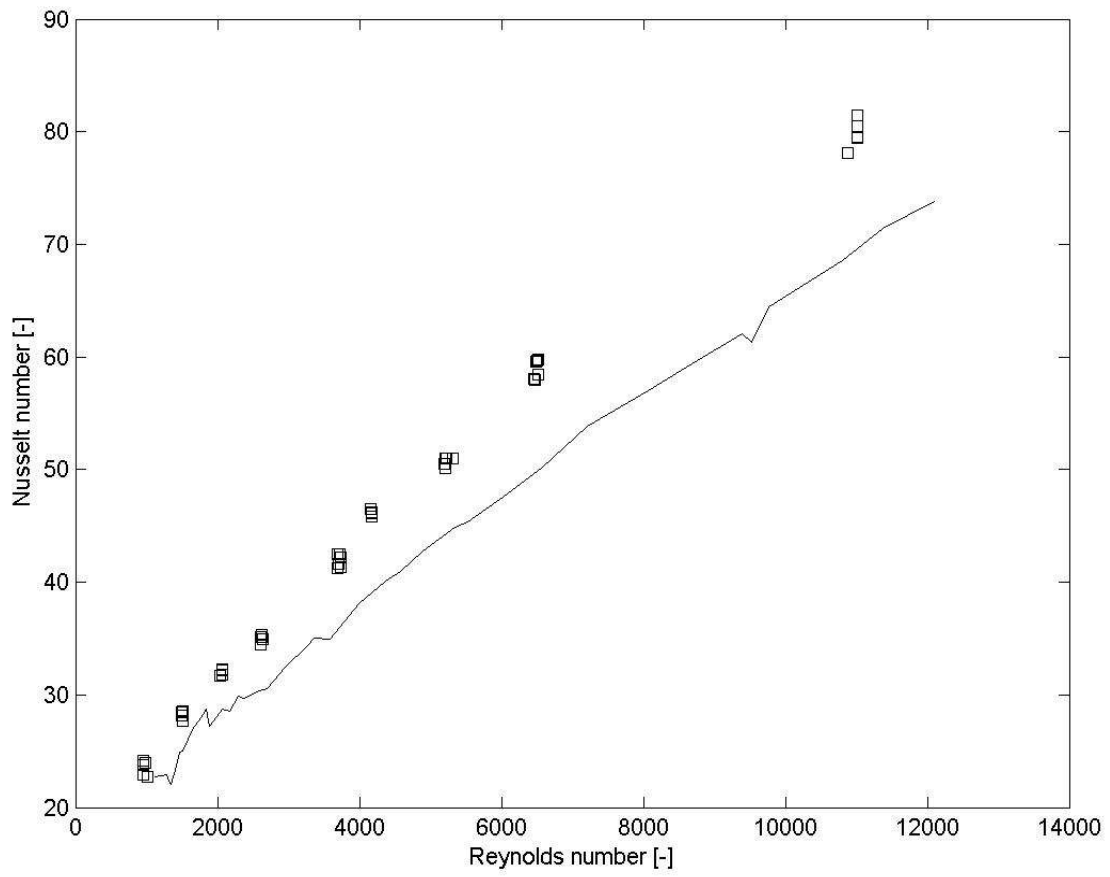


Figure 6.7 Nusselt number for Ovalrohr 2, $t_1=0,92$ and $t_q=1,73$.

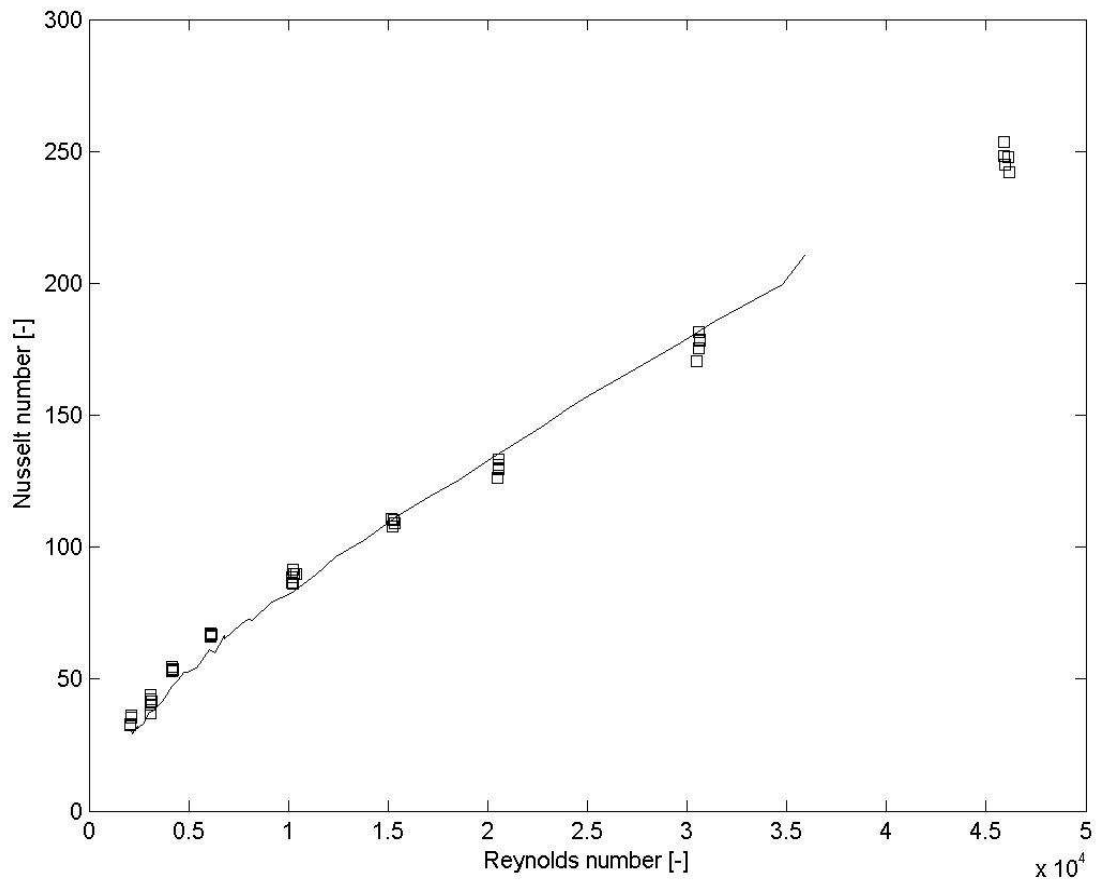


Figure 6.8 Nusselt number for Ovalrohr 2, $t_1=0,665$ and $t_q=2,21$.

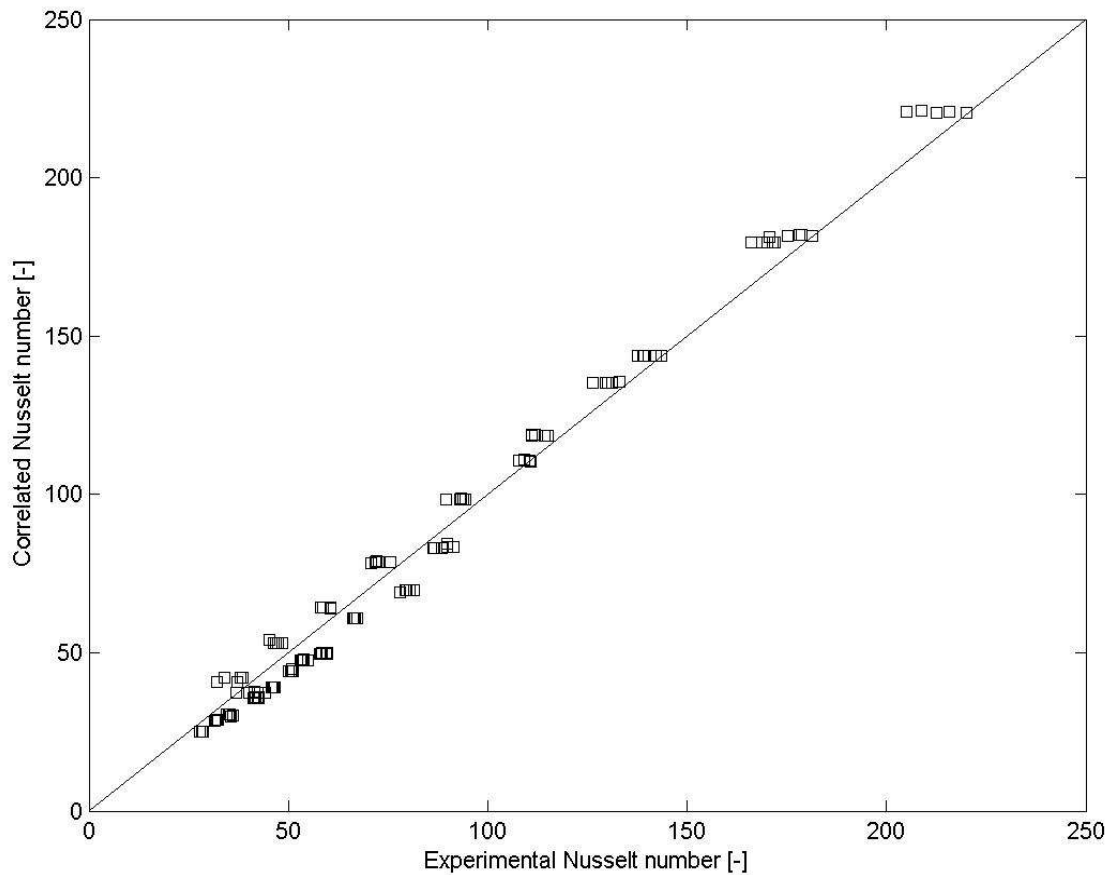


Figure 6.9 *Ovalrohr 2, Correlated Nusselt number vs experimental Nusselt number.*

As can be seen in the figures above the agreement is relatively good between the correlated and the experimental data. However, this does not mean that the method to calculate the reference velocity used here is valid for other tube geometries and bundle configurations, but only that the Reynold's analogy is able to deliver reliable heat transfer information if a meaningful reference velocity is found.

Since the velocity component across the tubes from the blunt side is very small, due to the tube geometry and bundle configuration, there is almost no movement in this direction. This means that it is less critical exactly what

velocity is used for this direction and therefore the velocity used in the correlation is just the geometrical velocity of this direction.

It was experimentally shown by Stephan and Traub that the turbulence level has some influence on the heat transfer but not on the drag. This means that when a Reynolds analogy is applied this effect can not be accounted for. However, the influence of the turbulence level was only seen in the first rows and the increase in Nusselt number when the turbulence level was raised from 0,8% to 25% was for the first rows in their staggered bundle 30-35%. In a real machine one could expect the turbulence level vary less and thus neglecting the influence of the turbulence should be acceptable.

7 Heat exchanger code

A FORTRAN code of around 6000 lines, containing a number of subroutines and functions, describing the flow and heat transfer process of the heat exchanger, described in the proceeding chapters, has been developed. This FORTRAN code is linked to the solver of a commercial CFD-software. The CFD-software chosen for this purpose is CFX-TASCflow, described in chapter 3.1, which like most commercial CFD software packages, offers the possibility to add source terms to the transport equations. One or more regions have to be defined for the heat exchanger where the sources are applied. The heat exchanger chosen for this study has been divided into several porous regions according to figure 7.1. The purpose of using several regions for the heat exchanger is to allow for the construction of local coordinate systems, the modelling of spacers, and a meaningful treatment of the heat exchanger bends. CFX-TASCflow works on block structured hexahedral grids and the heat exchanger is meshed with grid lines parallel to the heat exchanger tubes forming an O-grid.

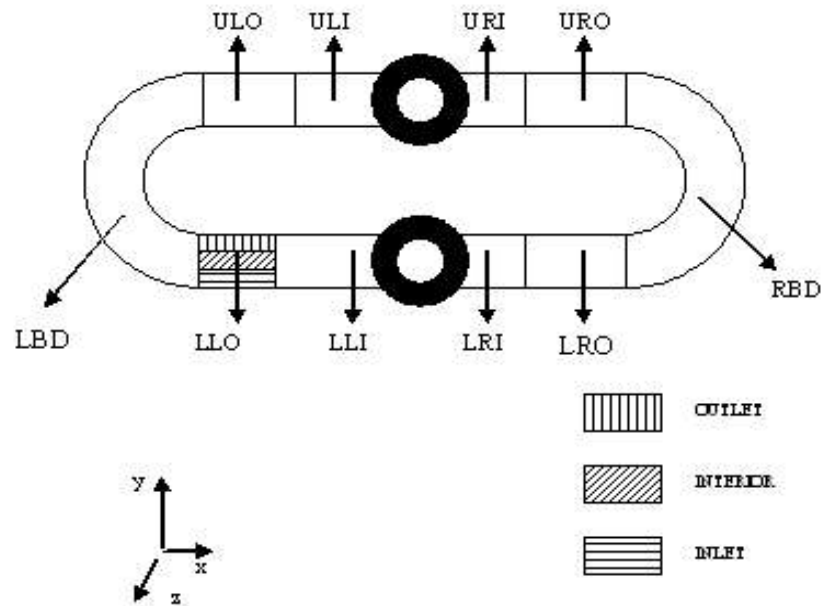


Figure 7.1 Regions and naming conventions for the heat exchanger porosity model.

In order for the porosity model subroutines to work the different parts of the heat exchanger need to have certain names. The different parts of the heat exchanger are, in this study, named in a way that may come natural when looking at the heat exchanger from the side in the direction of the collector and distributor tubes. In the straight parts of the heat exchanger the first letter (L or U) stands for lower or upper. The second letter (L or R) stands for left or right. The third letter (I or O) stands for inner or outer. The bends have the names LBD and RBD which are just short for Left BenD and Right BenD, see figure 7.1. These names of the different parts are followed by a number between 1 and 9 telling what heat exchanger they belong to.

When building a CFD model including a heat exchanger there is usually the need for having the global coordinate system positioned in a certain way. The global coordinate directions might very well be arbitrary relative to the heat exchanger. Some applications might also include more than one heat exchanger and the heat exchangers in most such cases do not all lie in the same directions. A way to overcome these problems is to use local coordinate systems for the heat exchangers in the computational domain. In the heat exchanger simulation code, described here, local Cartesian coordinate systems are used for the heat exchangers. These coordinate systems are constructed automatically by the code and the momentum sources and active coefficients

are transformed to the global Cartesian coordinate system, used by the solver. The local coordinate system, as shown in figure 7.1, is located in such a way that the x-axis is lying along the lower edge of the heat exchanger directed from left to right and the y-axis going upwards. The z-axis is then pointing out of the picture. Furthermore, the bends of the heat exchanger can not be handled easily with Cartesian coordinate systems and therefore local cylindrical coordinate systems are used for these.

As already mentioned, several heat exchangers might be used in some applications. Thus, the heat exchanger simulation software has been written in such a way that up to nine heat exchangers can be handled in the same computational model.

The heat exchanger needs spacers to stabilize the tube bundle and separate the tubes. These spacers are mounted in different parts of the tube bundle and could be simulated by either blocking the corresponding regions off or defining them as porous regions. However, if they are defined as porous regions they need to be given a porosity and momentum sinks have to be calculated for them. Since no information is available on the exact construction and fluid mechanical behaviour of these spacers they are considered impermeable in the current simulation subroutines.

The momentum source terms are calculated by sweeping over all nodes in the heat exchanger regions once for every outer iteration step. The calculation of the energy source terms, on the other hand, needs some further treatment, since additional constraints are put on the cold side flow field. Such a constraint is that the cold side flow is unidirectional and parallel to the tubes. For a prescribed heat flux the hot side energy source terms could be calculated in the same manner as the momentum source terms. However, since the cold and hot sides are coupled and the heat flux is dependent on both the cold and hot side temperatures, this is not possible. The calculation of the energy source terms needs information about the cold side temperature field, which in turn is dependent on the hot side temperature field. This means that a calculation procedure for the cold side temperature has to be implemented. The cold side temperature is calculated by a 4th order Runge-Kutta scheme in the cold side flow direction, and the calculation procedure is described in chapter 6.1. Due to the division of the heat exchanger in different regions the node indices do not follow the same directions in the entire heat

exchanger. This makes it necessary to determine the directions of the indices of the different heat exchanger regions in order to enable sweeps in the flow direction. The hot side source terms are determined in the same calculation procedure. The heat exchanger subroutine is called for, once for the energy equation and once for the momentum equations, in every outer iteration and after its execution the corresponding source terms are sent to the flow solver. The intermediate cold side temperature field is saved, at the end of each energy source term calculation, in a temporary file and read during the energy source term calculation of the following outer iteration.

7.1 Temperature calculation procedure

The temperature field on the cold side of the heat exchanger has to be calculated outside the flow solver of CFX-TASCflow. Thus the temperature fields can not be calculated coupled, but in an iterative manner. In this way the calculated cold side temperature field correspond to the hot side temperature field of the proceeding iteration. However, since the problems to be solved are steady this is of no importance. The cold and hot side temperatures are calculated according to the procedure described below.

Initial conditions:

$$T_{cold}(I, J, K)_0 = T_{inlet}$$

$$T_{hot}(I, J, K)_0 = \text{initial guess}$$

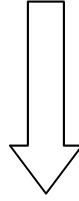
Outer iteration/false time step 1:

$$T_{cold}(I,J,K)_1 = f_c(T_{hot}(I, J, K)_0, T_{cold}(I, J, K)_0, S_x, S_y, S_z, Re_{cold}, Re_{hot}) \quad \text{Runge-Kutta method}$$

$$T_{hot}(I,J,K)_1 = f_h(T_{cold}(I, J, K)_0, T_{hot}(I, J, K)_0, S_x, S_y, S_z, Re_{cold}, Re_{hot}) \quad \text{CFX-TASCflow solver}$$

$$\Delta T_{cold,1} = \text{MAX}(T_{cold}(I, J, K)_1 - T_{cold}(I, J, K)_0)$$

Time marching direction



Outer iteration/false time step n:

$$T_{cold}(I,J,K)_n = f_c(T_{hot}(I, J, K)_{n-1}, T_{cold}(I, J, K)_{n-1}, S_x, S_y, S_z, Re_{cold}, Re_{hot}) \quad \text{Runge-Kutta method}$$

$$T_{hot}(I,J,K)_n = f_h(T_{cold}(I, J, K)_{n-1}, T_{hot}(I, J, K)_{n-1}, S_x, S_y, S_z, Re_{cold}, Re_{hot}) \quad \text{CFX-TASCflow solver}$$

$$\Delta T_{cold,n} = \text{MAX}(T_{cold}(I, J, K)_n - T_{cold}(I, J, K)_{n-1})$$

No convergence criterion has been applied for the cold side temperature, but the convergence behaviour can be observed by studying the maximum change in the cold side temperature field every outer iteration. The cold side temperature change of the last iteration is written to a file and can be visualized by using the CFX-TASCflow post processor. The above calculation procedure yields a fast and stable convergence without need for cold side temperature relaxation. An example of the convergence behaviour for the hot side energy equation and the cold side temperature field are shown below in figure 7.2 and 7.3. The figure shows that the maximum change in the cold side temperature drops very fast to the order 10^{-2} , i.e. 0,01 K, where the convergence criterion 10^{-4} , for the hot side energy equation is reached and the calculation stopped.

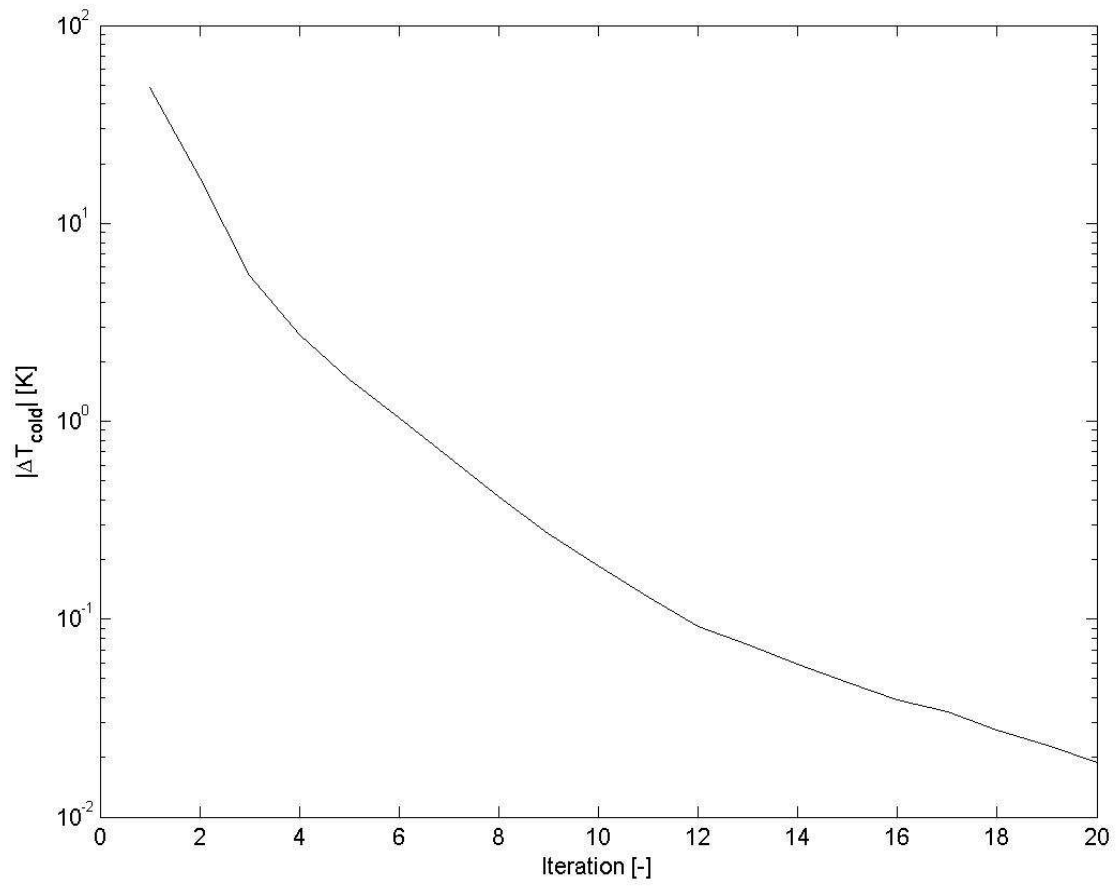


Figure 7.2 Cold side temperature convergence behaviour.

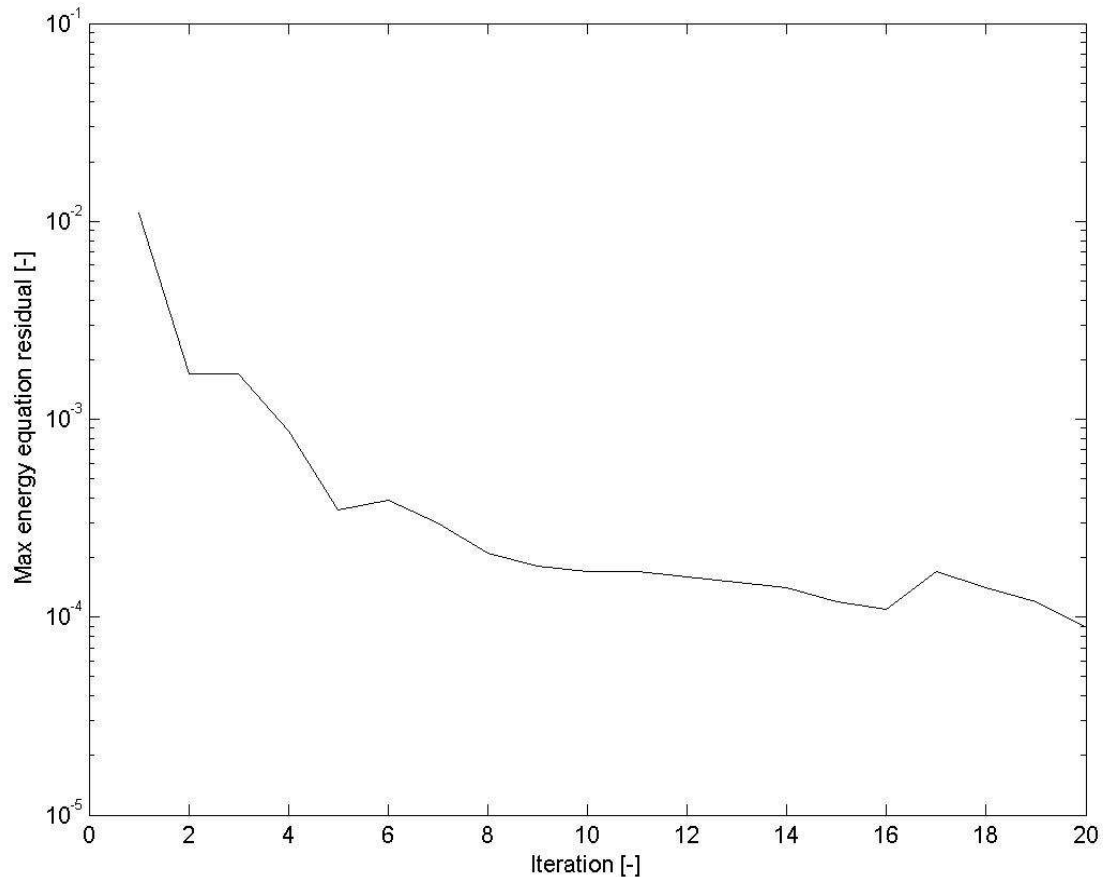


Figure 7.3 Hot gas energy equation convergence behaviour.

7.2 Cold gas flow distribution

In the heat exchanger simulation software the flow distribution on the cold side is prescribed and constant and has a homogeneous distribution over the entire inlet. In reality one could expect the flow not to be evenly distributed. The cold side flow distribution could be calculated by solving a non-linear algebraic equation system consisting of one equation for the pressure drop for each row of nodes, except for one, together with one mass conservation equation. However, this implies a relocation of the cold side inlet boundary to

where common flow conditions exist for all the rows of nodes. Furthermore, would precise flow resistance data and pressure loss coefficients be necessary for an accurate calculation of the cold side flow distribution. If no such reliable experimental information is available, calculations of the flow field will not lead to a flow distribution more accurate than the assumed homogeneous flow field.

7.3 Structure of the heat exchanger simulation code

The heat exchanger simulation code is built up by several subroutines and functions that are called for during the execution of the code. These subroutines and functions are called for in order to determine different quantities such as e.g. heat transfer coefficients, momentum and energy source terms, different physical quantities, or to determine index directions. A comprehensive description of the heat exchanger simulation code is given below where the main tasks performed in the code are described.

- Define workspace for required scalars, source terms and active coefficients.
- Read scalar values into workspace.
- Read input data from parameter list.
- Determine the number of sub regions in the different regions of the heat exchangers.
- Start the loop over the number of heat exchangers in the model.
- Find out the heat exchanger position.
- Build a local Cartesian coordinate system for the current heat exchanger.
- Calculate the transformation matrices.
- Build local cylindrical coordinate systems for the heat exchanger bends.
- Check if the momentum equations are to be solved and then:

-
- ◆ Start the momentum source term calculations.
 - Set the tensor elements for the bends equal to the corresponding elements of the straight parts.
 - Loop over all nodes in all subregions and calculate momentum source terms and active coefficients by using the subroutines for the straight parts and the bends respectively. Transform the source terms and active coefficients to the global coordinate system used by the solver.
 - Apply the momentum source terms and active coefficients.
 - If the computational model contains more than one heat exchanger then calculate the momentum source terms and active coefficients for those in the same manner as above.
 - ◆ End of the momentum source term calculations.
 - Check if the energy equation is to be solved and if heat transfer option is chosen and then:
 - ◆ Start the energy source term calculation
 - Find out the directions of the indices in all regions and sub regions by using the appropriate subroutines.
 - If an intermediate cold side temperature field exists in the temporary file then read the old cold side temperature field. If an intermediate cold side temperature field does not exist then create a temporary file with the cold side temperature field equal to the cold side inlet boundary temperature (e.g. as a start solution).
 - Determine the collector/distributor tube radius in order to calculate the distance from the cold side inlet.
 - Start looping over all nodes, in all parts of the hex, and advance in the cold side flow direction.

-
- If the index is lying on the cold side inlet boundary the temperature is kept equal to the cold side inlet temperature boundary condition. For other indices calculate the temperature by using the cold side upstream temperature, the local hot side temperature and the node distances in flow direction by using the Runge-Kutta scheme. For the first index in flow direction of one region the temperature is calculated by using the temperature of the last node in the upstream region. The hot side energy source terms and active coefficients are calculated during the same sweep as the cold temperature field.
 - During the temperature calculation procedure calls to subroutines for determining the index directions, the physical quantities and heat transfer data are made.
 - If the model contains more than one heat exchanger then the cold side temperature field and the hot side energy source terms and active coefficients for those are calculated in the same manner as above.
- ◆ End of energy source term calculation.
 - ◆ Write the cold side temperature field and node data to output file.
 - ◆ Write maximum local cold side temperature change (with sign) to the screen and to file.
- End of user defined subroutine.

8 Validation

For the validation of the heat exchanger simulation code experimental isothermal results from Prof. Goulas, head of the Laboratory of Fluid Mechanics and Turbomachinery (LFMT) at the University of Thessaloniki, and non-isothermal results from MTU have been made available. The, in chapter 5, derived resistance tensors have been used for a first calculation of the MTU experiments. With the MTU results as basis the resistance tensors are then tuned to reproduce nearly the same pressure drop as the MTU experiments.

The outlet temperatures, on both the cold and the hot sides, have then been compared with the experimental results. The experiments from LFMT have been calculated with the new set of tensors and comparisons have been made for the overall pressure drop and the velocity profiles down stream of the heat exchanger and between the heat exchanger matrices.

8.1 Hot gas experiments

Rig tests have been performed at MTU for investigations of heat exchanger performance (Reile). The tests were undertaken in a hot gas channel allowing for both pressure drop and heat transfer experiments. The tested heat exchanger was of the type described in proceeding chapters and of a 10/9/10-configuration. The cooling air was supplied to one of the sides of the heat exchanger, where also the heated air was returned, as shown in figure 8.1 below.

The pressures and temperatures on the hot side were measured in grids below and above the heat exchanger. Figure 8.2 shows the grid for the outlet temperature gauges and their positions. The inlet and outlet pressures and temperatures were evaluated as arithmetic means of the measured values at the different positions. The grid for the outlet temperature measurement consists of 5 times 8 gauges which make a total of 40 gauges. On the cold side devices for temperature, pressure and mass flow measurements were located inside the pipes upstream and downstream of the heat exchanger.

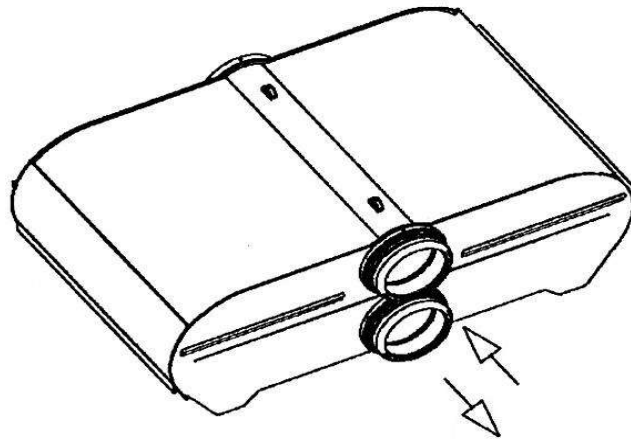


Figure 8.1 Sketch of the MTU heat exchanger showing the cold side inlet and outlet on the front.

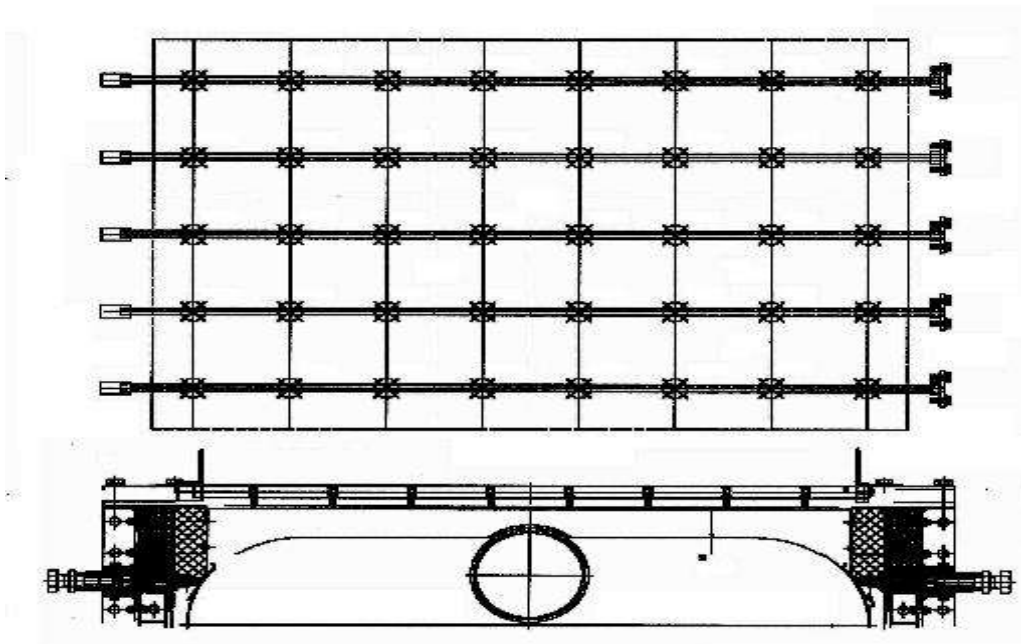


Figure 8.2 Temperature measurement positions on the heat exchanger. Top view above and side view below.

A three dimensional CFD-model was built for the experimental set-up with a symmetry plane adopted at the location corresponding to the middle of the heat exchanger depth.

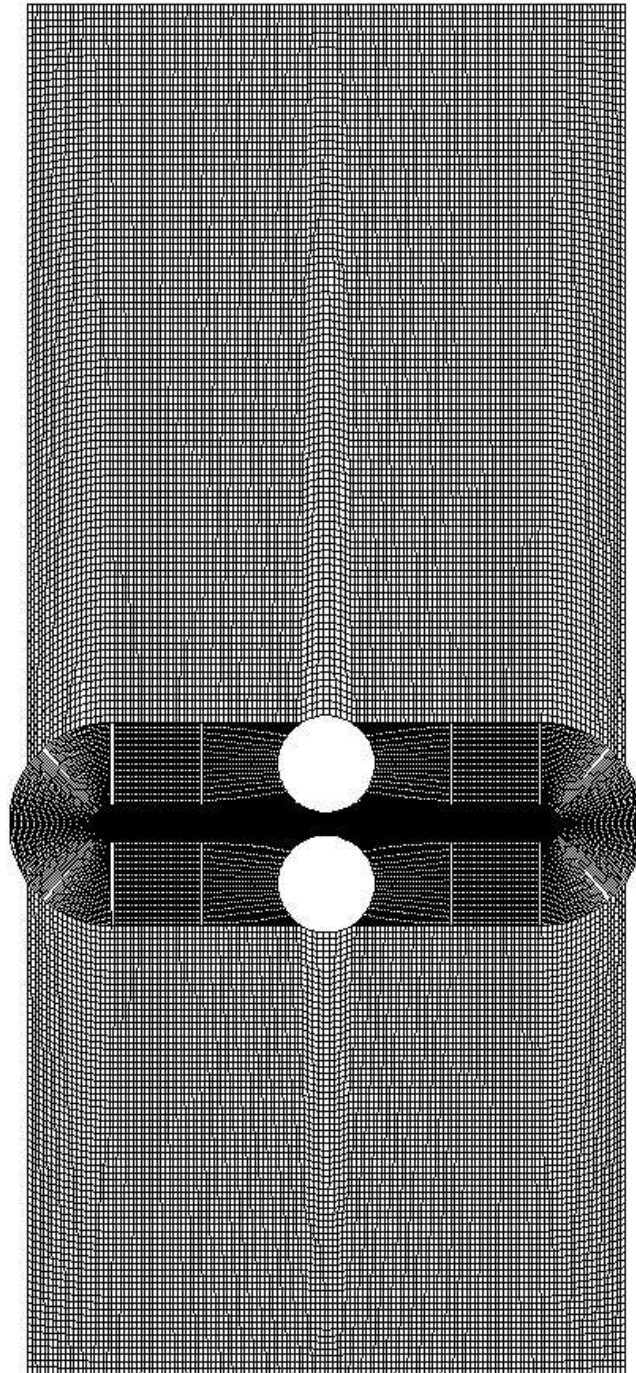


Figure 8.3 Grid for the CFD-model of the hot gas experimental set-up.

The total number of grid nodes is 1,3 million, half the heat exchanger depth is represented by 31 nodes, and the 10/9/10-matrix thickness by 25 nodes. In this way the cell thickness is smaller than the longitudinal pitch. The 31 nodes in the transversal direction make the cell depth correspond to about six tubes,

which is too little in order to catch strong temperature gradients. However, since the inflow is evenly distributed it is very unlikely that strong temperature gradients would occur in the transversal direction and thus the grid resolution is acceptable. The outlet region down stream of the heat exchanger is chosen long enough to avoid flow recirculating into the computational domain. The grid for the symmetry plane is shown in figure 8.3.

The settings for all the cases calculated are summarized the table below.

Property	Case1	Case2	Case3	
Inlet B.C., hot side	Mass flow	0,75 kg/s	2,12 kg/s	3,08 kg/s
	T	818,8 K	1064 K	1032 K
	Tu = 10% L = 35 transversal pitches			
Outlet B.C	Average static pressure			
Wall B.C.	No slip, fixed wall distance wall function			
Other B.C.	Symmetric			
Inlet B.C., cold side	Mass flux	20,7 kg/s,m ²	58,2 kg/s,m ²	84,1 kg/s,m ²
	T	394,1 K	572,9 K	705,3 K
Flow type	Compressible			
Turbulence model	SST			
Turbulent Prandtl number	0,9 and 9			
Advection scheme	2 nd order			
Convergence criteria	Maximum residuals < 10 ⁻⁴			

Table 8.1 Numerical settings for the hot gas cases.

The experimental Reynolds number, shown in table 8.2, are for all three investigated cases relatively low. On the hot side the Reynolds numbers range between 270 and 1150, which is in the lower end and in part outside of the data used for the heat transfer correlations. Unfortunately, this increases

somewhat the uncertainty of the calculated Nusselt numbers. As can be seen in table 8.2 the Reynolds numbers on the cold side are also relatively low indicating flow in transition. With the cold side heat transfer correlation valid for turbulent flows, thus exaggerated heat transfer on the cold side could be expected.

Hot gas case	Hot side Reynolds number	Cold side Reynolds number
Case 1	270 (Inlet) - 380 (Outlet)	810 (Outlet) - 1260 (Inlet)
Case 2	625 (Inlet) - 860 (Outlet)	1960 (Outlet) - 2740 (Inlet)
Case 3	880 (Inlet) - 1150 (Outlet)	2850 (Outlet) - 3470 (Inlet)

Table 8.2 *Approximate Reynolds numbers.*

Non-isothermal calculations, with variable physical quantities, of the experimental test cases with the resistance tensors derived in chapter 5 yield under estimations of the pressure drop for all three cases. The pressure drop and the mean temperature are, as the experimental quantities, calculated as arithmetic means of the values at the gauge positions. The deviation between the calculated and measured results is increasing with Reynolds number, see table 8.3, and lies between -8,2% and -18,5%. The resistance tensors in chapter 5 are derived from CFD calculations for laminar and fully turbulent flows. As is indicated from the Reynolds numbers in table 8.2 the flow in the test cases is likely to be in the transition region where the drag coefficient for a tube bundle goes from a linear to a quadratic velocity dependence. However, this transition is not completely smooth, see figure 2.1, but shows higher drag coefficients for the transition region than could be obtained from an interpolation between drag coefficients in the purely laminar and turbulent regions. This, in addition to the uncertainties in the underlying CFD-calculations (chapter 3), is most likely to be the reason for these deviations.

Hot gas case	$\Delta p_{calculated}$ [Pa]	$\Delta p_{measured}$ [Pa]	Deviation [%]
Case 1	990,8	1079	-8,2
Case 2	5248	6277	-16,4
Case 3	8868	10880	-18,5

Table 8.3 First numerical pressure drop results.

If the pressure drop in the heat exchanger is assumed to essentially depend on the velocity component in the normal direction to the heat exchanger, then the diagonal tensor elements for this direction drops could be adjusted to give good agreement with the experimental pressure drops. A couple of test calculations suggests the following adjustment of the reference tensor elements.

$$D_{ref}^{mod} = 1,438 \cdot D_{ref} \quad (8.1)$$

$$F_{ref}^{mod} = 1,538 \cdot F_{ref} \quad (8.2)$$

It is assumed that the cross wise components have the same relation to the normal components as the original components, and that the pipe flow assumption for flow along the tubes is kept. With these assumptions the tuned resistance tensors look like

$$\text{Inlet: } D_{ij} = \begin{bmatrix} 0,20 \cdot D_{ref}^{mod} & 0 & 0 \\ 0,42 \cdot D_{ref}^{mod} & 0,84 \cdot D_{ref}^{mod} & -1,85 \cdot D_{ref}^{mod} \\ 0 & 0 & 8,4 \cdot D_{ref}^{mod} \end{bmatrix} \quad (8.3)$$

$$F_{ij} = \begin{bmatrix} 0,19 \cdot F_{ref}^{mod} & 0 & 0 \\ 0,37 \cdot F_{ref}^{mod} & 0,74 \cdot F_{ref}^{mod} & -1,63 \cdot F_{ref}^{mod} \\ 0 & 0 & 7,4 \cdot F_{ref}^{mod} \end{bmatrix} \quad (8.4)$$

$$\text{Outlet: } D_{ij} = \begin{bmatrix} 0,20 \cdot D_{ref}^{mod} & 0 & 0 \\ -0,42 \cdot D_{ref}^{mod} & 0,84 \cdot D_{ref}^{mod} & 1,85 \cdot D_{ref}^{mod} \\ 0 & 0 & 8,4 \cdot D_{ref}^{mod} \end{bmatrix} \quad (8.5)$$

$$F_{ij} = \begin{bmatrix} 0,19 \cdot F_{ref}^{mod} & 0 & 0 \\ -0,37 \cdot F_{ref}^{mod} & 0,74 \cdot F_{ref}^{mod} & 1,63 \cdot F_{ref}^{mod} \\ 0 & 0 & 7,4 \cdot F_{ref}^{mod} \end{bmatrix} \quad (8.6)$$

$$\text{Interior: } D_{ij} = \begin{bmatrix} 0,21 \cdot D_{ref}^{mod} & 0 & 0 \\ 0 & D_{ref}^{mod} & 0 \\ 0 & 0 & 10 \cdot D_{ref}^{mod} \end{bmatrix} \quad (8.7)$$

$$F_{ij} = \begin{bmatrix} 0,20 \cdot F_{ref}^{mod} & 0 & 0 \\ 0 & F_{ref}^{mod} & 0 \\ 0 & 0 & 10 \cdot F_{ref}^{mod} \end{bmatrix} \quad (8.8)$$

Calculations with the new set of tensors lead to the results shown in tables 8.4 – 8.6.

Case 1	Δp [Pa]	$T_{hot\ out}$ [K]	$T_{cold, out}$ [K]
1 st order	1085	472,7	768,6
2 nd order	1072	471,7	768,7
2 nd order, $Pr_t=9$	1072	471,9	768,9
Experimental	1079	495,5	765,8

Table 8.4 Global results for hot gas case 1.

Case 2	Δp [Pa]	$T_{hot, out}$ [K]	$T_{cold, out}$ [K]
1 st order	6341	681,8	992,5
2 nd order	6278	680,5	991,8
2 nd order, $Pr_t=9$	6281	681,3	992,5
Experimental	6277	705,6	979,7

Table 8.5 Global results for hot gas case 2.

Case 3	Δp [Pa]	$T_{hot, out}$ [K]	$T_{cold, out}$ [K]
1 st order	10941	781,6	979,6
2 nd order	10834	780,7	979,1
2 nd order, $Pr_t=9$	10842	781,3	979,5
Experimental	10880	790,8	972,3

Table 8.6 Global results for hot gas case 3.

The CFD calculations predict higher heat transfer rates than is seen in the experiments. This is most prominent for the two cases with lowest Reynolds numbers. With arguments mentioned above, this is also what could be expected, with the heat transfer correlation on the cold side for turbulent flow and the uncertainties in the hot side heat transfer correlation. The calculated hot side outlet temperature profiles for the symmetry plane are shown in figures 8.4 – 8.6 together with the measured temperatures. The trend is captured in the CFD results, but with an under estimation of the temperatures close to the distributor tube. The experimental data shows a significant scatter in the heat exchanger outlet temperatures, on the hot gas side, with a tendency to lower temperatures for the rear end of the heat exchanger, especially near the bends. If this is a realistic behaviour or not is hard to say since this tendency is not seen closer to the distributor tube. It is therefore difficult to judge whether or not the variation is real or if it is just a result of measurement uncertainties. As also can be seen in figures 8.4 – 8.6 the difference between the 1st and the 2nd order advection schemes is almost negligible, with only slightly sharper temperature gradients for the 2nd order scheme. The increased turbulent Prandtl number leads to steeper gradients, as expected. However, the difference to the cases with $Pr_t=0,9$ is small, which

indicates that the turbulent heat transport along the tubes is of little importance.

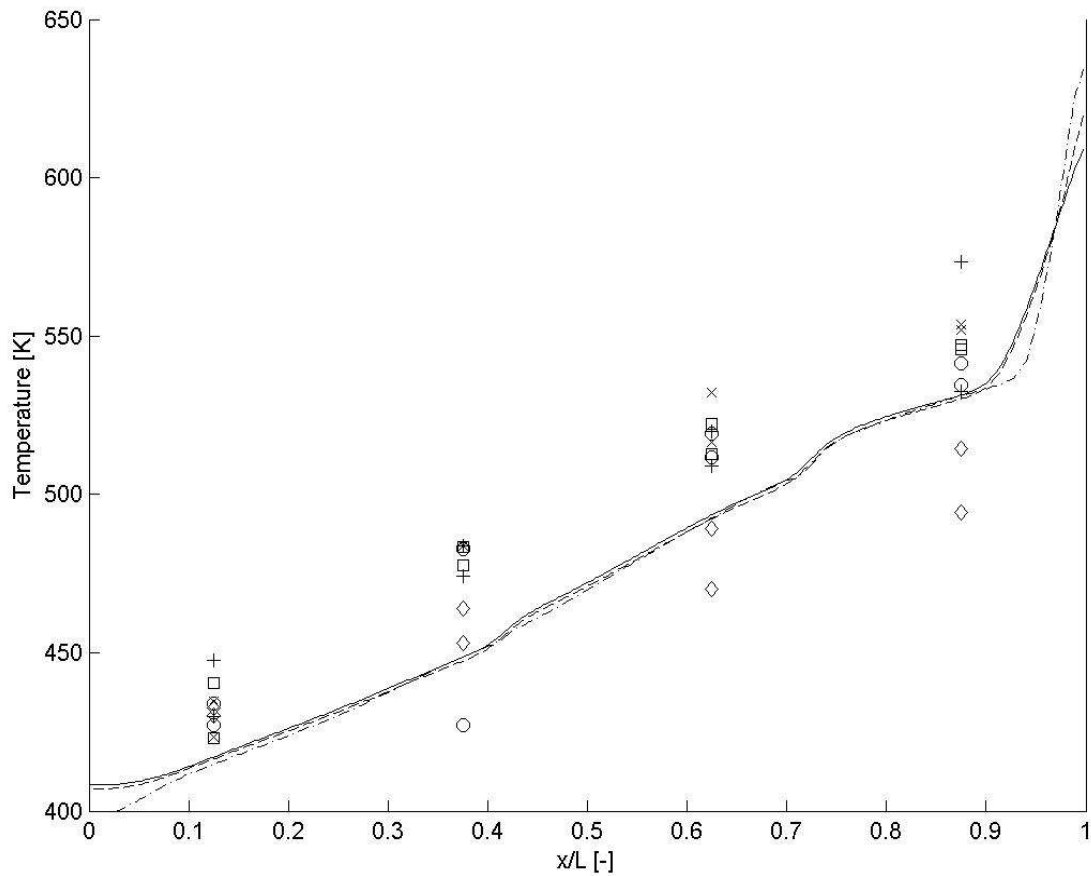


Figure 8.4 Outlet temperature distribution, case 1.

Solid: 1st order, dashed: 2nd order, dash-dotted: 2nd order, $Pr_t = 9$.

Square: front row, cross: 2nd row, circle: middle row, plus: 4th row, diamond: last row.

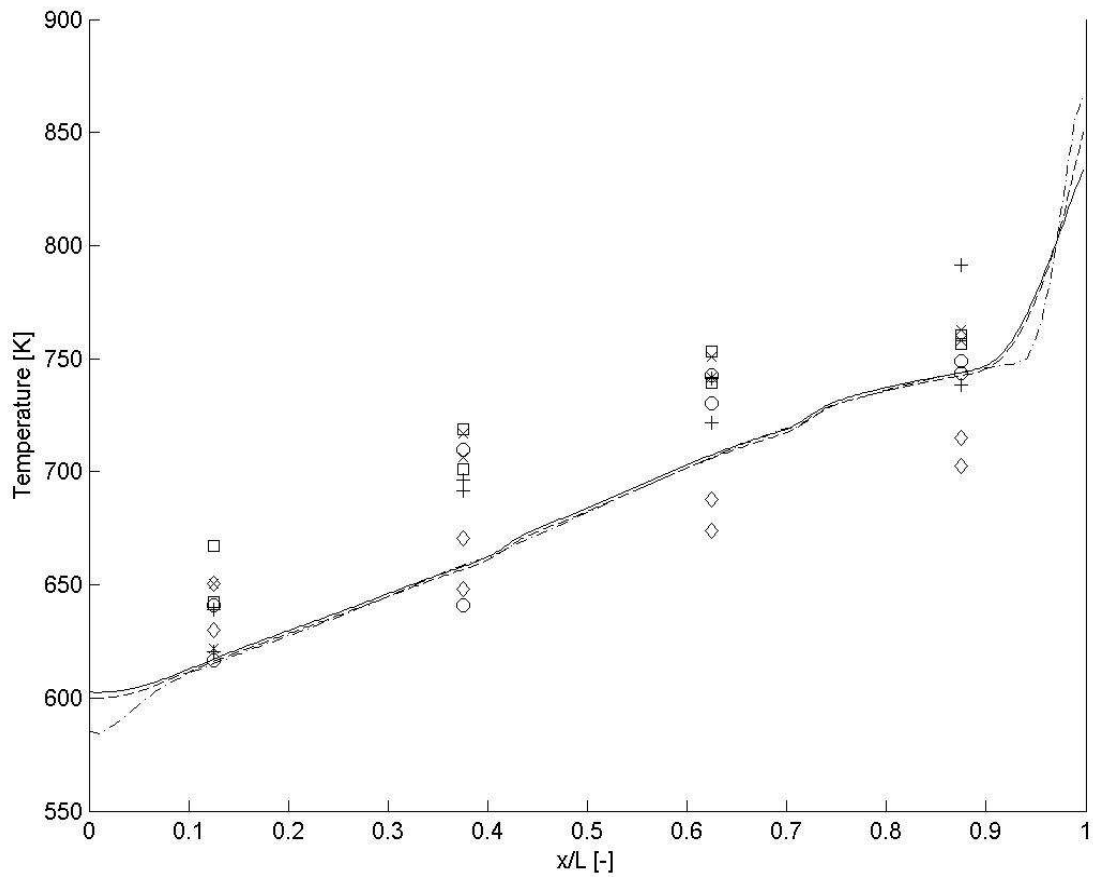


Figure 8.5 Outlet temperature distribution, case 2.

Solid: 1st order, dashed: 2nd order, dash-dotted: 2nd order, $Pr_t = 9$.

Square: front row, cross: 2nd row, circle: middle row, plus: 4th row, diamond: last row.

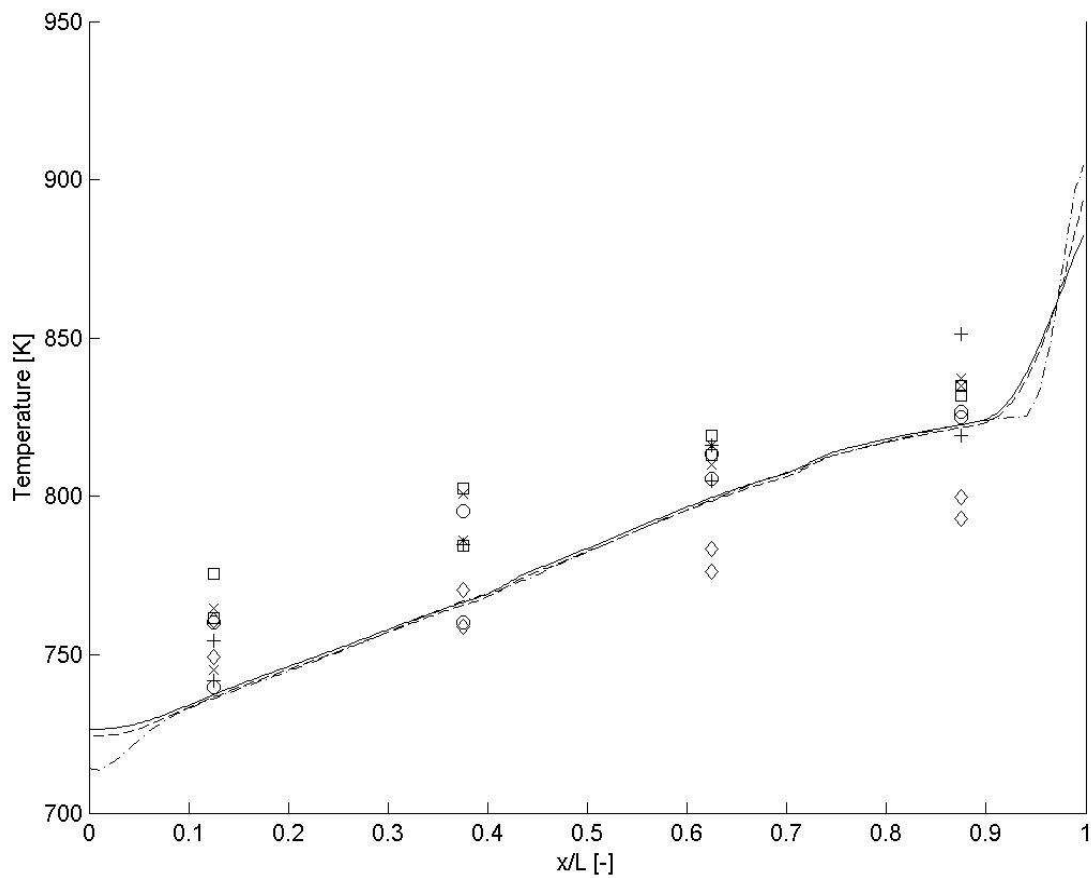


Figure 8.6 Outlet temperature distribution, case 3.

Solid: 1st order, dashed: 2nd order, dash-dotted: 2nd order, $Pr_t = 9$.

Square: front row, cross: 2nd row, circle: middle row, plus: 4th row, diamond: last row.

8.2 Experiments on a 1:1 half heat exchanger matrix

A number of experiments have been performed at LFMT on a 1:1 model of a half heat exchanger matrix mounted inside a wind tunnel (Goulas et al,

Goulas et al 2002, Goulas et al 2004). The experiments have been performed with different inflow conditions with the use of a three-hole probe. The probe was traversed over the inlet and outlet planes and measurements were taken every 10 or 20 mm, depending on the strength of the gradients. An average was made over the channel height, and the inlet profiles were used as inlet boundary conditions for the computations. The calculated pressure drop was derived averaging the pressure at the same locations and in the same way as the measured pressure drop. The wind tunnel tests were made on a heat exchanger with uncovered bend, covered front of the bend, and covered back of bend. The tests were run for different Reynolds numbers and inclination angles. The most detailed measurements have been used for the validation of the heat exchanger simulation code. For all cases with a non-zero inclination angle there was a small cover placed between the heat exchanger bend and the wind tunnel wall in order to avoid air leakage. This cover was also included in the numerical models. The calculations were performed as two dimensional with the most important settings described in table 8.7.

Property	All cases
Inlet B.C.	Velocity profiles Tu = 2,5% L = 35 transversal pitches
Outlet B.C	Average static pressure
Wall B.C.	No slip, fixed wall distance wall function
Other B.C.	Symmetric
Flow type	incompressible
Turbulence model	SST
Advection scheme	2 nd order
Convergence criteria	Maximum residuals < 10 ⁻⁴

Table 8.7 Numerical settings for the half heat exchanger cases.

8.2.1 Zero degree inclination angle

For the inlet flow angle of zero degree experiments were made on a set-up that is described in figure 8.7 below. The set-up was used for experiments on the heat exchanger without bend cover as well as for experiments done with either the back or front part of the heat exchanger bend covered. The cases without cover were impossible to mesh correctly, using hexahedral elements, in the region between the bend and the wind tunnel side wall. Therefore two different grids were built for these cases. One grid with a small leakage between the bend and the wind tunnel side wall and a second grid with this part blocked, as can be seen in figures 8.8 and 8.9 below. The grids have a total number of nodes of about 130000.

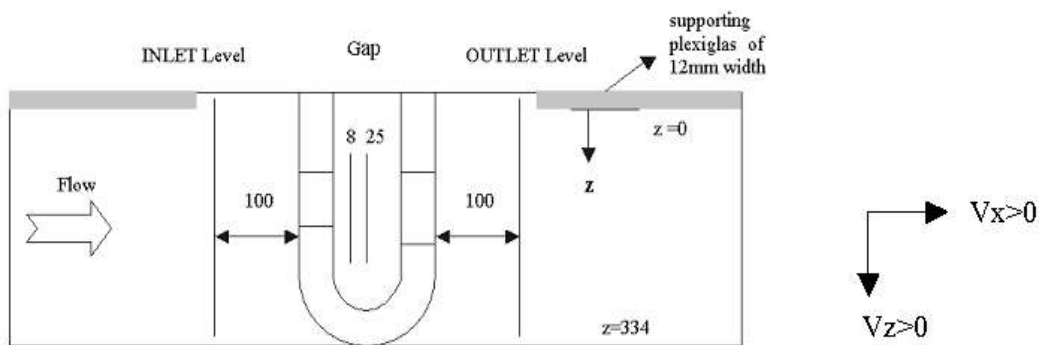


Figure 8.7 Experimental set-up for the zero inlet angle cases.

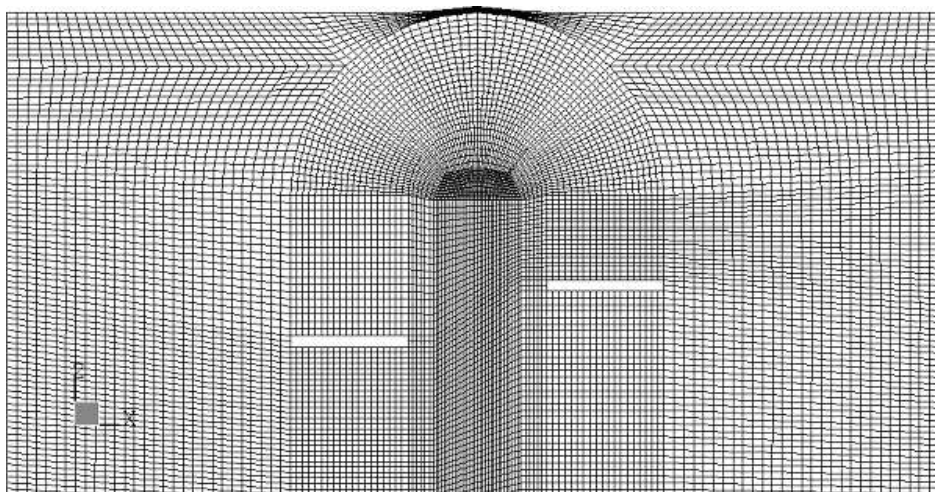


Figure 8.8 Part of the grid with a leakage between bend and side wall.

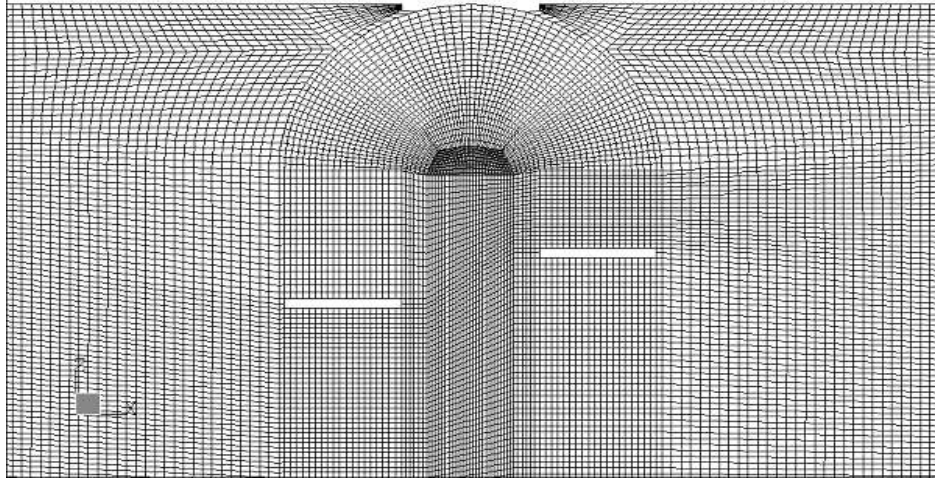


Figure 8.9 Part of the grid with a blockage between bend and side wall.

The measured cases were calculated isothermally and the pressure drops are presented in table 8.8. As can be seen in the pressure drop results the total pressure drop is over estimated for the cases with a blockage and under estimated for the leakage cases. The deviations are of the same order of magnitude (<9%) for both with and without leakage. If the true geometry could have been meshed it is most probable that the deviations then would have been somewhere in between these two. If the pressure drop would have been over or under estimated is hard to judge, but still the deviations would have been acceptable.

Reynolds number	Δp_{meas} [Pa]	Δp_{meas} [Pa]	Deviation [%]
1077	262,17	247,27	+6,0
2041	813,89	763,37	+6,6
3118	1798,6	1653,9	+8,8
3679	2441,3	2269,4	+7,6
3768	2482,0	2327,2	+6,7
1077 leakage	237,69	247,27	-3,9
2041 leakage	729,94	763,37	-4,4
3118 leakage	1596,2	1653,9	-3,5
3679 leakage	2086,7	2269,4	-8,1
3768 leakage	2125,6	2327,2	-8,7

Table 8.8 Total pressure drop results for the cases without cover.

In figures 8.10-8.15 the velocity profiles are shown for both the case with a leakage and the case with a blockage together with the measured velocities. It should be noted that the flow in the experiments separated from the downstream central tube. This is obvious in the results for the outlet where an increase in the measured U-component can be seen close to the central tube (left in the figure). The separation can also be noticed if the W-component at the outlet is studied. The calculations, on the other hand, do not show any separation, but this is to be expected since a wall function is used. Wall functions are developed for boundary layers in equilibrium, which means that a separation and a wall function are in contradiction. It is further worth noting that the crosswise component, W, always is very low, since the flow is mainly unidirectional. The main difference between the numerical results with and without leakage is of course seen in the bow region where the leakage case shows higher velocities. The U-component is under estimated between the matrices, but quite well predicted at the outlet, with some over estimation close to the bend. The reason for the under estimated U-component between the matrices could be that there, in the experiments, also is a separation downstream of the first central tube that reduces the flow area and increases the velocity. However, such a phenomenon has not been possible to verify.

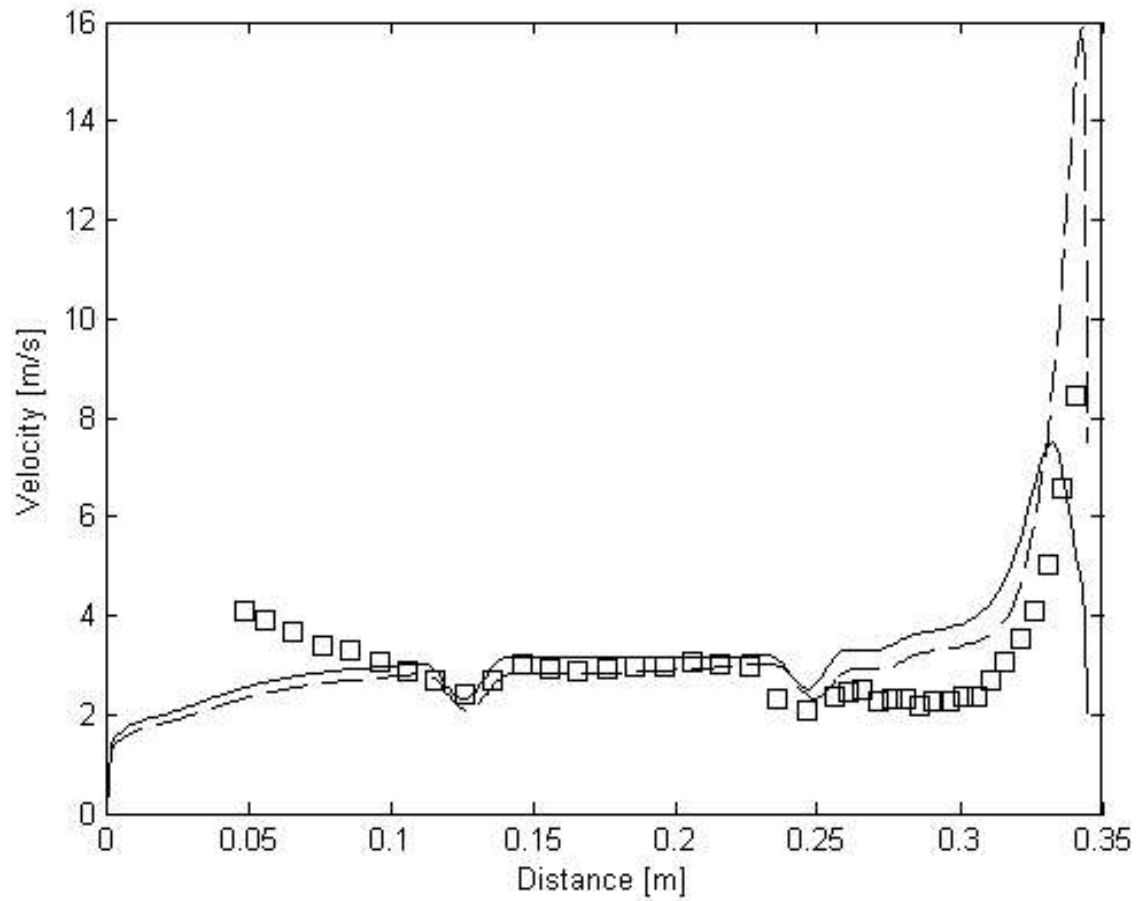


Figure 8.10 $Re = 1077$, U -component at the outlet plane.
Solid: blockage, Dashed: leakage, Squares: experimental results.

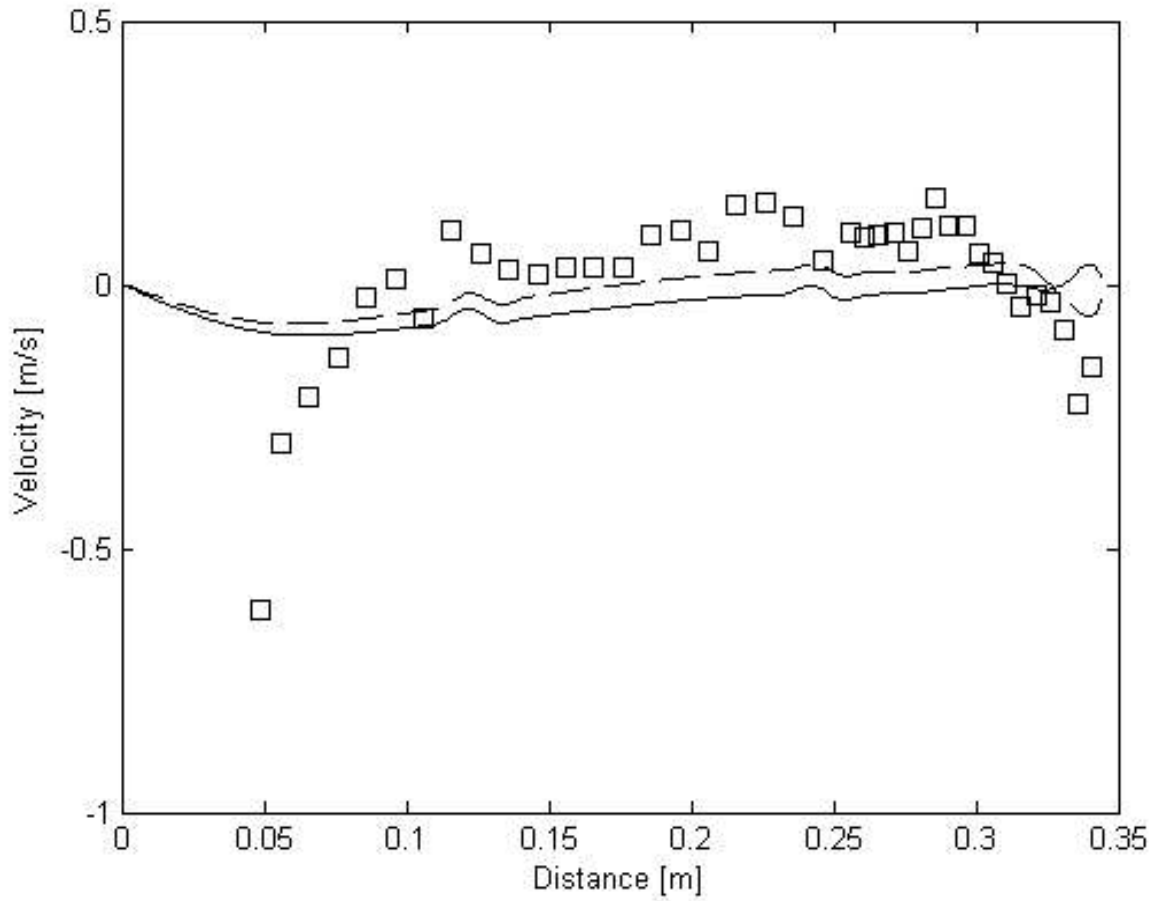


Figure 8.11 $Re = 1077$, W -component at the outlet plane.
Solid: blockage, Dashed: leakage, Squares: experimental results.

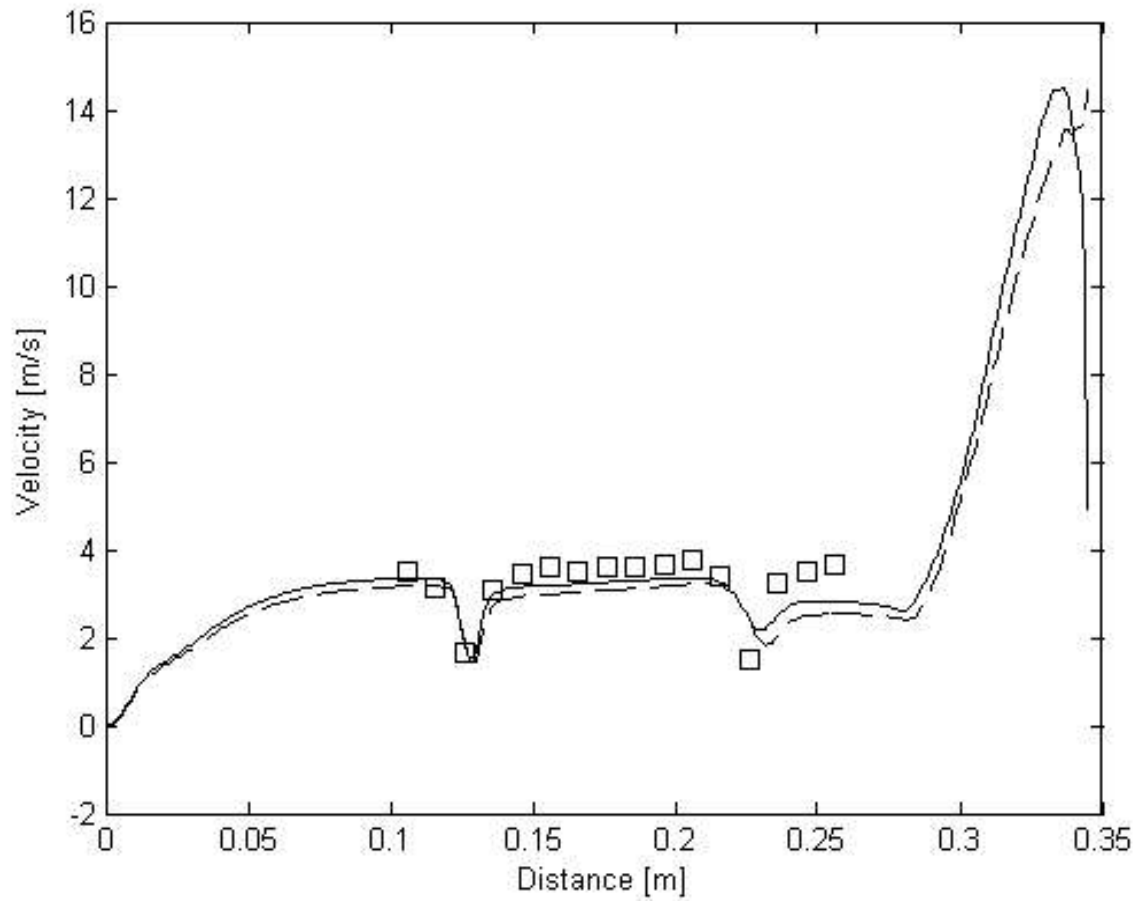


Figure 8.12 $Re = 1077$, U -component at the 25 mm plane.
Solid: blockage, Dashed: leakage, Squares: experimental results.

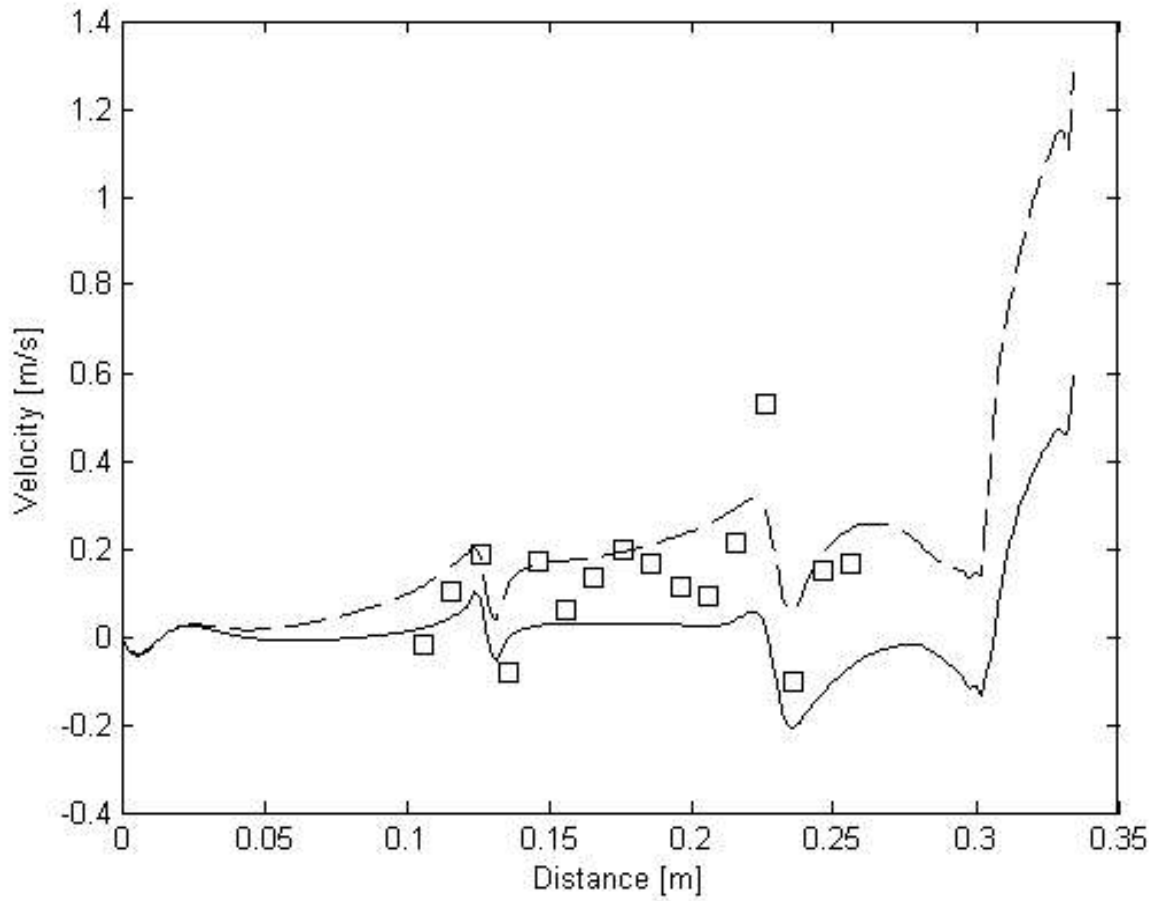


Figure 8.13 $Re = 1077$, W -component at the 25 mm plane.
Solid: blockage, Dashed: leakage, Squares: experimental results.

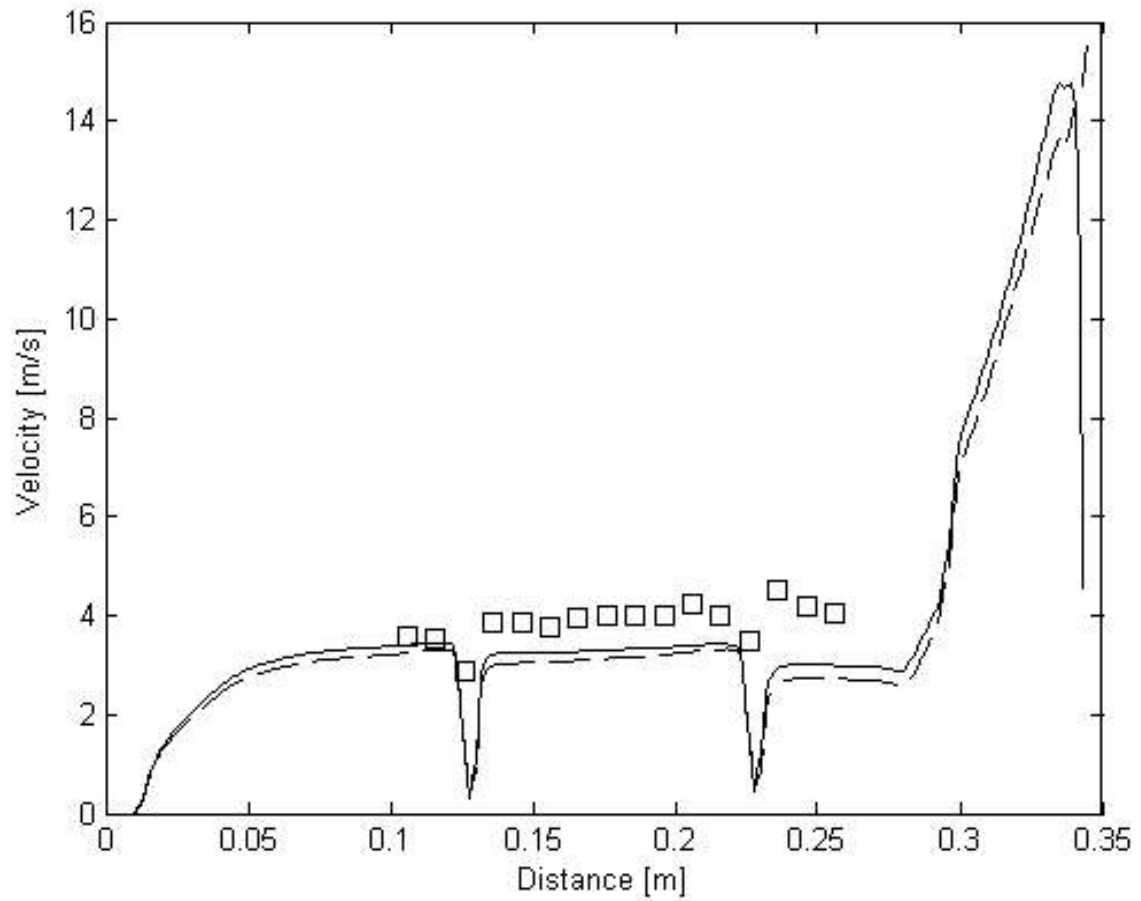


Figure 8.14 $Re = 1077$, U -component at the 8 mm plane.
Solid: blockage, Dashed: leakage, Squares: experimental results.

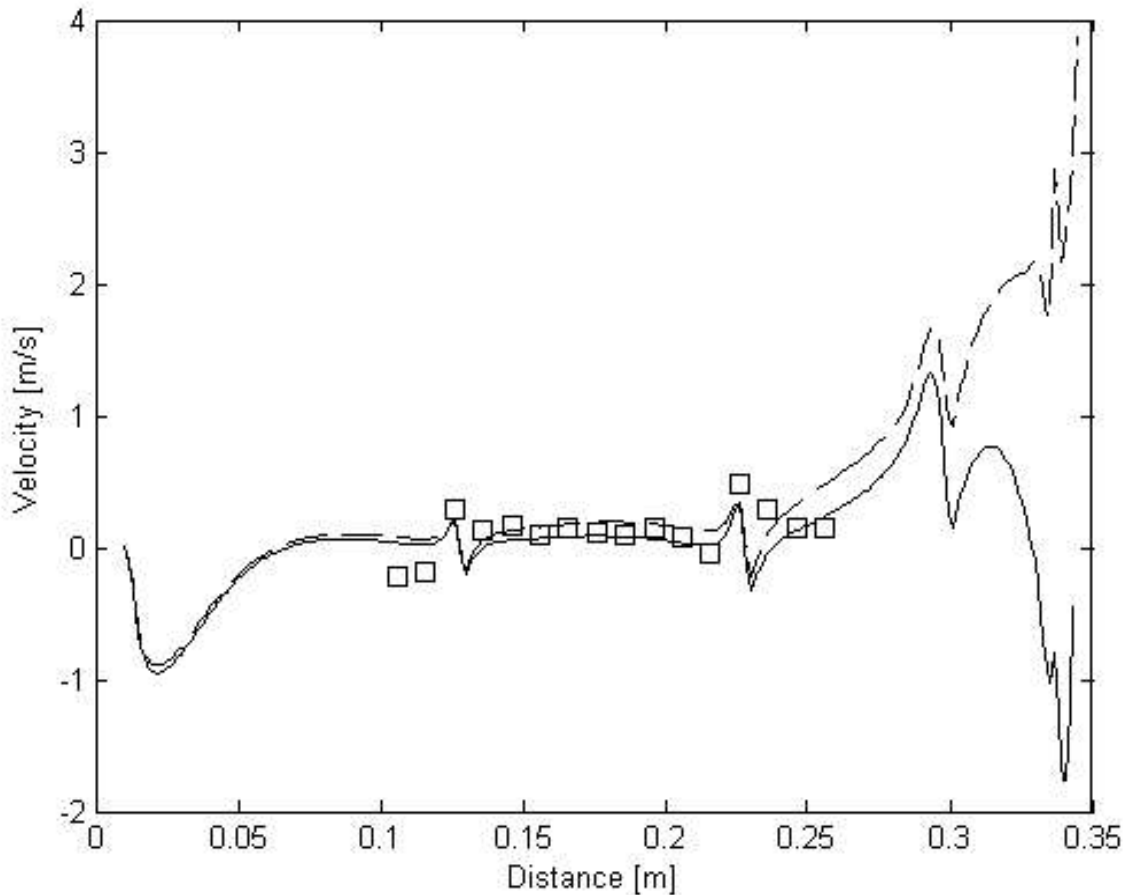


Figure 8.15 $Re = 1077$, W -component at the 8 mm plane.

Solid: blockage, Dashed: leakage, Squares: experimental results.

Since the heat exchanger in many applications has its bends partly covered, tests were performed at LFMT where the bend had its front and back covered. The covers are shown in figure 8.16. With the bend covered, the geometry could be meshed correctly and no simplifications of the geometry were necessary. Calculations were performed in the same manner as for the cases without cover and the pressure drops are presented in table 8.9. As can be seen in the pressure drop results the deviations are for all cases less than 6,2%, which must be considered to be acceptable.

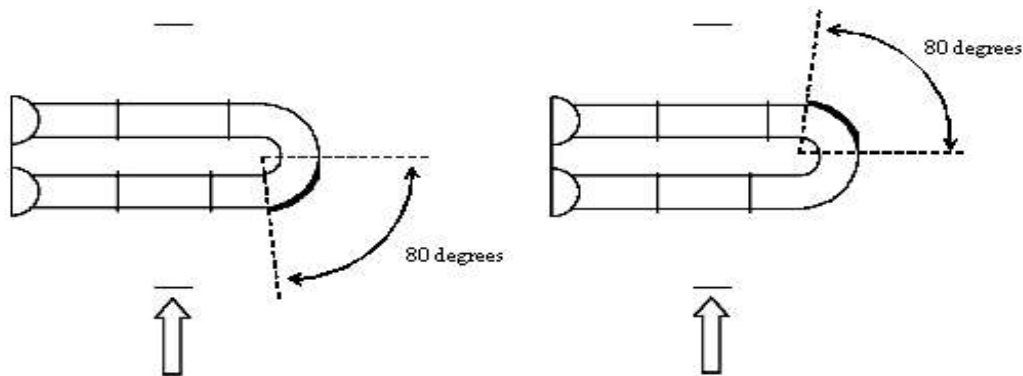


Figure 8.16 Front and back covers on the heat exchanger.

Reynolds number	Δp_{calc} [Pa]	Δp_{meas} [Pa]	Deviation [%]
2153	1047,3	1043,9	+0,3
2535	1414,6	1388,2	+1,9
2916	1831,9	1833,9	-0,1
3320	2571,9	2422,3	+6,2

Table 8.9 Total pressure drop results for the cases with covered back of the bend.

The velocity profiles were measured in the same planes as with the bend uncovered. In figures 8.17-8.22 the numerical results are presented together with the experimental data. The tendency is the same as without cover, with an underestimation of the U-component between the spacers for the planes between the matrices and a better agreement at outlet plane. At the outlet plane it is also obvious for this case that there is a separation zone downstream of the central tube leading to an increase in U-component close to that region. The results in the outlet plane also show the influence of the cover on the flow field with strong peaks in the velocity components, that are relatively well captured. Downstream of the bend there is a recirculation zone where the experiments show low velocities that are most probably incorrect. The numerical results show for this part negative velocities that are more realistic.

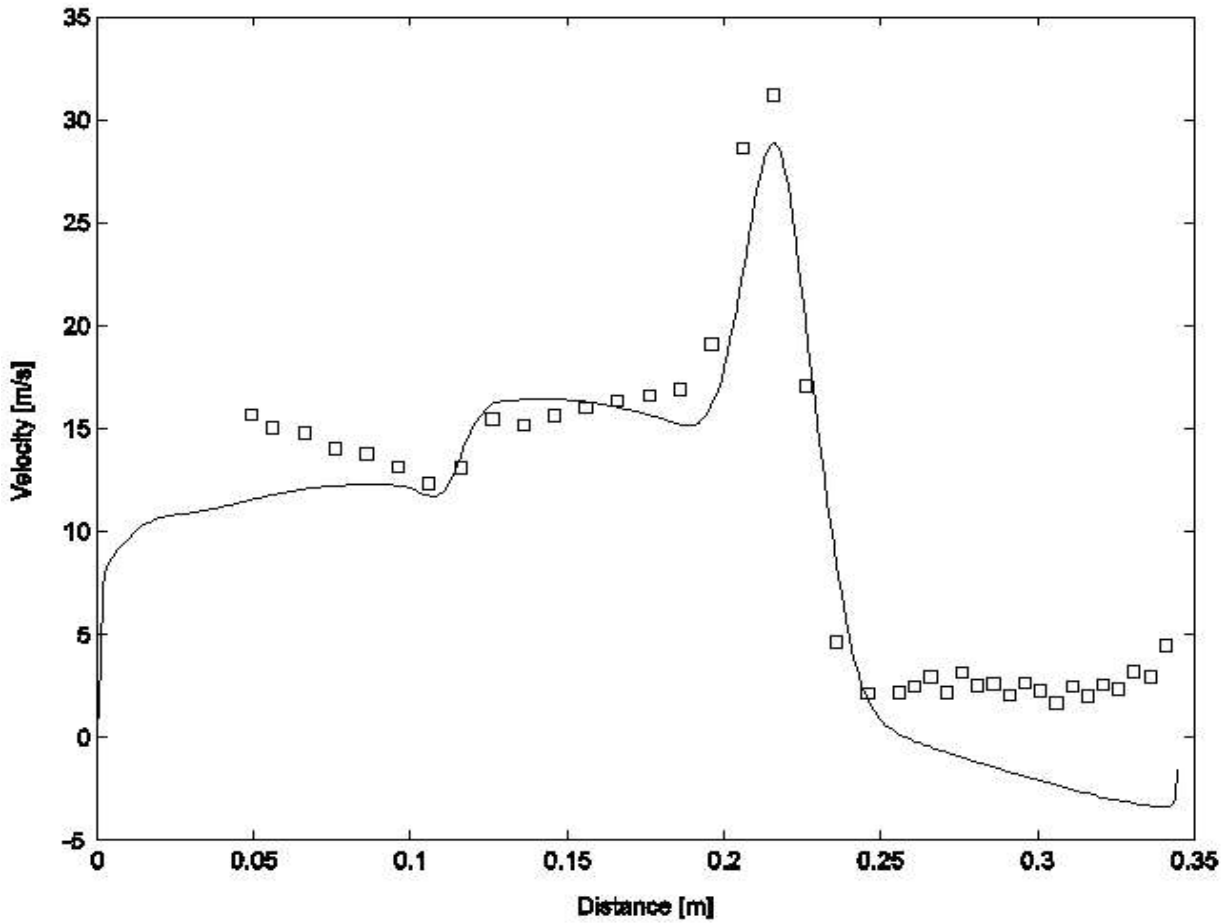


Figure 8.17 $Re = 3320$, covered back, U -component at the outlet plane.

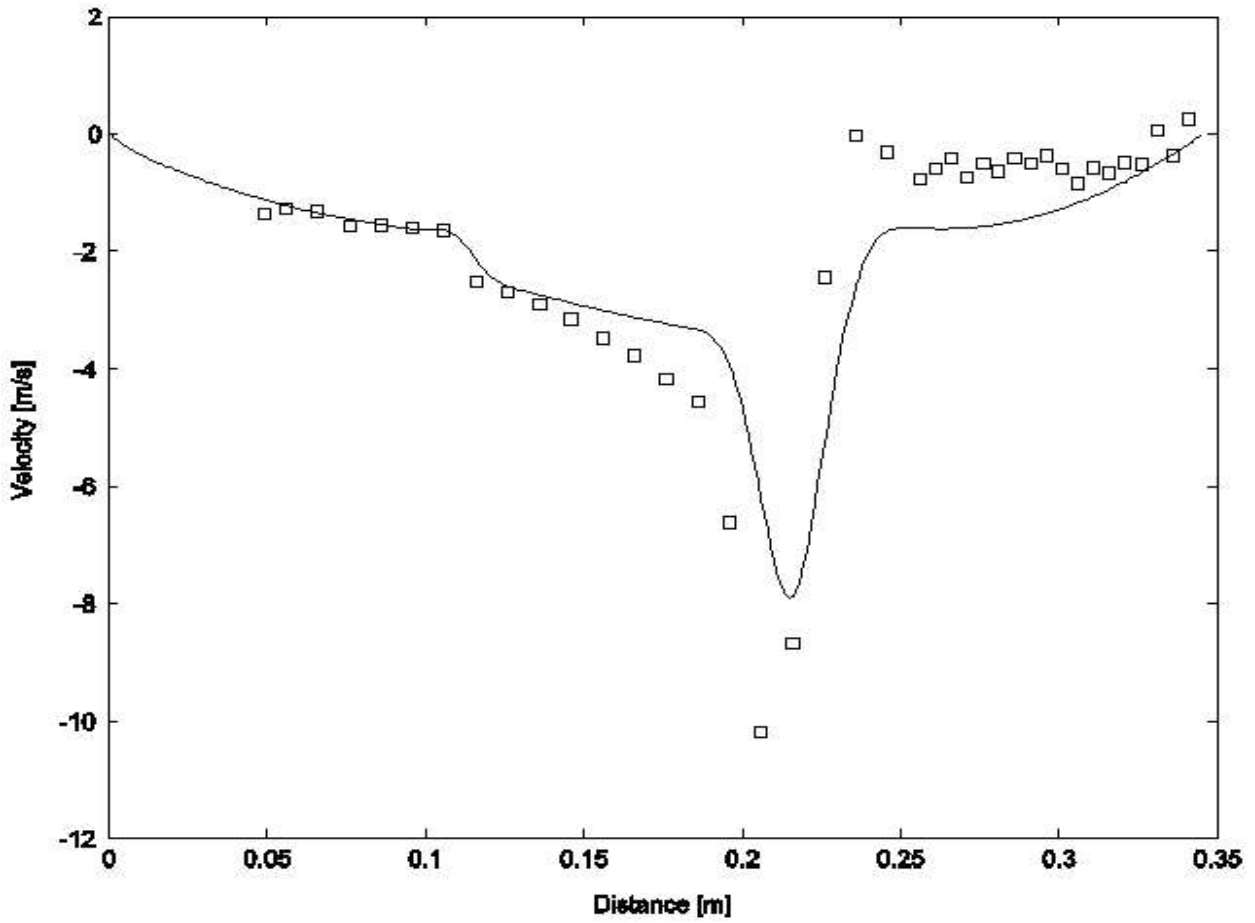


Figure 8.18 $Re = 3320$, covered back, W -component at the outlet plane.

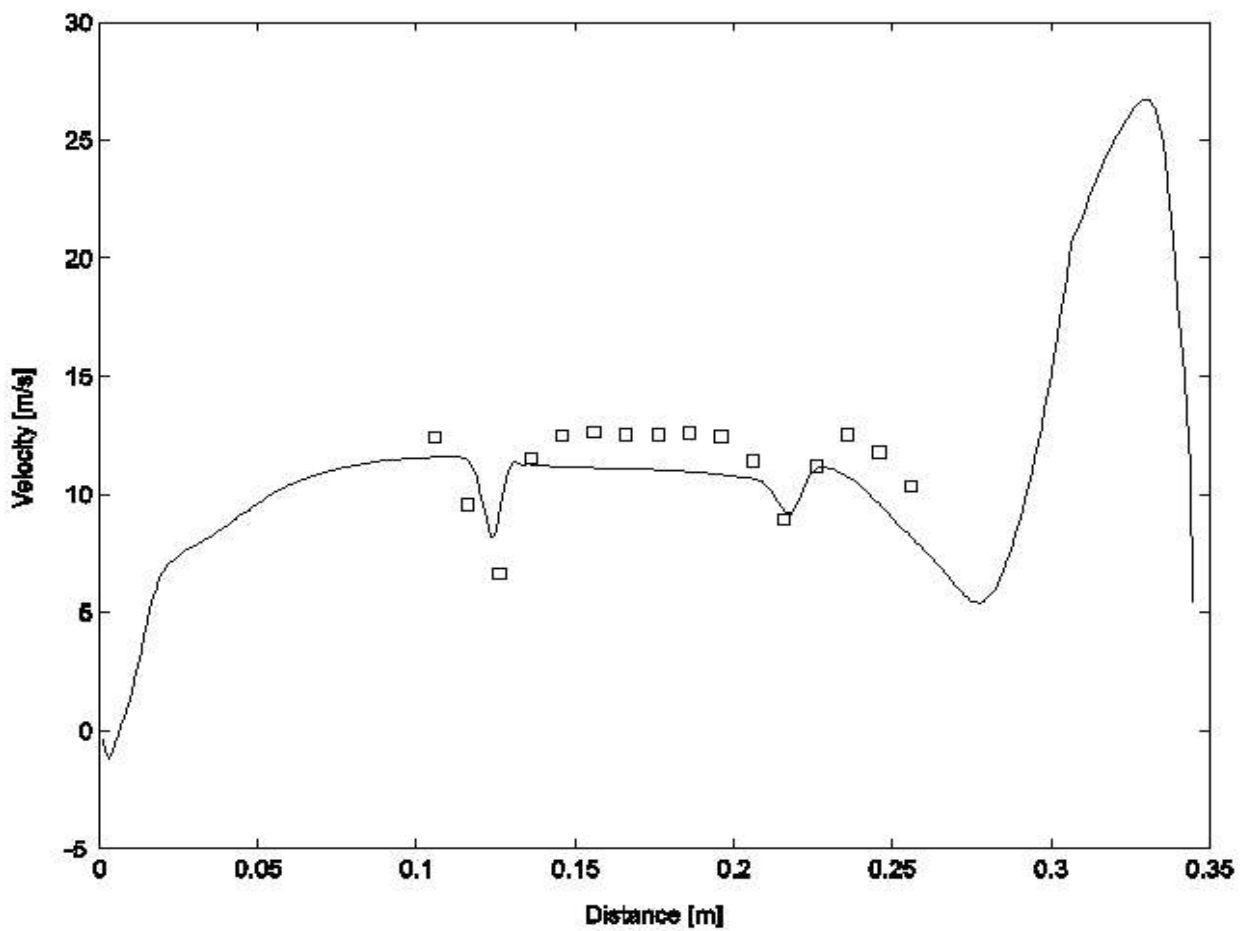


Figure 8.19 $Re = 3320$, covered back, U -component at the 25 mm gap plane.

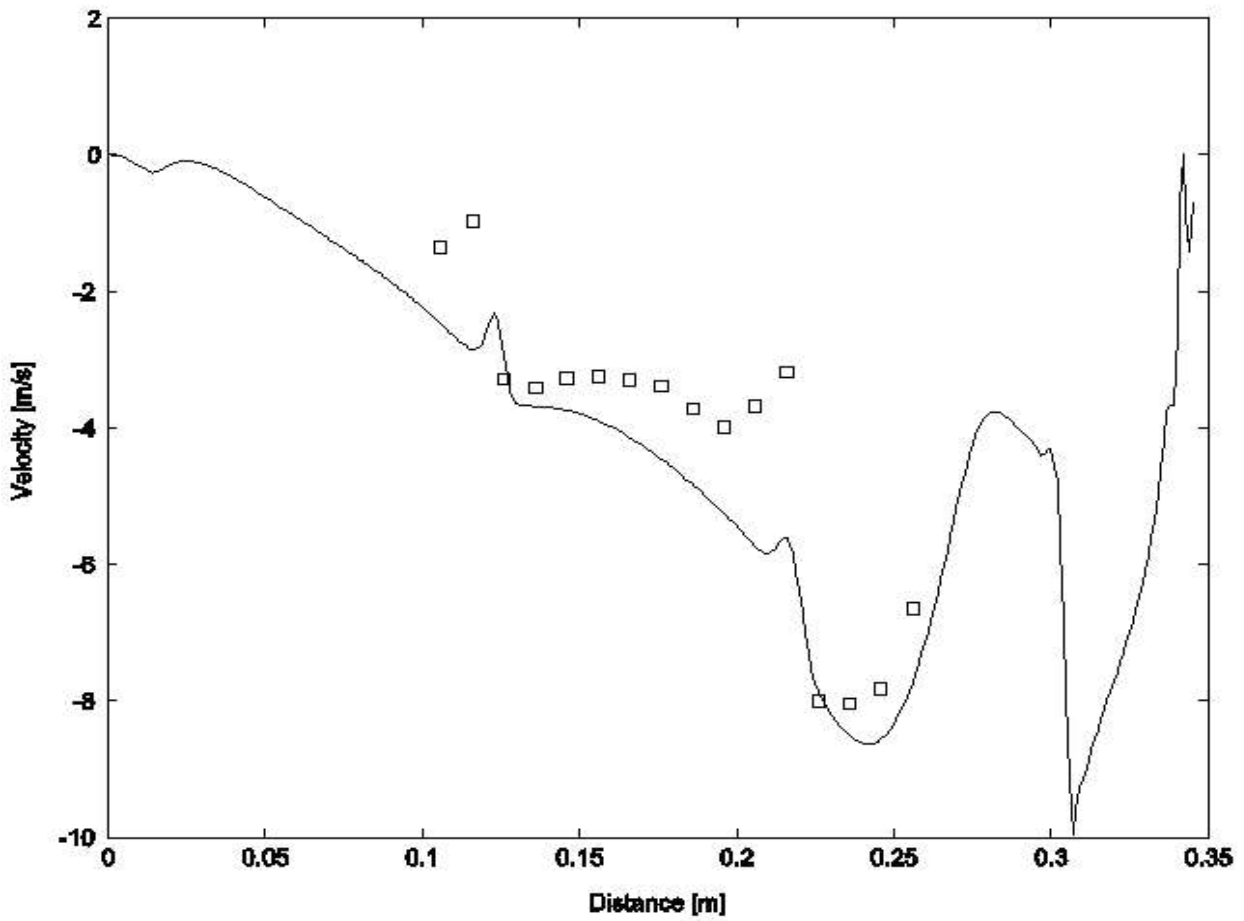


Figure 8.20 $Re = 3320$, covered back, W -component at the 25 mm gap plane.

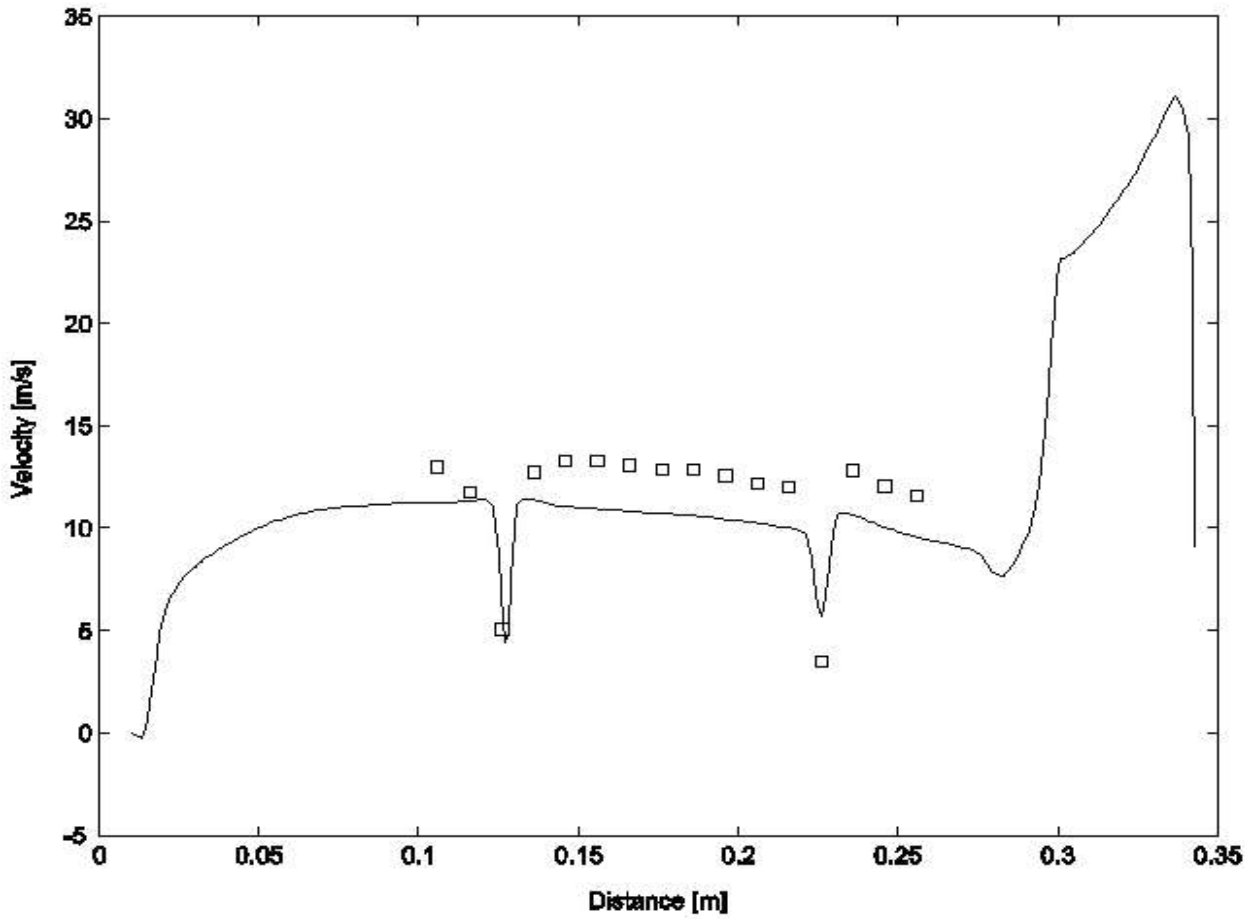


Figure 8.21 $Re = 3320$, covered back, U -component at the 8 mm gap plane.

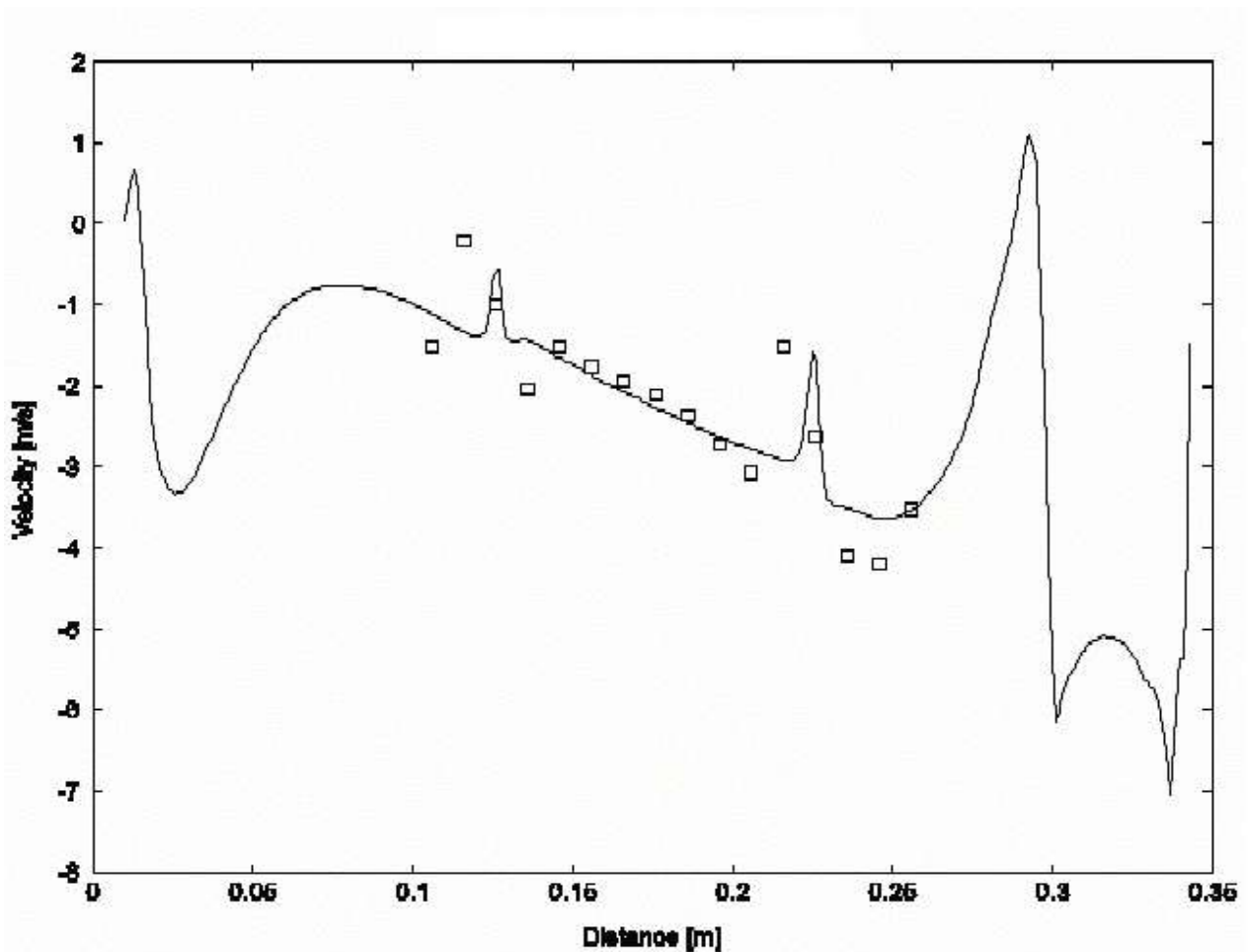


Figure 8.22 $Re = 3320$, covered back, W -component at the 8 mm gap plane.

The geometry could also for the configuration with a covered front be meshed correctly without simplifications. The calculated and measured pressure drops are presented in table 8.10 below for the different cases. As can be seen in the table the pressure drop is, for all the cases, over predicted by between 5 and 10%. This is slightly higher than for the cases with back cover, but still reasonable.

Reynolds number	Δp_{calc} [Pa]	Δp_{meas} [Pa]	Deviation [%]
1458	567,75	541,5	+4,8
1907	915,32	869,0	+5,3
2849	1923,6	1777,3	+8,2
3365	2532,3	2304,0	+9,9

Table 8.10 Total pressure drop results for the cases with covered front of the bend.

The measured and calculated velocity profiles at the different measurement planes are shown in figures 8.23-8.28 below. The tendency is the same as in the previous cases where the U-component is underestimated in the gap planes and the separation downstream of the central tube not captured. However, the trend in the numerical results is correct and the agreement between calculated and measured profiles is fairly good.

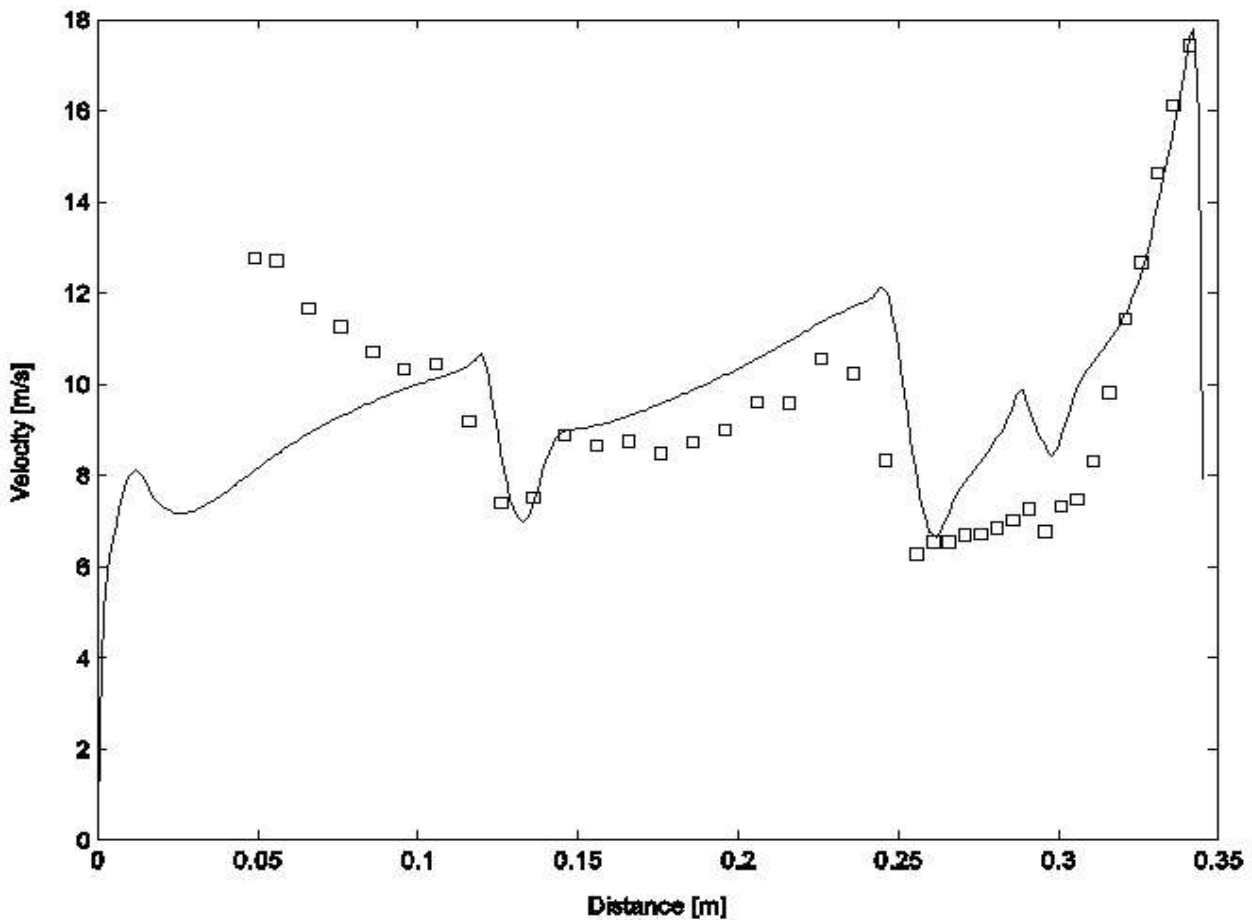


Figure 8.23 $Re = 3365$, covered front, U-component at the outlet plane.

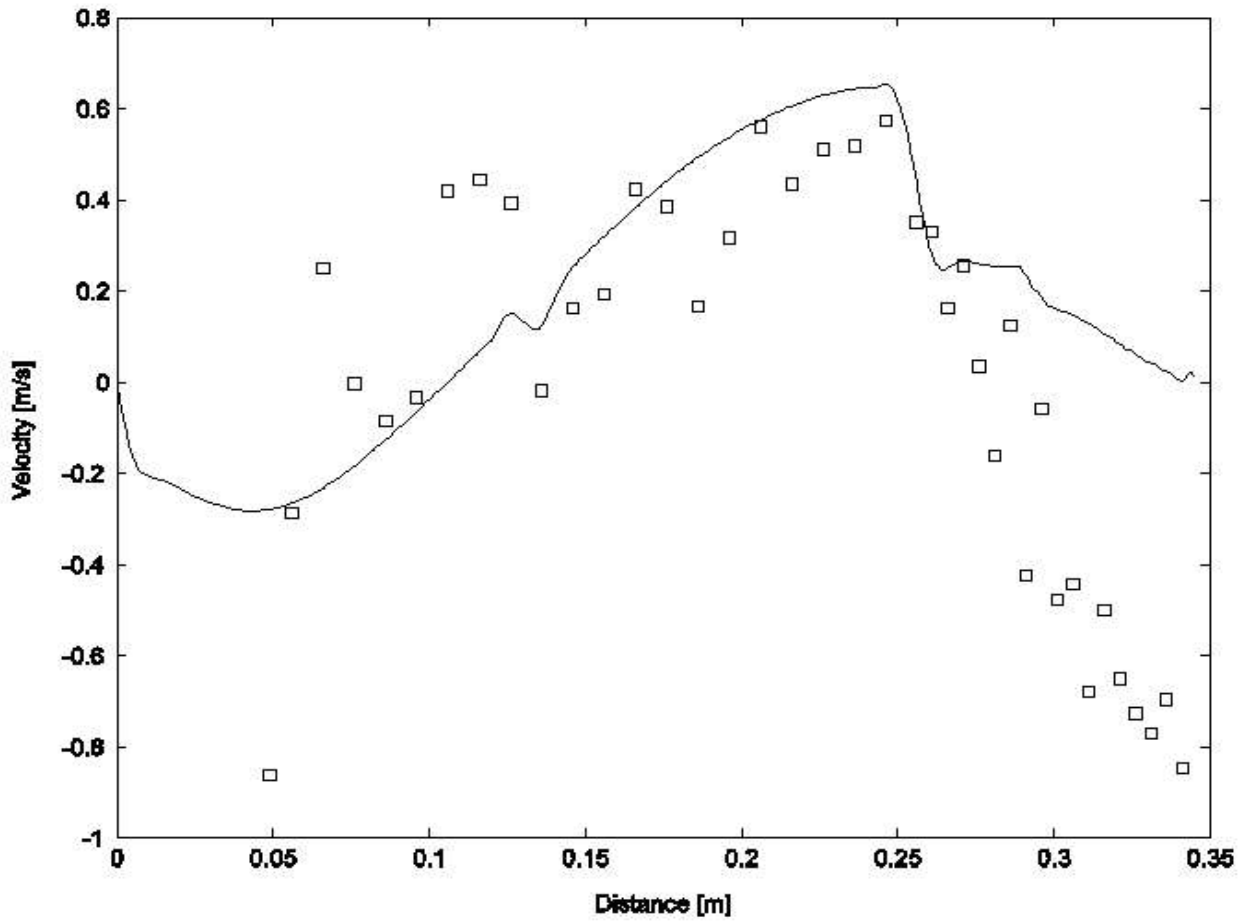


Figure 8.24 $Re = 3365$, covered front, W -component at the outlet plane.

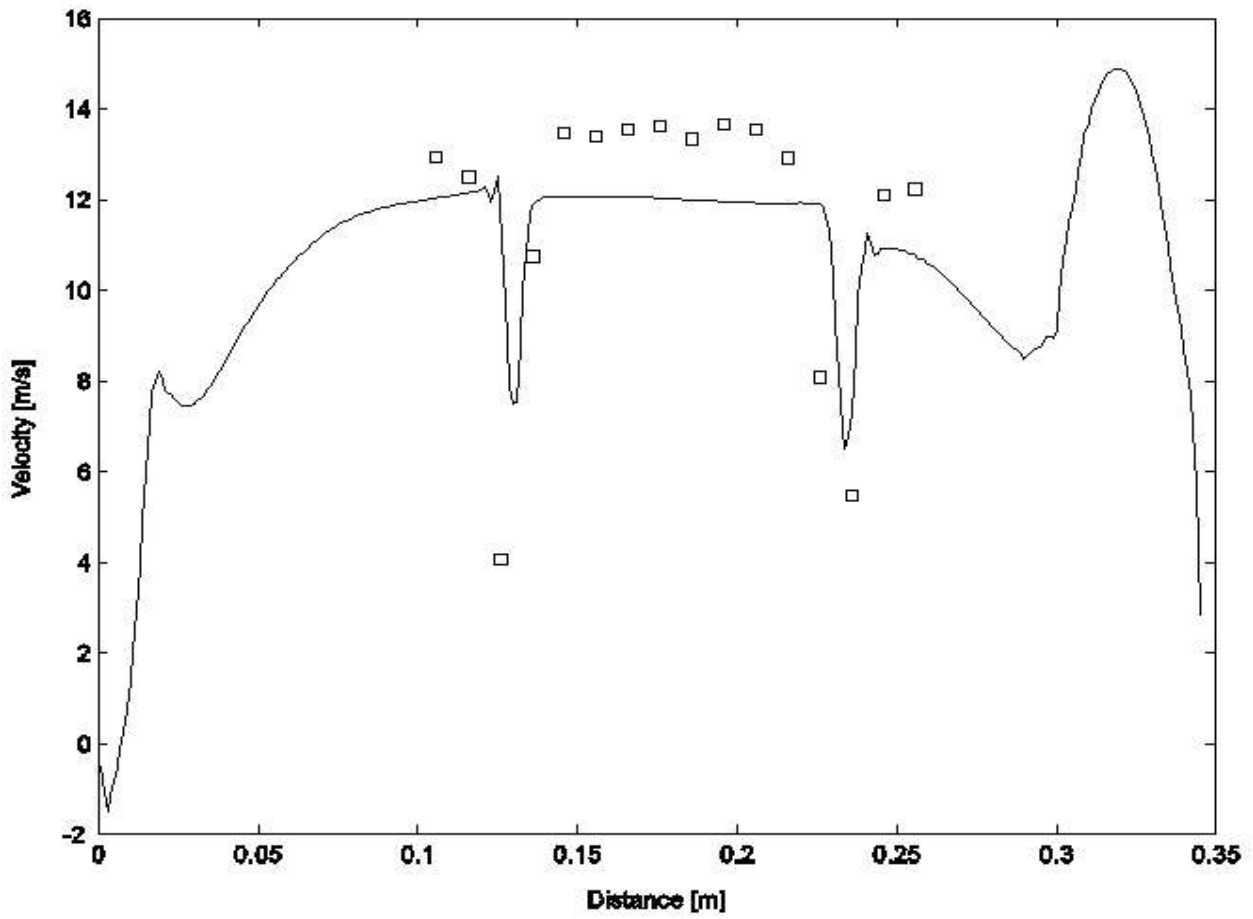


Figure 8.25 $Re = 3365$, covered front, U -component at the gap 25 mm plane.

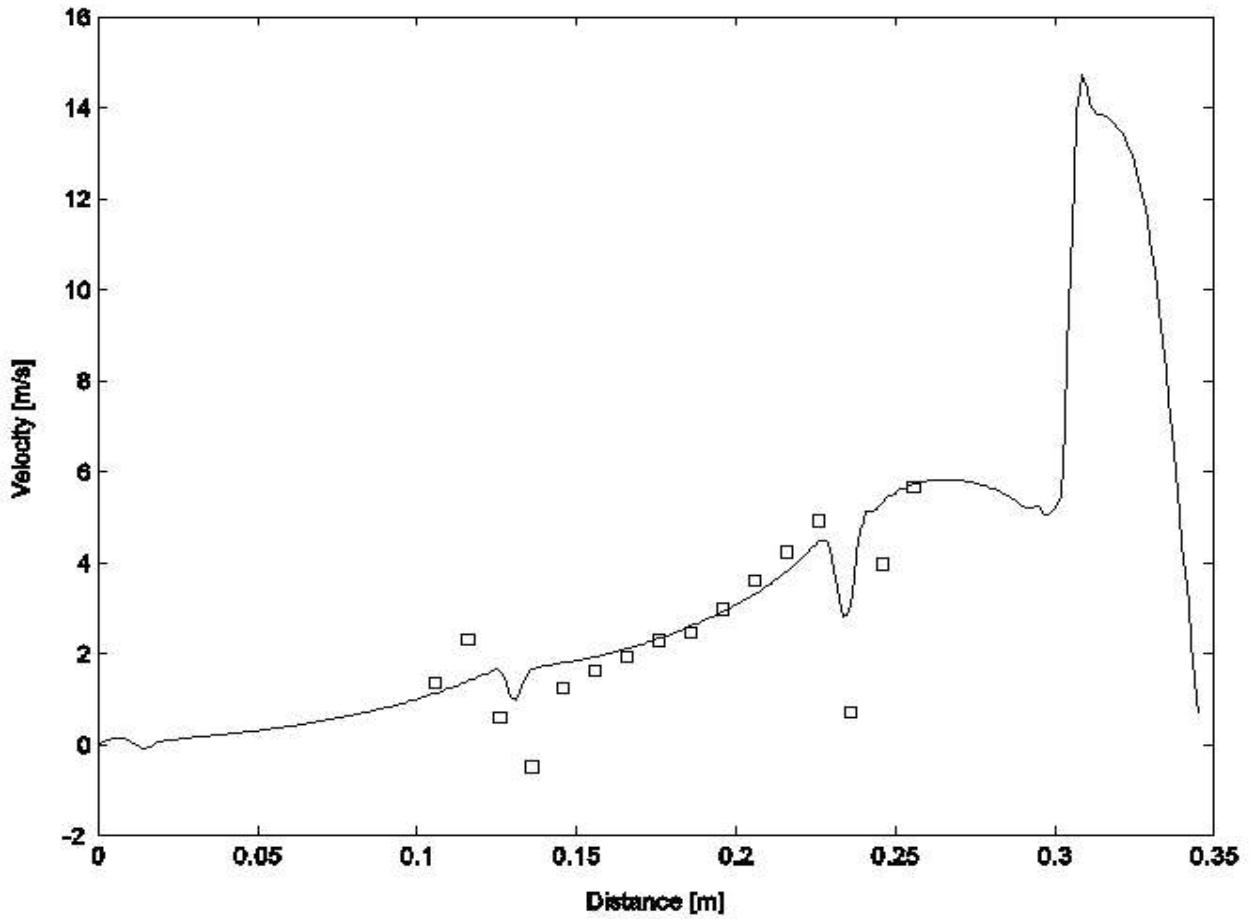


Figure 8.26 $Re = 3365$, covered front, W -component at the gap 25 mm plane.

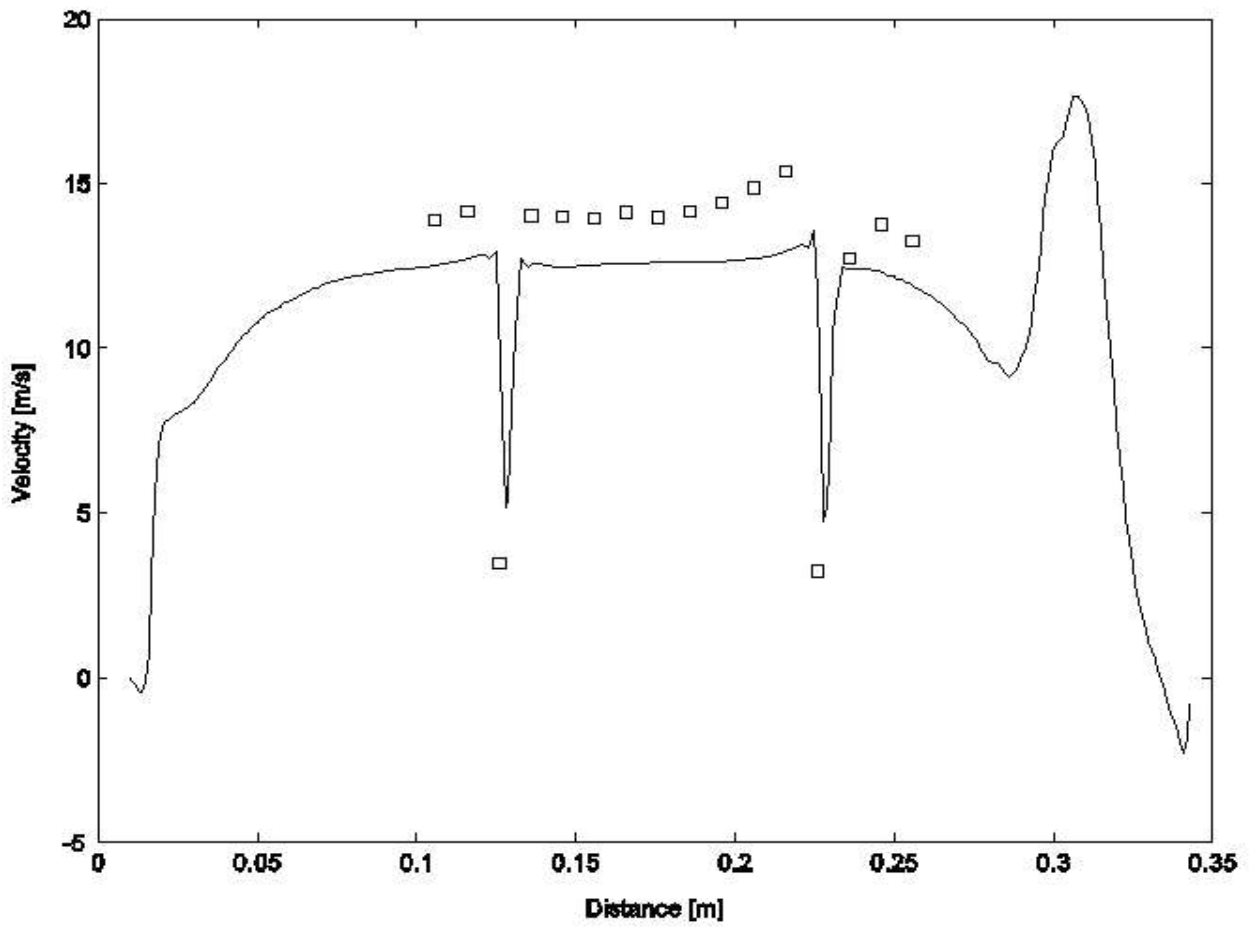


Figure 8.27 $Re = 3365$, covered front, U -component at the gap 8 mm plane.

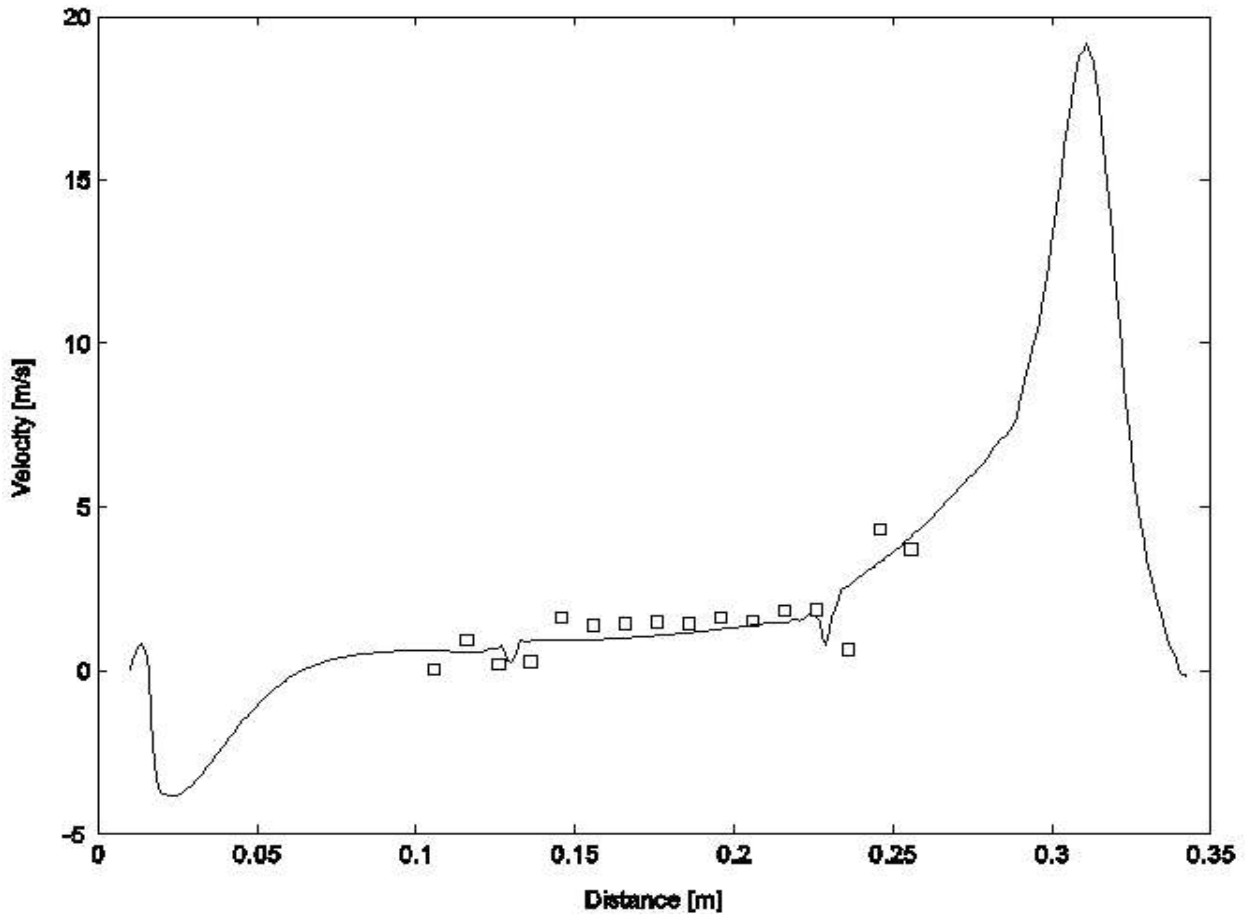


Figure 8.28 $Re = 3365$, covered front, W -component at the gap 8 mm plane.

8.2.2 Inclination angle of 15 degrees

A case with 15 degrees inclination angle was set up and tested at LFMT. The experimental configuration is shown in figure 8.29. The 15 degrees case was investigated without covered bend, but with a sealing between the wind tunnel wall and the bend. This is visible in the grid in figure 8.30. This small sealing made it possible to mesh the geometry without introducing any simplification. The grid contains around 150000 nodes.

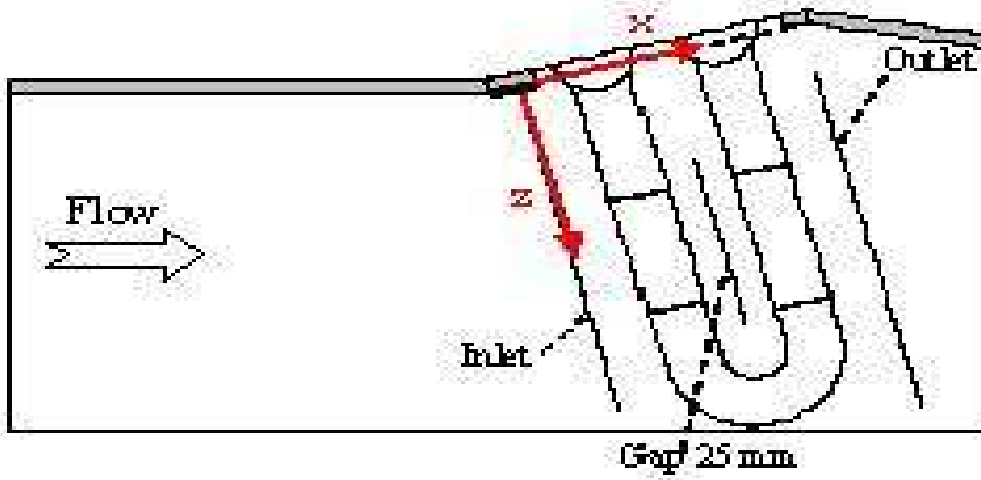


Figure 8.29 Measurement planes for 15 degrees inclination angle, top view.

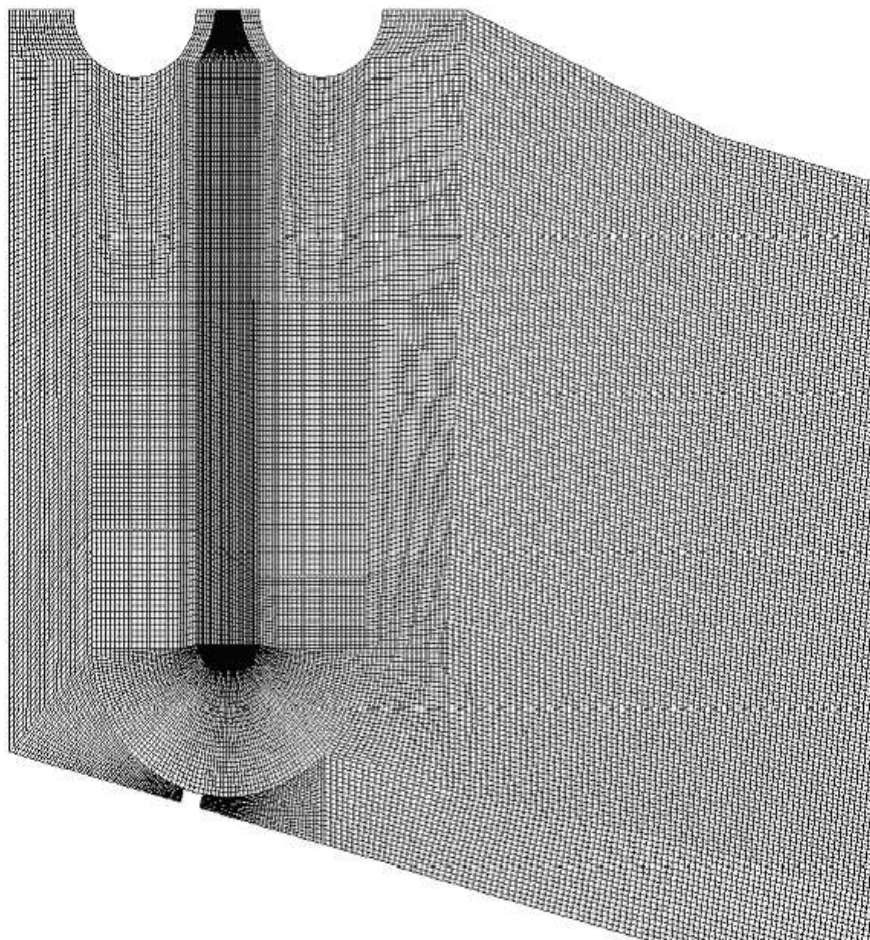


Figure 8.30 Grid for the 15 degrees inclination case.

The experimental case was calculated in the same manner as previous cases and the pressure loss results are presented in table 8.11. The calculated pressure drop is in very good agreement with the measured.

Reynolds number	Δp_{calc} [Pa]	Δp_{meas} [Pa]	Deviation [%]
3948	2282,4	2276,2	+0,3

Table 8.11 Total pressure drop results for the 15 degrees inclination case.

The velocity profiles at the outlet, figures 8.31-8.32, are captured reasonably well, but, as in previous cases, without the separation at the central tube. The behaviour in the bend region and downstream the spacers look more viscous in the numerical results, and this could be due to a resolution not sufficient or to a too high turbulent viscosity.

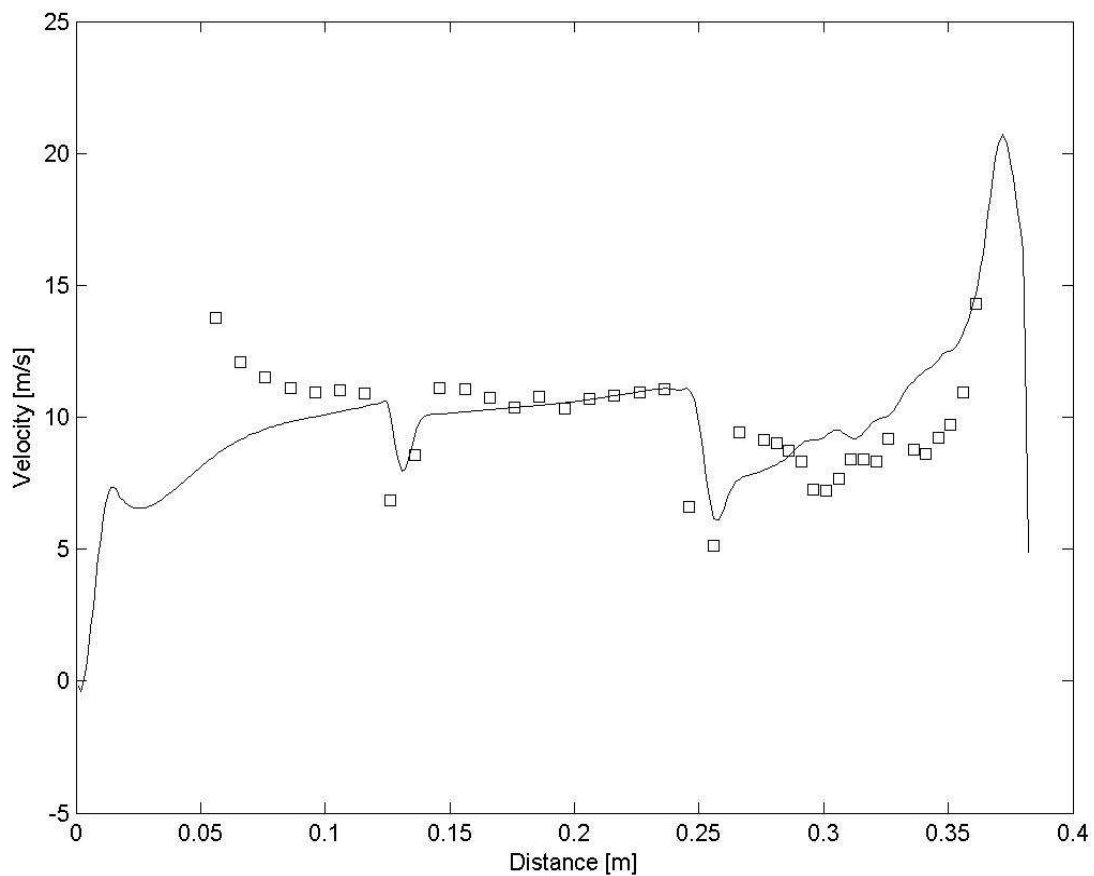


Figure 8.31 Inclination 15 degrees, U velocity component at the outlet plane.

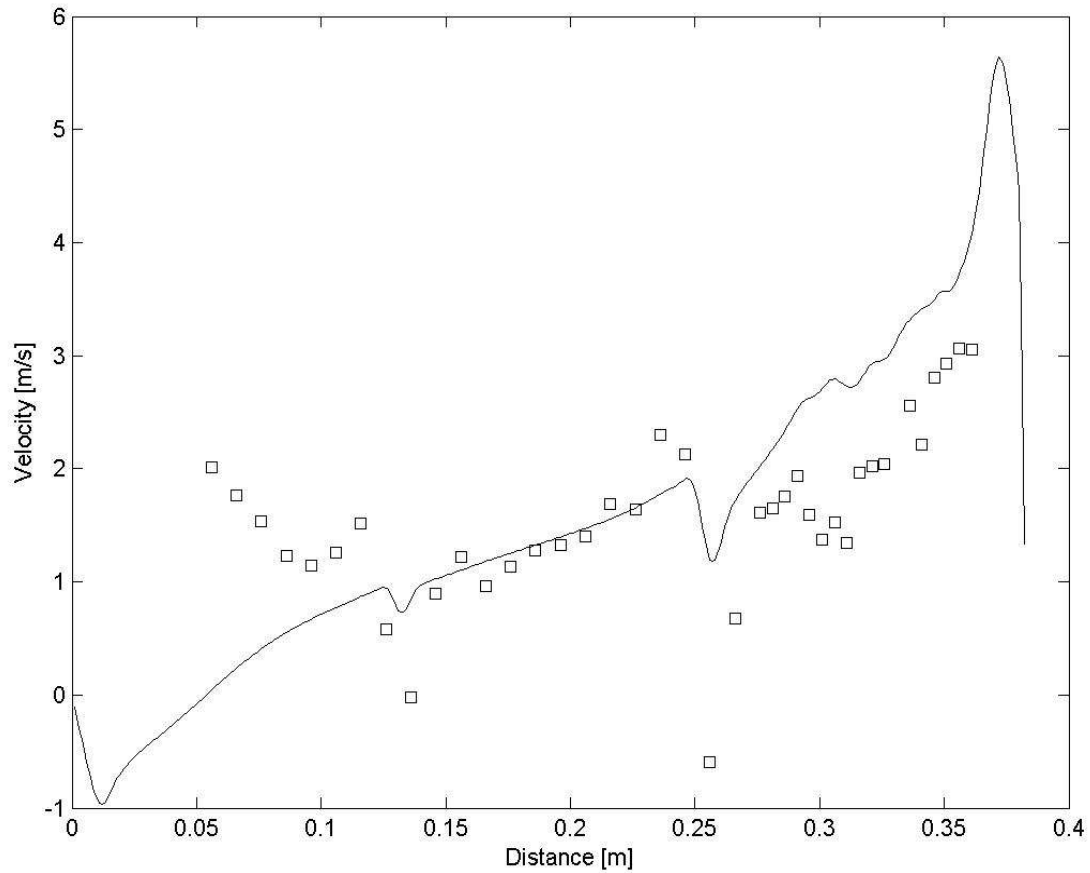


Figure 8.32 Inclination 15 degrees, W velocity component at the outlet plane.

8.2.3 Inclination angle of 45 degrees

For the inlet flow angle of 45 degrees experiments were made on a configuration described in figure 8.33 below. This set-up was used for experiments with an uncovered bend of the heat exchanger as well as for experiments done with the back part of the heat exchanger bend covered. Like the 15 degrees inclination angle case, the 45 degrees case without cover could be meshed correctly, since a small blockage between the bend and the wall was used in the experiments. The grid shown in figure 8.34 has the same resolution as the grid for the 15 degrees case and consists of around 150000 nodes.

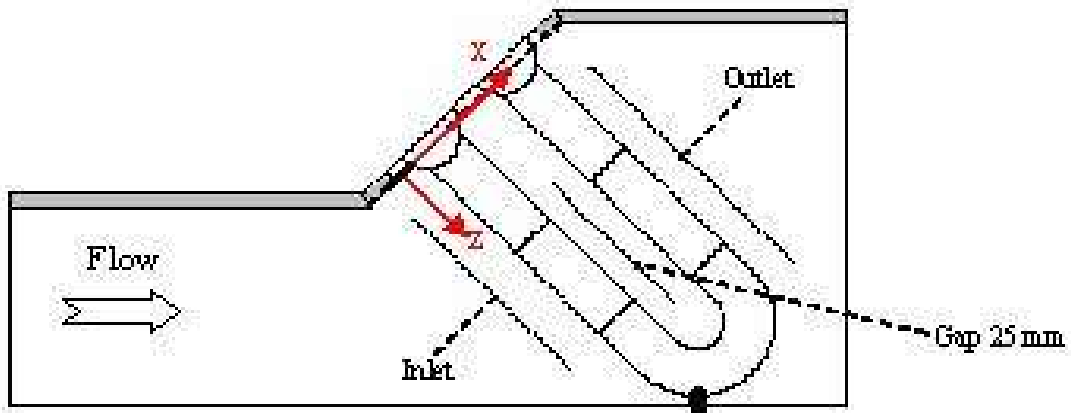


Figure 8.33 Measurement planes for 45 degrees inclination angle, top view.

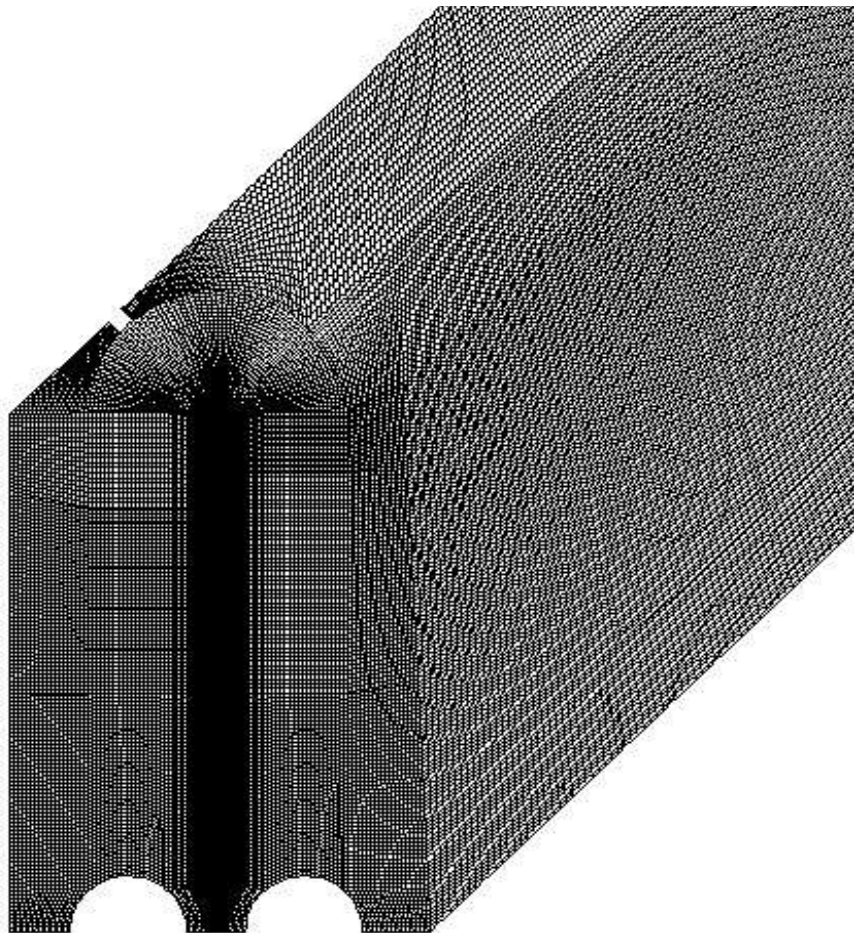


Figure 8.34 Part of the grid for the 45 degrees inclination case.

The calculated pressure drop over the heat exchanger is in very good agreement with the measured pressure drop, with a deviation less than 1%, as is shown in table 8.12.

Reynolds number	Δp_{calc} [Pa]	Δp_{meas} [Pa]	Deviation [%]
3656	2225,8	2241,4	-0,7

Table 8.12 Total pressure drop results for the 45 degrees inclination case without cover.

The measured and calculated velocity profiles for the different measurement planes are presented in figures 8.35-8.38 below. The trend is relatively well captured in the numerical results for both velocity components, but as in the 15 degrees case the sharp gradients e.g. downstream of the spacers are not fully captured. Furthermore, as in all previous cases the separation on the central tube is not reproduced.

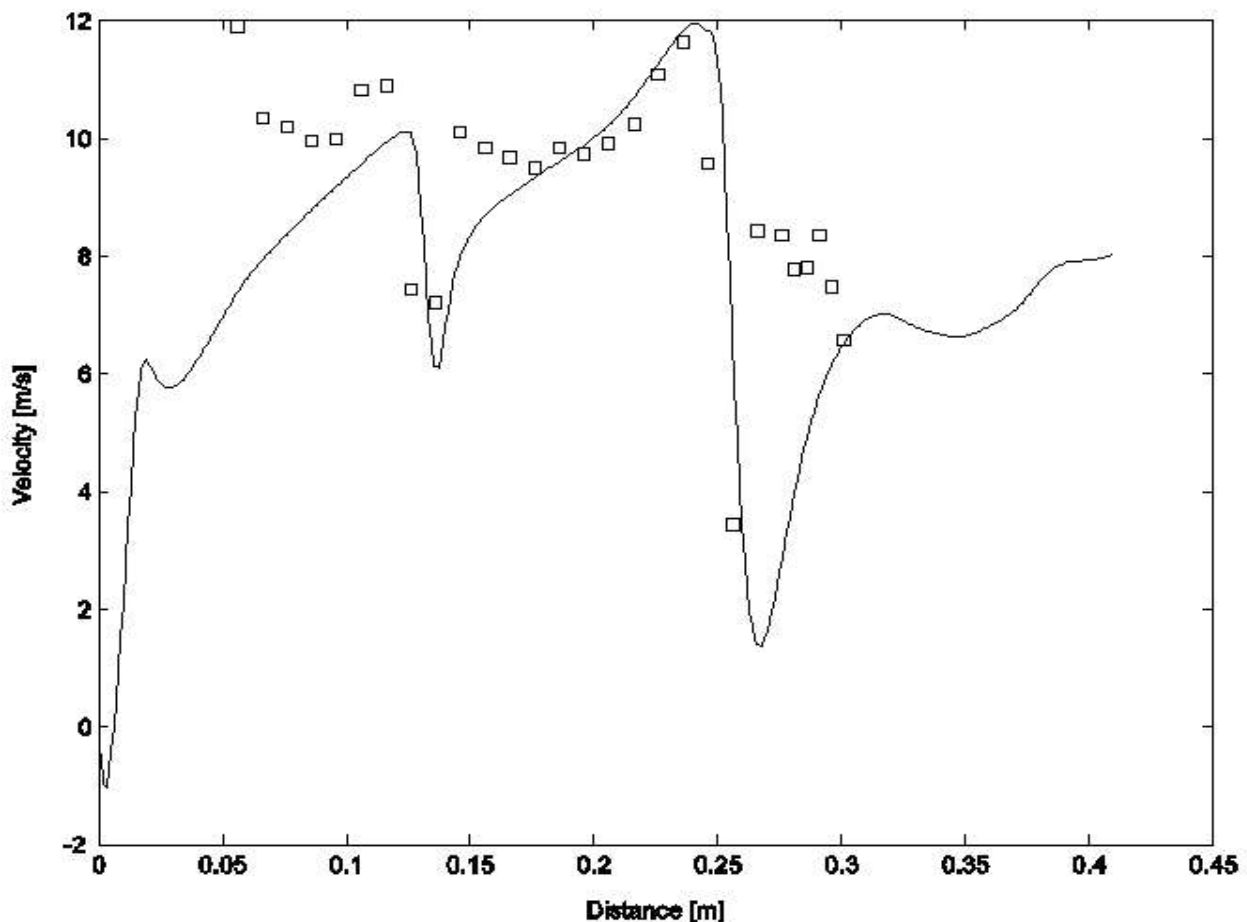


Figure 8.35 Inclination 45 degrees, U-component at the outlet plane.

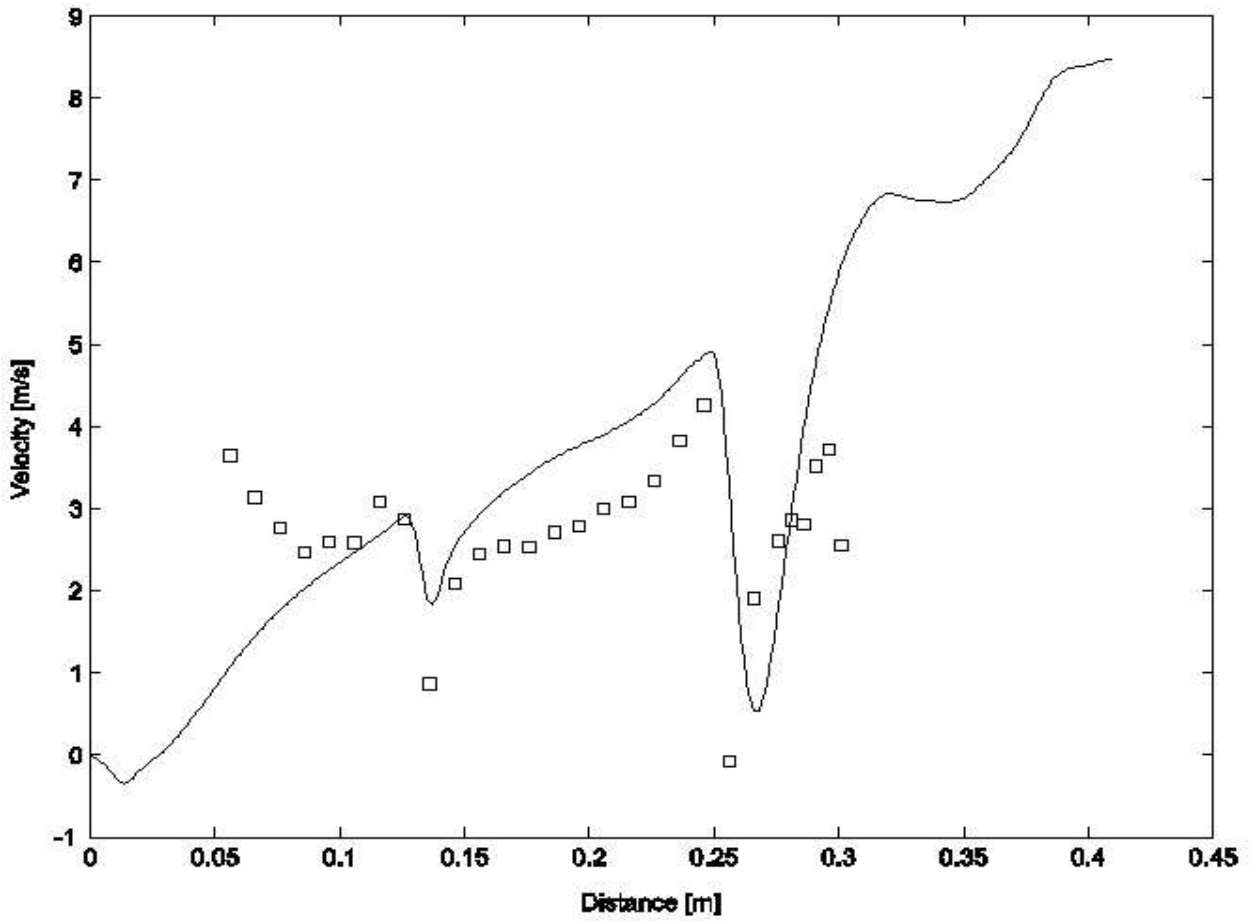


Figure 8.36 Inclination 45 degrees, W-component at the outlet plane.

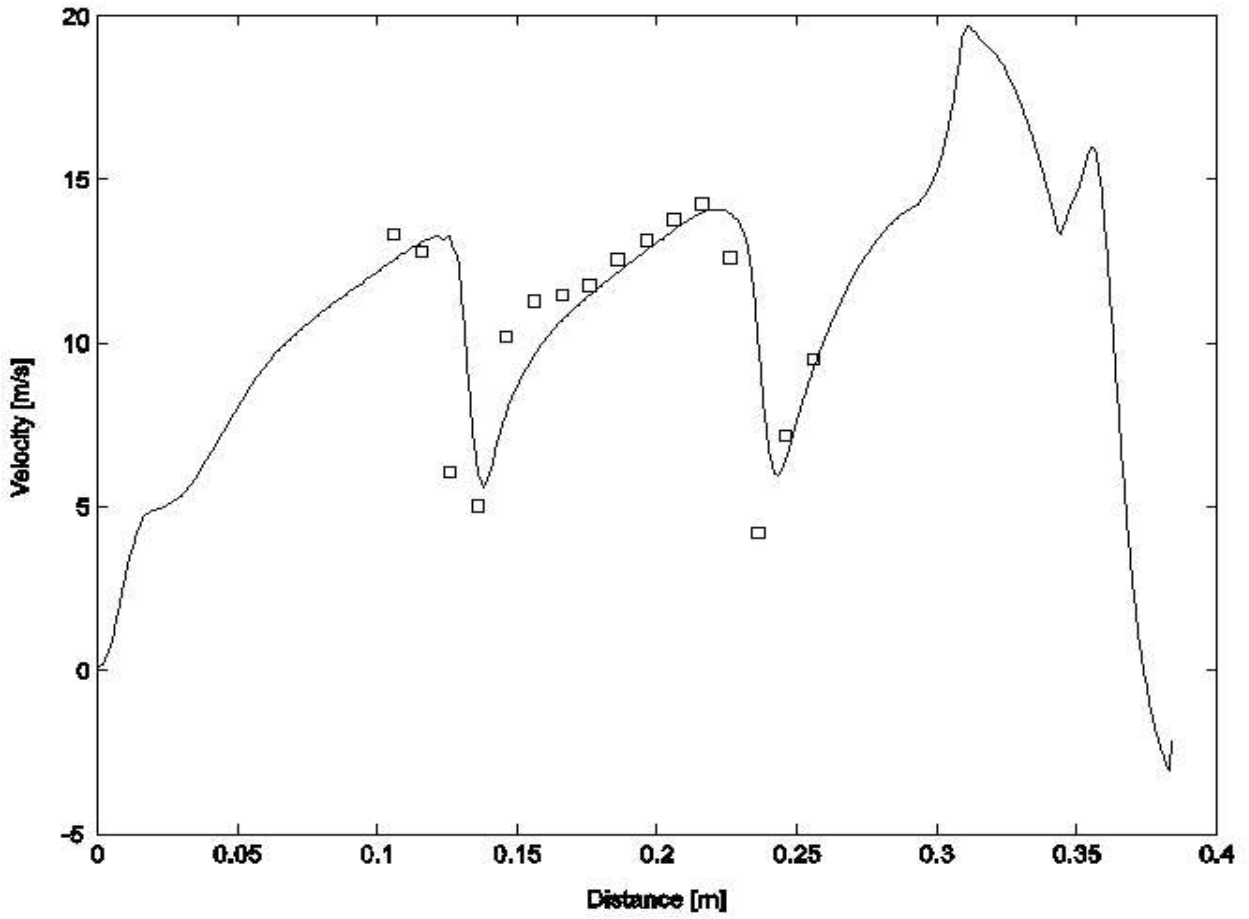


Figure 8.37 Inclination 45 degrees, U-component at the gap 25 mm plane.

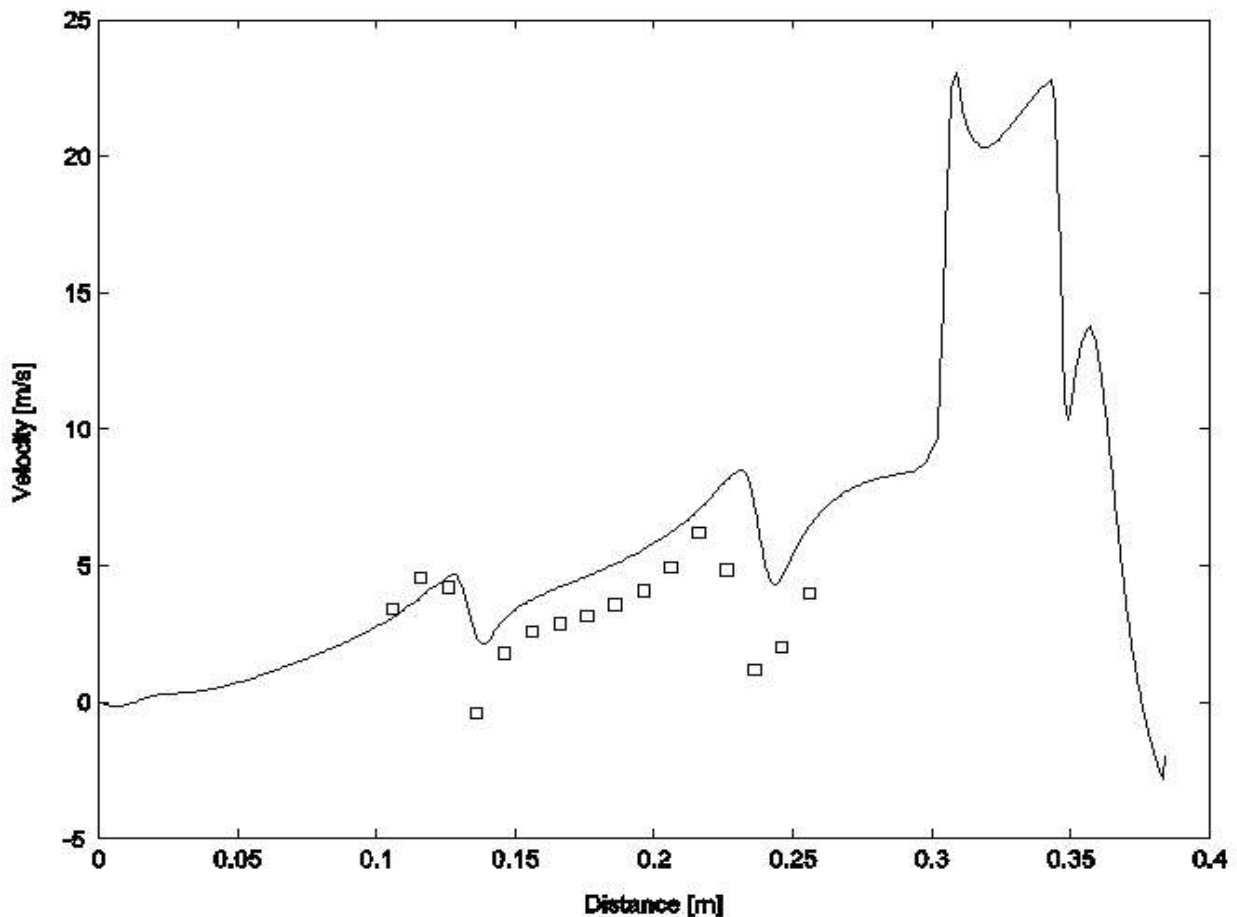


Figure 8.38 Inclination 45 degrees, W-component at the gap 25 mm plane.

The 45 degrees inclination case was also investigated with a cover mounted on the back side of the bend. This case was calculated on a grid similar to the grid for the standard 45 degrees case, just with the cover added. The pressure drop as seen in table 8.13, could not be calculated with the same good agreement as for the case without cover, but is over estimated by almost 10%. This is of the same order of magnitude as some of the results for the cases with no inclination, and still acceptable.

Reynolds number	Δp_{calc} [Pa]	Δp_{meas} [Pa]	Deviation [%]
3163	2397,9	2187,5	+9,6

Table 8.13 Total pressure drop results for the 45 degrees inclination case with covered back part of the bend.

The velocity profiles for the two investigated planes, figures 8.39-8.42, are quite well captured and the velocity components at the outlet plane show the same peaks as the experimental results, but they are slightly less marked. Otherwise the profiles show the same discrepancies as in the previous cases.

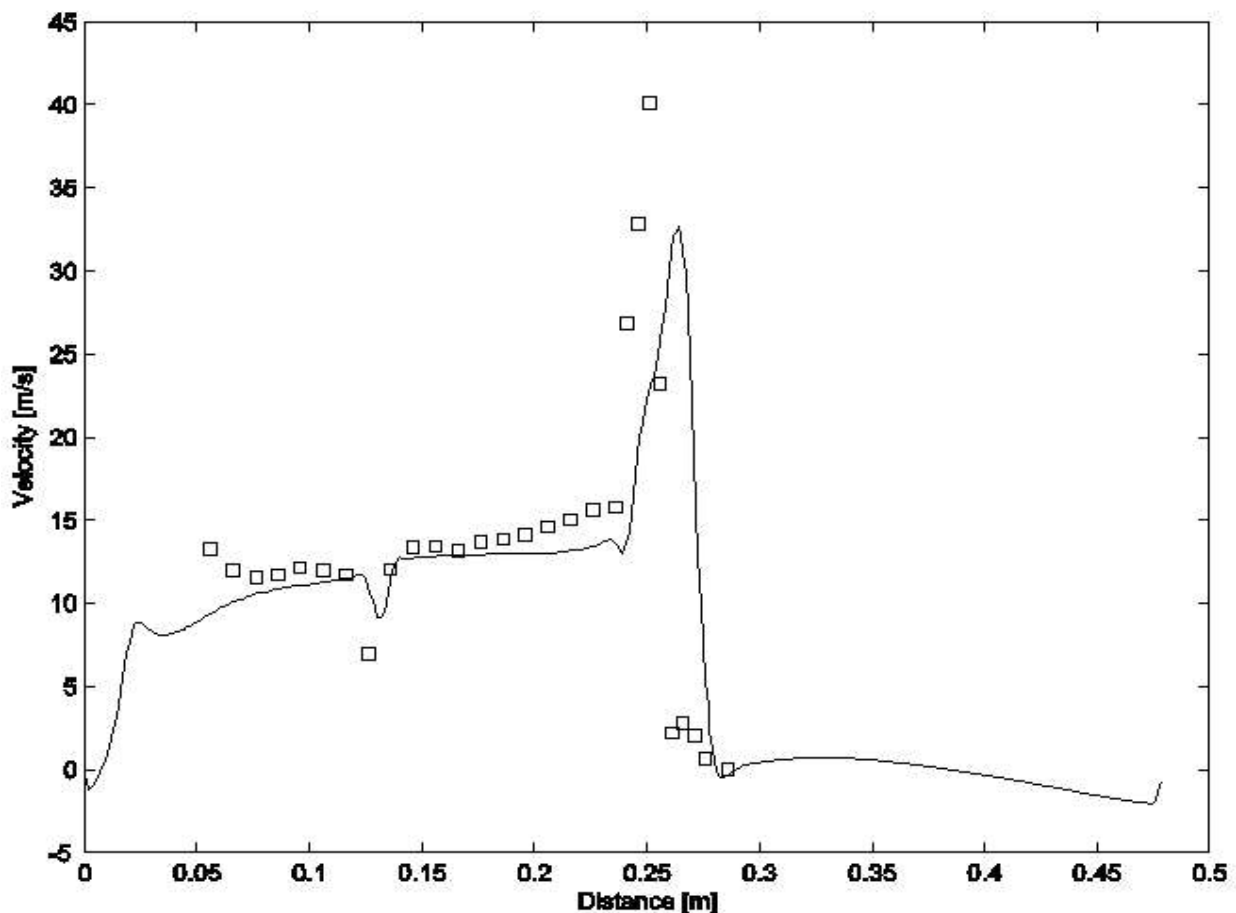


Figure 8.39 Inclination 45 degrees, covered back, U-component at the outlet plane.

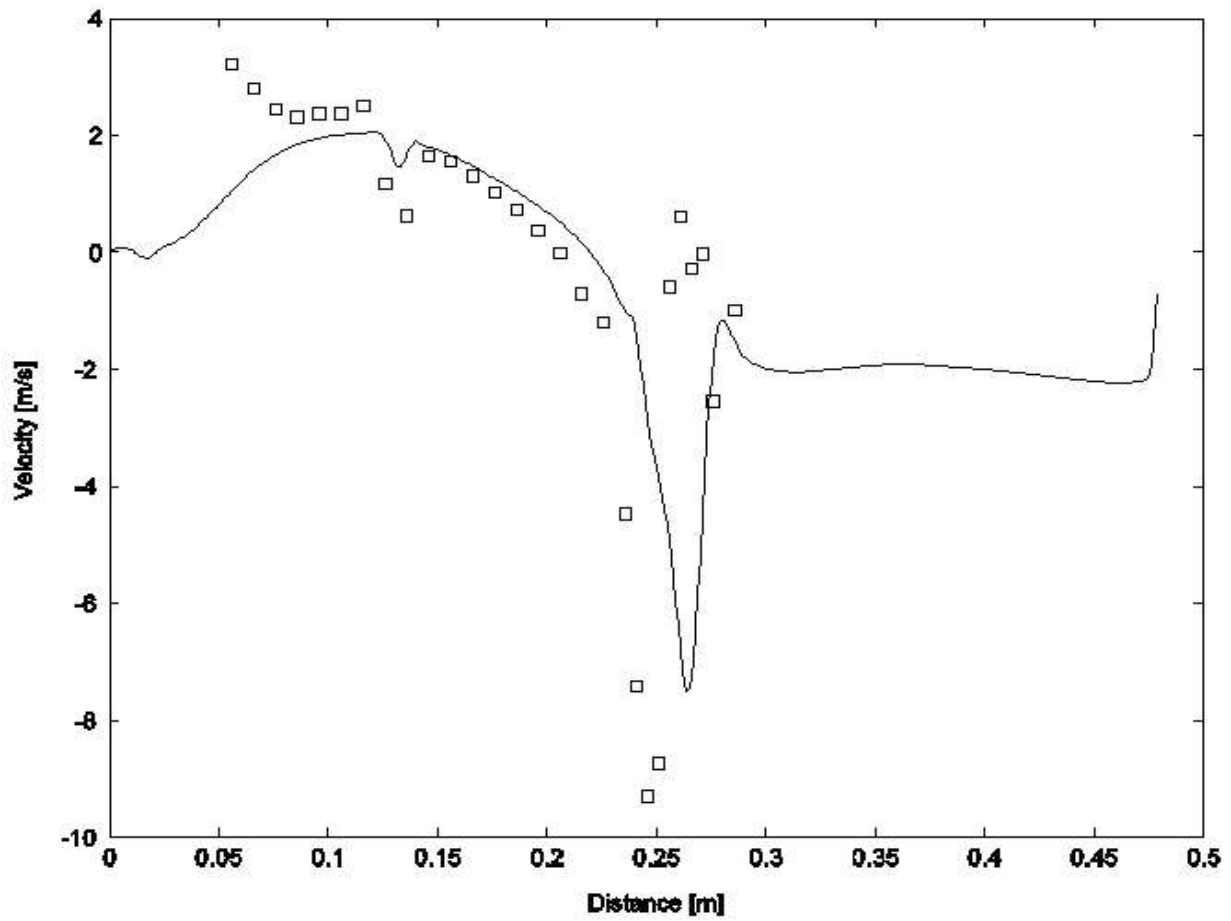


Figure 8.40 Inclination 45 degrees, covered back, W-component at the outlet plane.

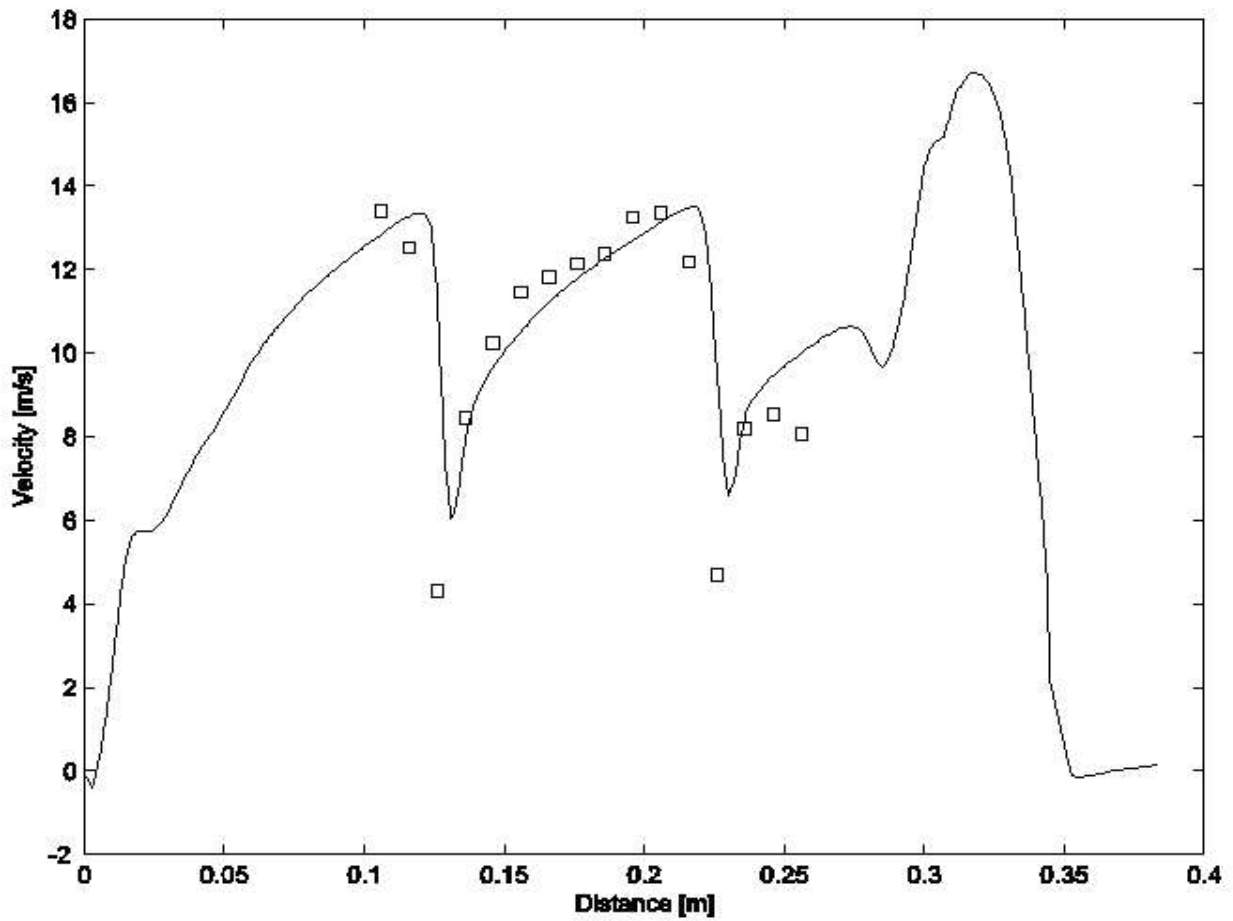


Figure 8.41 Inclination 45 degrees, covered back, U-component at the gap 25 mm plane.

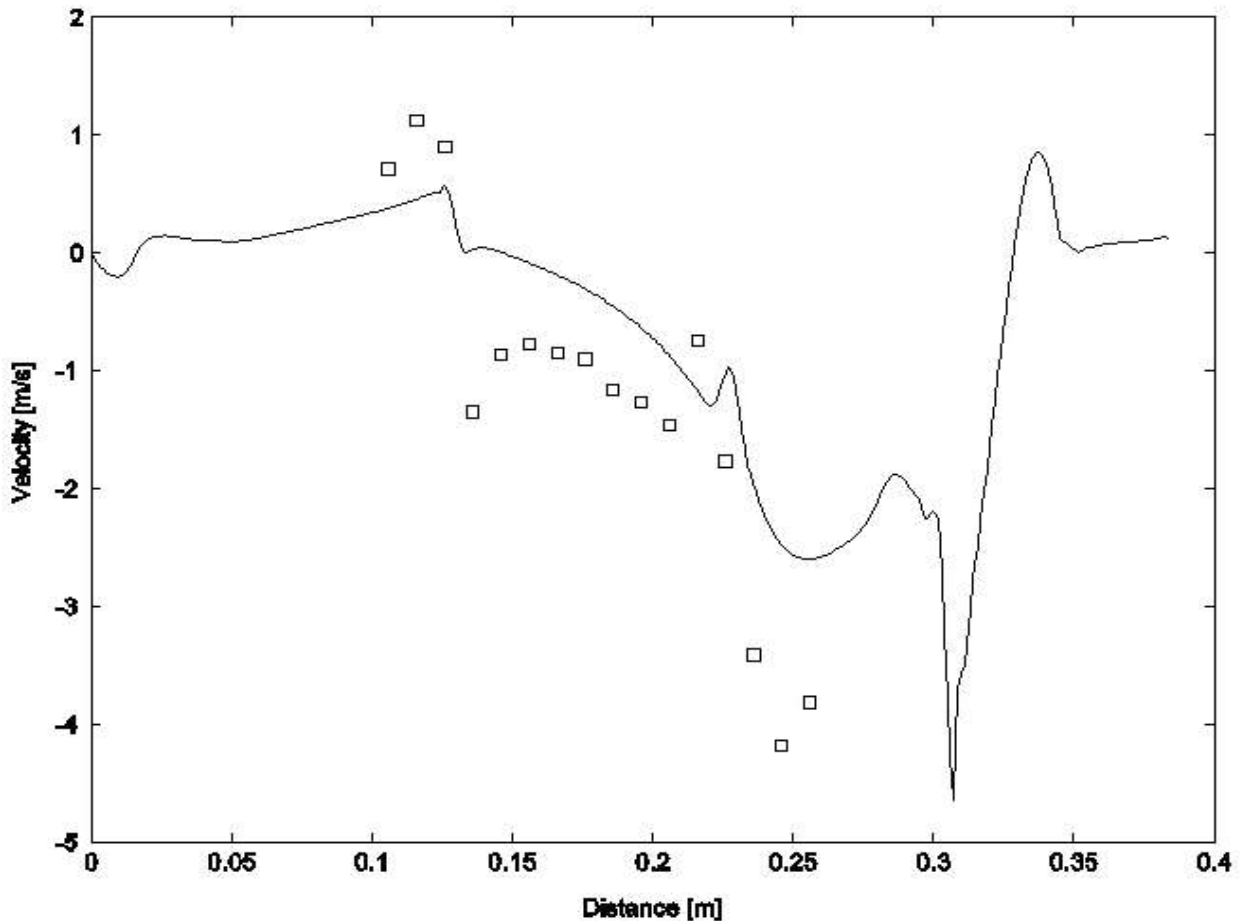


Figure 8.42 Inclination 45 degrees, covered back, W-component at the gap 25 mm plane.

8.3 Conclusions

The resistance tensors were tuned to produce good pressure drop agreement for the non-isothermal test cases. These were then calculated with an exaggerated heat transfer rate as a result. The overestimated heat transfer is most likely due to the treatment of the cold side flow as fully turbulent although the Reynolds numbers indicate that the flow is rather in transition. The calculated outlet temperature profiles showed the same trend, with the temperature rising towards the bends, as the experimental ones. The influence

of turbulent heat transport along the tubes was investigated by modifying the turbulent Prandtl number and the effect was minor indicating that the heat transport in that direction is mainly convective.

The isothermal cases were calculated with the new set of resistance tensors producing a pressure drop deviating less than 10% from the experiments, which must be considered to be acceptable. The velocity profiles were quite well predicted for all cases, although the separation that occurred in all experiments just downstream the central tube could not be captured. This is mainly due to the use of a wall function, which inhibits separation since it is developed for boundary layers in equilibrium. Furthermore, the sharp gradients could not be fully captured, which indicates that either the grid resolution or the turbulence viscosity or both are too high.

9 Applications

The heat exchanger simulation code can be applied to different heat exchanger applications in order to study the effect of the heat exchanger on the flow field of the engine and the flow and temperature distributions in the heat exchanger itself. This kind of calculations give hints on how the configuration of the heat exchanger can be modified within the engine in order to optimize e.g. the temperature load on the heat exchanger, the heat exchanger efficiency or the pressure drop. In the following two examples are presented. The first is the CLEAN demonstrator engine that is being investigated in the EU financed CLEAN project. The second example is a compact industrial gas turbine.

9.1 Exhaust gas casing of the CLEAN engine

The CLEAN engine (Component validator for Environmentally friendly Aero Engine) is a demonstrator that is built for testing new components, among others the heat exchanger, for a future aero engine concept (Scheugenpflug et al). The tests are to be undertaken at the high altitude test cell at the Technical University of Stuttgart where realistic operating conditions can be investigated.

9.1.1 Experimental Model

The exhaust gas casing of CLEAN is shown in figure 9.1 where the hot gas flow paths are visible. The exhaust gases from the turbine are coming from the left in the figure going partly through the heat exchangers and partly directly to a second outlet in model, located at the right in the figure. This second outlet is equipped with flaps that are used to control the amount of gas going out through this second outlet and thereby also the amount of gas going through the heat exchanger.

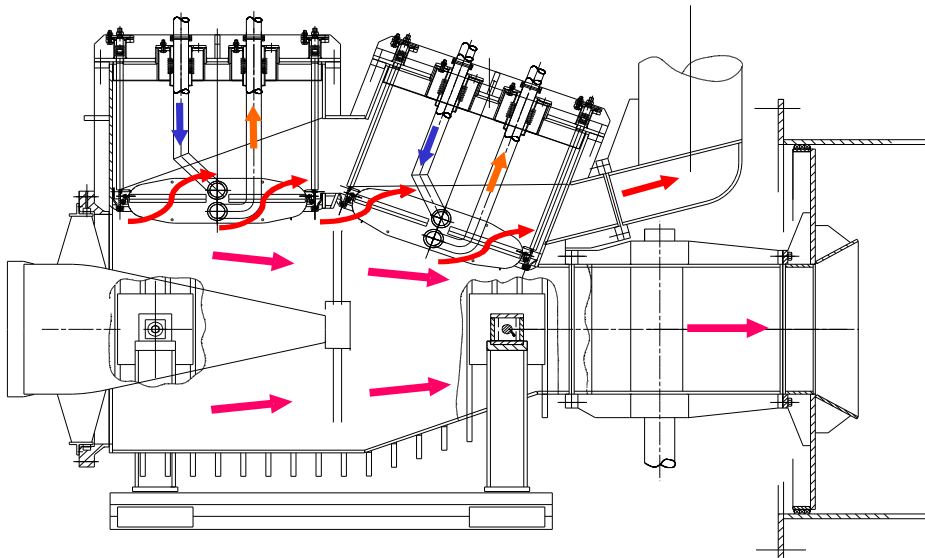


Figure 9.1 Heat exchanger shown in the 2 possible positions within the casing.

In the upper part of the experimental model heat exchanger casings are integrated at two locations. This allows for mounting of the heat exchanger in 2 different positions within the main casing. These two positions correspond to the positions of the first two heat exchangers in the IRA engine.

9.1.2 Operating Conditions

The operational conditions are derived from IRA engine requirements and adapted to the capacity of the high altitude test cell at the Technical University of Stuttgart. The operating condition chosen corresponds to average cruise flying conditions.

9.1.3 The CFD-model

For the calculations the heat exchanger code described in previous chapters was applied. Two grids were built, one for each of the heat exchanger positions. The CLEAN engine has a vertical symmetry plane along the main axis, which only makes it necessary to consider half of the real geometries. Because of the 2GB memory limitation that is put on the problems, by the 32 Bit version of the CFD software, the geometries could not be completely resolved, but had to be simplified. In figures 9.2 and 9.3 the simplifications are visible in the regions close to the bow parts of the heat exchangers. However, these simplifications should not have any major influence on the quantities to be studied, such as pressure drop and heat exchanger load distribution.

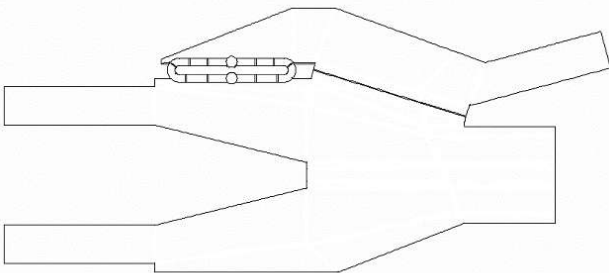


Figure 9.2 CFD model of configuration 1.

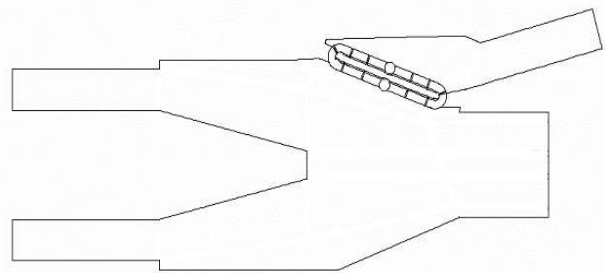


Figure 9.3 CFD model of configuration 2.

Due to the symmetry plane it was not necessary to mesh the geometries completely, but only the half of them, as can be seen in figure 9.4 where the

grid for the first configuration is shown. In both configurations the heat exchangers are meshed with the same resolution, 14 nodes across the lancet package, as can be seen in figure 9.5, which gives almost two cell rows per tube. The rest of the domains have approximately the same grid resolution in both grids and the total number of nodes are for both grids approximately 1,7 million.

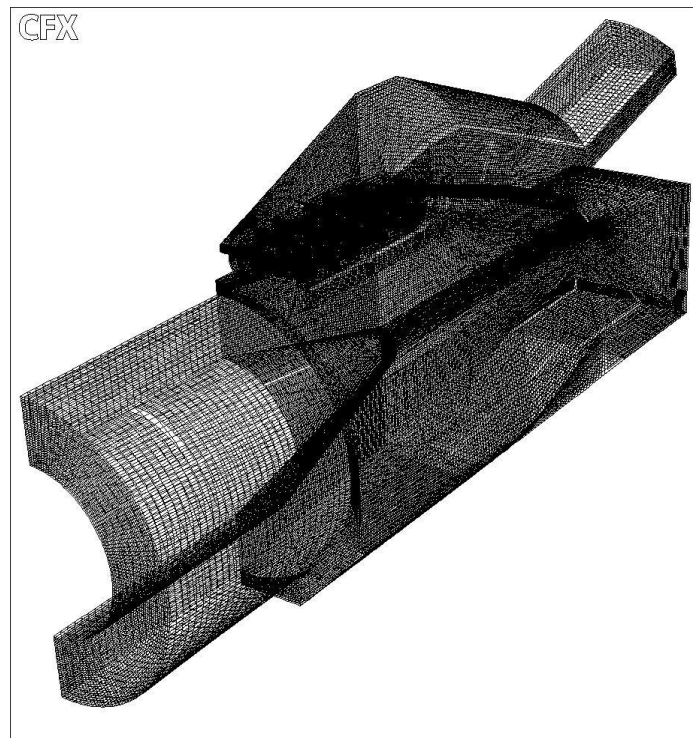


Figure 9.4 Grid for configuration 1.

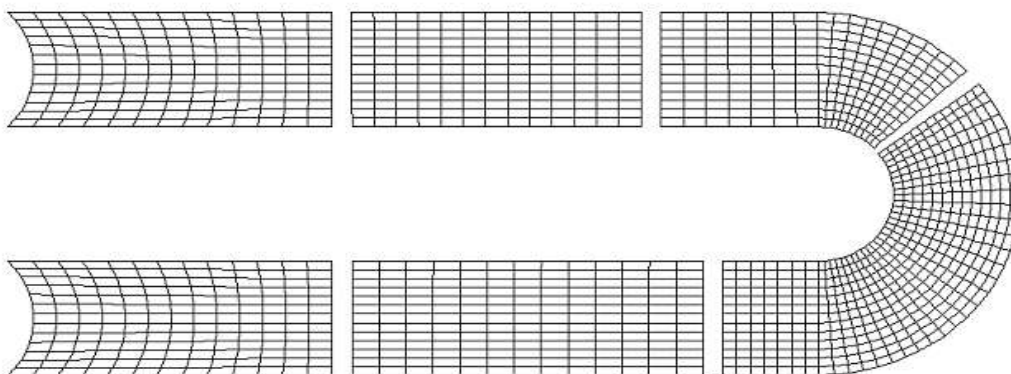


Figure 9.5 Grid for half of the heat exchanger

9.1.4 Numerical settings

The different numerical settings are summarized in table 9.1 below.

Property	Both configurations
Inlet B.C., hot side	Mass flow 0,815* kg/s Constant flux No inlet swirl Turbulence intensity=10 % Turbulence length scale=0,1 m Temperature=882,0 K
Outlet B.C., hex duct exit	Average static pressure=37400 Pa
Outlet B.C., main duct exit	Average static pressure=39500 Pa
Wall B.C.	No slip, fixed wall distance wall function Adiabatic
Inlet B.C., cold side	Mass flux=107 kg/s,m ² Temperature=505,0 K
Other B.C.	Symmetry
Flow type	Compressible
Turbulent Prandtl number	0,9
Turbulence model	SST
Advection scheme	Mass weighted skewed upstream (AEA technology)
Convergence criterion	10 ⁻³

Table 9.1 CLEAN application, numerical settings.

*Mass flow corresponding to half of the true inlet.

9.1.5 Results

The results of the calculations are summarized in table 9.2, where it is shown that configuration 2 has a lower pressure drop than configuration 1, although the mass flow through it is higher. It is also clear that the heat transfer is more efficient in configuration 2 due to the higher hot gas mass flow.

Configuration	Inlet pressure [Pa]	Mass flow* [kg/s]	Δp [Pa]	$T_{cold,out}$ [K]	$T_{hot,out}$ [K]
1	39436	~1,36	4564	762	631
2	39181	~1,45	4258	785	633

Table 9.2 CLEAN pressure drop and temperature results.

*Mass flow through the heat exchanger.

In figure 9.6 the flow field is illustrated and it can be seen that the flow, for both configurations, recirculates downstream of where the circular inlet part is mounted to the octagon like casing. Furthermore, there is a recirculation region just downstream of the cone and in configuration 1 the flow separates on the upper wall of the exhaust gas main exit duct. In configuration 1 there is also a quite large recirculation zone in the hex duct exit, but no recirculation of the flow back into the heat exchanger can be noted for any of the configurations. In figure 9.6 the poor flow distribution of the heat exchanger in configuration 1 can be noticed. In figure 9.7, where the temperature field of the entire CLEAN exhaust gas casing is shown, the influence of the unfavourable flow distribution on the temperature downstream of the heat exchanger is evident. The uneven flow distributions of the heat exchangers are also clear from figure 9.8 where the the velocity component in the normal direction to the heat exchanger is shown. In figures 9.9-9.14 the temperature fields are shown and where again the more even load of configuration 2 can be seen. The less satisfying temperature field in configuration 1 gives larger temperature differences of the cold side air coming from the two sides of the heat exchanger and might be the cause for thermal stresses, which might have to be considered for the collector tube. In figures 9.13-9.14 the temperature difference between the hot and the cold sides is shown. Interesting to note is that the heat flux in parts of the heat exchanger goes from the compressor air to the exhaust gas. This effect is more marked in configuration 1 especially in the left part of the heat exchanger

where the hot gas mass flow is lower. From figures 9.13-9.14 it is also evident that the highest temperature loads on the tubes are where the inner tube rows are mounted to the distributor tube. Another part where the temperature load is high is where the upstream bend is hit by the incoming hot gas stream.

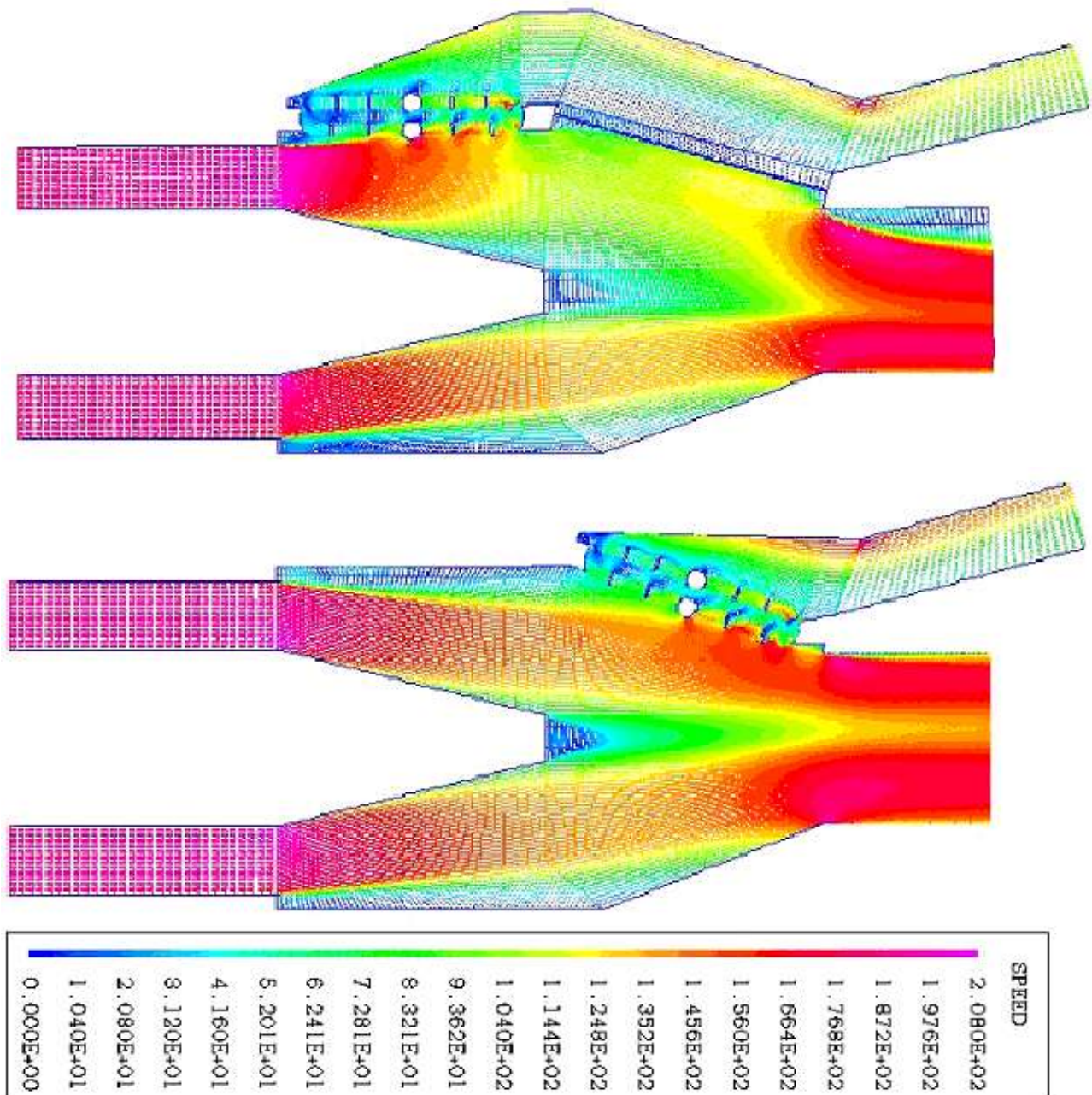


Figure 9.6 Vector plot with velocity distribution on the symmetry plane for both configurations.

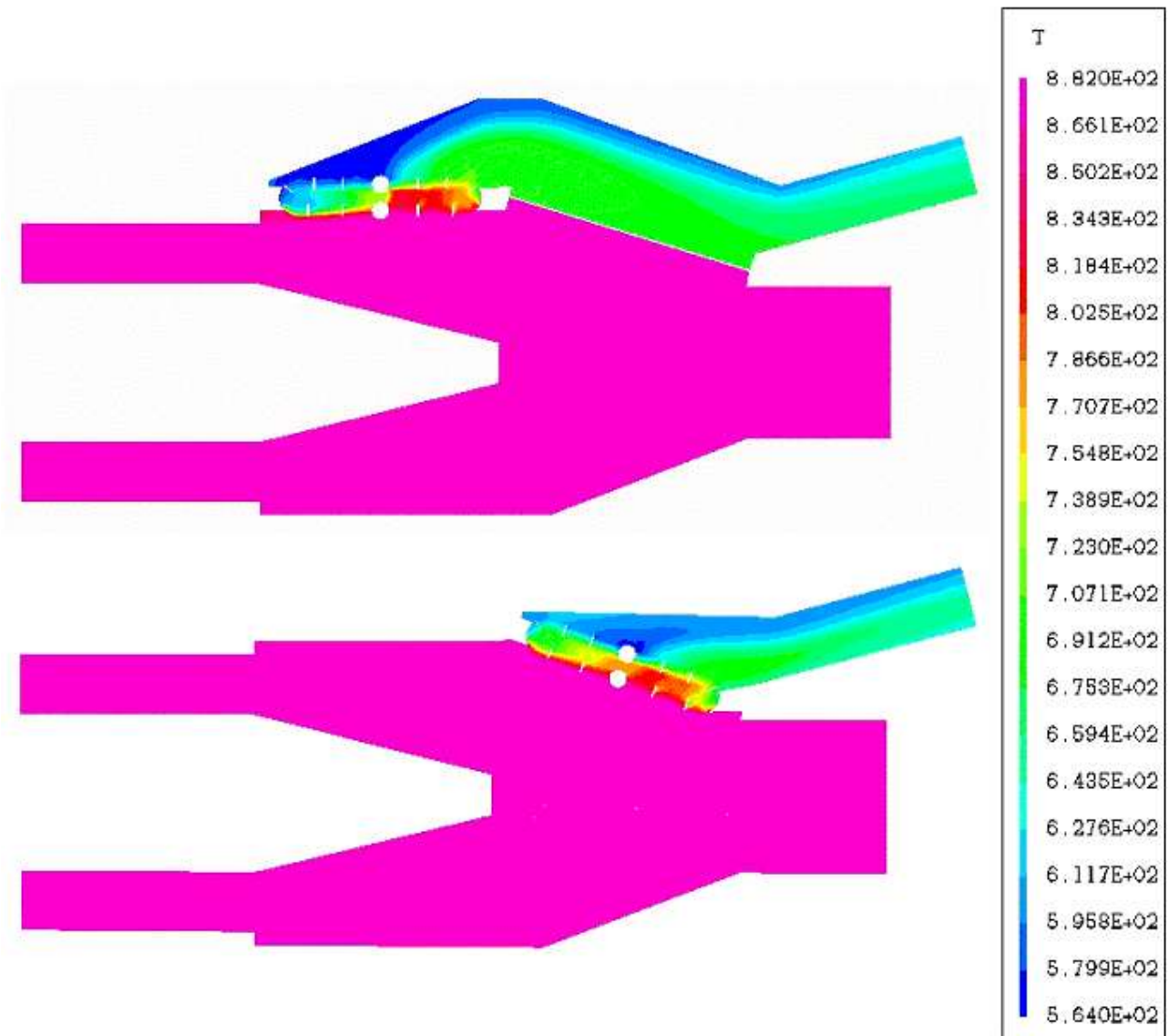


Figure 9.7 Hot gas temperature distributions in the symmetry plane for both configurations.

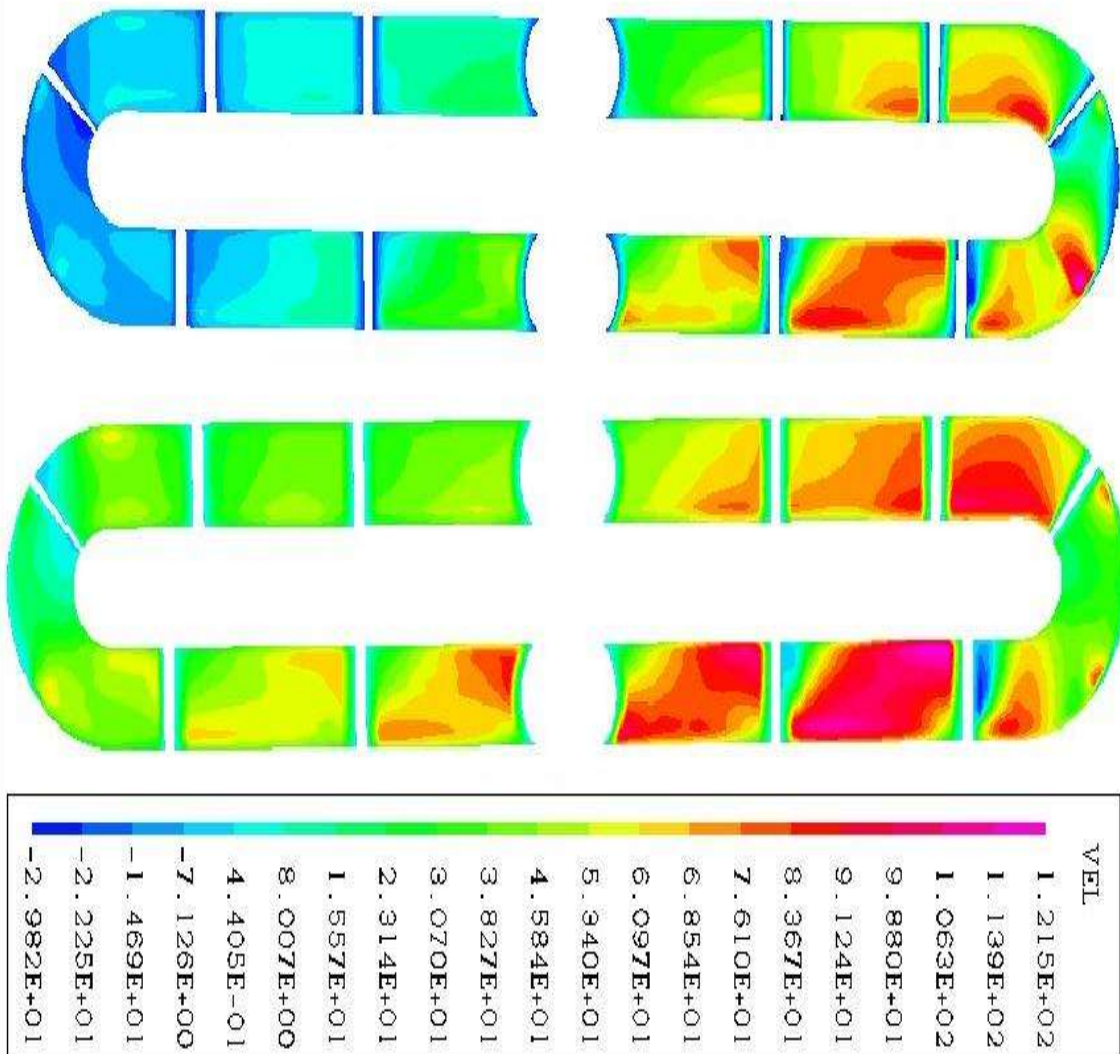


Figure 9.8 Velocity, in the normal direction, through the heat exchanger, symmetry plane. Configuration 1 above and configuration 2 below.

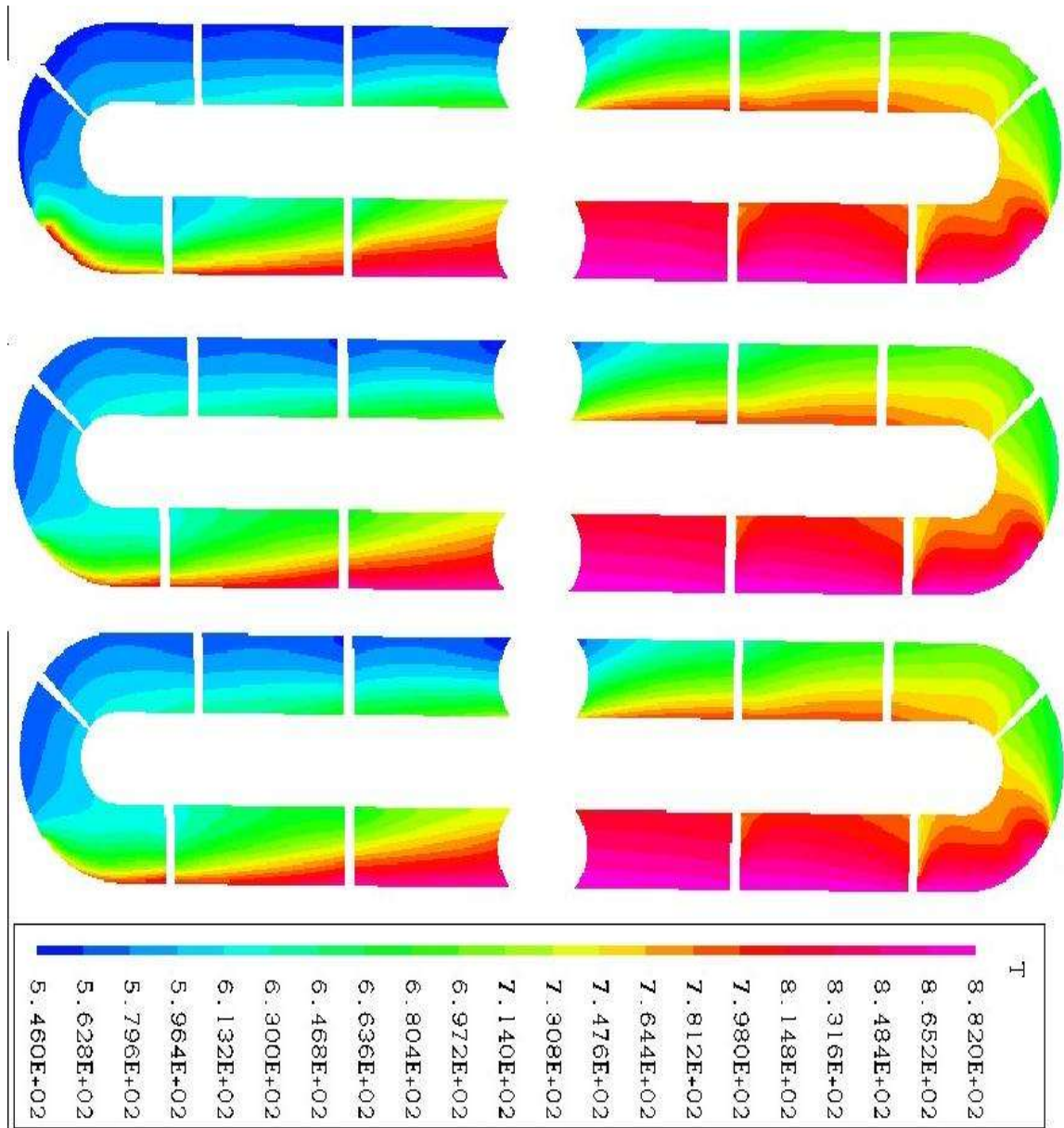


Figure 9.9 Configuration 1, hot gas temperature distribution in three different planes in the heat exchanger.

The uppermost slice lies on the symmetry plane and the lowest slice lies on the side wall.

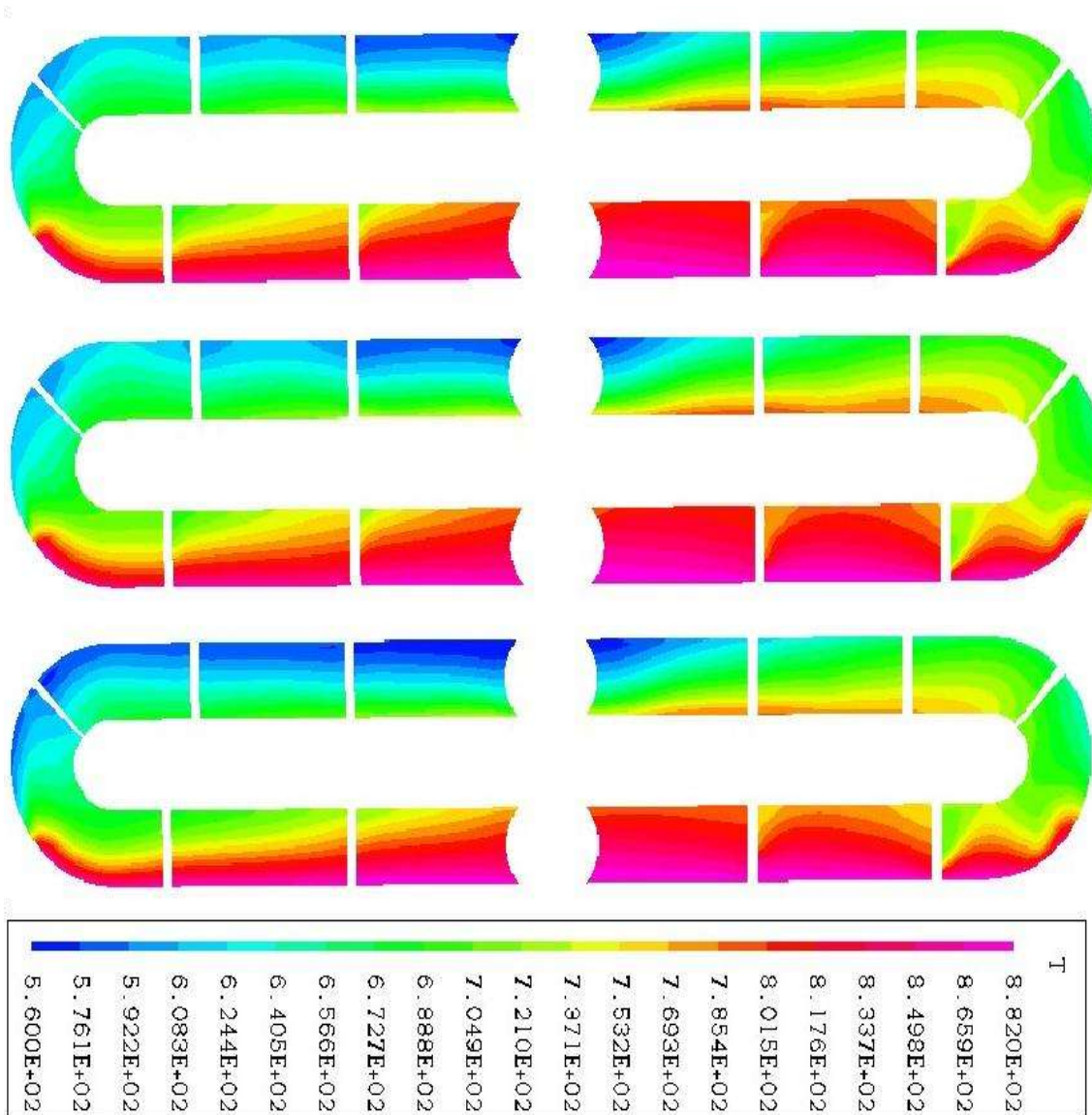


Figure 9.10 Configuration 2, hot gas temperature distribution in three different planes in the heat exchanger.

The uppermost slice lies on the symmetry plane and the lowest slice lies on the side wall.

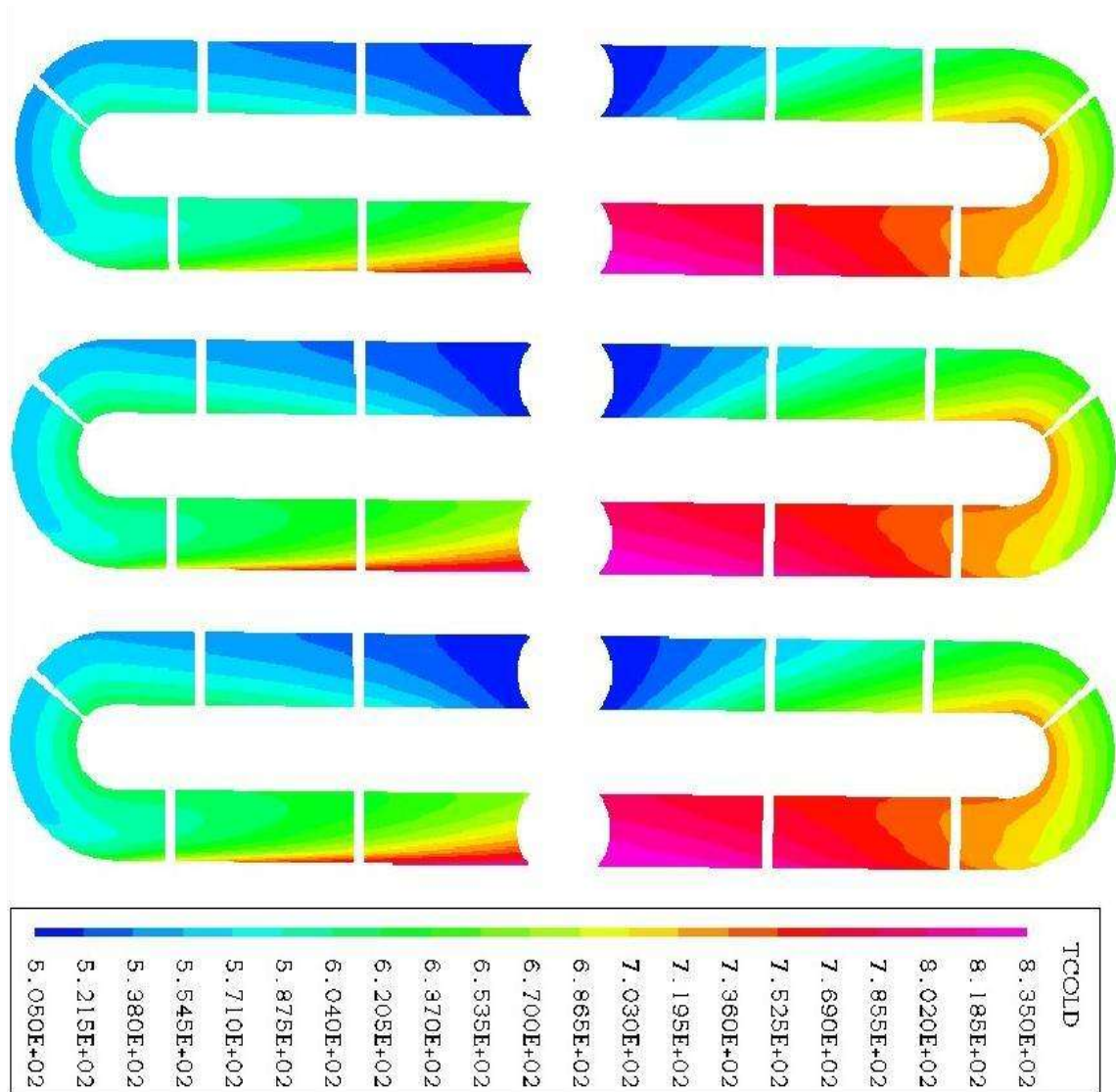


Figure 9.11 Configuration 1, cold gas temperature distribution in three different planes in the heat exchanger.

The uppermost slice lies on the symmetry plane and the lowest slice lies on the side wall.

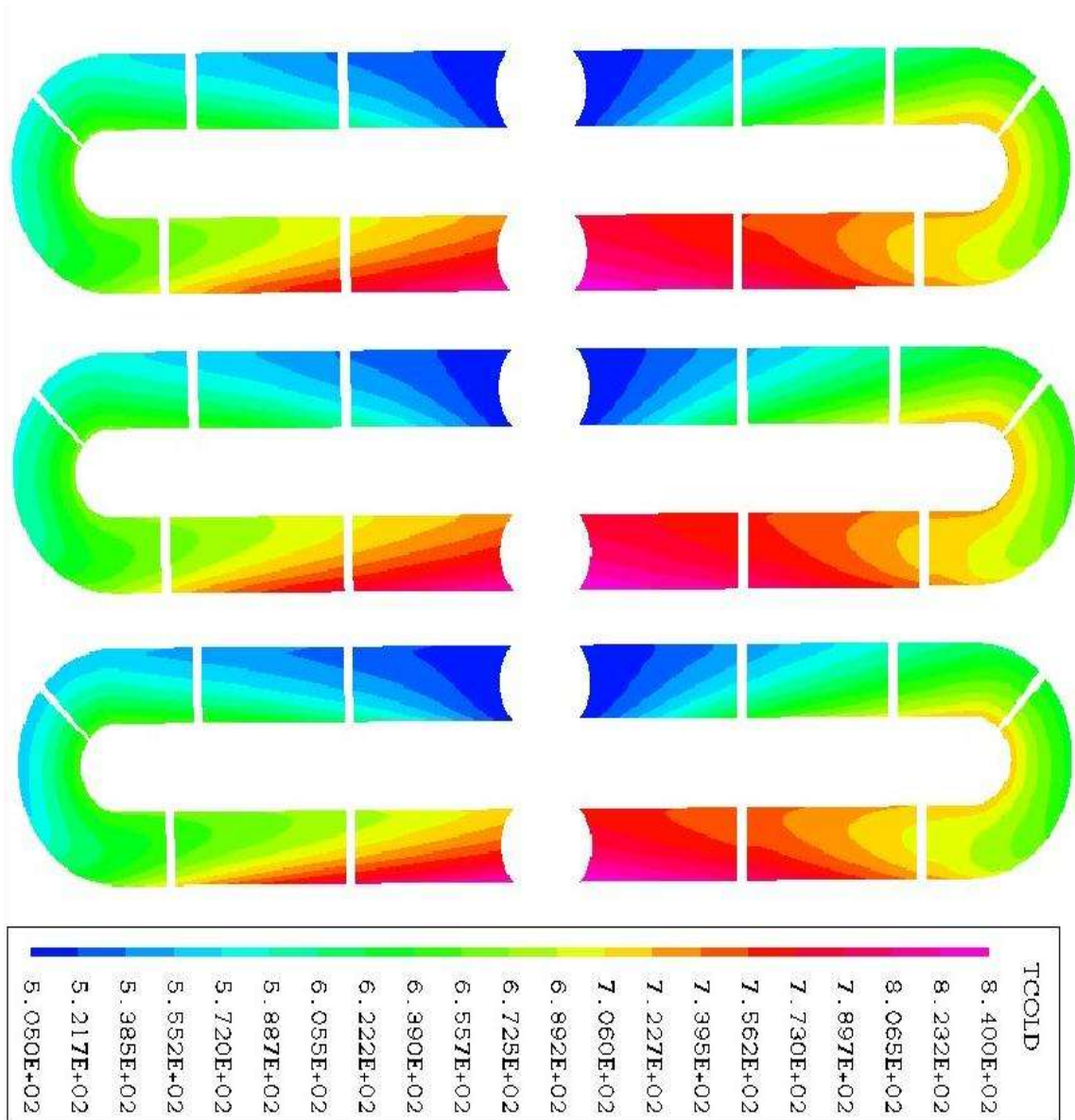


Figure 9.12 Configuration 2, cold gas temperature distribution in three different planes in the heat exchanger.

The uppermost slice lies on the symmetry plane and the lowest slice lies on the side wall.

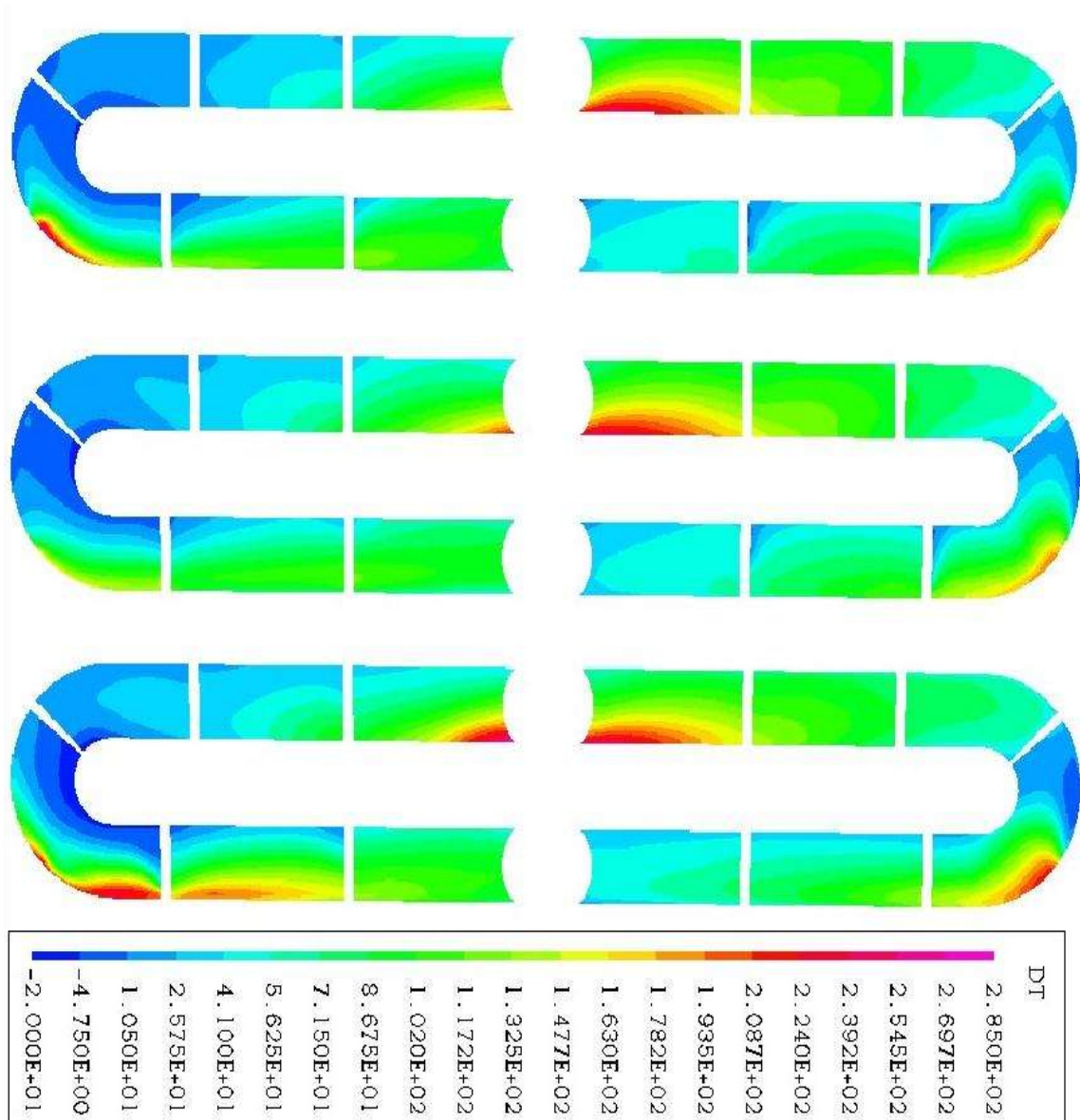


Figure 9.13 Configuration 1, distribution of the temperature difference between the hot and the cold gas in three different planes in the heat exchanger. The uppermost slice lies on the symmetry plane and the lowest slice lies on the side wall.

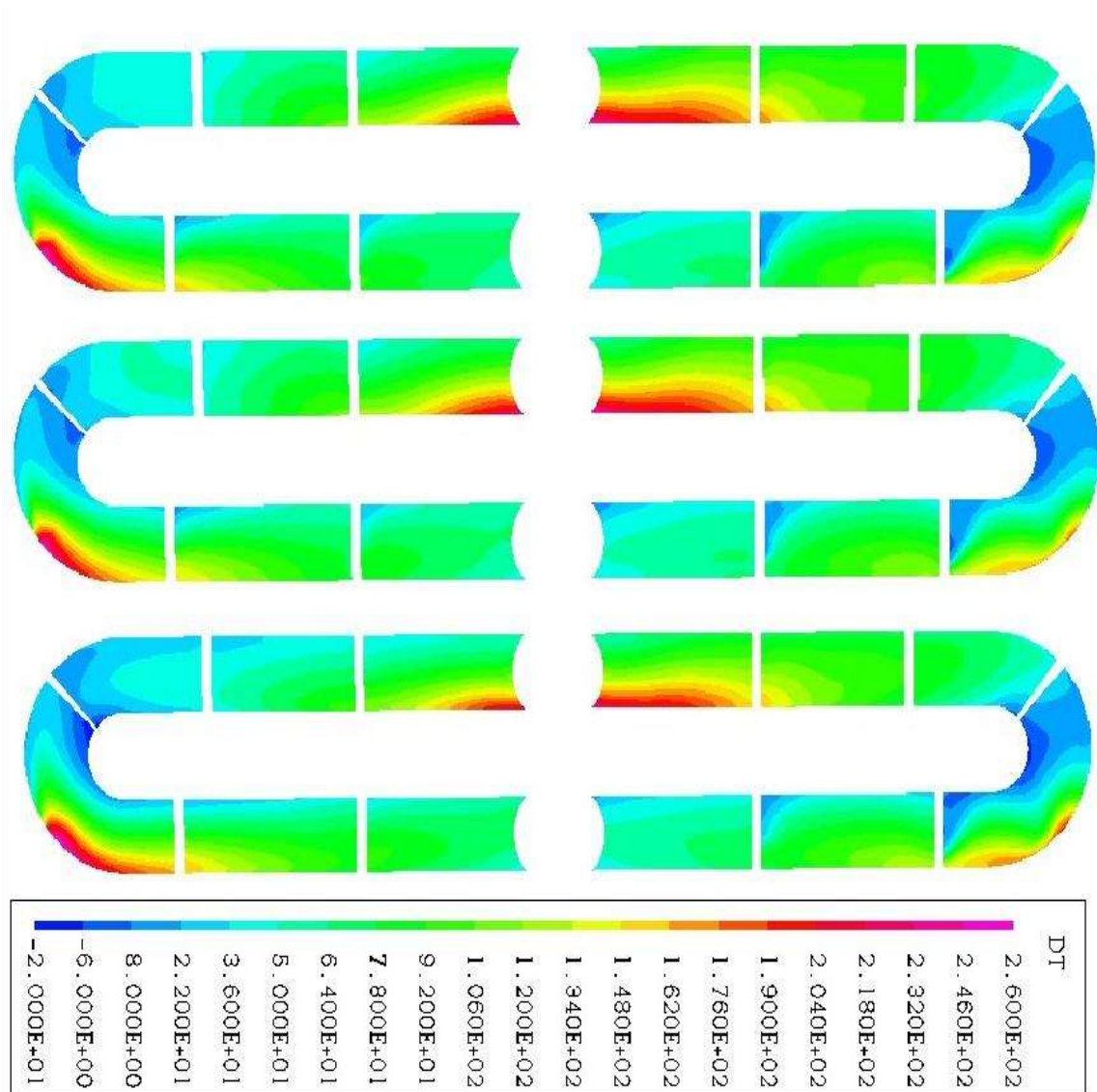


Figure 9.14 Configuration 2, distribution of the temperature difference between the hot and the cold gas in three different planes in the heat exchanger. The uppermost slice lies on the symmetry plane and the lowest slice lies on the side wall.

9.1.6 Conclusions

The two different CLEAN configurations have been calculated with heat transfer for average cruise operating conditions. The numerical simulations indicate that configuration 2 is more favourable from a fluid mechanical point of view. Interesting to note is that the heat flux in parts of the heat exchangers goes from the compressor air to the exhaust gas and that possible problem areas regarding thermal stresses might be where the inner tube rows are mounted on the distributor tube, as well as the collector tube itself.

9.2 Exhaust gas casing of an compact industrial gas turbine

As an additional application example a recuperated compact industrial gas turbine has been chosen. The turbine has a power output of around 1MW and is e.g. suitable for reserve power generation or vehicle applications. The outline of the gas turbine exhaust gas casing is presented in figures 9.15 and 9.16. The hot exhaust gases enter the casing through a diffuser and then proceed upwards through the heat exchanger to the outlet, located to the left in figure 9.15.

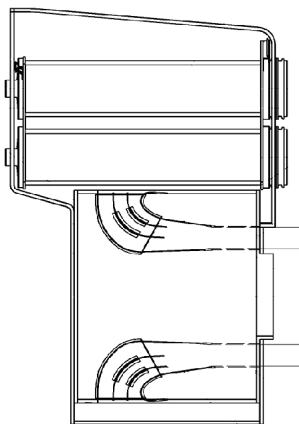


Figure 9.15 Side view of the compact industrial gas turbine.

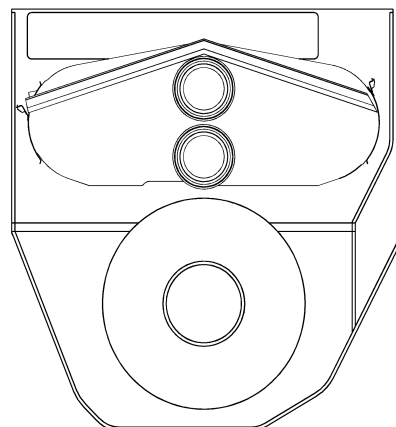


Figure 9.16 Front view of the compact industrial gas turbine.

9.2.1 The CFD model

A grid of about 1,8 million nodes was built for the industrial gas turbine. The grid size is close to the limit given by the 32-bit version of CFX-TASCflow that allows for 2GB memory to be addressed. The grid for the entire geometry is shown in figure 9.17 and in figures 9.18 and 9.19 the grid for the heat exchanger is presented. The size limitation mentioned, made it necessary to limit the number of nodes. A compromise between the resolutions in different regions led to a grid with 13 cell rows across the heat exchanger matrix corresponding to 19 tube rows. This makes the grid somewhat coarse for quantifying the pressure drop with high accuracy, but for qualitative judgements of the flow field it should be enough. In the figures, showing the mesh for the heat exchanger, the unmeshed parts between the different blocks are the spacers. The uneven distribution of the cells in figure 9.19 is due to the different grid resolution in the diffuser compared to the outer casing.

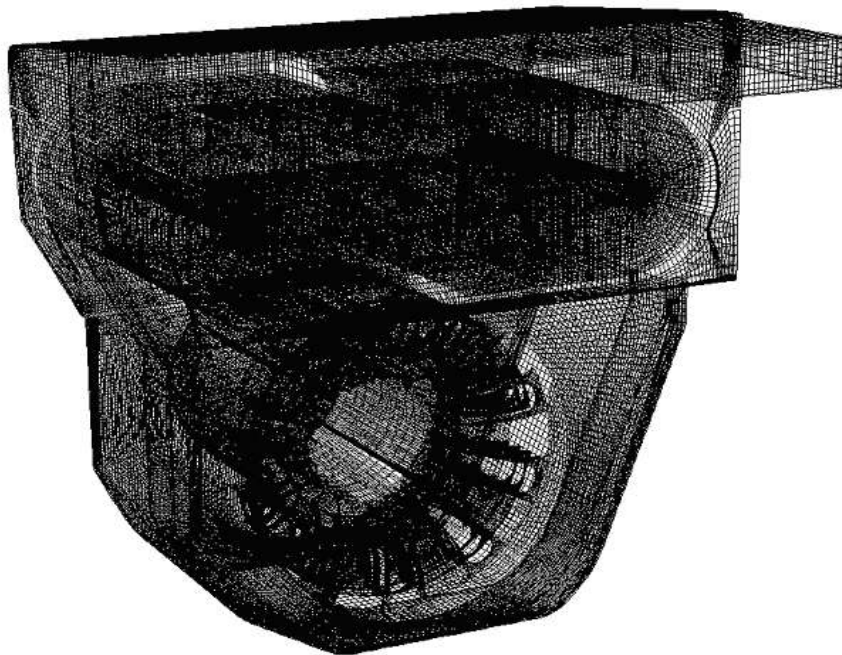


Figure 9.17 Industrial gas turbine grid.

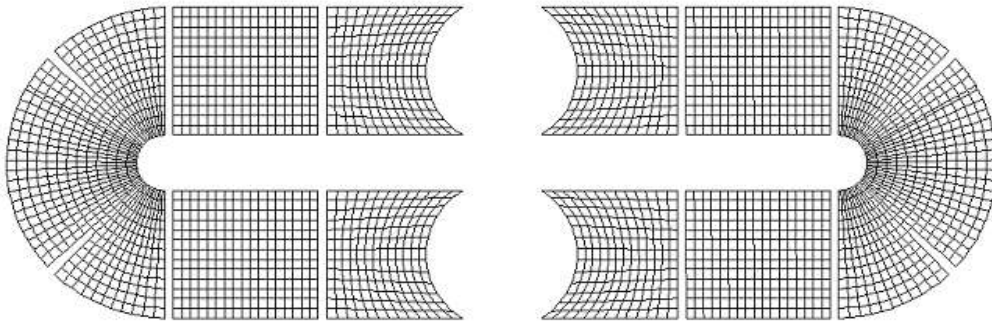


Figure 9.18 Heat exchanger grid, side view.

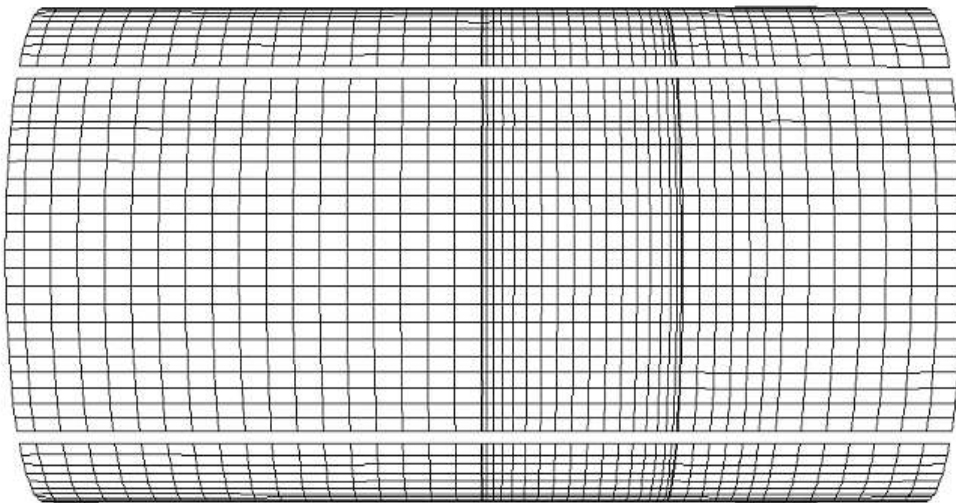


Figure 9.19 Grid in the heat exchanger bend, view parallel to the collector and distributor tubes.

9.2.2 Operating Conditions

The same operating conditions are chosen as for case 2 in chapter 8.1, which correspond to what could be expected to be full load for a gas turbine of this size.

9.2.3 Numerical Settings

Due to the memory limitations, a quite coarse mesh had to be used, which made it meaningless to apply a higher order numerical scheme for the calculations. Instead, a first order upwind scheme, which is known to be very robust, although less accurate, was used for the advection terms. The main numerical settings are summarized in table 9.3.

Property	Setting
Inlet B.C., hot side	Mass flow 2,12 kg/s Constant flux No inlet swirl Turbulence intensity=10 % Turbulence length scale=0,1 m Temperature=1064 K
Outlet B.C.	Average static pressure=94863 Pa
Wall B.C.	No slip, fixed wall distance wall function Adiabatic
Inlet B.C., cold side	Mass flux=57,84 kg/s,m ² Temperature=572,85 K
Flow type	Compressible
Turbulent Prandtl number	0,9
Turbulence model	SST
Advection scheme	1 st order upwind scheme (AEA technology)
Convergence criterion	5·10 ⁻³

Table 9.3 Industrial gas turbine, numerical settings.

9.2.4 Results

The global calculation results are summarized in table 9.4 below.

Pressure drop [Pa]	7879
Hot gas outlet temperature [K]	711
Cold gas outlet temperature [K]	987

Table 9.4 Industrial gas turbine, summary of the results.

In figure 9.20 the temperature field above the heat exchanger is presented showing a temperature variation of around 200K between the center and the side walls. The non-symmetry is due to the location of the exhaust duct, positioned slightly to the left. The heat exchanger temperature fields shown in figures 9.21 and 9.22 indicate that the temperature distributions on both the cold and the hot sides are relatively even. However, to what extent this is due to the influence of numerical diffusion and exaggerated turbulent viscosity is uncertain. The temperature difference between the hot and the cold sides is shown in figure 9.23. As in the CLEAN-cases the largest temperature differences are seen where the inner tube row is mounted to the distributor, but the difference is smaller for CLEAN due to smaller differences in inlet temperatures. The flow distribution through the heat exchanger is presented in figures 9.24 and 9.25 as averages for the inner and outer parts of the upper half of the heat exchanger. The inner parts are the regions closest to the distributor and the outer parts are the regions between the inner parts and the bends. The CFD-calculations predict higher velocities through the inner parts of the heat exchanger and a slightly higher velocities for the left parts of the heat exchanger. The higher velocities for the inner parts could be expected since the exhaust duct is located asymmetrically to the left. An increase of the flow through the heat exchanger in the direction towards the side of the exhaust could also be expected, since the exhaust duct causes an uneven pressure field above the heat exchanger. The results, mentioned above, indicate that a relocation of the exhaust duct or an additional exhaust duct could have a positive effect on flow distribution, heat exchange and pressure drop.

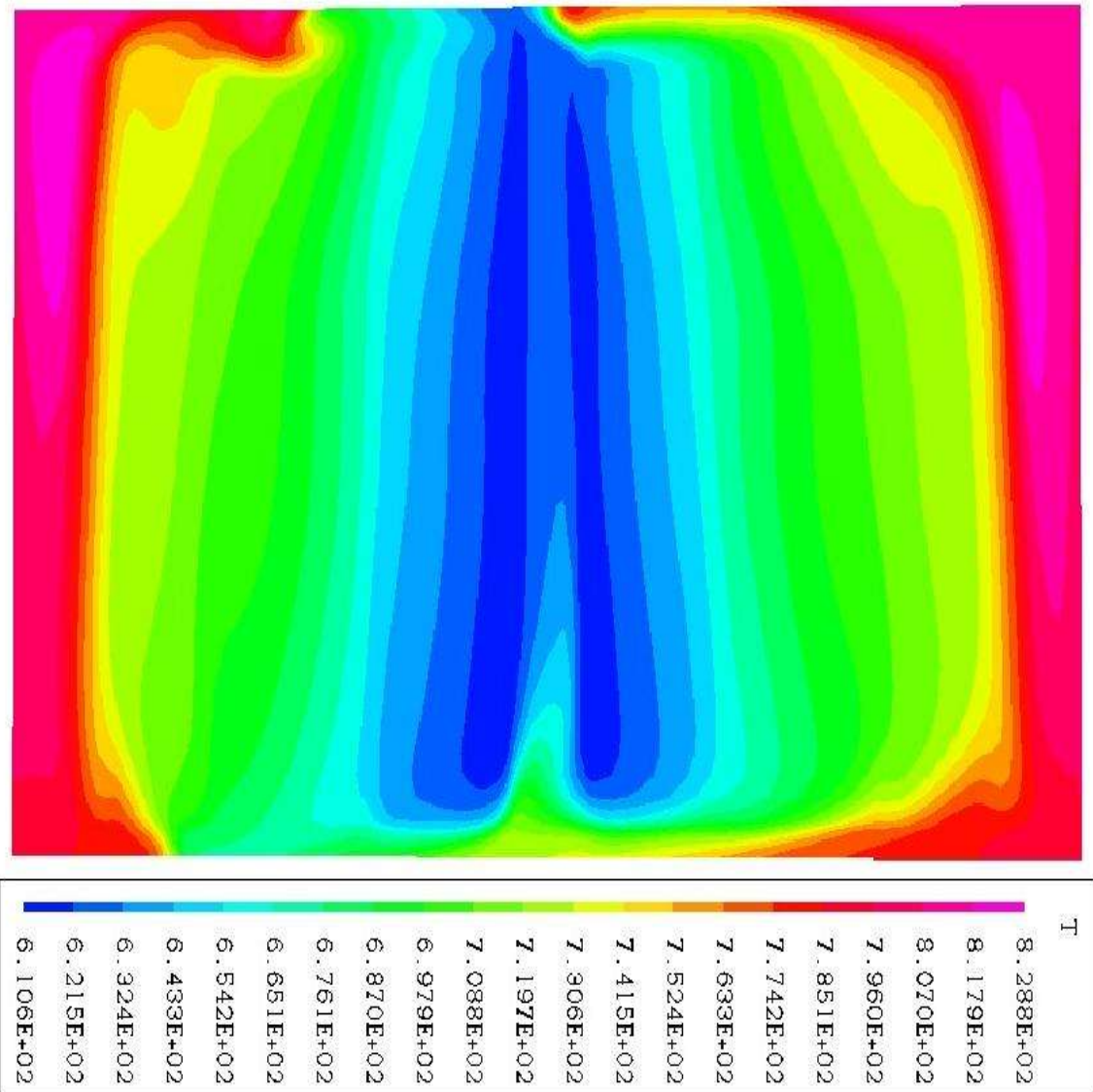


Figure 9.20 Hot gas temperature distribution 5 cm above the heat exchanger.

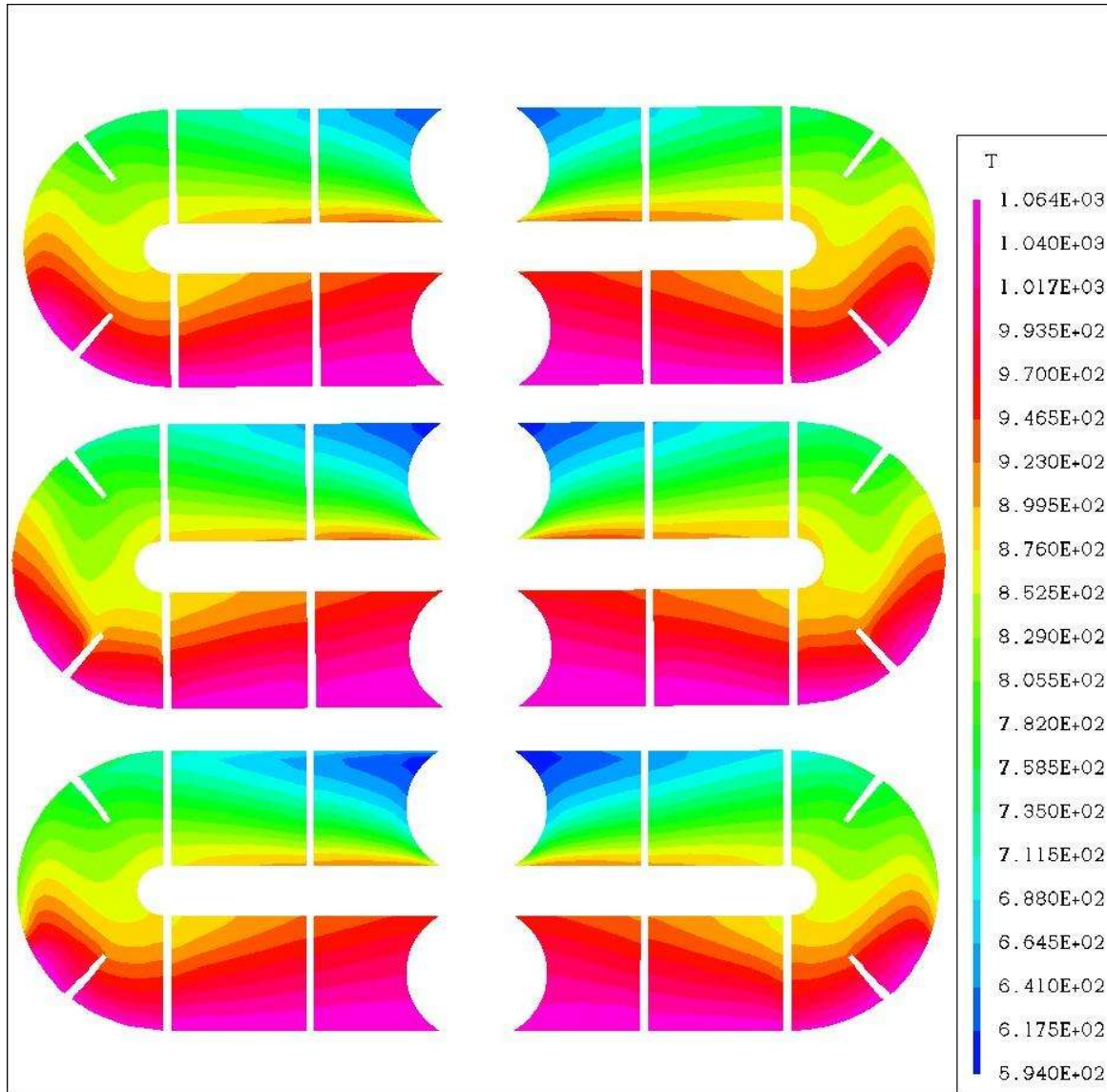


Figure 9.21 Hot gas temperature distribution in the heat exchanger. Above the plane at the wall on the exhaust gas outlet side. Below the plane at the wall closest to the turbine. In the middle a plane in the middle of the diffuser outlet.

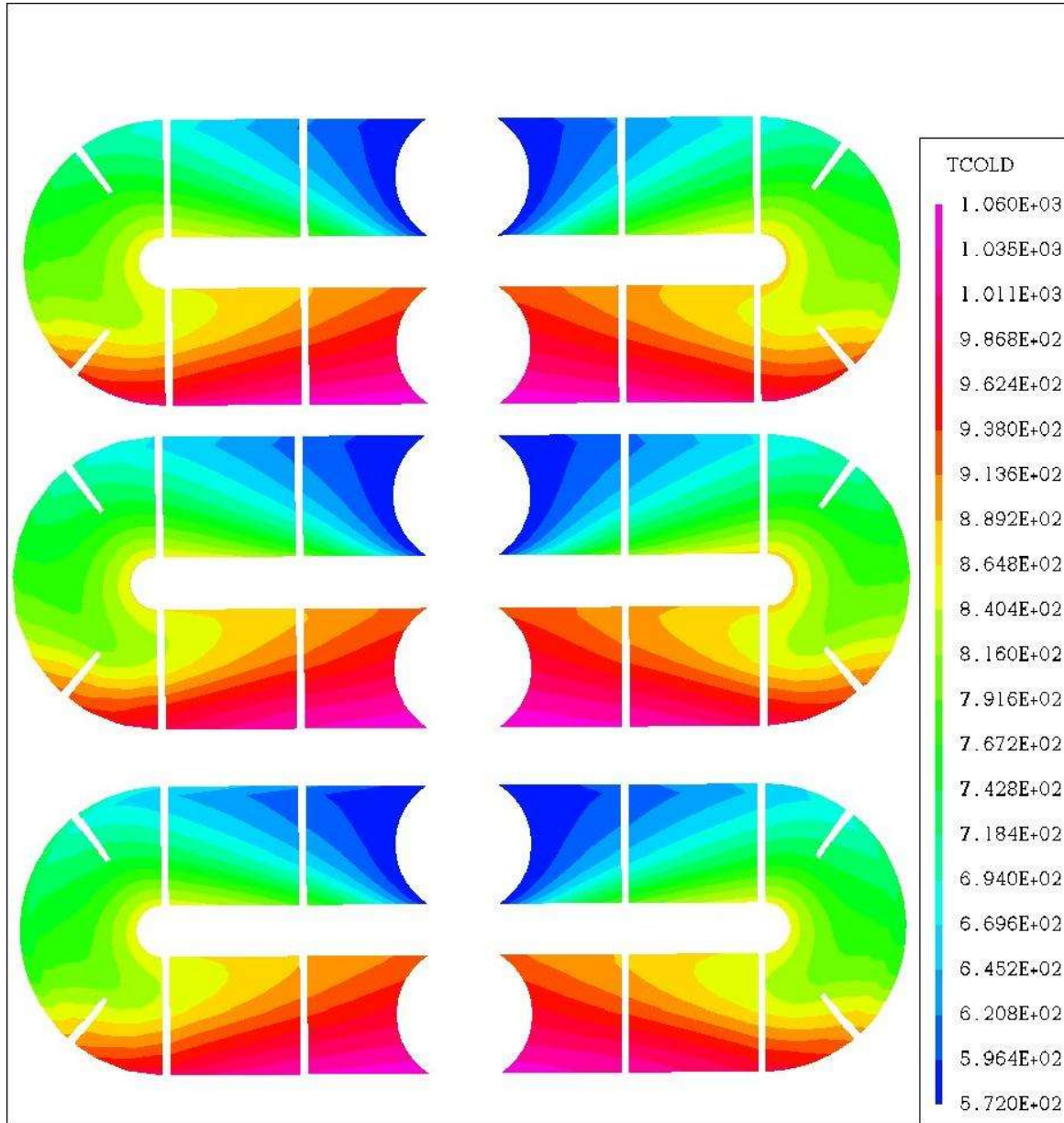


Figure 9.22 Cold gas temperature distribution in the heat exchanger. Above the plane at the wall on the exhaust gas outlet side. Below the plane at the wall closest to the turbine. In the middle a plane in the middle of the diffuser outlet.

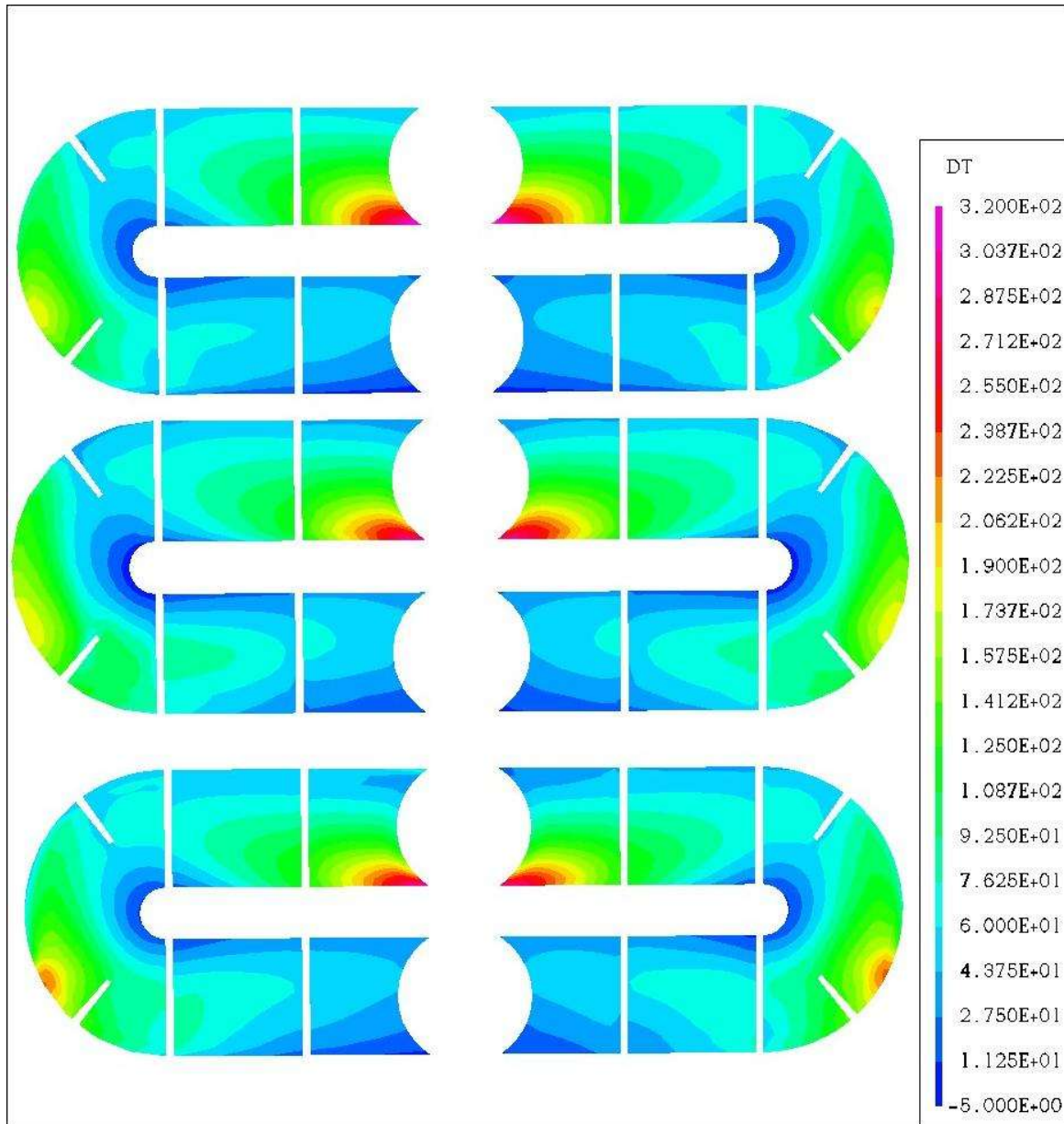


Figure 9.23 Distribution of the temperature difference between the hot and the cold gases in the heat exchanger. Above the plane at the wall on the exhaust gas outlet side. Below the plane at the wall closest to the turbine. In the middle a plane in the middle of the diffuser outlet.

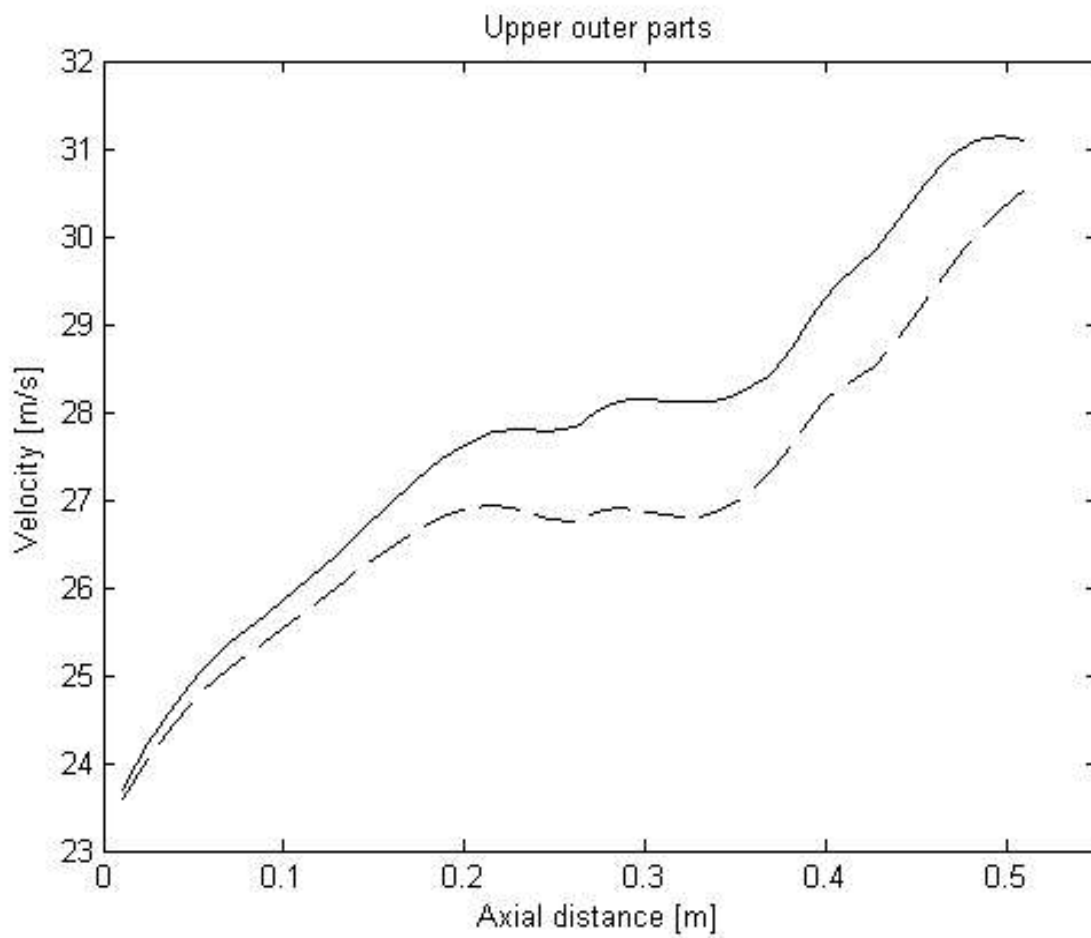


Figure 9.24 Velocity profiles for the heat exchanger outer parts.

Solid: left part, dashed: right part

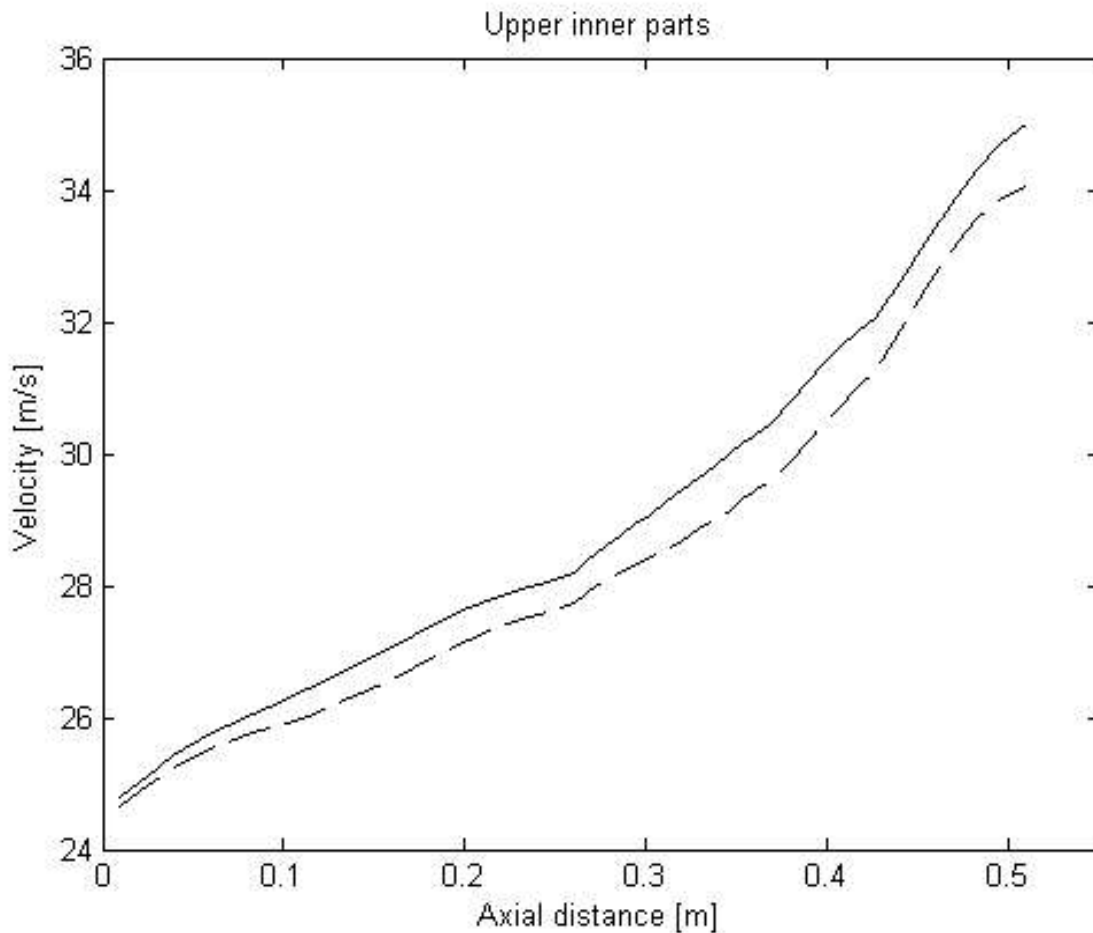


Figure 9.25 Velocity profiles for the heat exchanger inner parts.

Solid: left part, dashed: right part

9.2.5 Conclusions

The flow in an exhaust gas casing of a compact recuperated gas turbine has been simulated. One configuration and one operating condition, corresponding to what could be expected to be full load, were chosen. The numerical simulation indicate that the flow is unevenly distributed with higher heat exchanger load in the part closest to the exhaust gas duct. The

largest temperature differences are produced at the same positions as in the CLEAN simulations, i.e. where the inner tube rows meet the distributor. The temperature fields on both the hot and cold sides are smooth, however the amount of numerical diffusion and overestimated turbulence viscosity is unclear. For temperature field results of quantitatively higher quality one would be well advised to use a grid of higher resolution together with a 2nd order numerical scheme.

10 Suggestions for future work

The study of tube bundles, and the development of the heat exchanger simulation code, and the validation of it has resulted in a robust calculation tool and simple recommendations for the study of flow and heat transfer phenomena in recuperated gas turbine engine exhaust casings. The current level of the work presented constitutes a solid basis for further developments. Below are a number of recommendations for future work suggested for improving the analyses of the flow and heat transfer phenomena related to recuperated gas turbine engines.

- Parallelization of the temperature calculation procedure for shorter execution times of calculations involving heat transfer.
- Adaption of the code to CFD-solvers working on unstructured grids to facilitate the meshing procedure and enable a better grid cell size distribution.
- Implementation of a calculation procedure for the mass flow distribution on the cold side of the heat exchanger. However, this calls for data regarding the pressure losses for the cold side.
- Optimizing the non-convective heat transport, by adjusting the turbulent Prandtl number for the heat exchanger regions or modifying the energy source term by reducing it by a fraction of the turbulent transport. For this purpose experimental or high quality numerical data of temperature fields with strong temperature gradients would be necessary. Part of the non-convective heat transport is also the thermal dispersion that would have to

be accounted for. In order to do that the dispersion tensor would have to be estimated by detailed CFD calculations or experiments.

- Validation of the heat exchanger code for attack angles.
- Improvement of the heat transfer correlations. The correlations for the cold side should be valid for the entire range of Reynolds numbers up to fully turbulent flow and take the turbulent inlet boundary conditions and the flow development from the inlet into account. For the hot side the Reynolds analogy could be improved if experimental data for the tube bundle in question was available.
- Tensors as function of the entrance length could be derived for the momentum source terms. However, this would call for further experimental or numerical investigations of the response of the heat exchanger matrix to non normal inlet flow conditions.

11 Summary

A computational tool and a methodology for steady state heat exchanger simulations of recuperated gas turbines and aero-engines have been developed. As an example a compact tube bundle heat exchanger with oval shaped tubes was chosen. The simulation tool proved to work for different layouts of the heat exchanger and for different geometrical configurations of the gas turbine engine exhaust ducts. The resistance tensors were tuned against both CFD-data and experimental data and the computational model was to some extent validated against experimental results. For the validation isothermal experimental data from the Laboratory of Fluid Mechanics and Turbomachinery at the Technical University of Thessaloniki was used together with hot gas channel data from MTU. The calculated and measured velocity profiles showed an acceptable agreement that in some of the cases was even very good. The calculated pressure drop deviated less than 10% for the compared cases, which must be considered to be acceptable. The calculated results for the hot gas cases showed an exaggerated heat transfer rate, most likely due to the use of a cold side heat transfer correlation for fully turbulent flow, although the Reynolds numbers indicated transitional flow.

Radiation and thermal expansion were shown to play a negligible role for the heat exchanger chosen and was thus not accounted for in the analyses. However, for a heat exchanger of another material and configuration these effects might have to be taken into account.

The cell size of the porous medium representing the heat exchanger is suggested to be less or equal the size of the representative elementary volume (REV) of the problem. This has for a tube bundle the length scales of the longitudinal and transversal pitches. Since the velocity profiles close to the walls in the heat exchanger are unknown and the cell size is large the boundary layers were chosen to be modelled by a wall function. The fixed distance wall function available in CFX-TASCflow is recommended since it gives a friction Reynolds number dependent and not grid size dependent. As a compromise between the desired high accuracy in the domain outside the heat exchanger and the problems to resolve flow details in the porous medium it is recommended to use a two-equation turbulence model.

Without any modifications to the transport equations for turbulent quantities the turbulent heat transport is exaggerated. The heat transport in the heat exchanger is for two of the main directions dominated by convection, but for the third main direction diffusion and dispersion might be significant. For conservative analyses of the temperature fields, from a thermal stress point of view, the exaggerated turbulent heat transport should be left out from or compensated for in the hot side energy equation as should thermal radiation and thermal dispersion.

Acknowledgements

The work presented in this thesis has been financed partly by the EU in the Aerohex project (Contract Number G4RD-CT-1999-00069, Project Number GRD1-1999-10602) and partly by MTU, Motoren- und Turbinen-Union GmbH, Munich. The author greatly acknowledges this financial support.

Furthermore the author would like to express his thankfulness to

- Prof. H. P. Berg for the possibility to make a PhD out of this project and for supervising and giving support during the project.
- Prof. K. Vogeler for taking his time to go through the dissertation and give comments on the final draft
- Prof. C. Egbers for being the chairman of the committee
- Dr. Reile at MTU and Prof. Goulas and his team at the University of Thessaloniki for making their experimental results available for this dissertation
- Dr. Tinoco at Vattenfall AB for the encouragement to take the opportunity to do a PhD
- The colleagues at the Chair for Flight Propulsion and Internal Combustion Engines at BTU, Oleksiy Antoshkiv, Volker Biesold, Marian Bloch, Roland Dückerhoff, Christoph Feiler, Hosni Izweik, Fushui Liu, Michael Prinzler and Guido Rabe for contributing to an inspiring atmosphere at the Chair

and finally my wife Antonia Naumann for her patience and encouragement during this period in our life.

References

- AEA Technology, CFX-TASCflow, User Documentation, Version 2.11, June 2001.
- Ahlinder, S., and Biesold, V., EU Growth Project GRD1-1999-10602 “AEROHEX” , Deliverable 17a, Report on the hot side flow investigation on the exhaust case of a recuperated industrial gas turbine.
- Ahlinder, S., EU Growth Project GRD1-1999-10602 “AEROHEX” , Deliverable 20b, Report on the matrix orientation in the EEFAE-LSIP (CLEAN) demonstrator, CFD analysis.
- Alazmi, B., S., A., Analysis of transport models and computation algorithms for flow through porous media, PhD-Thesis, The Ohio State University, Columbus, Ohio 43210, USA , April , 2003
- Anderson, J., D., Computational fluid dynamics, the basics with applications, McGraw- Hill, 1995.
- Antohe, B. V. and Lage, J. L., A General Two-Equation Macroscopic Turbulence Model for Incompressible Flow in Porous Media, Int. J. Heat Mass Transfer, vol. 40, No. 13, pp. 3013-3024, 1997.
- ASME Boiler and Pressure Vessel Code, An International Code II, Part D, Properties, July 1, 2003. The American Society of Mechanical Engineers, New York.
- Bähr, M., Wärmeübergang und Druckverlust querangeströmter Rohrbündel mit versetzt und fluchtend angeordneten Profilrohren, Dissertation, TH Karlsruhe, 1989.
- Bear, J., Dynamics of fluids in porous media, Dover Publ., ISBN : 0-486-65675-6, New York, 1988.
- Bear, J., and Bachmat, Y., Introduction to modelling of transport phenomena in porous media, Kluwer, ISBN : 0-7923-0557-4, 1990.

-
- Bear, J., Transport processes in porous media, Kluwer ISBN : 0-7923-1363-1, 1991.
- Bejan, A., Convection Heat Transfer, Second Edition, Wiley, 1995.
- Bergelin, O. P., Brown, G. A., and Doberstein, S. C., Heat transfer and fluid friction during flow across banks of tubes – IV, Trans. ASME, 74, 1952, pp. 953-960.
- Boelter, L. M. K., Young, G., and Iversen, H. W., NACA TN 1451, Washington, July 1948.
- Boer, R., Porous media, a survey of different approaches, 1991.
- Brauer, H., Untersuchungen an Querstrom-Wärmetauschern mit verschiedenen Rohrformen, Mannesmann Forschungsbericht 126, pp. 3-18, 1961.
- Churchill, S. W., and Ozoe, H., Correlations for laminar forced convection in flow over an isothermal plate and in developing and fully developed flow in an isothermal tube, J. Heat Transfer 95 (1973), 416-419.
- Cohen, H., Rogers, G. F. C., and Saravanamutto, H. I. H., Gas Turbine Theory, 3rd Edition, Longman Scientific and Technical, 1987.
- Didierjean, S., Souto, H. P. A., Delannay, R. and Moyne, C., Dispersion in Periodic Porous Media. Experience versus Theory for Two-dimensional Systems, Chemical Engineering Science, Vol. 52, No. 12, pp. 1861-1874, 1997.
- Dittus, P. W., and Boelter, L. M. K., Heat transfer in automobile radiators of the tubular type, Univ. California Pub. Eng., Vol. 2, No. 13, Oct. 17, 1930, pp. 443- 461; reprinted in Int. Comm. Heat and Mass Transfer, Vol. 12, 1985, pp. 3-22.
- Dullien, F. A., Porous media, Academic Press ISBN : 0-12-223651-3, 1994.

-
- Eggebrecht, R. and Schlosser, W., Kompakter Hochtemperatur-Wärmetauscher für Wellenleistungsturbinen, *Motortechnische Zeitschrift* 47, 1986.
- Ferziger, J. H., and Peric, M., *Computational Methods for Fluid Dynamics*, Second Edition, Springer, 1999.
- Fletcher, C. A. J., *Computational Techniques for Fluid Dynamics*, Volume 1, Second Edition, Springer, 2000.
- Goulas, A., Yakinthos, K., and Misirlis, D., EU Growth Project GRD1-1999-10602 "AEROHEX" , Deliverable 6, Report on matrix flow tests, 2002.
- Goulas, A., Katheder, K., Palikaras, A., Yakinthos, K., Flow measurements and investigations in a staggered tube matrix of a heat exchanger, *Int. J. of Heat and Technology*, Vol 21, n.2, 2003.
- Goulas, A., Yakinthos, K., and Misirlis, D., Aristotle University of Thessaloniki, Dept. of Mechanical Engineering, Laboratory of Fluid Mechanics and Turbomachinery, Private Communication, 2004.
- Grotjans, H., Turbulenzmodelle höherer Ordnung für komplexe Anwendungen, *Fortschritt-Berichte VDI*, Reihe 7 Strömungstechnik, Nr. 371, 1999.
- Grotjans, H., and Menter, F. R., Wall Functions for General Application CFD Codes, *ECCOMAS 98*, John Wiley & Sons, Papailiou et al. (eds.), pp. 1112-1117.
- Hanke, H., Wärmeübergang und Druckverlust in querangeströmten Ovalrohrbündeln, PhD-Thesis, TH Karlsruhe, 1986.
- Hausen, H., *Heat Transfer in Counterflow, Parallel Flow and Cross Flow*, McGraw-Hill, 1983.
- Hsu, C. T., Cheng, P., Thermal Dispersion in a Porous Medium, *Int. J. Heat Mass Transfer*, Vol. 33, No. 8, pp. 1587-1597, 1990.

-
- Isachenko, V., P., Osipova, V., A., and Sukomel, A., S., Heat transfer, English translation, Mir publishers, 1977, Moscow.
- Joyner, V., T., and Palmer, C., B., An experimental survey of flow across banks of elliptical and pointed tubes, NACA-Report No. L-609, 1943.
- Katheder, K., MTU Aero Engines GmbH, Private Communication, 2003.
- Kaviany, M., Principles of Heat Transfer in Porous Media, Second Edition, Springer, 1995.
- Kaviany, M., Handbook of Fluid Dynamics, Chapter 21, Flow in Porous Media, CRC Press, 1998.
- Kays, W. M. and London, A. L., Hochleistungswärmeübertrager, Akademie-Verlag Berlin, 1973.
- Kays, W. M., and Crawford, M. E., Convective Heat and Mass Transfer, Third Edition, McGraw-Hill, 1993.
- Kreyszig, E., Advanced Engineering Mathematics, Sixth Edition, Wiley, 1988.
- Lauder, B., E., and Massey, T., H., The numerical prediction of viscous flow and heat transfer in tube banks, Trans. ASME, Journal of Heat Transfer, vol 100, Aug. 1978.
- Merker, G. P., Hanke, H., Bähr, M., Zur Analogie zwischen Impuls- und Wärmetransport in quer angeströmten Ovalrohrbündeln, Wärme- und Stoffübertragung 21, 95-102 (1987).
- Merker, G. P., Konvektive Wärmeübertragung, Springer, 1987.
- Nield, D. A., Bejan, A., Convection in Porous Media, Second Edition, Springer, 1999.
- Patankar, S. V., Numerical Heat Transfer and Fluid Flow, Taylor and Francis, 1980.

-
- Pedras, H. J., De Lemos, M. J. S., Adjustment of a Macroscopic Turbulence Model for a Porous Medium Formed by an Infinite array of Elliptic Rods, Proceeding of the 2nd International Conference on Computational Heat and Mass Transfer, COPPE/UFRJ – Federal University of Rio de Janeiro, Brazil, October 22-26, 2001.
- Pellischek, G., and Kumpf, B., Compact heat exchanger technology for aero engines, ISABE Paper 91-7019, 1991.
- Pellischek, G., and Reile, E., Compact energy recovery units for vehicular gas turbines, SAE technical paper series, International congress & exposition, Detroit, Michigan, February 24-28, 1992.
- Perry, R. H., Green, D. W., Perry's Chemical Engineers Handbook, McGraw-Hill.
- Pope, S. B., Turbulent Flows, Cambridge University Press, 2000.
- Råde, L. and Westergren, B., BETA Mathematics Handbook, Second Edition, Chartwell-Bratt Ltd, 1990.
- Reile, E., MTU Aero Engines GmbH, Private Communication, 2003.
- Rodi, W., Turbulence Models and Their Application in Hydraulics, Third Edition, A. A. Balkema, Rotterdam, 2000.
- Ruth, E., K., Experiments on a crossflow heat exchanger with tubes of lenticular shape, J. Heat Transfer 105, pp. 571-575, 1983.
- Sahimi, M., Flow and transport in porous media and fractured rock, from classical methods to modern approaches, VCH , ISBN : 3-527-29260-8, 1995 .
- Schad, O., Zum Wärmeübergang an elliptischen Rohren, Dissertation, TH Stuttgart, 1967.

-
- Scheuenpflug, H., Wilfert, G. and Simon, B., Erfüllung zukünftiger Umweltanforderungen durch den Einsatz eines Wärmetauschertriebwerks, DGLR-2001-039.
- Schlichting, H., Boundary-Layer theory, Seventh Edition, McGraw-Hill, 1979.
- Scholz, F., Einfluß der Rohrreihenanzahl auf den Druckverlust und Wärmeübergang von Rohrbündeln bei hohen Reynolds Zahlen, Chemie-Ing.-Tech. 40 (1968) Nr. 20, S. 988/95.
- Skjetne, E., High-Velocity Flow in Porous Media, Analytical, Numerical and Experimental Studies, PhD Thesis, Department of Petroleum Engineering and Applied Geophysics, Norwegian Institute of Technology, University of Trondheim, 1995.
- Stephan, K. and Traub, D., Einfluß auf Rohrreihenanzahl und Anströmungsturbulenz auf die Wärmeleistung von quer angeströmten Rohrbündeln, Wärme- und Stoffübertragung 21, 103-113 (1987).
- Swanson, C. J., Julian, B., Ihas, G. G., and Donnelly, J. R., Pipe Flow Measurements Over a Wide Range of Reynolds Numbers Using Liquid Helium and Various Gases., J. Fluid Mechanics, 2002, Vol. 461, pp. 51-60, 2002 Cambridge University Press.
- Tannehill, J. C., Anderson, D. A., and Pletcher, R. H., Computational Fluid Mechanics and Heat Transfer, Second Edition, Taylor and Francis, 1997.
- Vafai, K., Handbook of porous media, Dekker ISBN : 0-8247-8886-9, New York, 2000.
- VDI-Wärmeatlas, 8. Auflage 1997.
- Wilcox, D. C., Turbulence Modeling for CFD, DCW Industries, Inc, La Canada, CA, 1993.
- Zukauskas, A., Ulinskas, R., Katinas, V., Fluid Dynamics and Flow-Induced Vibrations of Tube Banks, Edited by J. Karni, Hemisphere, 1988.

Zukauskas, A., Heat Transfer in Tube Banks in Crossflow, Taylor & Francis, 1988.

Zukauskas, A., High-Performance Single-Phase Heat Exchangers, Hemisphere, 1989.

Appendix A, Water channel tests

The flow field in the exhaust gas casing of the compact industrial gas turbine above was investigated experimentally in a water channel at the Chair of Combustion Engines and Flight Propulsion at BTU. For this purpose a Perspex model with a real heat exchanger mounted inside was used in a water analogy test facility. Numerical calculations were performed for water with the same Reynold' number and compared qualitatively with the experiments. The Reynold' number was chosen to correspond to 100% load, i.e. The non-isothermal case above. The numerical calculations were done using the same computational grid as for the non-isothermal calculations above. The reason for using a water channel, for this kind of investigations, is that for the same Reynolds number as in a real machine, with gas as working medium, the flow velocities are significantly lower, which enables better possibilities for flow visualisations. The flow was visualized experimentally by laser cuts, through the perspex walls. In this way the air bubbles and particles in the water were lit up and could be photographed. During the investigations the inlet flow angle, the Reynolds number and the geometry were varied. It was shown both experimentally and numerically that the influence from the inlet flow angle on the flow field was negligible, as was the Reynolds number for the range of flows investigated. The geometry up stream of the heat exchanger had also a minor influence on the flow field. The major flow structures that were observed experimentally were also seen in the numerical results. The observed flow structures are sketched in figure A.1 below. In the figures following it can be observed that the flow field produced by the CFD code agrees well with the experimental one. In each figure the numbers of the vortices shown refer to the vortices sketched in figure A.1. When studying the figures, however, it should be noted that the experimental model and the numerical model are mirrored compared to eachother.

For further information, please see Ahlinder and Biesold.

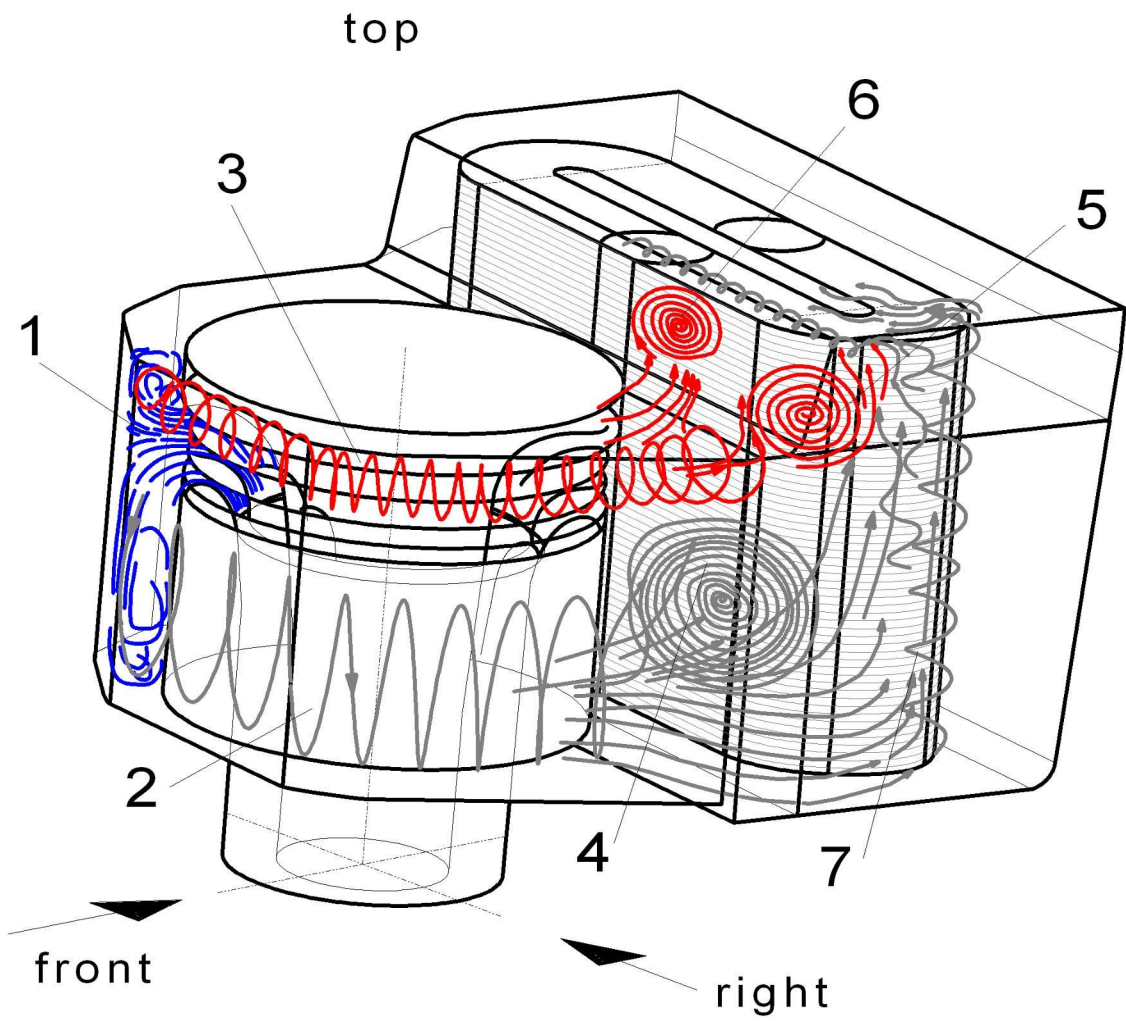


Figure A.1 Flow characteristics in the exhaust gas casing.

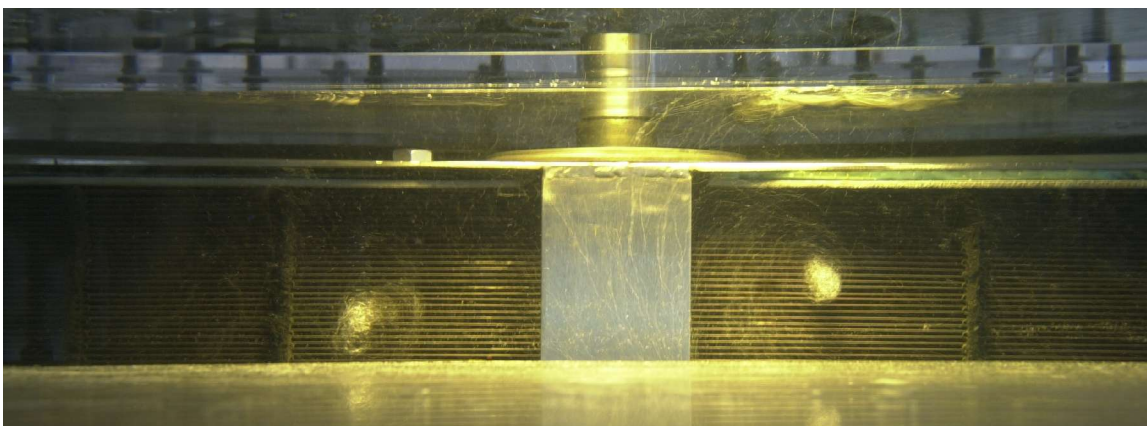


Figure A.2 Vortices at the HEX inlet, position 6.

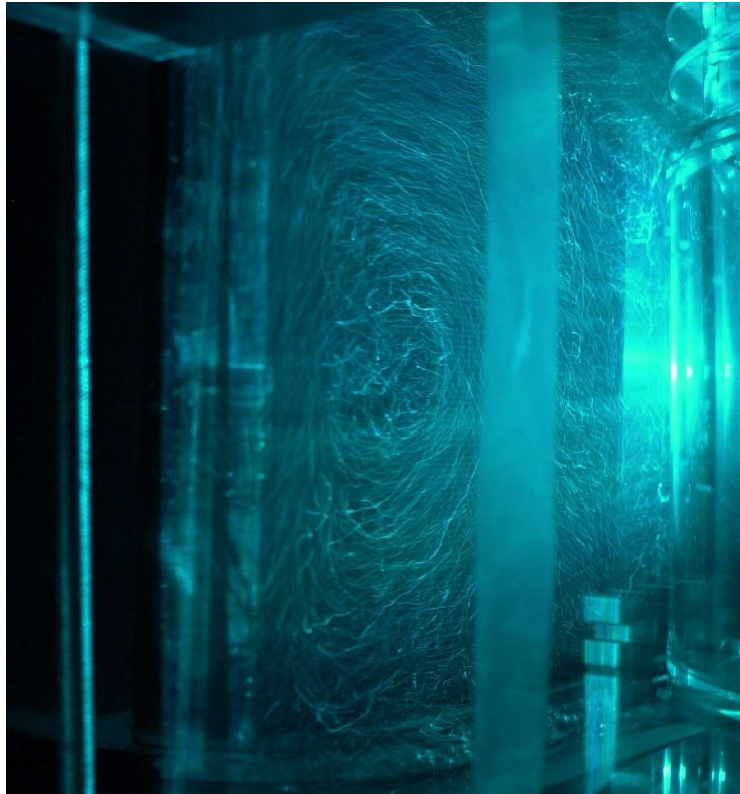


Figure A.3 Flow field below the HEX, position 4.

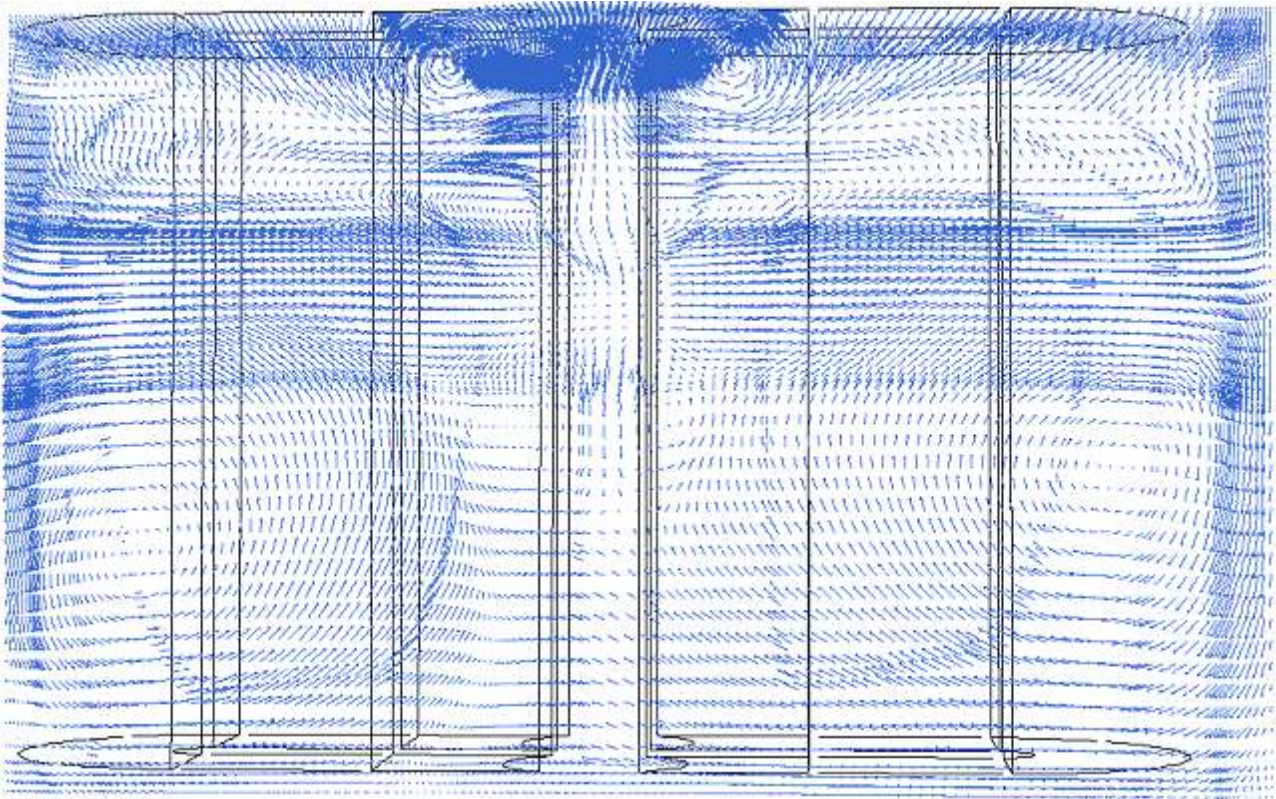


Figure A.4 Calculated flow field just below the HEX, positions 4 and 6

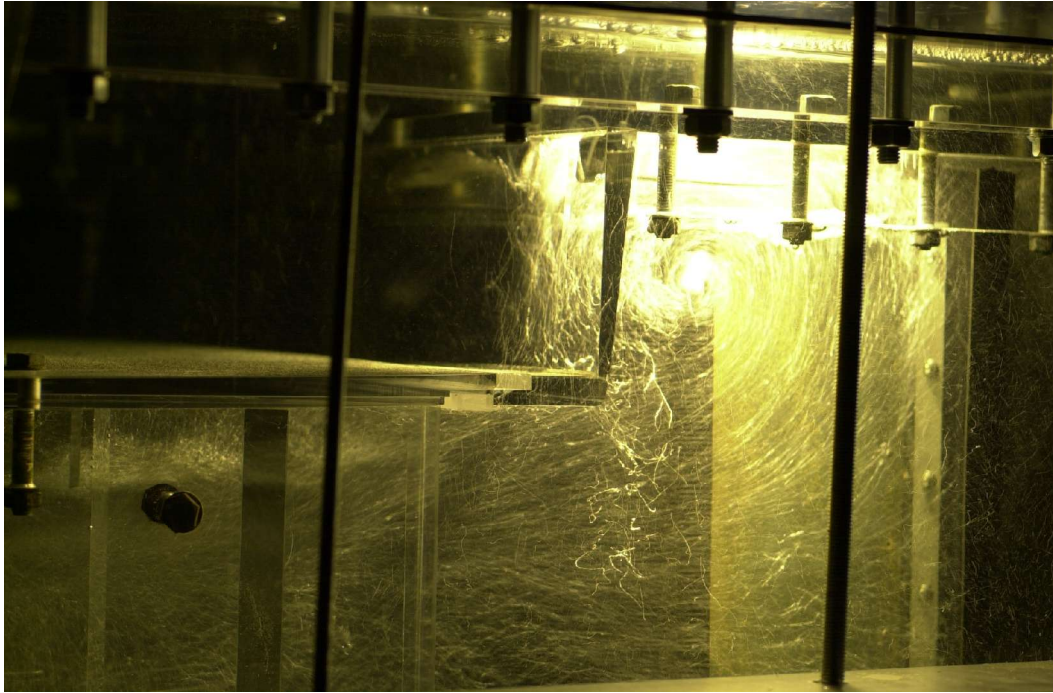


Figure A.5 Flow field at the side below the HEX, position 5.

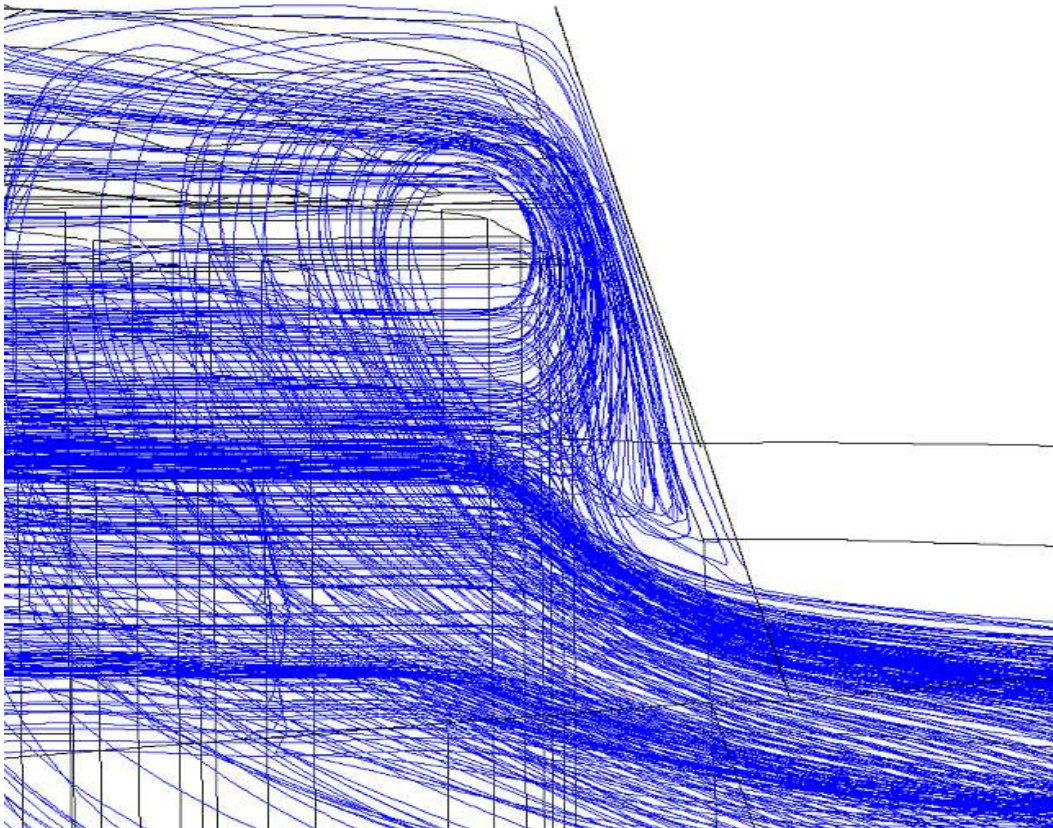


Figure A.6 Calculated flow field at the side below the HEX, position 5.

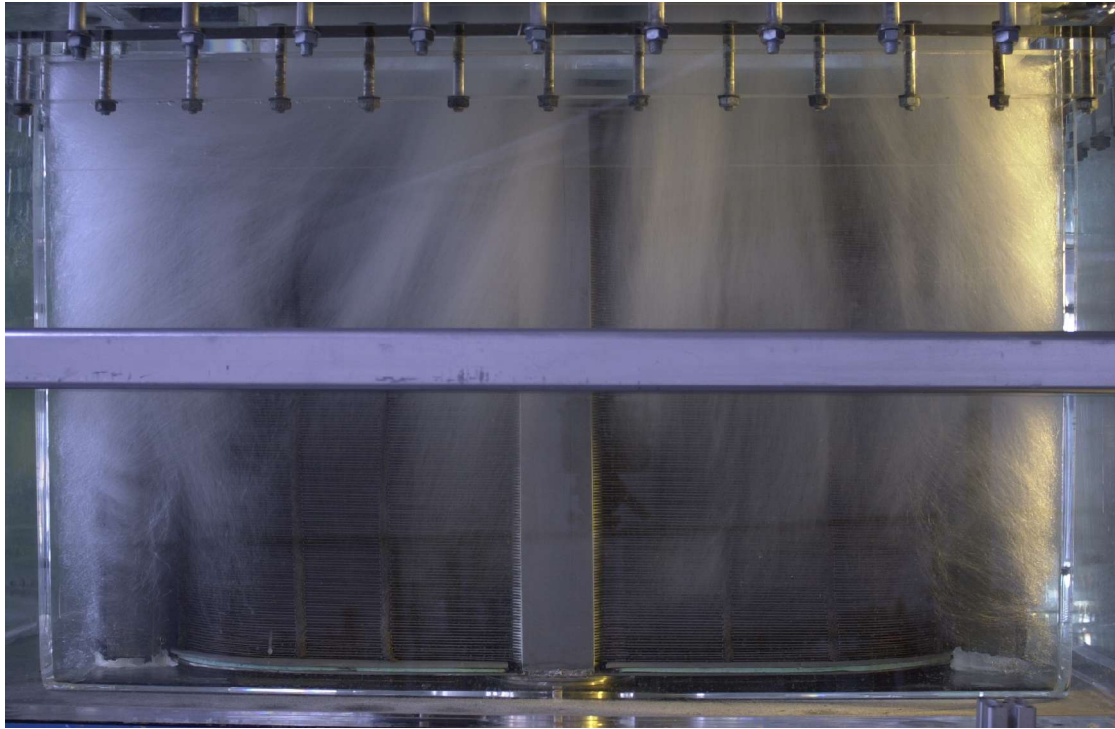


Figure A.7 HEX outlet flow field.

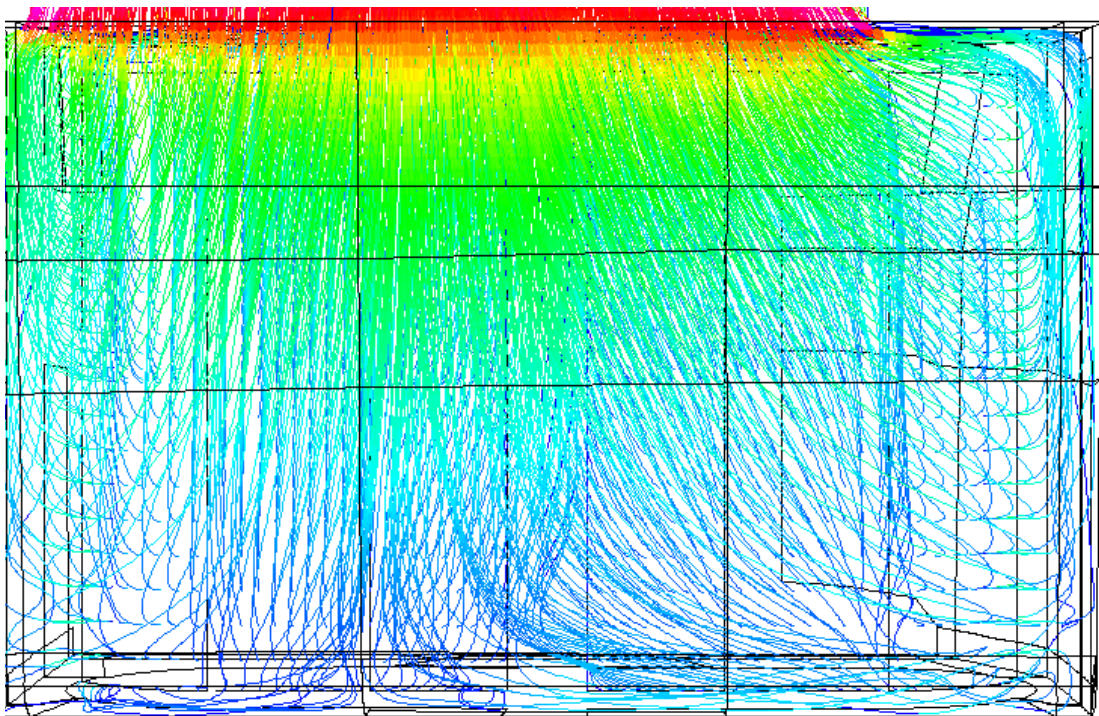


Figure A.8 Calculated HEX outlet flow field.

Appendix B, Angles used in the transformation matrices

In order to be able to easily transform coordinates between the local and the global systems the following angles are defined:

- α_1 - Angle between local x-axis and global x-axis
- α_2 - Angle between local y-axis and global x-axis
- α_3 - Angle between local z-axis and global x-axis
- β_1 - Angle between local x-axis and global y-axis
- β_2 - Angle between local y-axis and global y-axis
- β_3 - Angle between local z-axis and global y-axis
- γ_1 - Angle between local x-axis and global z-axis
- γ_2 - Angle between local y-axis and global z-axis
- γ_3 - Angle between local z-axis and global z-axis

With the local coordinate directions defined, in global coordinates, as:

$$\text{x-axis: } (x_X, x_Y, x_Z)$$

$$\text{y-axis: } (y_X, y_Y, y_Z)$$

$$\text{z-axis: } (z_X, z_Y, z_Z)$$

the different angles used in the transformation matrices are calculated by using the following general relation

$$\cos \theta = \frac{a \cdot b}{|a| \cdot |b|}$$

The individual angles are then calculated as

$$\alpha_1 = \arccos \frac{(x_X, y_X, z_X) \cdot (1, 0, 0)}{\|(x_X, y_X, z_X)\| \cdot \|(1, 0, 0)\|} = \arccos \frac{x_X}{\sqrt{x_X^2 + y_X^2 + z_X^2}}$$

$$\alpha_2 = \arccos \frac{(x_Y, y_Y, z_Y) \cdot (1, 0, 0)}{\|(x_Y, y_Y, z_Y)\| \cdot \|(1, 0, 0)\|} = \arccos \frac{x_Y}{\sqrt{x_Y^2 + y_Y^2 + z_Y^2}}$$

$$\alpha_3 = \arccos \frac{(x_Z, y_Z, z_Z) \cdot (1, 0, 0)}{\|(x_Z, y_Z, z_Z)\| \cdot \|(1, 0, 0)\|} = \arccos \frac{x_Z}{\sqrt{x_Z^2 + y_Z^2 + z_Z^2}}$$

$$\beta_1 = \arccos \frac{(x_X, y_X, z_X) \cdot (0, 1, 0)}{\|(x_X, y_X, z_X)\| \cdot \|(0, 1, 0)\|} = \arccos \frac{y_X}{\sqrt{x_X^2 + y_X^2 + z_X^2}}$$

$$\beta_2 = \arccos \frac{(x_Y, y_Y, z_Y) \cdot (0, 1, 0)}{\|(x_Y, y_Y, z_Y)\| \cdot \|(0, 1, 0)\|} = \arccos \frac{y_Y}{\sqrt{x_Y^2 + y_Y^2 + z_Y^2}}$$

$$\beta_3 = \arccos \frac{(x_Z, y_Z, z_Z) \cdot (0, 1, 0)}{\|(x_Z, y_Z, z_Z)\| \cdot \|(0, 1, 0)\|} = \arccos \frac{y_Z}{\sqrt{x_Z^2 + y_Z^2 + z_Z^2}}$$

$$\gamma_1 = \arccos \frac{(x_X, y_X, z_X) \cdot (0, 0, 1)}{\|(x_X, y_X, z_X)\| \cdot \|(0, 0, 1)\|} = \arccos \frac{z_X}{\sqrt{x_X^2 + y_X^2 + z_X^2}}$$

$$\gamma_2 = \arccos \frac{(x_Y, y_Y, z_Y) \cdot (0, 0, 1)}{\|(x_Y, y_Y, z_Y)\| \cdot \|(0, 0, 1)\|} = \arccos \frac{z_Y}{\sqrt{x_Y^2 + y_Y^2 + z_Y^2}}$$

$$\gamma_3 = \arccos \frac{(x_Z, y_Z, z_Z) \cdot (0, 0, 1)}{\|(x_Z, y_Z, z_Z)\| \cdot \|(0, 0, 1)\|} = \arccos \frac{z_Z}{\sqrt{x_Z^2 + y_Z^2 + z_Z^2}}$$

Appendix C, Momentum sources and active coefficients

In the following two sections the equations solved in the code for the momentum source terms and active coefficients are presented.

C1. Source Terms and Active Coefficients for the Straight Parts

The momentum source components in local Cartesian coordinates look like

$$S_x = -\mu \cdot (D_{xx} \cdot u + D_{xy} \cdot v + D_{xz} \cdot w) - \frac{1}{2} \cdot \rho \cdot |\vec{U}| \cdot (F_{xx} \cdot u + F_{xy} \cdot v + F_{xz} \cdot w)$$

$$S_y = -\mu \cdot (D_{yx} \cdot u + D_{yy} \cdot v + D_{yz} \cdot w) - \frac{1}{2} \cdot \rho \cdot |\vec{U}| \cdot (F_{yx} \cdot u + F_{yy} \cdot v + F_{yz} \cdot w)$$

$$S_z = -\mu \cdot (D_{zx} \cdot u + D_{zy} \cdot v + D_{zz} \cdot w) - \frac{1}{2} \cdot \rho \cdot |\vec{U}| \cdot (F_{zx} \cdot u + F_{zy} \cdot v + F_{zz} \cdot w)$$

The source terms in global Cartesian coordinates then become

$$S_X = S_x \cdot \cos \alpha_1 + S_y \cdot \cos \alpha_2 + S_z \cdot \cos \alpha_3$$

$$S_Y = S_x \cdot \cos \beta_1 + S_y \cdot \cos \beta_2 + S_z \cdot \cos \beta_3$$

$$S_Z = S_x \cdot \cos \gamma_1 + S_y \cdot \cos \gamma_2 + S_z \cdot \cos \gamma_3$$

and the active coefficients in global Cartesian coordinates

$$A_X = \frac{\partial S_X}{\partial U} = \frac{\partial S_x}{\partial U} \cdot \cos \alpha_1 + \frac{\partial S_y}{\partial U} \cdot \cos \alpha_2 + \frac{\partial S_z}{\partial U} \cdot \cos \alpha_3$$

$$A_Y = \frac{\partial S_Y}{\partial V} = \frac{\partial S_x}{\partial V} \cdot \cos \beta_1 + \frac{\partial S_y}{\partial V} \cdot \cos \beta_2 + \frac{\partial S_z}{\partial V} \cdot \cos \beta_3$$

$$A_Z = \frac{\partial S_Z}{\partial W} = \frac{\partial S_x}{\partial W} \cdot \cos \alpha_1 + \frac{\partial S_y}{\partial W} \cdot \cos \alpha_2 + \frac{\partial S_z}{\partial W} \cdot \cos \alpha_3$$

The U-derivatives of the local Cartesian components

$$\begin{aligned} \frac{\partial S_x}{\partial U} = & -\mu \cdot (D_{xx} \cdot \cos \alpha_1 + D_{xy} \cdot \cos \alpha_2 + D_{xz} \cdot \cos \alpha_3) \\ & - \frac{1}{2} \cdot \rho \cdot \left[\frac{U}{|\vec{U}|} \cdot (F_{xx} \cdot u + F_{xy} \cdot v + F_{xz} \cdot w) + |\vec{U}| \cdot (F_{xx} \cdot \cos \alpha_1 + F_{xy} \cdot \cos \alpha_2 + F_{xz} \cdot \cos \alpha_3) \right] \end{aligned}$$

$$\begin{aligned} \frac{\partial S_y}{\partial U} = & -\mu \cdot (D_{yx} \cdot \cos \alpha_1 + D_{yy} \cdot \cos \alpha_2 + D_{yz} \cdot \cos \alpha_3) \\ & - \frac{1}{2} \cdot \rho \cdot \left[\frac{U}{|\vec{U}|} \cdot (F_{yx} \cdot u + F_{yy} \cdot v + F_{yz} \cdot w) + |\vec{U}| \cdot (F_{yx} \cdot \cos \alpha_1 + F_{yy} \cdot \cos \alpha_2 + F_{yz} \cdot \cos \alpha_3) \right] \end{aligned}$$

$$\begin{aligned} \frac{\partial S_z}{\partial U} = & -\mu \cdot (D_{zx} \cdot \cos \alpha_1 + D_{zy} \cdot \cos \alpha_2 + D_{zz} \cdot \cos \alpha_3) \\ & - \frac{1}{2} \cdot \rho \cdot \left[\frac{U}{|\vec{U}|} \cdot (F_{zx} \cdot u + F_{zy} \cdot v + F_{zz} \cdot w) + |\vec{U}| \cdot (F_{zx} \cdot \cos \alpha_1 + F_{zy} \cdot \cos \alpha_2 + F_{zz} \cdot \cos \alpha_3) \right] \end{aligned}$$

The V-derivatives of the local Cartesian components

$$\frac{\partial S_x}{\partial V} = -\mu \cdot (D_{xx} \cdot \cos \beta_1 + D_{xy} \cdot \cos \beta_2 + D_{xz} \cdot \cos \beta_3)$$

$$-\frac{1}{2} \cdot \rho \cdot \left[\frac{V}{|\vec{U}|} \cdot (F_{xx} \cdot u + F_{xy} \cdot v + F_{xz} \cdot w) + |\vec{U}| \cdot (F_{xx} \cdot \cos \beta_1 + F_{xy} \cdot \cos \beta_2 + F_{xz} \cdot \cos \beta_3) \right]$$

$$\frac{\partial S_y}{\partial V} = -\mu \cdot (D_{yx} \cdot \cos \beta_1 + D_{yy} \cdot \cos \beta_2 + D_{yz} \cdot \cos \beta_3)$$

$$-\frac{1}{2} \cdot \rho \cdot \left[\frac{V}{|\vec{U}|} \cdot (F_{yx} \cdot u + F_{yy} \cdot v + F_{yz} \cdot w) + |\vec{U}| \cdot (F_{yx} \cdot \cos \beta_1 + F_{yy} \cdot \cos \beta_2 + F_{yz} \cdot \cos \beta_3) \right]$$

$$\frac{\partial S_z}{\partial V} = -\mu \cdot (D_{zx} \cdot \cos \beta_1 + D_{zy} \cdot \cos \beta_2 + D_{zz} \cdot \cos \beta_3)$$

$$-\frac{1}{2} \cdot \rho \cdot \left[\frac{V}{|\vec{U}|} \cdot (F_{zx} \cdot u + F_{zy} \cdot v + F_{zz} \cdot w) + |\vec{U}| \cdot (F_{zx} \cdot \cos \beta_1 + F_{zy} \cdot \cos \beta_2 + F_{zz} \cdot \cos \beta_3) \right]$$

The W-derivatives of the local Cartesian components

$$\frac{\partial S_x}{\partial W} = -\mu \cdot (D_{xx} \cdot \cos \gamma_1 + D_{xy} \cdot \cos \gamma_2 + D_{xz} \cdot \cos \gamma_3)$$

$$-\frac{1}{2} \cdot \rho \cdot \left[\frac{W}{|\vec{U}|} \cdot (F_{xx} \cdot u + F_{xy} \cdot v + F_{xz} \cdot w) + |\vec{U}| \cdot (F_{xx} \cdot \cos \gamma_1 + F_{xy} \cdot \cos \gamma_2 + F_{xz} \cdot \cos \gamma_3) \right]$$

$$\frac{\partial S_y}{\partial W} = -\mu \cdot (D_{yx} \cdot \cos \gamma_1 + D_{yy} \cdot \cos \gamma_2 + D_{yz} \cdot \cos \gamma_3)$$

$$-\frac{1}{2} \cdot \rho \cdot \left[\frac{W}{|\vec{U}|} \cdot (F_{yx} \cdot u + F_{yy} \cdot v + F_{yz} \cdot w) + |\vec{U}| \cdot (F_{yx} \cdot \cos \gamma_1 + F_{yy} \cdot \cos \gamma_2 + F_{yz} \cdot \cos \gamma_3) \right]$$

$$\frac{\partial S_z}{\partial W} = -\mu \cdot (D_{zx} \cdot \cos \gamma_1 + D_{zy} \cdot \cos \gamma_2 + D_{zz} \cdot \cos \gamma_3)$$

$$-\frac{1}{2} \cdot \rho \cdot \left[\frac{W}{|\vec{U}|} \cdot (F_{zx} \cdot u + F_{zy} \cdot v + F_{zz} \cdot w) + |\vec{U}| \cdot (F_{zx} \cdot \cos \gamma_1 + F_{zy} \cdot \cos \gamma_2 + F_{zz} \cdot \cos \gamma_3) \right]$$

where the local Cartesian velocity components can be expressed in global Cartesian velocity components

$$u = U \cdot \cos \alpha_1 + V \cdot \cos \beta_1 + W \cdot \cos \gamma_1$$

$$v = U \cdot \cos \alpha_2 + V \cdot \cos \beta_2 + W \cdot \cos \gamma_2$$

$$w = U \cdot \cos \alpha_3 + V \cdot \cos \beta_3 + W \cdot \cos \gamma_3$$

C2. Source Terms and Active Coefficients for the Bends

The source components in cylindrical coordinates look like

$$S_r = -\mu \cdot (D_{rr} \cdot u_r + D_{r\theta} \cdot u_\theta + D_{rz} \cdot u_z) - \frac{1}{2} \cdot \rho \cdot |\vec{U}| \cdot (F_{rr} \cdot u_r + F_{r\theta} \cdot u_\theta + F_{rz} \cdot u_z)$$

$$S_\theta = -\mu \cdot (D_{\theta r} \cdot u_r + D_{\theta\theta} \cdot u_\theta + D_{\theta z} \cdot u_z) - r \cdot \frac{1}{2} \cdot \rho \cdot |\vec{U}| \cdot (F_{\theta r} \cdot u_r + F_{\theta\theta} \cdot u_\theta + F_{\theta z} \cdot u_z)$$

$$S_z = -\mu \cdot (D_{zr} \cdot u_r + D_{z\theta} \cdot u_\theta + D_{zz} \cdot u_z) - \frac{1}{2} \cdot \rho \cdot |\vec{U}| \cdot (F_{zr} \cdot u_r + F_{z\theta} \cdot u_\theta + F_{zz} \cdot u_z)$$

In local Cartesian coordinates the velocity components in cylindrical coordinates are

$$u_r = u \cdot \cos \theta + v \cdot \sin \theta$$

$$u_\theta = v \cdot \cos \theta - u \cdot \sin \theta$$

$$u_z = w$$

The local Cartesian velocity components can be expressed in global Cartesian velocity components

$$u = U \cdot \cos \alpha_1 + V \cdot \cos \beta_1 + W \cdot \cos \gamma_1$$

$$v = U \cdot \cos \alpha_2 + V \cdot \cos \beta_2 + W \cdot \cos \gamma_2$$

$$w = U \cdot \cos \alpha_3 + V \cdot \cos \beta_3 + W \cdot \cos \gamma_3$$

Finally we can express the cylindrical velocity components in the global Cartesian velocity components

$$u_r = \cos \theta \cdot (U \cdot \cos \alpha_1 + V \cdot \cos \beta_1 + W \cdot \cos \gamma_1) \\ + \sin \theta \cdot (U \cdot \cos \alpha_2 + V \cdot \cos \beta_2 + W \cdot \cos \gamma_2)$$

$$u_\theta = \cos \theta \cdot (U \cdot \cos \alpha_2 + V \cdot \cos \beta_2 + W \cdot \cos \gamma_2) \\ - \sin \theta \cdot (U \cdot \cos \alpha_1 + V \cdot \cos \beta_1 + W \cdot \cos \gamma_1)$$

$$u_z = U \cdot \cos \alpha_3 + V \cdot \cos \beta_3 + W \cdot \cos \gamma_3$$

In local Cartesian coordinates the source components can be expressed as

$$S_x = S_r \cdot \cos \theta - \frac{1}{r} \cdot S_\theta \cdot \sin \theta$$

$$S_y = S_r \cdot \sin \theta + \frac{1}{r} \cdot S_\theta \cdot \cos \theta$$

$$S_z = S_z$$

The source terms for the bends in global coordinates can then be calculated as for the straight parts

$$S_x = S_x \cdot \cos \alpha_1 + S_y \cdot \cos \alpha_2 + S_z \cdot \cos \alpha_3$$

$$S_y = S_x \cdot \cos \beta_1 + S_y \cdot \cos \beta_2 + S_z \cdot \cos \beta_3$$

$$S_z = S_x \cdot \cos \gamma_1 + S_y \cdot \cos \gamma_2 + S_z \cdot \cos \gamma_3$$

Knowing the local Cartesian components the active coefficients can be calculated in the same manner as for the straight parts

$$A_x = \frac{\partial S_x}{\partial U} = \frac{\partial S_x}{\partial U} \cdot \cos \alpha_1 + \frac{\partial S_y}{\partial U} \cdot \cos \alpha_2 + \frac{\partial S_z}{\partial U} \cdot \cos \alpha_3$$

$$A_y = \frac{\partial S_y}{\partial V} = \frac{\partial S_x}{\partial V} \cdot \cos \beta_1 + \frac{\partial S_y}{\partial V} \cdot \cos \beta_2 + \frac{\partial S_z}{\partial V} \cdot \cos \beta_3$$

$$A_z = \frac{\partial S_z}{\partial W} = \frac{\partial S_x}{\partial W} \cdot \cos \alpha_1 + \frac{\partial S_y}{\partial W} \cdot \cos \alpha_2 + \frac{\partial S_z}{\partial W} \cdot \cos \alpha_3$$

To calculate the active coefficients the different derivatives of the local pressure gradient components have to be determined.

The U-derivatives:

$$\frac{\partial S_x}{\partial U} = \frac{\partial S_r}{\partial U} \cdot \cos \theta - \frac{1}{r} \cdot \frac{\partial S_\theta}{\partial U} \cdot \sin \theta$$

$$\frac{\partial S_y}{\partial U} = \frac{\partial S_r}{\partial U} \cdot \sin \theta + \frac{1}{r} \cdot \frac{\partial S_\theta}{\partial U} \cdot \cos \theta$$

$$\frac{\partial S_z}{\partial U} = \frac{\partial S_z}{\partial U}$$

The V-derivatives:

$$\frac{\partial S_x}{\partial V} = \frac{\partial S_r}{\partial V} \cdot \cos \theta - \frac{1}{r} \cdot \frac{\partial S_\theta}{\partial V} \cdot \sin \theta$$

$$\frac{\partial S_y}{\partial V} = \frac{\partial S_r}{\partial V} \cdot \sin \theta + \frac{1}{r} \cdot \frac{\partial S_\theta}{\partial V} \cdot \cos \theta$$

$$\frac{\partial S_z}{\partial V} = \frac{\partial S_z}{\partial V}$$

The W-derivatives:

$$\frac{\partial S_x}{\partial W} = \frac{\partial S_r}{\partial W} \cdot \cos \theta - \frac{1}{r} \cdot \frac{\partial S_\theta}{\partial W} \cdot \sin \theta$$

$$\frac{\partial S_y}{\partial W} = \frac{\partial S_r}{\partial W} \cdot \sin \theta + \frac{1}{r} \cdot \frac{\partial S_\theta}{\partial W} \cdot \cos \theta$$

$$\frac{\partial S_z}{\partial W} = \frac{\partial S_z}{\partial W}$$

To calculate the derivatives above the following derivatives of the cylindrical gradient components are needed

The U-derivatives:

$$\begin{aligned} \frac{\partial S_r}{\partial U} = & -\mu \cdot [D_{rr} \cdot (\cos \theta \cdot \cos \alpha_1 + \sin \theta \cdot \cos \alpha_2) + D_{r\theta} \cdot (\cos \theta \cdot \cos \alpha_2 - \sin \theta \cdot \cos \alpha_1) \\ & + D_{rz} \cdot \cos \alpha_3] - \frac{1}{2} \cdot \rho \cdot \frac{U}{|\vec{U}|} \cdot (F_{rr} \cdot u_r + F_r \theta \cdot u_\theta + F_{rz} \cdot u_z) \\ & - \frac{1}{2} \cdot \rho \cdot |\vec{U}| \cdot [F_{rr} \cdot (\cos \theta \cdot \cos \alpha_1 + \sin \theta \cdot \cos \alpha_2) \end{aligned}$$

$$+F_{r\theta} \cdot (\cos \theta \cdot \cos \alpha_2 - \sin \theta \cdot \cos \alpha_1) + F_{rz} \cdot \cos \alpha_3]$$

$$\begin{aligned} \frac{\partial S_\theta}{\partial U} = & -r \cdot \mu \cdot [D_{\theta r} \cdot (\cos \theta \cdot \cos \alpha_1 + \sin \theta \cdot \cos \alpha_2) + D_{\theta\theta} \cdot (\cos \theta \cdot \cos \alpha_2 - \sin \theta \cdot \cos \alpha_1) \\ & + D_{\theta z} \cdot \cos \alpha_3] - r \cdot \frac{1}{2} \cdot \rho \cdot \frac{U}{|\vec{U}|} \cdot (F_{\theta r} \cdot u_r + F_{\theta\theta} \cdot u_\theta + F_{\theta z} \cdot u_z) \\ & - r \cdot \frac{1}{2} \cdot \rho \cdot |\vec{U}| \cdot [F_{\theta r} \cdot (\cos \theta \cdot \cos \alpha_1 + \sin \theta \cdot \cos \alpha_2) \\ & + F_{\theta\theta} \cdot (\cos \theta \cdot \cos \alpha_2 - \sin \theta \cdot \cos \alpha_1) + F_{\theta z} \cdot \cos \alpha_3] \end{aligned}$$

The V-derivatives:

$$\begin{aligned} \frac{\partial S_r}{\partial V} = & -\mu \cdot [D_{rr} \cdot (\cos \theta \cdot \cos \beta_1 + \sin \theta \cdot \cos \beta_2) + D_{r\theta} \cdot (\cos \theta \cdot \cos \beta_2 - \sin \theta \cdot \cos \beta_1) \\ & + D_{rz} \cdot \cos \beta_3] - \frac{1}{2} \cdot \rho \cdot \frac{V}{|\vec{U}|} \cdot (F_{rr} \cdot u_r + F_{r\theta} \cdot u_\theta + F_{rz} \cdot u_z) \\ & - \frac{1}{2} \cdot \rho \cdot |\vec{U}| \cdot [F_{rr} \cdot (\cos \theta \cdot \cos \beta_1 + \sin \theta \cdot \cos \beta_2) \\ & + F_{r\theta} \cdot (\cos \theta \cdot \cos \beta_2 - \sin \theta \cdot \cos \beta_1) + F_{rz} \cdot \cos \beta_3] \end{aligned}$$

$$\begin{aligned} \frac{\partial S_\theta}{\partial V} = & -r \cdot \mu \cdot [D_{\theta r} \cdot (\cos \theta \cdot \cos \beta_1 + \sin \theta \cdot \cos \beta_2) + D_{\theta\theta} \cdot (\cos \theta \cdot \cos \beta_2 - \sin \theta \cdot \cos \beta_1) \\ & + D_{\theta z} \cdot \cos \beta_3] - r \cdot \frac{1}{2} \cdot \rho \cdot \frac{V}{|\vec{U}|} \cdot (F_{\theta r} \cdot u_r + F_{\theta\theta} \cdot u_\theta + F_{\theta z} \cdot u_z) \\ & - r \cdot \frac{1}{2} \cdot \rho \cdot |\vec{U}| \cdot [F_{\theta r} \cdot (\cos \theta \cdot \cos \beta_1 + \sin \theta \cdot \cos \beta_2) \\ & + F_{\theta\theta} \cdot (\cos \theta \cdot \cos \beta_2 - \sin \theta \cdot \cos \beta_1) + F_{\theta z} \cdot \cos \beta_3] \end{aligned}$$

The W-derivatives:

$$\frac{\partial S_r}{\partial W} = -\mu \cdot [D_{rr} \cdot (\cos \theta \cdot \cos \gamma_1 + \sin \theta \cdot \cos \gamma_2) + D_{r\theta} \cdot (\cos \theta \cdot \cos \gamma_2 - \sin \theta \cdot \cos \gamma_1)]$$

$$\begin{aligned}
& + D_{rz} \cdot \cos \gamma_3] - \frac{1}{2} \cdot \rho \cdot \frac{W}{|\vec{U}|} \cdot (F_{rr} \cdot u_r + F_r \theta \cdot u_\theta + F_{rz} \cdot u_z) \\
& - \frac{1}{2} \cdot \rho \cdot |\vec{U}| \cdot [F_{rr} \cdot (\cos \theta \cdot \cos \gamma_1 + \sin \theta \cdot \cos \gamma_2) \\
& + F_{r\theta} \cdot (\cos \theta \cdot \cos \gamma_2 - \sin \theta \cdot \cos \gamma_1) + F_{rz} \cdot \cos \gamma_3]
\end{aligned}$$

$$\begin{aligned}
\frac{\partial S_\theta}{\partial W} = & -r \cdot \mu \cdot [D_{\theta r} \cdot (\cos \theta \cdot \cos \gamma_1 + \sin \theta \cdot \cos \gamma_2) + D_{\theta \theta} \cdot (\cos \theta \cdot \cos \gamma_2 - \sin \theta \cdot \cos \gamma_1) \\
& + D_{\theta z} \cdot \cos \gamma_3] - r \cdot \frac{1}{2} \cdot \rho \cdot \frac{W}{|\vec{U}|} \cdot (F_{\theta r} \cdot u_r + F_{\theta \theta} \cdot u_\theta + F_{\theta z} \cdot u_z) \\
& - r \cdot \frac{1}{2} \cdot \rho \cdot |\vec{U}| \cdot [F_{\theta r} \cdot (\cos \theta \cdot \cos \gamma_1 + \sin \theta \cdot \cos \gamma_2) \\
& + F_{\theta \theta} \cdot (\cos \theta \cdot \cos \gamma_2 - \sin \theta \cdot \cos \gamma_1) + F_{\theta z} \cdot \cos \gamma_3]
\end{aligned}$$